

1-1-2013

Understanding the Effect of Balance of Plant Contaminants On PEMFCS Performance: Models, Mechanisms, Functional Group

Hyun-Seok Cho
University of South Carolina

Follow this and additional works at: <https://scholarcommons.sc.edu/etd>

 Part of the [Chemical Engineering Commons](#)

Recommended Citation

Cho, H.(2013). *Understanding the Effect of Balance of Plant Contaminants On PEMFCS Performance: Models, Mechanisms, Functional Group*. (Doctoral dissertation). Retrieved from <https://scholarcommons.sc.edu/etd/571>

This Open Access Dissertation is brought to you by Scholar Commons. It has been accepted for inclusion in Theses and Dissertations by an authorized administrator of Scholar Commons. For more information, please contact digres@mailbox.sc.edu.

UNDERSTANDING THE EFFECT OF BALANCE OF PLANT CONTAMINANTS ON
PEMFCs PERFORMANCE: MODELS, MECHANISMS, FUNCTIONAL GROUP

by

Hyun-Seok Cho

Bachelor of Engineering
Sogang University, 2005

Submitted in Partial Fulfillment of the Requirements

For the Degree of Doctor of Philosophy in

Chemical Engineering

College of Engineering and Computing

University of South Carolina

2013

Accepted by:

John W. Van Zee, Major Professor

James A. Ritter, Committee Member

Christopher T. Williams, Committee Member

Yeomin Yoon, Committee Member

John W. Weidner, Chair of Chemical Engineering, Committee Member

Lacy Ford, Vice Provost and Dean of Graduate Studies

© Copyright by Hyun-Seok Cho, 2013
All Rights Reserved.

DEDICATION

To my parents and brother,

Beomsuk Cho, Myungha Park and Ki-Young Cho

사랑하는 부모님과 동생에게 바칩니다.

ACKNOWLEDGEMENTS

I can not help but let my mind drift back to the very first day at USC. To be assigned the advisor, I was asked to see Dr. Van Zee and that 5 minute was the longest talking time ever I had with second lanaguage. I cannot forget that moment. I believe that it was just start of my luck in U.S.A. I am grateful for my adavisor, Dr. John W. Van Zee, for his excellence guidance and commitment through my doctoral research. “You are the one who made I am today, Dr. Van Zee.” Thank you.

Special thanks to committee members, Drs. Ritter, Williams, and Yoon for their insightful comments and suggestions during achievement of this work. You have contributions to this studty in a variety of ways.

And a very special thanks to my teacher, Dr. Ohashi who has generously accept my questions and discussions. I am also most grateful to my group members, classmates, Korean associate students, and former boss, SMK who led me to USC.

My parents, Myungha Park and Ki-Young Cho, as well as other family members have provided care, physical and emotional. This is dedicated to you all.

I also would like to thank my wife, Na Young, has assisted me in innumerable ways, whatever I might say here cannot extent the value of her contribution.

Finally, I send gratitude separately to my son, Kenneth (Heejae). To anyone I may have omitted my apologies: I appreciated your efforts nonetheless.

ABSTRACT

This dissertation considers contamination of a proton exchange membrane fuel cell (PEMC) that may result from chemicals that reach from balance of plant materials. Both model predictions and experimental data are addressed. The model for contamination of a PEMFC includes adsorption on Pt catalysts, absorption or ion-exchange with ionomeric components into electrode structure and the membrane. The measurable variables for inputs to the model are obtainable the ex-situ experiments and allow comparison of the model to the in-situ infusion studies.

The model is used to predict the cathode contamination impact on Pt/C electrode and membrane assuming no transport of contaminant from cathode to anode. The model prediction accounts for the three contamination mechanisms such as adsorption, ion-exchange, absorption and three sources of voltage (i.e., performance) loss. The model is developed by considering well known chemical engineering concepts of Langmuir adsorption, partition coefficients, plug flow reactors (PFRs), and dimensionless analysis. The three important dimensionless groups that result from the analysis are the Da (contamination reaction rate), ψ (capacity ratio), and Γ (coverage ratio).

Selected model compounds were identified in leachate solutions during the screening of off-the-shelf BOP materials. Ex-situ studies using a rotating disk electrode and a membrane conductivity device allow the preparation of isotherms based on functionality and fundamental mechanisms. The isotherms for each mechanism provide a

quantitative effect of coverage by these compounds. The in-situ data obtained from segmented cell experiments is also reported.

The comparison of the model predictions with *in-situ* experiment data shows consistent predicted coverage and performance loss. The prediction results for different species that drive the contamination mechanisms agree with experimentally determined voltage losses for each mechanism. The voltage loss for the ionomer by an ion-exchange mechanism shows the slowest contamination rate but the greatest performance loss relative to other mechanisms (i.e., adsorption/absorption). That is, voltage losses by ion-exchange continued with feed contaminant until the cell totally lost the performance. In addition, the maximum coverage by contaminants with absorption and adsorption mechanisms is determined by the leachate concentration. Finally, the tolerance limit for the each mechanism is provided from the predictions allows for the establishment of qualification standards for BOP materials.

TABLE OF CONTENTS

DEDICATION	iii
ACKNOWLEDGEMENTS.....	iv
ABSTRACT	v
LIST OF TABLES	xii
LIST OF FIGURES	xiv
LIST OF SYMBOLS	xxiii
LIST OF ABBREVIATIONS.....	xxvii
CHAPTER 1: RESEARCH OBJECTIVE AND BACKGROUND	1
1.1 PROTON EXCHANGE MEMBRANE FUEL CELLS	1
1.2 COST AND DURABILITY.....	2
1.3 DISSERTATION OBJECTIVE AND OUTLINE	3
CHAPTER 2: LITERATURE REVIEW	8
2.1 INTRODUCTION	8
2.2 CONTAMINATION MECHANISMS.....	10
2.3 SYSTEM CONTAMINANTS	21
2.4 CONTAMINATION MODELS	24
CHAPTER 3: A MODEL FOR PREDICTING PERFORMANCE LOSS IN PEMFCs FROM BOP LEACHATES	26
3.1 INTRODUCTION	27
3.2 MODEL.....	30

3.3 MODEL PREDICTION.....	45
3.4 COMPARISON TO EXPERIMENTAL DATA.....	66
3.5 CONCLUSION	79
CHAPTER 4: UNDERSTANDING THE FUNDAMENTAL MECHANISMS AND PREDICTING PERFORMANCE LOSS IN PEMFCs FROM ANILINE AS A CONTAMINANT	82
4.1 INTRODUCTION	83
4.2 EXPERIMENTAL	89
4.3 RESULT AND DISCUSSION.....	93
4.4 CONCLUSION	114
CHAPTER 5: THE CONTAMINATION BEHAVIOR OF ORGANIC MODEL COMPOUNDS ON PEMFC BASED UPON FUNCTIONALITIES: URETHANE BASED ASSEMBLY AIDS	116
5.1 INTRODUCTION	117
5.2 EXPERIMENTAL	120
5.3 RESULT AND DISCUSSION.....	123
5.4 CONCLUSION	146
CHAPTER 6: THE CONTAMINATION MECHANISM AND BEHAVIOR OF AMIDE BOND CONTAINING ORGANIC CONTAMINANT ON PEMFC: PPA	149
6.1 INTRODUCTION	150
6.2 EXPERIMENTAL	153
6.3 RESULT AND DISCUSSION.....	156
6.4 CONCLUSION	185
CHAPTER 7: ABSORPTION BEHAVIOR OF VANADIUM IN NAFION [®] MEMBRANE	187
7.1 INTRODUCTION	187
7.2 EXPERIMENTAL	189
7.3 RESULT AND DISCUSSION.....	192

7.4 CONCLUSION	200
CHAPTER 8: CONCLUSION AND PROPOSED FUTURE WORK.....	202
8.1 CONCLUSION	202
8.2 PROPOSED FUTURE WORK	203
REFERENCES	204
APPENDIX A – ESTIMATION OF RH CHANGE IN THE CHANNEL AND SCALING FACTOR.....	217
APPENDIX B – MATLAB CODE FOR THE CONTAMINATION MODEL	220
APPENDIX C – CALCULATION OF AMMONIA FEEDS INTO RDE	223
APPENDIX D – DIFFUSION COEFFICIENTS FOR CATIONS	224
APPENDIX E – RAW DATA OF VANADIUM ABSORPTION	229

LIST OF TABLES

Table 1.1 Technical targets for automotive and for stationary applications	6
Table 2.1 Origin of common fuel and air impurities	9
Table 3.1 Consideration of experiment conditions for selecting dimensionless numbers: Pt contamination	46
Table 3.2 Consideration of experiment conditions for selecting dimensionless numbers: ionomer contamination	47
Table 3.3 Consideration of experiment conditions for selecting dimensionless numbers: membrane contamination.....	48
Table 3.4 Selected dimensionless numbers for the prediction.....	49
Table 3.5 Experimental conditions shown in Figure 3.15 and comparison $\Delta ECSA$	74
Table 3.6 Dimensionless numbers for model prediction in Figure 3.15.....	74
Table 3.7 Dimensionless numbers for model prediction in Figures 3.16 and 17	77
Table 4.1 Properties of aniline in H_2O	84
Table 4.2 Measured capacity of membranes and MEA by different cations.....	97
Table 4.3 Equilibrium constants for N117 different cations.....	97
Table 4.4 Comparison electrode properties for various experiment conditions after 200 potential cycles (0-0.6V vs. RHE) in 0.04mN aniline solution ($HClO_4$)	110
Table 4.5 Consideration of experiment conditions for selecting dimensionless numbers: Pt contamination	139
Table 4.6 Consideration of experiment conditions for selecting dimensionless numbers: membrane and ionomer contamination.....	145
Table 5.1 Prediction of voltage change (ΔV_{pt}) by Pt contamination.....	139
Table 5.2 Prediction of voltage change ($\Delta V_{ionomer}$) by ionomer contamination	139

Table 5.3 Comparison of prediction and measured total voltage change by contamination	139
Table 5.4 Dimensionless numbers to use for prediction in Figure 5.11	145
Table 5.5 Comparison predicted Δ ECSA to in-situ CV measurements	145
Table 6.1 Slopes of cation exchanged NRE211 membrane conductivity	164
Table 6.2 Kinetic constants of caprolactam for ring opening reaction	164
Table 6.3 pK value for ring opening reaction of ϵ -caprolactam at different temperatures	164
Table 6.4 Assignments of ATR-IR peaks of ϵ -caprolactam exchanged form Nafion [®] ...	180
Table 7.1 Vanadium ion form in acid solution (octahedral shape)	196
Table 7.2 Comparison of absorption isotherm curves of Nafion [®] with VO ²⁺ in different concentration of H ₂ SO ₄ solutions	196
Table 7.3 Comparison of membrane conductivity of N115 with VO ²⁺ , V ³⁺ , Na ⁺ , and Ca ²⁺	199

LIST OF FIGURES

Figure 1.1 Schematic of proton exchange membrane fuel cell.....	5
Figure 1.2 BOP & Stack cost comparison in PEMFCs	7
Figure 1.3 Classification of polymers by performance and cost	7
Figure 2.1 Schematic of the Pt/C electrode structure with ionomer	11
Figure 2.2 Chemical structure of proton & sodium form Nafion [®]	13
Figure 2.3 Ion-exchange isotherms for Nafion [®] 117 of alkali metal cations.....	14
Figure 2.4 Water contents (λ) of Nafion [®] 117 membrane with various cations	15
Figure 2.5 Conductivity at $25.0 \pm 0.1^\circ\text{C}$ in Nafion [®] 117 plotted against ammonium content in the membrane phase. The linear interpolation between the pure proton and the pure ammonium form Nafion [®] 117 conductivity is also shown in both plots.....	16
Figure 2.6 Line scan and BSE images of sodium and calcium contaminated MEA blue line (bottom): 2.5mM, red line (above): 5.0mM calcium at 0.6V operating	19
Figure 2.7 Kinetic current of oxygen reduction on platinum covered with Nafion film in 0.1N H ₂ SO ₄ solution containing various kinds of impurity cations with various amounts as compared with H ⁺ . The kinetic current j_k , c (film) for contaminated film normalized by the kinetic current j_k , r(film) for noncontaminated film is plotted as a function of soaking time. Impurity level: 0.1% (\square), 1% (Δ), or 10% (O). (a) Li ⁺ , (b) Ca ²⁺ , (c) Fe ³⁺ , (d) Ni ²⁺	20
Figure 2.8 (a) CO stripping graph of Pt electrode. The electrode was exposed to 100 sccm 50% CO ₂ /50% H ₂ for 10 h before flushing with N ₂ for 5 min. Scan rate = 10mV/s, T _{cell} =70°C, RH(A/C)=100%. (b) Same electrode exposed only to H ₂	22
Figure 2.9 Potential sources of contamination.....	23
Figure 3.1 Schematic of channel and control volume for a model (a) top view, (b) Pt/ionomer cotamination (c) membrane contamination.....	32
Figure 3.2 Predicting ΔV with Butler-Volmer equation and conductivity * RH=60%, I=10A, Na ⁺ contamination data	44

Figure 3.3 a) Dimensionless concentration at the interface (@ $\xi=0$), b) Coverage and Pt availability, c) Voltage changes as varies with Da_1 and Ψ_1 and fixed $\Gamma_1=6.0$ by Pt contamination (a) High/High (b) Low/High & High/Low (c) Low/Low	52
Figure 3.4 a) Dimensionless concentration at the interface (@ $\xi=0$), b) Coverage and Pt availability, c) Voltage changes by Pt contamination as varies with Γ_1 (a) 0.2 (b) 2.0 (c) 6.0 and Da_1 and Ψ_1 are fixed.	55
Figure 3.5 a) Dimensionless concentration at the interface (@ $\xi=0$), b) Coverage and acid sites availability, c) Voltage changes as varies with Da_2 and Ψ_2 and fixed $\Gamma_2=1.0$ (a) High/High (b) Low/High & High/Low (c) Low/Low.....	58
Figure 3.6 a) Dimensionless concentration at the interface (@ $\xi=0$), b) Coverage and acid sites availability, c) Voltage changes by ionomer contamination as varies with Γ_2 (a) 80 (b) 10 (c) 1 and Da_2 and Ψ_2 are fixed.	60
Figure 3.7 a) Dimensionless concentration at the interface (@ $\xi=0$), b) Coverage and acid sites availability, c) Voltage changes by membrane contamination as varies with Da_3 and Ψ_3 and fixed $\Gamma_3=1.0$ (a) High/High (b) Low/High & High/Low (c) Low/Low	63
Figure 3.8 a) Dimensionless concentration at the interface (@ $\xi=0$), b) Coverage and acid sites availability c) Voltage changes by membrane contamination as varies with Γ_3 (a) 80 (b) 10 (c) 1 and Da_3 and Ψ_3 are fixed	65
Figure 3.9 Local coverage and ΔV distributions for contaminant A to the dimensionless length as varies of Da , a) adsorption, $1X(Da_1=0.03, \Psi_1=0.14, \Gamma_1=6)$, b) ion-exchange, $1X(Da_2=0.056, \Psi_2=0.003, \Gamma_2=1.0)$	67
Figure 3.10 Local coverage and ΔV distributions for contaminant A to the dimensionless length as varies of Ψ , a) adsorption, $1X(Da_1=0.03, \Psi_1=0.14, \Gamma_1=6)$, b) ion-exchange, $1X(Da_2=0.056, \Psi_2=0.003, \Gamma_2=1.0)$	68
Figure 3.11 <i>Ex-situ</i> adsorption isotherm curve of Pt/C for DEGEE and 4-MBSA	70
Figure 3.12 Comparison of <i>ex-situ</i> and <i>in-situ</i> for Pt contamination scaling	71
Figure 3.13 Comparison of model predictions and <i>in-situ</i> DEGEE infusion voltage loss (iR corrected).....	73
Figure 3.14 Analysis of total voltage loss by contamination sources.....	76
Figure 3.15 Comparison of model predictions and <i>in-situ</i> 30ppm of NaOH infusion voltage loss.....	80
Figure 3.16 <i>In-situ</i> measurements of $\Delta ECSA$ during 30ppm of NaOH infusion for 80 h.....	81
Figure 4.1 Schematic of aniline and hydration form (a) aniline; (b) hydrated anilinium ion	

.....	86
Figure 4.2 Identify model compounds from SBR leachants by GCMS	87
Figure 4.3 Schematic of adsorbed aniline on Pt site	88
Figure 4.4 Ion-exchange isotherms of MEA (Pt loading 0.4/0.4 mg/cm ²) for different cations (a) sodium (b) ammonium (c) aniline (anilinium) (d) calcium at T=23°C.....	96
Figure 4.5 a) Comparison of water uptake of pristine, sodium, aniline exchanged N117s at different RHs b) Membrane conductivity of anilinium exchanged NRE211 membranes as a function of proton mole fraction of NRE211 and RH	99
Figure 4.6 In plane membrane conductivity of NRE211 membranes as a function of RH and concentration of contaminants (a) pristine (b) 99% of sodium (c) 99% of ammonium (d) 99% of potassium (e) 50% of aniline (f) 70% of aniline (g) 99% of aniline	100
Figure 4.7 ATR-IR spectrums of (a) pristine (b) aniline (c) sodium (d) sodium and aniline absorbed N117	103
Figure 4.8 a) Cyclic voltammograms of aniline contaminated carbon supported 20% Pt catalyst (a) 0.0 mM (b) 0.04 mM (c) 0.10 mM (d) 0.19 mM of aniline in 0.1M HClO ₄ solution. b) Cyclic voltammograms of aniline contaminated (0.04 mM) Vulcan XC-72R and growth of electrochemically synthesized PANI after (a) 5 (b) 10 (c) 30 (d) 100 CV cycles The electrode had an area of 0.24 cm ² , the temperature was 23°C, and the scan rate was 25mV/s.	104
Figure 4.9 a) Partial cyclic voltammograms scan of aniline contaminated carbon supported 45.5% platinum catalyst (a) 0.0 mM (b) 1.2 μM (c) 0.04 mM (d) 0.08 mM (e) 0.8 mM of aniline in 0.1M HClO ₄ solution. b) Partial cyclic voltammograms scan of benzene contaminated carbon supported 45.5% platinum catalyst (a) 0.0 mM (b) 1.2 μM (c) 0.04 mM (d) 0.08 mM (e) 0.8 mM of aniline in 0.1M HClO ₄ solution.....	105
Figure 4.10 Adsorption isotherms of aniline and benzene for 45.5 wt% Pt/C electrode at 0.4V vs. RHE, T=23°C, Pt loading=0.02mg/cm ²	106
Figure 4.11 a) Aniline contamination effect of ORR current for a 45.5% Pt supported on carbon catalyst in 0.1M HClO ₄ at 5mV/s with O ₂ purge: (a) 0mM; (b) 0.008mM; (c) 0.08mM; (d) 0.4mM ; ω=1600rpm. b) Tafel slopes of a) (a) 0mM; (b) 0.008mM; (c) 0.08mM; (d) 0.4mM	107
Figure 4.12 Predicting voltage change depends on coverage for each contamination source (a) ionomer (b) Pt (c) membrane at RH=60%, (d) membrane at RH=40%, (e) membrane at RH=80%	113
Figure 5.1 Chemical structures of model compounds chosen for study	118
Figure 5.2 Ion-exchange isotherm for N-H containing organic model compounds	125

Figure 5.3 Comparison of membrane conductivity for model compounds: ion-exchange and absorption	128
Figure 5.4 Comparison of membrane conductivity for model compounds	129
Figure 5.5 Cyclic voltammograms for contaminated Pt/C catalyst: T=23 °C, 0.1M HClO ₄ , scan rate=20mv/s, 0.0 – 1.05V, Pt loading=0.02mg/cm ²	131
Figure 5.6 Adsorption isotherm of Pt/C electrode at 0.4V for model compounds	134
Figure 5.7 <i>In-situ</i> voltage response for model compound infusion: Infusion on cathode T _{cell} = 80 °C, RH=32/32 %, stoich.=2.0/2.0, back pressure=150/150 kPa.....	136
Figure 5.8 <i>In-situ</i> voltage response for DEGEE: Infusion on cathode: T= 80 °C, RH=32/32 %, stoich.=2.0/2.0, back pressure=150/150 kPa	141
Figure 5.9 Prediction for the coverage by ex-situ adsorption isotherm for DEGEE	142
Figure 5. 10 Comparison of predictions to the experiment results of 2,6-DAT infusion	144
Figure 5.11 Schematic for the prediction of voltage change: correlation between <i>ex-situ</i> and <i>in-itu</i>	148
Figure 6.1 (a) ε-caprolactam (b) 1, 8-diaza cyclotetradecane-2, 7-dione (DCDD)	151
Figure 6.2 a) UV-vis spectrum of various concentration of ε -caprolactam solutions in 0.1M HCl(aq) (a)10mN (b)5mN (c)5mN after soaking a piece of N117 (3×3cm ²) soak (d)1mN b) various concentration aqueous ε -caprolactam solutions (a)0.25mN (b)0.50mN (c)1.0mN (d)5.0mN (e)10mN (f)1.0mN after soaking of a piece of NR211(3×3cm ²) c) various concentration of ε-caprolactam solutions in 10mM HCl(aq) (a)5mN (b)5mN after soaking of N117 (3cm×3cm) at RT (c)1mN (d)1mN after soaking of SGL 35 BC (e) 5mN after soaking a piece of N117 (3×3cm ²) at 90°C	158
Figure 6.3 Schematic of protonated ε-caprolactam by acid-catalyzed hydrolysis mechanism and possible electrostatic interaction with sulfonic group	160
Figure 6.4 Conductivity of NE211 and comparison of various contaminants for the effect of RH and contaminant (% ion-exchanged) concentration	162
Figure 6.5 Comparison of ion-exchange isotherm of Nafion [®] membrane for (a) ammonium (b) sodium (c) aniline (d) ε -caprolactam	167
Figure 6.6 a) Cyclic voltammograms of 45.5% Pt/C and polycrystalline Pt catalyst as concentration of caprolactam increasing a) 0μM b) 8μM (≅ 100ML) c) 40μM (≅ 500ML) d) 80μM (≅ 1000ML) e) 0.4mM (≅ 5000ML) f) 0.8mM (≅ 10000ML) (b) Caprolactam effect on cyclic voltammograms of Pt/C catalyst electrode at 73°C (a) 0 (b) 8μM (c) 16μM (d) 40μM (e) 80μM (f) 0.4mM	170

Figure 6.7 ORR kinetic current density and Tafel slopes of 45.5% Pt/C catalyst as concentration of ϵ -caprolactam is increasing; a) ORR at pH=1; a) 0 b) 8 μ M c) 80 μ M d) 0.4mM b) ORR at pH=2; a) 0 b) 8 μ M c) 80 μ M d) 0.4mM	172
Figure 6.8 pH effect on ECSA loss of Pt/C electrode in the presence of ϵ -caprolactam at T=25°C (a) pH=1 (b) pH=2	173
Figure 6.9 a) CV of Nafion [®] coated on Pt/C electrode (a) pristine (b) CH ₃ COOH (c) After potential cycles up to 1.2V with clean electrolyte b) (a) pristine (b) 5000ML NH ₃ (g) (c) saturated NH ₃ (g) (d) after potential cycles to 1.2V in clean 0.1M HClO ₄	177
Figure 6.10 a) ATR-IR analysis of various exchanged form of Nafion [®] b) ATR-IR analysis of methanol solutions (a) ϵ -caprolactam (b) ϵ -amino caproic acid (c) extract solution of ϵ -caprolactam out of N115 (d) extract solution of ϵ -amino caproic acid out of N115 (e) methanol	179
Figure 6.11 <i>in-situ</i> response for ϵ -caprolactam at different temperatures on a single cell in PEMFCs a) voltage response (a) T=50 °C (b) T=80 °C b) CV graphs (a) T=50 °C (b) T=80 °C	183
Figure 6.12 Hydration of Nafion [®] membrane at various temperatures and humidity	184
Figure 7.1 Absorption isotherm curves of vanadium ions for Nafion [®]	193
Figure 7.2 Comparison of absorption isotherm curves of Nafion [®] with VO ²⁺ in different concentration of H ₂ SO ₄ solutions compared to Na ⁺ and Ca ²⁺	195
Figure 7.3 Comparison of membrane conductivity of Nafion [®] with VO ²⁺ , V ³⁺ , Na ⁺ and Ca ²⁺	198

LIST OF SYMBOLS

B = maximum coverage measured by *ex-situ* isotherms

C_A = concentration of contaminant A on the channel, [mol/cm³]

C_A^* = concentration of contaminant A at the interface, [mol/cm³]

C_{A0} = feed concentration of contaminant A on the channel, [mol/cm³]

C_{AS} = concentration of the adsorbed contaminant A on the Pt sites [mol/cm²]

C_{AM} = concentration of exchanged acid sites by contaminant A, [mol/cm³]

C_{ij} = concentration of species i on surface j, [mol/cm²]

C_H = concentration of proton, [mol/cm³]

C_{HM} = concentration of available acid sites, [mol/cm³]

$C_{HM}(t=0)$ = initial concentration of available acid sites, [mol/cm³]

C_s = surface concentration of Pt sites, [mol/cm²]

$C_s(t=0)$ = initial Pt concentration on the surface, [mol/cm²]

C_w = concentration of water on the channel, [mol/cm³]

C_w^* = concentration of water at the interface, [mol/cm³]

$C_{w,a}$ = water concentration on anode interface [moles/cm³]

$C_{w,c}$ = water concentration on cathode interface [moles/cm³]

D_{GDL} = diffusion coefficient for contaminant A through GDL, [cm²/s]

$D_{ionomer}$ = diffusion coefficient for contaminant A in ionomer, [cm²/s]

D_{eff} = effective diffusion coefficient for contaminant A, [cm²/s]

D_{mem} = diffusion coefficient for contaminant A in membrane, [cm²/s]

D_w = diffusion coefficient for water through membrane, [cm²/s]

Da = dimensionless number, reaction rate, see Eq. [3.16] and Eq. [3.28]

F = Faraday's constant, 96,487 [C/equiv]

h = height of channel, 8.38×10^{-4} [cm]

i = current density [A/ cm²]

i_0 = exchange current density [A/ cm²]

K_{eq} = equilibrium constant for the Langmuir isotherm or partition coefficient
for the ion-exchange isotherms

L = channel length, 102.4 [cm]

N_m = MacMullin number, 2 for GDL and CL

N_w = flux of water [mol/cm² s]

n = number of electrons transferred in electrode reaction

n_d = electro-osmotic drag coefficient

p_{ij}, q_{ij} = Butler-Volmer coefficient, see Eq. [3.44]

R = Gas constant, 8314 [kPa cm³/mol K]

r = rib width, 6.60×10^{-2} [cm]

s = stoichiometric coefficient in electrode reaction

T = temperature [K]

u_f = a linear fluid velocity, [cm/s]

V_{ocv} = open circuit voltage [V]

w = channel width, 8.89×10^{-2} [cm]

X_i = mole fraction of species i in solution, $i=A$ and H

i_M = mole fraction of species i in membrane, $i=A$ and H

z_A = charge number of species A

z_{mem} = thickness of membrane, 25×10^{-4} [cm]

z_{ionomer} = thickness of ionomer, 1×10^{-4} [cm]

z_{GDL} = thickness of GDL, [cm] see Table 3.1 to 3.3

Greek

α = ratio of net water flux per proton flux

$\alpha_{a,c}$ = transfer coefficients

β = dimensionless number for geometry of the channel, see Eq. [3.16]

Γ = dimensionless number, coverage ratio, see Eq. [3.16] and Eq. [3.28]

Γ_{max} = dimensionless number, maximum coverage ratio, see Eq. [3.16]

δ = effective diffusion length [cm], see Table 3.1 to 3.3

η = overpotential [V]

θ = coverage by contaminant on Pt surface

κ = conductivity [S/cm]

λ = water contents in membrane

ξ = dimensionless length

τ = dimensionless time

Φ_A = dimensionless concentration of contaminant A on the channel

Φ_A^* = dimensionless concentration of contaminant A at the interface

χ = coverage by contaminant in acid sites

Ψ = dimensionless number, capacity ratio, see Eq. [3.16] and Eq. [3.28]

LIST OF ABBREVIATIONS

BOP	Balance of Plant
BP	Bipolar Plate
CV	Cyclic Voltammetry
DAT	Di Amino Toluene
DEGEE	Di Ethylene Glycol monoEthly Ether
DEGMEA	Di Ethylene Glycol Monoethly Ether Acetate
DOE	Department Of Energy
ECSA	Electro Chemical Surface Area
EIS	Electro Impedence Spectrometer
GDL	Gas Diffusion Layer
HFCIT	Hydrogen, Fuel Cells and Infrastructure Technologies
HFR	High Frequency Resistance
LSV	Linear Sweep Voltage
MBSA	Methyl Benzen Sulfon Amine
MEA	Membrane Electrode Assembly
OCV	Open Circuit Voltage
PEM	Proton Exchange Membrane
PEMFC	Proton Exchange Membrane Fuel Cell
PPA	Poly Phthalate Amide
RDE	Rotating Disk Electrode
RFB	Redox Flow Battery

CHAPTER 1

RESEARCH OBJECTIVE AND BACKGROUND

1.1 PROTON EXCHANGE MEMBRANE FUEL CELLS

PEMFCs have shown great promise as an alternative energy conversion devices which have the potential to reduce various problems associated with present combustion technologies. Fuel cell technology may provide many benefits, including environmental, economic, and the security of energy source.

PEMFCs are being developed as electrical power for portable devices, vehicles, and stationary applications since PEMFCs can operate at relatively low temperatures (70 – 120 °C). Higher-temperature PEMFCs are also being studied for vehicles and stationary applications; however, transient responses such as slow start-up and shut-down processes are not amenable to vehicular applications.

A PEMFC operates as an energy conversion device with hydrogen fuel supplied on the anode, and feeds such as air, oxygen etc., on the cathode. The hydrogen gas splits into protons and electrons on the Pt catalyst electrode, and the proton goes through the Proton Exchange Membrane (PEM) from the anode to the cathode, followed by oxygen reduction reaction (ORR) to produce only water as a byproduct, while the electrons run through electrical circuits to generate electrical energy. Figure 1.1 shows a schematic of the PEMFC system and illustrates the flow of the gases. PEMFCs are also theoretically

more efficient than present combustion technology in their energy conversion from chemical to electrical energy since PEMFCs do not need to be recharged with an external energy source. They just need refilling of the the fuel tank to produce more energy.



1.2 COST AND DURABILITY

Even though PEMFC developers have shown significant technological advances, there are two major obstacles to commercializing PEMFCs for vehicles. PEMFCs are not cost competitive and do not have a guaranteed lifetime for most applications, so the critical issue for the commercialization of PEMFCs is to ensure their durability and stability without increasing their cost.

The U.S. DOE office of Energy Efficiency and Renewable Energy's Hydrogen, Fuel Cells and Infrastructure Technologies (HFCIT) Program is working to overcome critical technological problems with fuel cell commercialization. The DOE's technological targets for automotive and stationary applications regarding cost and durability are shown in Table 1.1. The DOE plan describes the milestones, targets, requirements, time plans, etc., of automotive fuel cell systems, and also of stationary applications. Automotive fuel cell systems must last for at least 5,000 hours, and stationary fuel cell systems must last 40,000 hours, with less than 5 % performance degradation. The important fact is that cost and durability are interrelated.

1.3 DISSERTATION OBJECTIVE AND OUTLINE

Contamination research for the wider commercialization of proton exchange membrane fuel cells (PEMFCs), has received much attention. Also, the analysis of cost in PEMFC systems shows that the cost of Balance of Plant (BOP) materials can be as much as 30% of the stack cost. One opportunity to decrease these costs is to use off-the-shelf materials rather than custom-made materials if leachates from the less expensive materials would not effect the performance of PEMFCs. The research of this dissertation is focused on system-derived contaminants cases, but it also addresses possible contamination mechanisms of system contaminant. Another objective of this dissertation is to gain general fundamental understanding of the importance of functional groups and compounds. This understanding will allow us to predict contaminants' effects. We already know that they have functional groups and what compounds they are composed of. Thus, this dissertation proposes that we produce a materials catalogue with acceptable level of contaminants to guide the fuel cell industry in making material selection based on cost-benefit analysis of system components. Selected model compounds to study were identified in leachate solutions during the screening of off-the-shelf BOP materials.

A predictive and mechanistic model is expected to help not only in understanding performance loss by contamination based on mechanisms, but also in providing mitigation strategies. The requirements for the contamination model are simple, measureable variables which are widely applicable to the various contaminants. The model should also be based on a fundamental understanding of contamination mechanisms through common sources such as Pt, ionomer, and membrane. The main

advantage of this model is that the tolerance limit for each mechanism is predictable. This allows for the establishment of qualification standards for BOP materials.

We also study fundamental mechanisms so that correlation between chemical species, functional groups, and PEMFC responses can be developed. The mechanisms are quantified for the catalyst electrode and membrane in order to examine *in-situ* and *ex-situ* data. The *ex-situ* studies using a rotating disk electrode and a membrane conductivity device allow the preparation of isotherms based on functionality and fundamental mechanisms. The isotherms for each mechanism provide a quantitative effect of coverage by these compounds and are included in the developed model. The *in-situ* data obtained from segmented cell experiments is also reported.

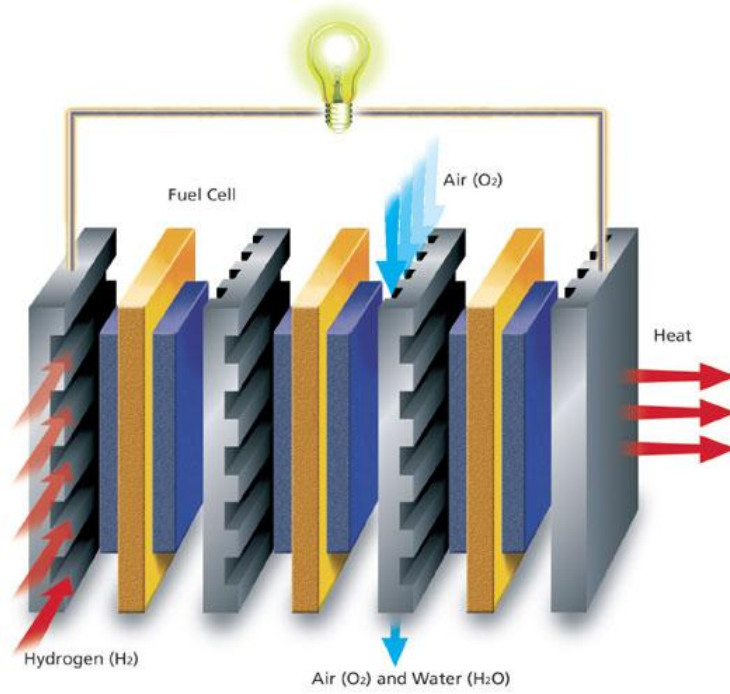


Figure 1.1 Schematic of a PEMFC [2]

Table 1.1 Technical targets for automotive and for stationary applications [4]

80-kW Integrated Transportation Fuel Cell Power Systems Operating on Direct Hydrogen					
Characteristic	Units	2003	2005	2010	2015
Cost	\$/kW	200	110	45	30
Durability with cycling	hours	N/A	~1,000	5,000	5,000
Integrated Stationary PEM Fuel Cell Power Systems(5-250kW) Operating on Reformate					
Characteristic	Units	2003	2005	2011	
Cost	\$/kW	2,500	2,500	750	
Durability with cycling	hours	15,000	20,000	40,000	

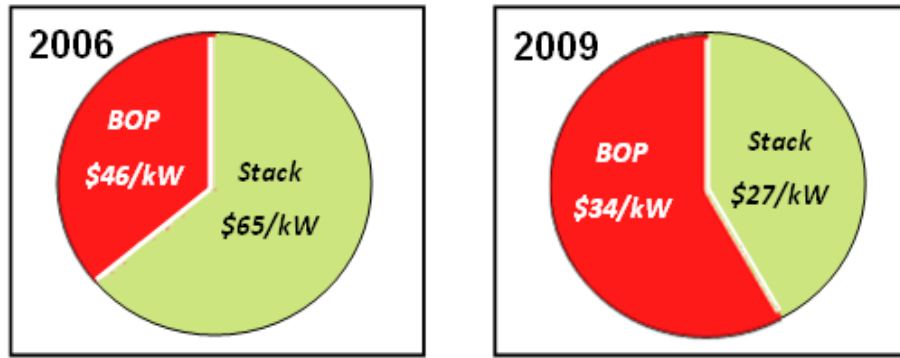
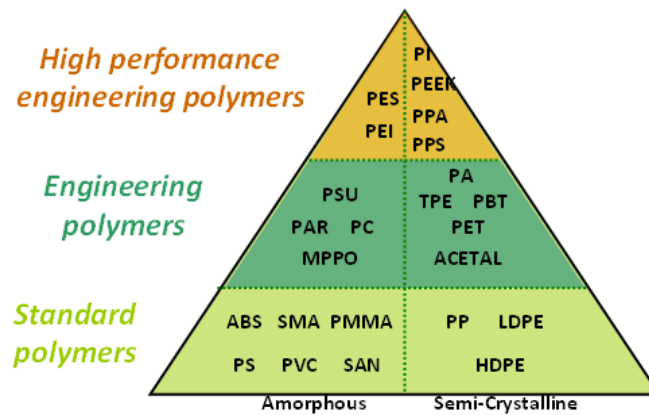


Figure 1.2 BOP & Stack cost comparison in PEMFCs [3]



PSU: Polysulfone
 PC: Polycarbonate
 PBT: Polybutylene Terephthalate
 PPS: Polyphenylene Sulfide
PPA: Polyphthalamide
 PA: Polyamide
 PPO: Polyphenylene Oxide
 POM: Polyoxymethylene
 PET: Polyethylene Terephthalate
 Phenolic
 Melamine
 ABS: Acrylonitrile-Butadiene-Styrene
 PS: Polystyrene
 PE: Polyethylene
 PP: Polypropylene
 PVC: Polyvinylchloride

High cost



Low cost

Figure 1.3 Classification of polymers by performance and cost

CHAPTER 2

LITERATURE REVIEW

2.1 INTRODUCTION

It is important to understand the degradation of key materials such as platinum, ionomer, carbon support, bipolar plate, Gas Diffusion Layer (GDL) in PEMFCs, Membrane Electrode Assembly (MEA) in order to meet DOE targets for PEMFCs. Many previous studies of contamination [5-18] in PEMFCs have shown the sensitivity of performance to the low levels of contamination. The cation leachates from gaskets or seals or fuel or catalyst metals [5-21] are well known contaminants of the membrane, using an ion-exchange mechanism. The catalyst contamination by an adsorption mechanism from feed gas contaminants such as SO₂ [18-19], CO [21], and H₂S [20], has also been shown. However, organic contaminants have received relatively little attention, while metal cation, air, and fuel contamination of PEMFCs have been studied extensively. In addition to understanding reasons for contamination, we must study the impact from the system point of view. However, previous studies are generally focused on understanding how contamination impacts the separate components such as PEM and Pt/C electrode by *ex-situ* or a single cell infusion test for MEA by *in-situ*.

Table 2.1 Origin of common fuel and air impurities [3]

Hydrogen Fuel Impurities	
Fuel for hydrogen	Potential impurities
crude oil:	CO, NH ₃ , H ₂ S, HCN
gasoline	hydrocarbons, aldehydes
diesels	mercaptans
natural gas	CO, NH ₃ , H ₂ S, HCN
	hydrocarbons, mercaptans
methanol/DME	CO, odorants, alcohols
Biomass	cations, aldehydes, alcohols, formic acid, NH ₃ , H ₂ S, HCN
water electrolysis	anions, cations
Air Impurities	
fuel combustion pollution	SO _x , NO _x , hydrocarbons, soots and particulates
ambient air, farming	NH ₃
natural sources	ocean salts, dust
Others	
de-icers	NaCl, CaCl ₂
FC system corrosion products	cations, anions

2.2 CONTAMINATION MECHANISMS

The fundamental contamination mechanisms of a PEMFC include adsorption on Pt catalysts, absorption or ion-exchange with ionomeric components into electrode structure and the membrane. Figure 2.1 shows a schematic of the electrode structure of a Pt/C catalyst with an ionomer binder on the surface of the PEM. Two mechanisms, adsorption on Pt active sites and ion-exchange by cationic contaminants in proton sites of ionomeric components, will be discussed. For each contamination mechanism, the different contamination sources such as Pt, ionomer, and membrane need to be explained.

2.2.1 MEMBRANE CONTAMINATION BY ION-EXCHANGE/ABSORPTION

In 1968 Dupont released a proton exchange membrane (or, alternatively, polymer electrolyte membrane) based on poly perfluorosulfonic acid with the trade name Nafion[®] [22]. A perfluorosulfonic acid based ionomer (Nafion[®]) has been the industry standard proton exchange membrane material and binder for PEMFCs. Figure 2.2 shows the chemical structure of the Nafion[®] membrane for proton and sodium form. The fluorinated back bond (C-F) back bone gives much greater resistance to chemical and physical degradation. The sulfonic acid group has proton conducting sites which require humidified gas streams to hydrate the PEM.

For the proton conduction in PEM, vehicle and hopping mechanisms are suggested. The vehicle mechanism provides proton conduction through the water cluster in the PEM, and the hopping mechanism provides proton conduction through the hopping of protons from water molecules. From the contamination point of view, the cation ion-exchange reaction can block the proton pathway in PEM so as to retard proton conduction by the

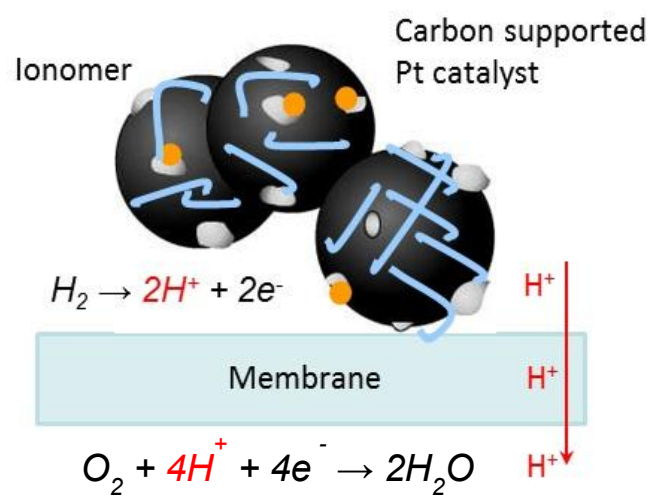


Figure 2.1 Schematic of the Pt/C electrode structure with ionomer

hopping mechanism. Again, the cations can electrostatically interact with sulfonic acid sites in PEM, resulting in the loss of proton conductivity. Previous studies support the idea that the Nafion[®] and other PEM favor metal cations over protons except the Li ion [6-14]. Okada et al. [10-12] reported that ion-exchange isotherms for the Nafion[®] membrane of alkali and metal cations (and in general, the divalent and multivalent cations) show much higher affinity to PEM.

As a result of the ion-exchange reaction, the proton conductivity of PEM is drastically decreased by the blocking effect as well as by dehydration of the membrane. If the proton sites which are the sulfonic acid groups of PEM are occupied by cations, the proton conduction pathway is interfered. However, the water cluster of PEM can aid in conducting the proton by vehicle mechanism. Unfortunately, the contamination by ion-exchange also leads the dehydration of PEM. As shown Figure 2.4, Okada et al. [10-12] reported that the water content in Nafion[®] 117 membrane lowers as various cations replace the proton sites of the sulfonic acid group in Nafion[®] 117. The dehydration of PEM also supports the increase of ohmic resistance, resulting in loss of conductivity. The extent of dehydration to the PEM strongly depends on the size, hydrophobicity (or hydrophilicity) and functionality of the contaminants.

Likewise, alkali and alkaline earth metals, ammonia (NH₃) are easily protonated in liquid water and/or acid solution so that those cationic form contaminants lower the proton conductivity of the PEM. The exposure of NH₃ as low as 13 ppm produced a rapid decrease in PEMFC performance [23]. Uribe et al. [24] (shown in Figure 2.5) studied the effect of NH₃ and NH₄⁺ on the conductivity of the Nafion[®] membrane in the aqueous and

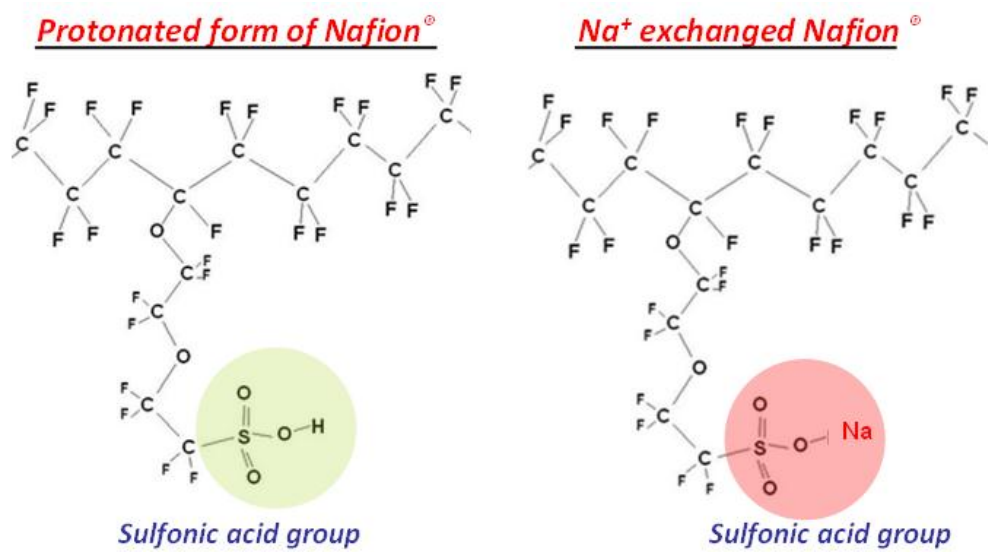


Figure 2.2 Chemical structure of proton & sodium form Nafion[®]

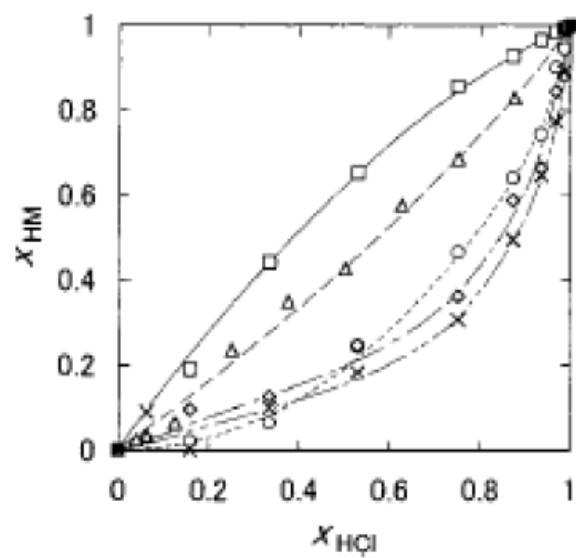


Figure 2.3 Ion-exchange isotherms for Nafion® 117 of alkali metal cations [8]

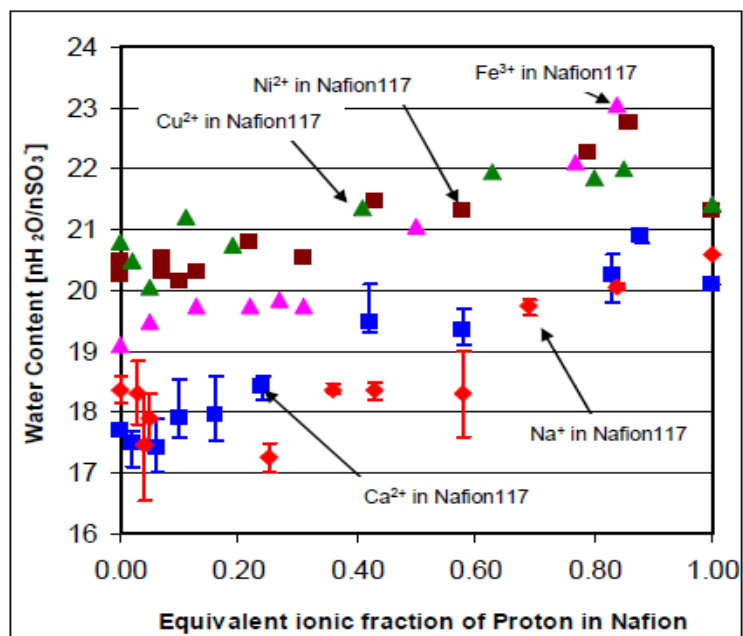


Figure 2.4 Water contents (λ) of Nafion[®] 117 membrane with various cations

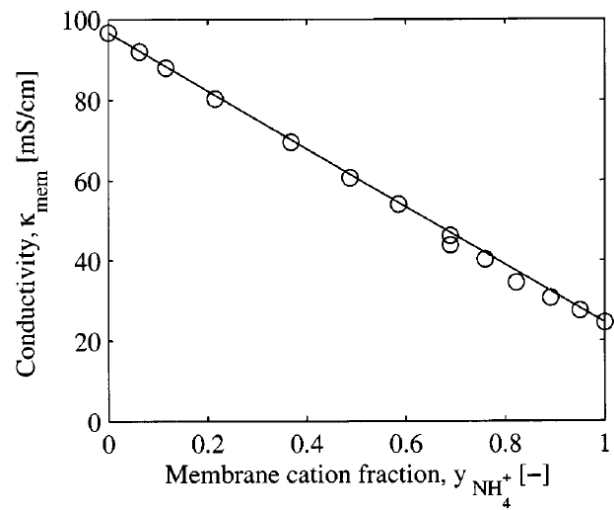


Figure 2.5 Conductivity at $25.0 \pm 0.1^\circ\text{C}$ in Nafion[®] 117 plotted against ammonium content in the membrane phase (y_{NH_4}). The linear interpolation between the pure proton and the pure ammonium form Nafion[®] 117 conductivity is also shown in both plots [24]

vapor phases. The proton conductivity decreases as increasing molar fraction of ammonium to proton in PEM. Hongsirikarn [25] also reported that the operation of PEM fuel cells at relatively high humidity improves the ammonia tolerance. Ohashi et al. [26] presented that a great deal of sodium and calcium is found in PEM (shown in Figure 2.6) in relative to electrode and GDL. The performance loss by calcium contamination is partially recovered, while the monovalent sodium contamination showed greater recovery than calcium [26].

The study of correlation between water contents in PEM and proton conductivity is well introduced in the work of Zawodzinski et al. [22]. They compared the water uptake of three chemically similar membranes (Nafion 117, Membrane C, and Dow) to describe the transport of mobile species in a Fuel Cell. Even though all of the membranes were studied based on PEM proton sites, the Dow membranes showed much higher proton conductivity in liquid water. This would be explained by water content differences in the PEM. Even though the characteristic of the PFSA groups of each membrane is identical (sulfonic acid group to conduct proton through a membrane) the water content (λ , the number of water molecules per the number of sulfonate groups for a membrane immersed in liquid water) of the immersed membrane for Dow was 15% higher than others. Thus, a membrane which has more swelling morphology in liquid water would show increasing proton conductivity in the PFSA membrane. In similar experiments [22-25] by other researchers, the conductivity of various equivalent weights of Nafion[®] was presented as the conductivity versus water contents (i.e., λ , the molar ratio of water molecules to sulfonic acid sites). That is, the membrane hydration with optimized acid sites of PEM is a critical factor for the proton conduction mechanism.

The presence of cations in the ionomer (binder) of the electrode may also compensate for the electrochemical reaction on the catalyst. Okada et al. [6-8] studied especially for ORR on a platinum plate rotating disk electrode (RDE) covered with Nafion[®] ionomer in the presence of different cation contaminants such as alkali and alkaline earth metal ions, alkylammonium in an H₂SO₄ solution. The decay of cathode electrode kinetic current is confirmed with as few as 0.1% cation contaminants introduced into the system as shown in Figure 2.7. However, cation contaminant interaction with Pt/C electrode may be explained by a different mechanism compared to contaminant adsorption on the Pt/C catalyst surface, as will be shown in the next section. The ion-exchange reaction which occurs by cations can change the formation of the polymer binder at the interface of the ionomer and the Pt surface and removal of the water from the electrode. This result is very similar to the ion exchange in PEM. The decay is interrelated with the water content in the Nafion[®] membrane. Thus, this contamination effect produces a slower reaction compared to other contaminants on the Pt/C electrode by adsorption mechanism [6-8].

2.2.2 Pt/C ELECTRODE CONTAMINATION BY ADSORPTION

Some of contaminants can be adsorbed on the surface of the Pt/C catalyst surface. This results in a loss of electrochemical surface area (ECSA). The best known contaminants by adsorption mechanism are carbon monoxide (CO) [21], hydrogen sulfide (H₂S) [22], sulfur dioxide (SO₂) [23], etc. The CO can chemisorb strongly on the Pt surface, resulting in a reduction of electro-oxidation rates and raising electrode

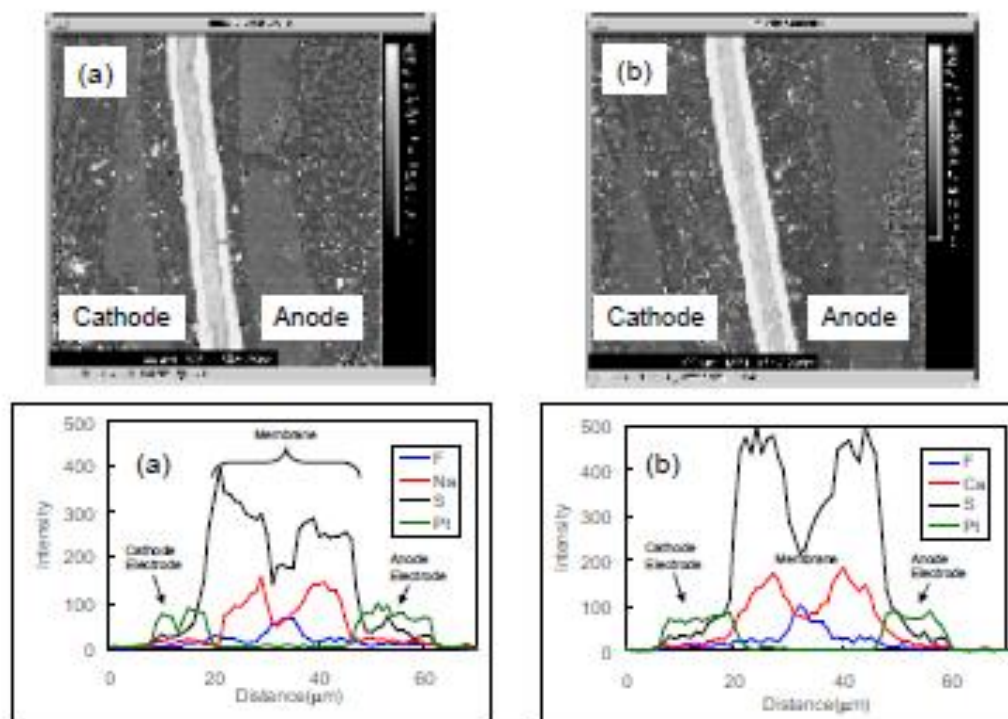


Figure 2.6 Line scan and BSE images of sodium and calcium contaminated MEA [26]

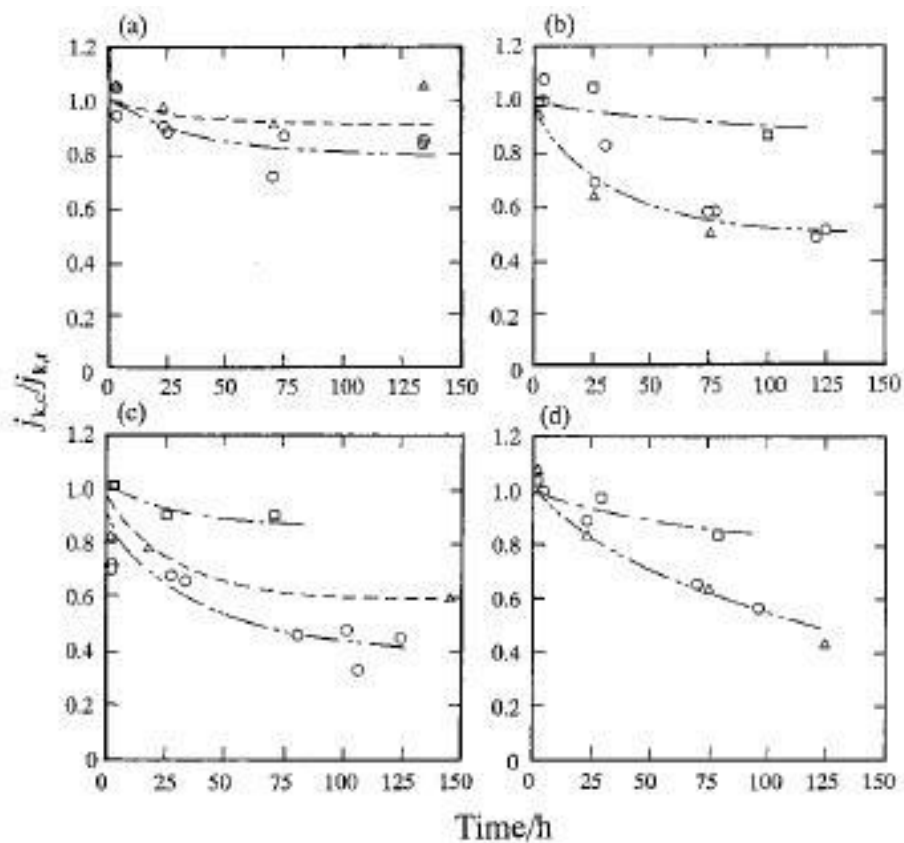


Figure 2.7 Kinetic current of oxygen reduction on platinum covered with Nafion film in 0.1 N H₂SO₄ solution containing various kinds of impurity cations with various amounts as compared with H⁺. The kinetic current $j_{k,c}(\text{film})$ for contaminated film normalized by the kinetic current $j_{k,r}(\text{film})$ for noncontaminated film is plotted as a function of soaking time. Impurity level: 0.1% (\square), 1% (\triangle), or 10% (\circ). (a) Li⁺, (b) Ca²⁺, (c) Fe³⁺, (d) Ni²⁺ [9].

overpotentials [21]. Also, the CO adsorption is followed by the oxidation of CO which may compete with the main PEMFCs reactions. Figure 2.8 shows that the oxidation peak (i.e., 0.6V vs. RHE) for CO followed by the decrease of adsorption peak of proton (0.25V vs. RHE). 1 ppm of H₂S exposed to the PEMFCs also showed a complete loss of performance after 20 hrs while running at a constant voltage 0.5V due to strong chemical affinity of H₂S to Pt [22]. The SO₂ contaminant effect in PEMFCs also showed similar results to the H₂S study. For the sulfur contaminations, the only partial recovery (i.e., irreversible) were observed.

2.3 SYSTEM DERIVED CONTAMINANTS

General Motors [31-32] reported that contaminants from system components have been shown to affect the performance and durability of fuel cell systems. As we described earlier, the requirements for durability and stability are that the performance loss by system contaminants should be less than a few mV over required lifetimes (1000 cycles). The definition of materials subject to system contamination can be plastic structural materials, coolants, sealant, assembly aids, hoses, membrane degradation products, bipolar plates and metal ions from catalysts. In analytical studies from the Nation Renewable Energy Laboratory (NREL), [33-34] many organic and inorganic compounds were identified in leachates of urethane based assembly materials through GC-MS. Clay was tracking pH, total organic carbon (TOC), and conductivity of solutions and used induced coupled plasma (ICP) for quantification of inorganic compounds.

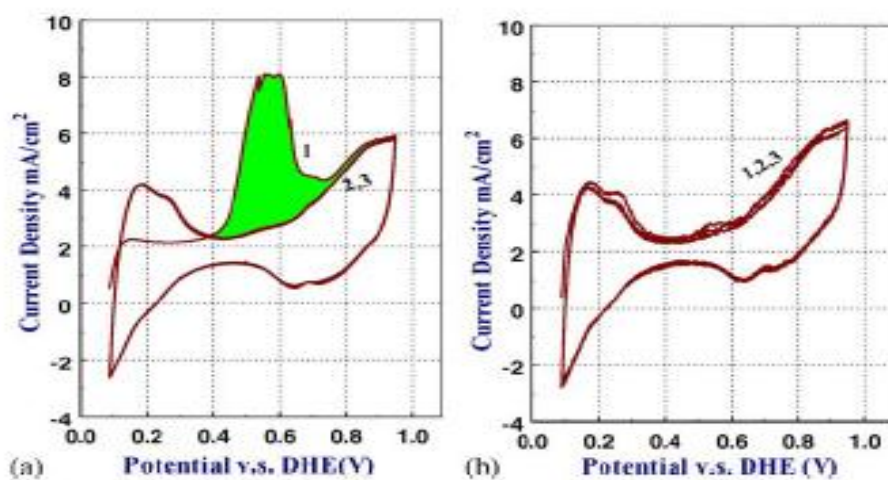


Figure 2.8 (a) CO stripping graph of Pt electrode. The electrode was exposed to 100 sccm 50% CO₂/50% H₂ for 10h before flushing with N₂ for 5 min. Scan rate = 10mV/s, T_{cell}=70 °C, RH(A/C)=100%. (b) Same electrode exposed only to H₂ [21]

2.4 CONTAMINATION MODELS

In previous modeling studies for the membrane/ionomer contamination, Okada et al., [38-39] developed a 1-D membrane model which correlates the cation impact on performance loss with water transport, but it was limited due to the assumption of no ability of cation in the membrane. Besides, the model prediction was focused on the contamination impact on the membrane. Kienitz et.al., [40] also proposed the 1-D membrane cation contamination model on cathodes in PEMFCs, which accounts for the mobility and distribution of cations in membranes as a function of current density by diluted solution theory. Kienitz and Springer [41] extend the work more rigorously with concentrated solution theory. Weber et.al., [42] also developed the membrane contamination model using concentrated solution theory, but both models had difficulty in setting values in the model by experimental data such as the binary interaction coefficient etc. Greszler et.al, [43] added thermodynamic effects (i.e., the proton gradient between the anode and cathode) in their H_2 pump and H_2/O_2 model. However, proposed previous models did not account for the ion exchange physics in their models. Serincan et.al, [44] included the ion-exchange physics in their model with Langmuir isotherms, but this may cause a deviation to explain ion-exchange behavior of cation in the ionomer/membrane. St-Pierre et.al, [45-46] proposed the simple 1-D ionomer contamination model, which includes a term to characterize ion-exchange physics by the separation factor of cation in the membrane. However, the lumped model neglects the importance of the distribution of the contaminant to the channel length. The exception of the consideration of distribution along the channel may cause deviation from real physics of contamination, especially for the longer channel length.

For the adsorption mechanism, many contamination models have also been developed and introduced. However, they are not only limited to single species such as CO, SO₂, NO₂, and H₂S, etc., but they also have difficulty in obtaining sufficient experimental data to use for their predictions. St-Pierre et. al., [47-48] proposed the simple adsorption contamination model which includes kinetic and ohmic voltage loss. The model was validated with well-known adsorbed contaminants such as CO, SO₂, NO₂, and H₂S. However, even though he suggested the experimental determination for the kinetic rate constant, difficulties still exist in obtaining the value. Again, no distribution prediction for the coverage of contaminants along channel length was reported. The distribution to the length of channel may be important for high concentration of contaminant and longer channel length.

CHAPTER 3

A MODEL FOR PREDICTING PERFORMANCE LOSS IN PEMFCs FROM BOP LEACHATES

In this chapter, a model for contamination of a proton exchange membrane fuel cell (PEMFC) which includes adsorption on the Pt catalyst, absorption into the membrane, and ion-exchange with ionomeric components. The model predictions for three sources of voltage (i.e., performance) loss account for two-dimensional time-dependent contamination along the channel and into the membrane. The model is developed by considering the well-known chemical engineering concepts of Langmuir adsorption, partition coefficients, plug flow reactors (PFRs), and dimensionless analysis. The phenomena are shown to be controlled by three important dimensionless groups: a Damhköler number for the contamination reaction rate, a capacity ratio, and a coverage ratio for each contamination mechanism. The model predictions are shown to be reasonable when compared to in-situ experiment data once ex-situ data is used to provide reaction and equilibrium parameters. The predictions provide tolerance for leachates according to each mechanism. For typical parameters, the predicted voltage loss in the electrode ionomer by an ion-exchange mechanism shows slower reaction rates but greater performance losses than other mechanisms.

Supporting works for this chapter is provided in Appendix A to B and D. Appendix B shows the Matlab codes for design equations for each mechanism. Appendix D presents literature reviews of diffusion coefficients for different cations in Nafion[®] membrane which are needed for the calculation of effective diffusion coefficient for the model.

3.1 INTRODUCTION

Contamination of the membrane and the electrodes can affect performance and durability during the commercialization of proton exchange membrane fuel cells (PEMFCs) and therefore research for understanding the degree of this effect has been receiving attention [31-32]. Also, the analysis of cost in PEMFCs systems shows that the cost of Balance of Plant (BOP) materials can be as much as 30% of the stack cost. One opportunity to decrease these costs would be to use off-the-shelf materials rather than custom-made materials if leachates from the less expensive materials do not affect performance and lifetime [4]. Many previous studies for contamination [5-21] in PEMFCs have shown the sensitivity of performance to the low levels of contamination. For example, cation leachates from gaskets or seals, from NH₃ in the fuel, or from catalyst metals [5-17] are well known contaminants for the membrane through an ion-exchange mechanism. Catalyst contamination by an adsorption mechanism from feed gas contaminants such as SO₂ [18-19], CO [21], and H₂S [20] etc. has also been shown. The fundamental mechanisms of contamination from organic contaminants such as aniline, ϵ -caprolactam, diaminotoluene (DAT) [49-50], which have been identified as possible system contaminants, have been studied only recently and it has been shown that their impact on PEMFC performance depends on their functional groups. For example, the ion-exchange

reaction of the amine group in aniline with the Nafion® membrane/ionomer caused a decrease in the number of available proton sites thereby hindering the transport of protons and increasing ohmic and impedance losses. Aniline is also adsorbed on the platinum catalyst and carbon support through interactions between the aromatic ring and the platinum metal [49].

A predictive and mechanistic model could help the understanding of the performance loss by contamination based on mechanisms and it could also help in the establishment of tolerance limits for exposure to give an idea for the mitigation strategy. Also, the contamination model should be simple and widely applicable to the various contaminations. In other words, the parameters for the model should be easy to obtain and measurable from the experiment. The design equation should account for fundamental contamination mechanisms. In this paper, we have attempted to develop a predictive, mechanistic, and more applicable contamination model in PEMFCs based on fundamental understanding of contamination mechanisms on main sources such as Pt, ionomer, and membrane contamination.

In previous modeling studies for the membrane/ionomer contamination, Okada et al., [37-38] developed a 1-D membrane model which correlates the cation impact on performance loss with water transport but was limited due to the assumption of no mobility of cation in membrane. Besides, the model prediction was focused on the contamination impact on membrane. Kienitz et.al., [40] also proposed the 1-D cation contamination models on cathode in PEMFCs which account for the mobility and distribution of cations in membrane as a function of current density by diluted solution theory. Kienitz and Springer [39] extend the work by using concentrated solution theory.

Weber et.al., [41] also developed the contamination model on membrane using concentrated solution theory but both models are 1-D and have require additional experimental data such as binary interact coefficients. Greszler et.al, [42] added thermodynamic effects (i.e., proton gradient between the anode and cathode) in their H₂ pump and H₂/O₂ model. However, proposed previous models did not account for the ion exchange physics in their models. Serincan et.al, [43] included the ion-exchange physics in their model with Langmuir isotherms. St-Pierre et.al, [44-45] proposed a ionomer contamination model which includes terms to characterize ion-exchange physics with a separation factor for the cation in membrane. Note that the lumped model neglected the importance of the distribution of the contaminant to the channel length. In the model developed in this chapter we account for a distribution along the length of the channel that may be necessary as one scale from laboratory lengths to full scale cells with longer channel length.

For the absorption mechanism, models are not existed. On the other hand, for the adsorption mechanism, many contamination models are also developed and introduced. Typically these consider only a single gaseous species such as CO, SO₂, NO₂, and H₂S and also have difficulty obtaining a sufficiently large experimental data set to use for the parameters and for verification of the predictions. St-Pierre et.al, [46-47] proposed the 1-D simple adsorption contamination model which includes kinetic and ohmic voltage loss. The model was validated with well-known adsorbed contaminants such as CO, SO₂, NO₂, and H₂S. However, even though he suggested the experimental determination for the kinetic rate constant, there still exist the difficulties to obtain the value. Again, no

distribution prediction for the coverage by contaminant along the channel length was reported.

In considering the limits of the proposed contamination models in PEMFCs, it may be useful to start out by introducing the simplicity to the model which easily obtains values from *ex-situ* experiments and also includes the fundamental contamination mechanisms with the consideration of coverage distribution along the channel. The segmented cell experiment with the infusion of contaminant would be proposed for the future work. It is worth to point out that the most of discussion for the contamination model in this paper will focus on the system derived contaminants which identified in BOP materials which may be considered to use for structural materials or assembly aids [33-34]. The model is developed by considering well known chemical engineering concepts of Langmuir adsorption, partition coefficients, plug flow reactors (PFRs). After the model is presented, it will be discussed in terms of dimensionless groups. The three dimensionless groups are shown to be important. Finally, the model prediction is compared to *in-situ* infusion experiment data by using parameters obtained from *ex-situ* data obtained with thin-film electrodes and membranes ion-exchange and absorption experiments.

3.2 MODEL

The model is developed by considering Figure 3.1 and using concept for adsorption (or absorption or ion-exchange) processes. Figure 3.1 shows the channels, gas diffusion layer (GDL), and catalyst layer (CL) of proton exchange membrane fuel cell (PEMFC) and dotted line represents the control volume of interest. Note that control volume can be changed depends on consideration of contamination mechanism. From the cross section

view of channel, contaminant A is fed into the direction of x along the channel, and then the contaminant A diffused in the z direction (e.g., CL through GDL).

The assumptions of the model are: (1) the contaminant is dilute relative to the humid gas stream; (2) only the x (along the channel) and the z (perpendicular to the membrane) direction are important; (3) negligible pressure drop along the channel; (4) isothermal conditions exist; (5) the effective diffusion coefficients in the porous GDL, ionomer, and membrane can be written by using the MacMullin number³⁰⁻³²; (6) constant physical and transport parameters; (7) ideal gas law; (8) well-developed laminar flow in the channel; (9) the Butler-Volmer equation can be used to describe the cathode reaction with the Tafel assumption; (10) The rate of contamination is governed by the rate of mass transport of contaminant A by diffusion; (11) Langmuir adsorption isotherms apply for the adsorption behavior.; (12) Gas phase transport of contaminant (Note that contaminant is fed in the liquid state but flash prior to entering the cell).; (13) no interaction between contamination mechanisms.; (15) neglect migration and convection.; (16) contaminants concentration are equal in liquid and gas phase due to the concentration is very low.

3.2.1 CONTAMINATION BY ADSORPTION

A reversible adsorption reaction of contaminant A on the surface of Pt catalyst (S, available sites) is expressed as: $A + Pt(S) \leftrightarrow A - Pt(AS)$. The material balance for contaminant A is made on a control volume of channels with the above assumptions. The fluid stream including contaminant A is on x-direction through the channels, the contaminant A diffuses into z-direction (the direction perpendicular to fluid flow).

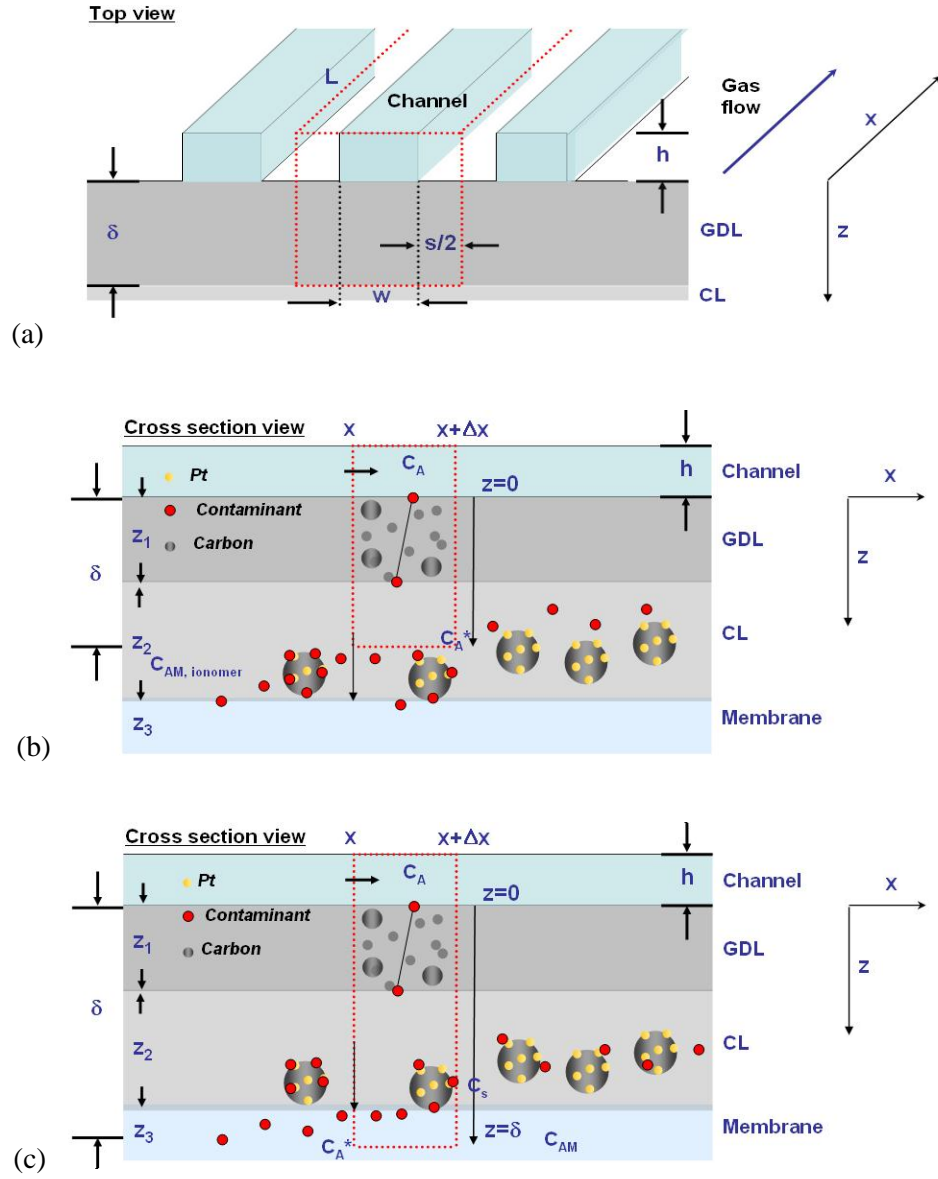


Figure 3.1 Schematic of channel and control volume for a model (a) top view, (b) electrode cotamination (c) membrane contamination

The rate of mass transfer by diffusion in the fluid phase is equal to the rate of reaction (adsorption) on the surface of Pt catalyst. The material balance on contaminant A is made on the volume $(w + s) \cdot h \cdot \Delta x$ over the time period from t to $t + \Delta t$.

$$\begin{aligned} & \int_t^{t+\Delta t} \left[u_f \cdot w \cdot h \cdot C_A \Big|_{x,t} - u_f \cdot w \cdot h \cdot C_A \Big|_{x+\Delta x,t} - N \cdot (w + s) dx \right] dt \\ &= \int_x^{x+\Delta x} \left[w \cdot h \cdot C_A \Big|_{x,t+\Delta t} - w \cdot h \cdot C_A \Big|_{x,t} \right] dx \end{aligned} \quad [3.1]$$

Application of the mean value theorems followed by the limiting (Δx and $\Delta t \rightarrow 0$) yields the following results.

$$-u_f \cdot h \frac{\partial C_A}{\partial x} - \left(\frac{w + r}{w} \right) N = h \frac{\partial C_A}{\partial t} \quad [3.2]$$

From the film diffusion model, the rate of contaminant accumulation in the solid phase (Pt sites) is equal to that of contaminant transfer across the GDL according to the mass balance.

$$N = -D_{eff} \frac{\partial C_A}{\partial z} = -\frac{D_{eff}}{N_m} \frac{C_A(z = \delta) - C_A(z = 0)}{\delta}, \text{ where } C_A(z = \delta) = C_A^* \quad [3.3]$$

C_A^* is the interface concentration assumed to be instantaneously in equilibrium with the Pt surface species, C_{AS} , to be described in Eq. [3.7]. Thus, the material balance equation for C_A can be written:

$$-u_f \frac{\partial C_A}{\partial x} + \left(\frac{w + r}{w} \right) \left(\frac{D_{eff}}{h} \right) \frac{(C_A^* - C_A)}{\delta} = \frac{\partial C_A}{\partial t} \quad [3.4]$$

Also, the change in coverage by contaminant, C_{AS} , with time is equal to the change in equilibrium concentration of contaminant A, C_A^* , with time. Assumption 10 states that the rate of mass transfer by diffusion from the channel, through the GDL, is equal to the rate of reaction (i.e., adsorption) on the surface of Pt catalyst. Thus, the coverage change

with time is equal to the mass transfer by diffusion. The diffusion of contaminant is assumed to be in the gas phase and the coefficient can be corrected by the McMullin number which accounts for the porosity and tortuosity of the GDL through measurable properties [51-53].

$$\frac{\partial C_{AS}}{\partial t} = -\left(\frac{w+r}{w}\right)\left(\frac{D_{eff}}{\delta}\right)(C_A^* - C_A) \quad [3.5]$$

From the chain rule,
$$\frac{\partial C_{AS}}{\partial t} = \left(\frac{\partial C_{AS}}{\partial C_A^*}\right)\left(\frac{\partial C_A^*}{\partial t}\right) \quad [3.6]$$

As we mentioned before, coverage and equilibrium concentration of contaminant A at the interface between GDL and CL can be expressed by the Langmuir adsorption isotherm [Eq. 3.7] as below.

$$C_{AS} = \frac{C_S(t=0)BK_{eq}C_A^*}{1 + K_{eq}C_A^*} \quad [3.7]$$

$$\frac{\partial C_{AS}}{\partial C_A^*} = \frac{C_S(t=0)BK_{eq}}{1 + K_{eq}C_A^*} \left[1 - \frac{K_{eq}C_A^*}{1 + K_{eq}C_A^*}\right] \quad [3.8]$$

Substituting Eq. [3.8] into Eq. [3.6],

$$\frac{\partial C_{AS}}{\partial t} = \frac{C_S(t=0)BK_{eq}}{1 + K_{eq}C_A^*} \left[1 - \frac{K_{eq}C_A^*}{1 + K_{eq}C_A^*}\right] \left(\frac{\partial C_A^*}{\partial t}\right) \quad [3.9]$$

Substituting Eq. [3.9] into Eq. [3.5],

$$\frac{C_S(t=0)BK_{eq}}{1 + K_{eq}C_A^*} \left[1 - \frac{K_{eq}C_A^*}{1 + K_{eq}C_A^*}\right] \left(\frac{\partial C_A^*}{\partial t}\right) = -\left(\frac{w+r}{w}\right)\left(\frac{D_{eff}}{\delta}\right)(C_A^* - C_A) \quad [3.10]$$

Rearranges the Eq. [3.10] for the interface concentration change with time,

$$\frac{\partial C_A^*}{\partial t} = \frac{-\left(\frac{w+r}{w}\right)\left(\frac{D_{eff}}{N_m \delta}\right)(C_A^* - C_A)}{\frac{C_S(t=0)BK_{eq}}{1 + K_{eq}C_A^*} \left[1 - \frac{K_{eq}C_A^*}{1 + K_{eq}C_A^*}\right]} = -\frac{\left(\frac{w+r}{w}\right)\left(\frac{D_{eff}}{\delta}\right)(C_A^* - C_A)}{\frac{C_S(t=0)BK_{eq}}{(1 + K_{eq}C_A^*)^2}} \quad [3.11]$$

$$\frac{\partial C_A^*}{\partial t} = -\frac{(1 + K_{eq}C_A^*)^2 \left(\frac{w+r}{w}\right)\left(\frac{D_{eff}}{\delta}\right)(C_A^* - C_A)}{C_S(t=0)BK_{eq}} \quad [3.12]$$

Thus in summary we have two coupled partial differential equations (PDEs) shown by Eq. [3.8] and [3.12] as below which requires two initial conditions and one boundary condition. These could be written:

@ t=0, $C_A = 0$ and $C_A^* = 0$ for $0 < x < L$

@ z=0, $C_A = C_{A0}$

$$\frac{\partial C_A}{\partial t} = -u_f \frac{\partial C_A}{\partial x} + \frac{D_{eff}}{h\delta} (C_A^* - C_A) \quad [3.8]$$

$$\frac{\partial C_A^*}{\partial t} = -\frac{(1 + K_{eq}C_A^*)^2 \left(\frac{w+r}{w}\right)\left(\frac{D_{eff}}{\delta}\right)(C_A^* - C_A)}{C_S(t=0)BK_{eq}} \quad [3.12]$$

Defining dimensionless for distance (ξ), concentration (Φ_A), coverage by contaminant

(θ), time (τ).

$$\xi = \frac{x}{L}, \Phi_A = \frac{C_A}{C_{A0}}, \Phi_A^* = \frac{C_A^*}{C_{A0}}, \theta = \frac{C_{AS}}{C_S(t=0)}, \tau = \frac{t}{(L/u_f)} \quad [3.13]$$

and substituting Eq. [3.13] into Eq. [3.8] and [3.12] yields the dimensionless partial

differential governing equations for contaminant A (Φ_A), interface concentration A (Φ_A^*),

and the Pt coverage (θ).

$$\frac{\partial \Phi_A}{\partial \tau} = -\frac{\partial \Phi_A}{\partial \xi} + \beta Da (\Phi_A^* - \Phi_A) \quad [3.14]$$

$$\frac{\partial \Phi_A^*}{\partial \tau} = -\beta Da \Psi \left(\frac{(1 + \Gamma \Phi_A^*)^2}{\Gamma_{\max}} \right) (\Phi_A^* - \Phi_A) \quad [3.15]$$

Here, β is the geometric ratio of channel rib and width, ψ is the capacity ratio of Pt loading and inlet concentration of contaminant A, the Damkohler number (Da) is routinely used by chemical engineers, Da is a measure of rate of reaction (i.e., to z-direction relative to convection to x-direction) at inlet condition, and Γ is the coverage ratio of contaminant A which is associate with Langmuir parameters (B, K_{eq}).

$$\beta = \left(\frac{w+r}{w} \right), \psi = \frac{C_{A0} h}{C_s(t=0)}, Da = \left(\frac{L}{u_f h} \right) \left(\frac{D_{eff}}{\delta} \right), \Gamma = K_{eq} C_{A0}, \Gamma_{\max} = B K_{eq} C_{A0} \quad [3.16]$$

Thus, the two coupled dimensionless equations, dimensionless initial and boundary conditions can be written:

$$\frac{\partial \Phi_A}{\partial \tau} = -\frac{\partial \Phi_A}{\partial \xi} + \beta Da (\Phi_A^* - \Phi_A) \quad [3.14]$$

$$\frac{\partial \Phi_A^*}{\partial \tau} = -\beta Da \Psi \left(\frac{(1 + \Gamma \Phi_A^*)^2}{\Gamma_{\max}} \right) (\Phi_A^* - \Phi_A) \quad [3.15]$$

The initial and boundary conditions are also defined again with the dimensionless variables.

@ $\tau = 0$, $\Phi_A = 0$ and $\Phi_A^* = 0$ for $0 < \xi < 1$

@ $\xi = 0$, $\Phi_A = 1$

Finally, using the dimensionless Langmuir isotherm Eq. [3.16] below from Eq. [3.7], we can obtain coverage change with time and distribution along the channel.

$$\theta = \frac{\Gamma_{\max} \Phi_A^*}{1 + \Gamma \Phi_A^*} \quad [3.16]$$

3.2.2 CONTAMINATION BY ION-EXCHANGE

The ion exchange reaction of monovalent cation can be expressed as: $A^+ + (H - M) \leftrightarrow (A^+ - M) + H$ where, A=contaminant, H-M= available acid sites in membrane, A-M= exchanged acid sites by contaminant A, H=proton. Similarly, the material balance for the contaminant A can be derived as we described earlier for the adsorption model.

$$-u_f \frac{\partial C_A}{\partial x} + \left(\frac{w+r}{w} \right) \left(\frac{D_{eff}}{h} \right) \frac{(C_A^* - C_A)}{\delta} = \frac{\partial C_A}{\partial t} \quad [3.17]$$

$$\frac{\partial C_{AM}}{\partial t} = - \left(\frac{w+r}{w} \right) \left(\frac{D_{eff}}{\delta h} \right) (C_A^* - C_A) \quad [3.18]$$

In addition, partition coefficient (K_{eq}) [54] and coverage (χ) of acid sites by contaminant can define in terms of concentrations (e.g., C_A , C_{AM} , C_H , and C_{HM}).

$$K_{eq} = \frac{[X_{AM}][X_H]}{[X_A^*][X_{HM}]} = \frac{(1 - X_A^*)\chi}{X_A^*(1 - \chi)} \quad [3.19]$$

$$\chi = 1 - X_{HM} = X_{AM} = \frac{C_{AM}}{C_{HM}(t=0)} \quad [3.20]$$

Rearrange the Eq. [3.22] by concentrations:

$$\frac{C_A^*}{C_H} = \frac{C_A^*}{C_{A0} - C_A^*} = \frac{\chi}{K_{eq}(1 - \chi)} \quad [3.21]$$

Accordingly, the concentration for the exchanged acid site by contaminant A can be represented by the two operating conditions (i.e., $C_{HM}(t=0)$ and C_{A0}), and one known dependent variable (i.e., C_A^*), and one equilibrium parameter (i.e., K_{eq}).

$$C_{AM} = C_{MH}(t=0) \frac{C_A^*}{C_A^* + K_{eq}(C_{A0} - C_A^*)} \quad [3.22]$$

$$\frac{\partial C_{AM}}{\partial C_A^*} = \frac{C_{A0} C_{HM}(t=0) K_{eq}}{[C_{A0} + (K_{eq} - 1)C_A^*]^2} \quad [3.23]$$

The chain rule can apply for the Eq. [3.18]:

$$\frac{\partial C_{AM}}{\partial t} = \frac{\partial C_{AM}}{\partial C_A^*} \frac{\partial C_A^*}{\partial t} = -\left(\frac{w+r}{w}\right) \left(\frac{D_{eff}}{\delta h}\right) (C_A^* - C_A) \quad [3.24]$$

Substituting Eq. [3.23] into Eq. [3.24], and rearranging those yields the Eq. [3.25] for the interface concentration change with time.

$$\frac{\partial C_A^*}{\partial t} = -\left(\frac{w+s}{w}\right) \left(\frac{D_{eff}}{\delta h}\right) (C_A^* - C_A) \frac{[C_{A0} + (K_{eq} - 1)C_A^*]^2}{C_{A0} C_{HM}(t=0) K_{eq}} \quad [3.25]$$

In summary we have two coupled partial differential equations (PDEs) shown by Eq. [26] and [3.27] as below which requires two initial conditions and one boundary condition.

These could be written:

$$-u_f \frac{\partial C_A}{\partial x} + \left(\frac{w+r}{w}\right) \left(\frac{D_{eff}}{h}\right) \frac{(C_A^* - C_A)}{\delta} = \frac{\partial C_A}{\partial t} \quad [3.26]$$

$$\frac{\partial C_A^*}{\partial t} = -\left(\frac{w+r}{w}\right) \left(\frac{D_{eff}}{\delta h}\right) (C_A^* - C_A) \frac{[C_{A0} + (K_{eq} - 1)C_A^*]^2}{C_{A0} C_{HM}(t=0) K_{eq}} \quad [3.27]$$

The initial and boundary conditions are followed by

@ t=0, $C_A = 0$ and $C_A^* = 0$ for $0 < x < L$

$$@ z=0, C_A = C_{A0}$$

Defining dimensionless distance (ξ), concentration (Φ_A), coverage by contaminant (χ), and time (τ)

$$\xi = \frac{x}{L}, \Phi_A = \frac{C_A}{C_{A0}}, \chi = \frac{C_{AM}}{C_{HM}(t=0)}, \tau = \frac{t}{(L/u_f)} \quad [3.28]$$

and substituting Eq. [3.28] into Eq. [3.26] and [3.27] yields the dimensionless partial differential governing equations for the concentration for contaminant A at the channel (Φ_A) and the interface (Φ_A^*).

$$\frac{\partial \Phi_A}{\partial \tau} = -\frac{\partial \Phi_A}{\partial \xi} + \beta Da(\Phi_A^* - \Phi_A) \quad [3.29]$$

$$\frac{\partial \Phi_A^*}{\partial t} = -\beta Da(\Phi_A^* - \Phi_A) \frac{\psi}{K_{eq}} [1 + (\Gamma - 1)\Phi_A^*]^2 \quad [3.30]$$

The initial and boundary conditions are also defined again with the dimensionless variables.

$$@ \tau=0, \Phi_A = 0 \quad \Phi_A^* = 0 \text{ for } 0 < \xi < 1$$

$$@ \xi=0, \Phi_A = 1$$

Here, β is the geometric ratio of channel rib and width, ψ is the molar ratio of acid sites and inlet concentration of contaminant A, the Da number is a measure of rate of reaction (i.e., to z-direction relative to convection to x-direction) at inlet condition, and Γ is the partition coefficient for contaminant A.

$$\beta = \left(\frac{w+r}{w} \right), \psi = \frac{hC_{A0}}{z_{mem} (or z_{ionomer}) C_{HM} (t=0)}, Da = \left(\frac{L}{u_f h} \right) \left(\frac{D_{eff}}{\delta} \right), \Gamma = K_{eq} \quad [3.31]$$

Finally, using the Eq. [3.35] below from Eq. [3.24], we can obtain coverage change with time and distribution along the channel.

$$\chi = \frac{\Gamma \Phi_A^*}{(1 - \Phi_A^*) + \Gamma \Phi_A^*} \quad [3.32]$$

Also, for an effective diffusion coefficient of contaminant A (D_{eff}) can be approximated by assuming the series of stagnant films in an electrode and membrane (i.e., ionomer). First, the contaminant A diffuse through the GDL, then contaminates an ionomer in the electrode, and then diffuses through the membrane/catalyst layer interface followed by the membrane contamination. Thus, we assume three stagnant films on the electrode and membrane and the effective diffusion coefficient can be written as below. Here, we assume that a diffusion coefficient through ionomer is equal to that in Nafion[®] membrane which generally measured by mass uptake or NMR methods [56-61].

$$\frac{\delta}{D_{eff}} = \frac{z_{ionomer}}{D_{ionomer}} + \frac{N_{m,GDL} z_{GDL}}{D_{GDL}} \text{ for electrode contamination} \quad [3.33]$$

$$\frac{\delta}{D_{eff}} = \frac{N_{m,CL} z_{CL}}{D_{CL}} + \frac{N_{m,GDL} z_{GDL}}{D_{GDL}} + \frac{z_{mem}/2}{D_{mem}} \text{ for membrane contamination} \quad [3.34]$$

where, $\delta = z_{GDL} + z_{CL} + z_{mem}/2$ for membrane contamination and $\delta = z_{GDL} + z_{ionomer}$ for electrode contamination. Finally, an average coverage along the channel can be obtained by an integration of local coverage for the length of channel: $0 < \xi < 1$.

$$\theta_{avg,i} = \int_0^1 \theta d\xi, \chi_{avg,i} = \int_0^1 \chi d\xi \quad [3.35]$$

3.2.3 CONSIDERATION OF DILUTION BY WATER GENERATION AND TRANSPORT

It should be noted that the water generated on cathode by the ORR may change the concentrations of contaminant A at the interface and channel depending on operating conditions. If we assume (1) the current to be uniform over the length (i.e., x-direction, channel) and (2) no water accumulation at the interface, the flux balance at the interface on cathode for the water vapor can be written:

$$\frac{D_w}{N_m \delta} (C_w^* - C_w) = \frac{i}{F} \left(\frac{1}{2} + \alpha \right) (w + s) L \quad [3.36]$$

Here, the α represents the ratio of net water flux per proton flux and has physical meaning of the back diffusion from cathode to anode and electro-osmotic drag (e.g., migration) from anode to cathode [62]. Note that negative α represents that the back diffusion of water vapor from cathode to anode is dominant. As shown in Table A1, previous studies reported that the α is -0.053 for 25% RH and 0.28 for 50% RH with $i=0.4\text{A/cm}^2$ [62-64]. Using these values one can estimate that a maximum of dilution produces 10% error in predictions with the simple model.

3.2.4 PREDICTING ΔV BY THE BUTLER-VOLMER EQUATION AND CONDUCTIVITY

Total voltage change by a contamination can be written:

$$\Delta V = \Delta V_{ocv} - i_p (R_p - R_c) + \Delta \eta_a + \Delta \eta_c, \text{ where } p=\text{pristine, } c=\text{contamination} \quad [3.37]$$

Eq. [3.37] can be simplified if we assume no change in OCV by the contamination and negligible anodic overpotential change ($\Delta \eta_a$). Thus,

$$\Delta V = -i_p (R_p - R_c) + \Delta \eta_c, \text{ where } p=\text{pristine, } c=\text{contamination} \quad [3.38]$$

For the membrane contamination, we can use Ohm's law (i.e., $V=iR$) as described below.

$$\Delta V_{iR} = -\left(\frac{iZ_{mem}}{\kappa_p} - \frac{iZ_{mem}}{\kappa_c}\right) = -\Delta\left(\frac{iZ_{mem}}{\kappa}\right), \text{ where p=pristine, c=contamination} \quad [3.39]$$

Here, conductivity (κ) can be obtained from the *ex-situ* conductivity studies as function of coverage. Generally, the conductivity (κ) and coverage (χ) have a following exponential relation at constant RHs.

$$\ln \kappa = a\chi + b, \text{ where a and b are constants} \quad [3.40]$$

Thus, Eq. [3.39] can be written in terms of coverage (χ) by contaminant in membrane for specified RHs.

$$\Delta V_{iR} = -\Delta\left(\frac{iZ_{mem}}{\kappa}\right) = -\Delta\left(\frac{iZ_{mem}}{e^{a\chi+b}}\right) \quad [3.41]$$

Secondly, to explain the cathodic overpotential ($\Delta\eta_c$), we used the Butler-Volmer equation for reaction j to explain dependency between surface overpotential (η_s) and current density (i) on electrode [65].

$$i = i_{0,j} \left[\Pi \left(\frac{C_j}{C_{j,ref}} \right)^{p_{ij}} \exp \left(\frac{\alpha_a F \eta_s}{RT} \right) - \Pi \left(\frac{C_j}{C_{j,ref}} \right)^{q_{ij}} \exp \left(\frac{-\alpha_c F \eta_s}{RT} \right) \right] \quad [3.42]$$

Again, the Butler-Volmer equation can be simplified where valid for assumption of large cathodic over-potential for oxygen reduction reaction in PEMFCs.

$$-i = i_{0,j} \left[\Pi \left(\frac{C_j}{C_{j,ref}} \right)^{q_{ij}} \exp \left(\frac{-\alpha_c F \eta_s}{RT} \right) \right] \quad [3.43]$$

According to the ORR, (i.e., $2H_2O \leftrightarrow O_2 + 4H^+ + 4e^-$) Eq. [3.43] for a pristine and a contaminated electrode can be written using q_{ij} on the stoichiometric coefficients:

$$\eta_{pristine} = -\frac{RT}{\alpha_c F} \ln \left\{ -\left(\frac{i}{i_0}\right) \cdot \left(\frac{C_{O_2}}{C_{O_2,ref}}\right) \left(\frac{C_{H^+,pristine}}{C_{H^+,ref}}\right)^{1/4} \left(\frac{C_{Pt,pristine}}{C_{Pt,ref}}\right) \right\} \quad [3.44]$$

$$\eta_{contamination} = -\frac{RT}{\alpha_c F} \ln \left\{ -\left(\frac{i}{i_0}\right) \cdot \left(\frac{C_{O_2}}{C_{O_2,ref}}\right) \left(\frac{C_{H^+,contamination}}{C_{H^+,ref}}\right)^{1/4} \left(\frac{C_{Pt,contamination}}{C_{Pt,ref}}\right) \right\} \quad [3.45]$$

, where C_{H^+} and C_{O_2} = surface concentration of H^+ and O_2 on Pt respectively

Finally, Eq. [3.45] can rearrange with Eq. [3.44],

$$\Delta V = \eta_{contamination} - \eta_{pristine} = -\frac{RT}{\alpha_c F} \ln \left\{ \left(\frac{C_{H^+,pristine}}{C_{H^+,contamination}}\right)^4 \left(\frac{C_{Pt,pristine}}{C_{Pt,contamination}}\right) \right\} \quad [3.46]$$

Eq. [3.46] shows two contributions on voltage losses. One is from ECSA changes by Pt contamination and the other is proton concentration changes by ionomer contamination. Note that we used the stoichiometry numbers (i.e., $q_{ij}=1$ for Pt contamination, $q_{ij}=4$ for ionomer contamination) of ORR for the q_{ij} which accounts for reaction rate for each contamination mechanism. Although the measurement value is uncertain, one literature report gave the reaction order for ionomer contamination may be 1.5 rather than 4.0.

In summary the total voltage loss by the contamination may have three contributions from the Pt, ionomer, or membrane. Figure 3.2 shows the predicted voltage as change of coverage. Note that to calculate the ΔV_{mem} , one needs data for Eq. [3.32] at a given RH to calculate the line of (c) in Figure 3.2. Here we used Na-exchange membrane data for at 60% RH and $0.2A/cm^2$ [63-64].

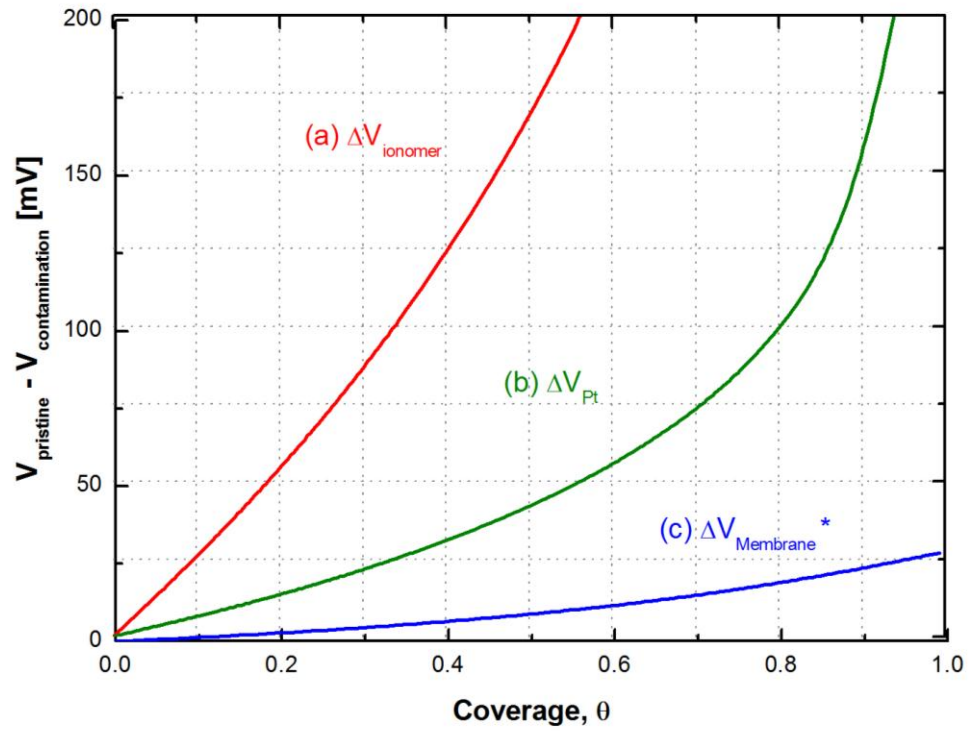


Figure 3.2 Predicted ΔV with Butler-Volmer equation and conductivity *RH=60%, I=10A, Na⁺ contamination data

3.2.5 SOLUTION TECHNIQUE

To solve the hyperbolic two coupled PDEs, we used a $\Theta(\Delta x^2)$ finite difference method for the length direction and the Gear algorithm for the time derivative set of discretized ODEs.

3.3 MODEL PREDICTIONS

3.3.1 SELECTION OF REASONABLE VALUES FOR DIMENSIONLESS NUMBERS

Before proceeding to the predictions of the model, it discusses numbers (i.e., Da, ψ , Γ) consistent with contamination experiments and PEMFC operation. We selected dimensionless numbers in consideration of general operating variables (T, i, RH, backpressure, stoic, C_{A0}), system geometry (w, s, h) and the physical constants (N_m , δ , D, K, B) used *in-situ* infusion experiments. Tables 3.1 to 3.3 list the variables for each contamination source. For the purpose of exploring the parameter space for the model predictions, we choose a 2^2 factorial design for each source in terms of the dimensionless numbers (i.e., high and low) as summarized in Table 3.4 for each mechanism.

For the Ψ_1 , Ψ_2 , and Ψ_3 (capacity ratio), the Pt catalyst and H^+ ionomer and membrane concentrations change with feed contaminant concentrations for a specified MEA. For the feed concentrations, we selected values from the analytical study (i.e., GC and ICP) of BOP leachates [13-14]. The Pt surface concentration can be fixed for same Pt loading and electrochemical surface area (ECSA=68m²/g_{pt}). The ion exchange capacity (IEC=0.97mmeq/g) of Nafion[®] was used for the calculation of H^+ concentration in ionomer and membrane. The Da number (reaction rate to convection transport to the channel) depends on effective diffusion toward the electrode or membrane (i.e., z-

Table 3.1 Consideration of experiment conditions for selecting dimensionless numbers:
Pt contamination

i [A/cm ²]	C _{A0} [mol/cm ³]	C _s (t=0) [mol/cm ²]	Ψ ₁
1	3.00E-09	5.65E-07	4.46E-04
0.2	2.00E-08	5.65E-07	2.97E-03
0.2	5.00E-08	5.65E-07	7.43E-03
i [A/cm ²]	u _f [cm/s]	D _{eff} [cm ² /s]	Da ₁
1	1.25E+03	3.00E-05	1.30E-03
0.2	2.40E+02	3.00E-05	6.76E-03
0.2	2.40E+02	3.00E-04	6.76E-02
C _{A0} [mol/cm ³]	Species	K _{eq} [cm ³ /mol]	Γ ₁
3.00E-09	DEGEE	6.0E+07	0.18
2.00E-08	DEGEE	6.0E+07	1.2
5.00E-08	4-MBSA	2.7E+08	13.5

DEGEE (Diethlyene glycol monoethyl ether)

4-MBSA(4-methly benzensulfonamide)

Table 3.2 Consideration of experiment conditions for selecting dimensionless numbers:
ionomer contamination

i [A/cm ²]	C _{A0} [mol/cm ³]	C _{HM} (t=0) [mol/cm ³]	Ψ ₂
1	5.0E-09	2.4E-03	1.7E-03
0.2	4.0E-08	2.4E-03	1.4E-02
0.2	7.0E-09	8.4E-03	7.0E-04
i [A/cm ²]	u _r [cm/s]	D _{eff} [cm ² /s]	Da ₂
1	1.3E+03	3.0E-06	1.3E-04
0.2	2.4E+02	3.0E-05	6.7E-03
0.2	2.4E+02	3.0E-04	2.2E-02
Species		K _{eq}	Γ ₂
Sodium (Na ⁺)		1.2	1.2
Potassium (K ⁺)		5.0	5.0
Aniline (C ₆ H ₅ NH ₃ ⁺)		72	72

Table 3.3 Consideration of experiment conditions for selecting dimensionless numbers:
membrane contamination

i [A/cm ²]	C _{A0} [mol/cm ³]	C _{HM} (t=0) [mol/cm ³]	Ψ ₃
1	5.0E-09	2.2E-03	7.8E-05
0.2	4.0E-08	2.2E-03	6.2E-04
0.2	7.0E-09	2.2E-03	1.1E-03
i [A/cm ²]	u _r [cm/s]	D _{eff} [cm ² /s]	Da ₃
1	1.3E+03	3.0E-06	1.2E-04
0.2	2.4E+02	3.0E-05	8.4E-03
0.2	2.4E+02	3.0E-04	2.1E-02
Species		K _{eq}	Γ ₃
Sodium (Na ⁺)		1.2	1.2
Potassium (K ⁺)		5.0	5.0
Aniline (C ₆ H ₅ NH ₃ ⁺)		72	72

Table 3.4. Selected dimensionless numbers for the prediction

$\Psi_1 \backslash Da_1$	3.0E-04	3.0E-02	Γ_1
1.4E-03	LL	LH	6.0
1.40-01	HL	HH	
$\Psi_2 \backslash Da_2$	5.6E-03	5.6E-02	Γ_2
3.0E-04	LL	LH	1.0
3.0E-03	HL	HH	
$\Psi_3 \backslash Da_3$	5.6E-04	5.6E-03	Γ_3
3.0E-04	LL	LH	1.0
3.0E-03	HL	HH	

direction, see Figure 3.1) and geometric numbers of systems (e.g., 50cm² single cell hardware which assembled with bipolar plates of triple serpentine gas channels). Finally, the Γ (coverage ratio) can be obtained from adsorption and ion-exchange isotherms of Pt and Nafion[®] membrane for selected compounds [49-50].

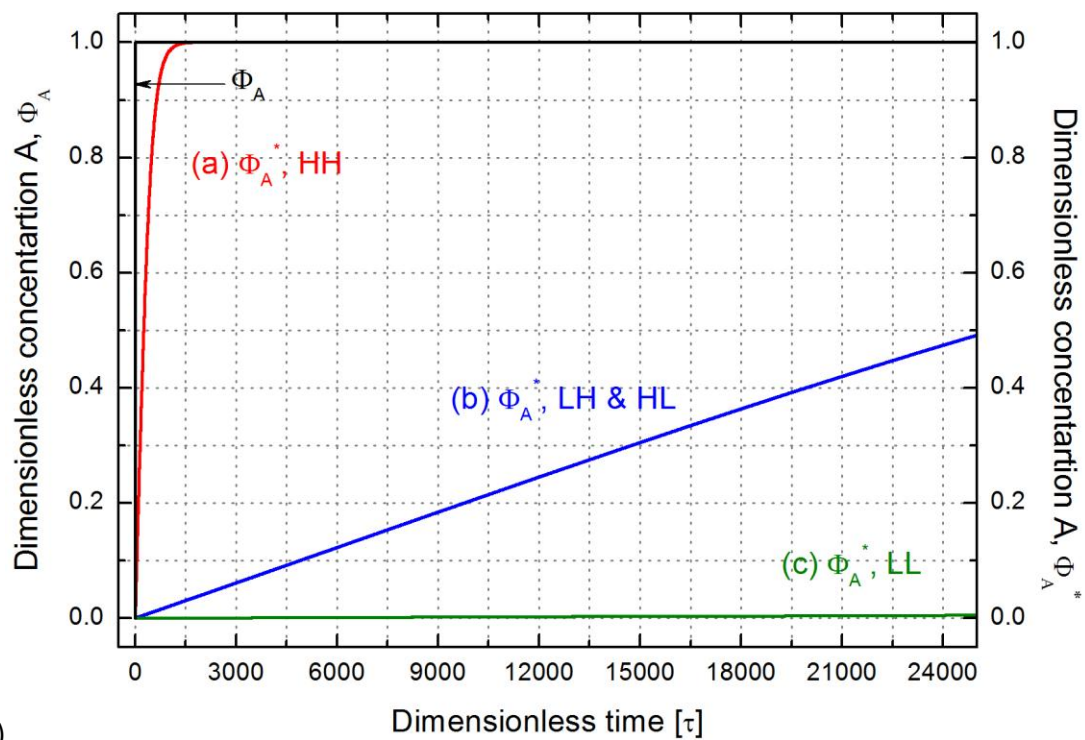
3.3.2 PT CONTAMINATION

Figure 3.3a represents the dimensionless concentration for contaminant A at $\xi=0$ in the channel (Φ_A) and at the interface between GDL and CL (Φ_A^*) predicted by the model for the case where $\Gamma_1=6.0$, $B=0.6$, and Da_1 and Ψ_1 are varied as shown in Table 3.4. The predicted concentration of contaminant A in the channel has a step change from 0 to 1 at $\xi=0$ and concentration of contaminant A at the interface (i.e., GDL and CL) approaches 1.0 from an initial value of 0.0 at different rates for different combination of Da_1 and Ψ_1 . The fastest concentration change is for the $(Da_1, \Psi_1)=HH$, moderate change and indistinguishable change for LH (or HL) and LL values. That is the driving force in Eq. [3.14] and [3.15] decreases rapidly for high diffusion of A through the GDL relative to convection down the channel and decreases rapidly for a large value of initial moles of contaminant relative to the active sites of Pt (i.e., HH in Table 3.4 and Figure 3.3a). Thus steady state is approached very quickly for the HH conditions. This approach to steady state is shown with LH and HL conditions and slowest for LL conditions. Again these are all for $\xi=0$.

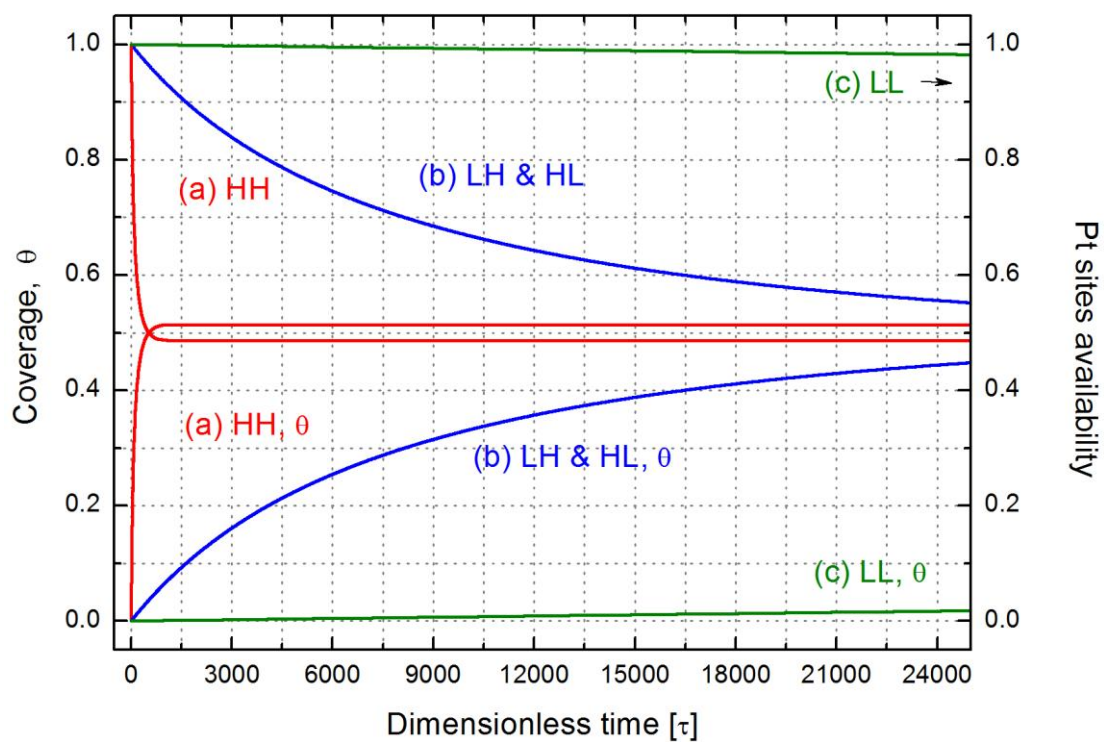
Figure 3b and 3c show average coverage and voltage change (in the spatial dimension) for the change of Da , and Ψ . Again, fast decay of Pt availability is observed for the high dimensionless numbers of Da_1 and Ψ_1 . It is interesting to note that all cases

reached same coverage losses at steady state because Γ_1 is fixed for all combinations. Figure 3.4a represents the dimensionless concentration for contaminant A at $\xi=0$ in the channel (Φ_A) and at the interface between GDL and CL (Φ_A^*) predicted by the model for the case where Da_1 , Ψ_1 , and B are fixed and Γ_1 is varied as shown in Table 3.4. The averaged coverage and voltage change are also shown in Figure 3.4b and 3.4c. The higher Γ_1 shows severe loss of the Pt availability and the voltage due to the larger coverage ratio. Here, the slopes of predicted voltage line for each case are same. That is, the contamination reaction rates are equal because the Da_1 and Ψ_1 are fixed.

In summary the analysis of dimensionless numbers for the Pt contamination reveals that the high Da_1 and Ψ_1 yield fast contamination reaction and the high Γ_1 cause the greater coverage ratio. If one considers the use of these prediction to establish tolerance levels, the prediction results show that coverage (i.e., ECSA loss) needs to be less than 0.3 to keep the voltage loss less than 20mV if only the Pt contamination is relevant (see Figure 3.2). Thus the only $(Da_1, \Psi_1)=LL$ case satisfies these tolerance limits. Clearly, lower Da_1 and Ψ_1 are required to mitigate Pt contamination impact. High current and high RH conditions are preferred due to the high flow rate/dilution effect. Other changes in geometry and capacity (i.e., higher loadings or more moles of ionomer) may not yield desirable higher economic tolerances.



a)



b)

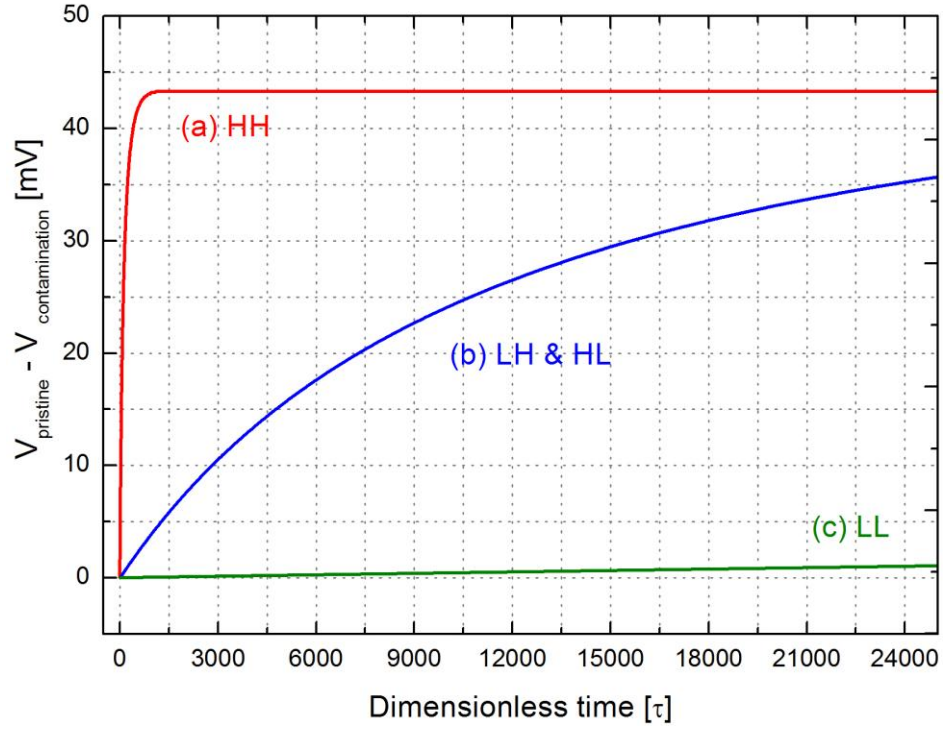
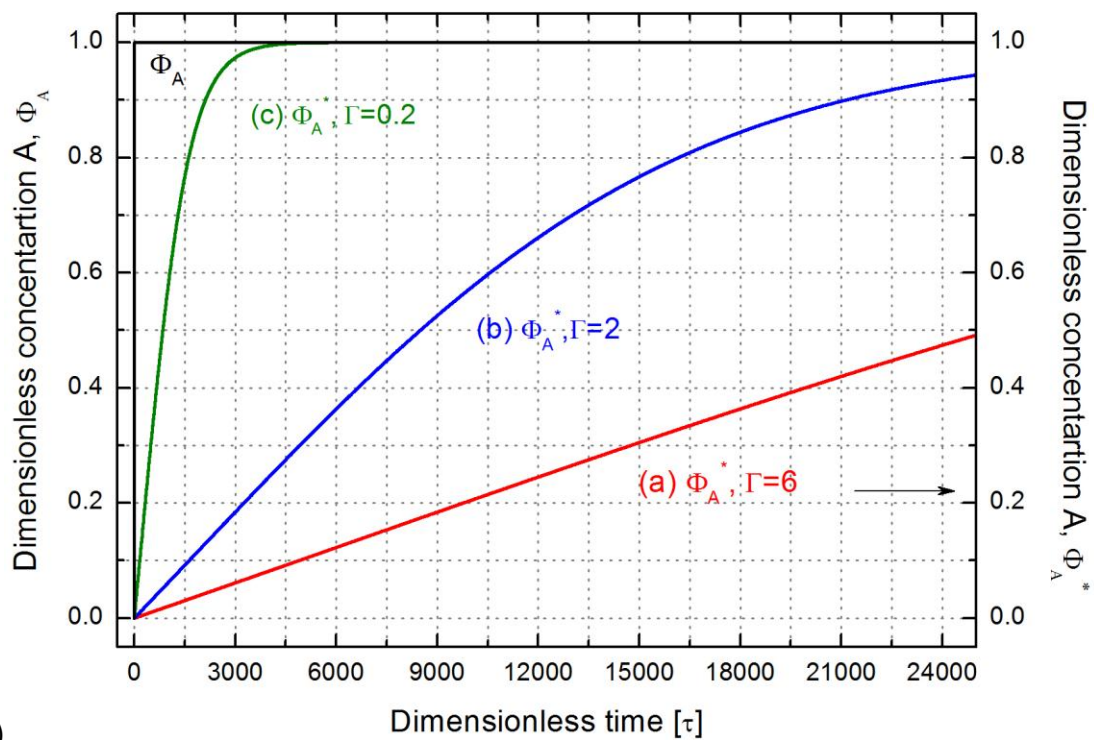
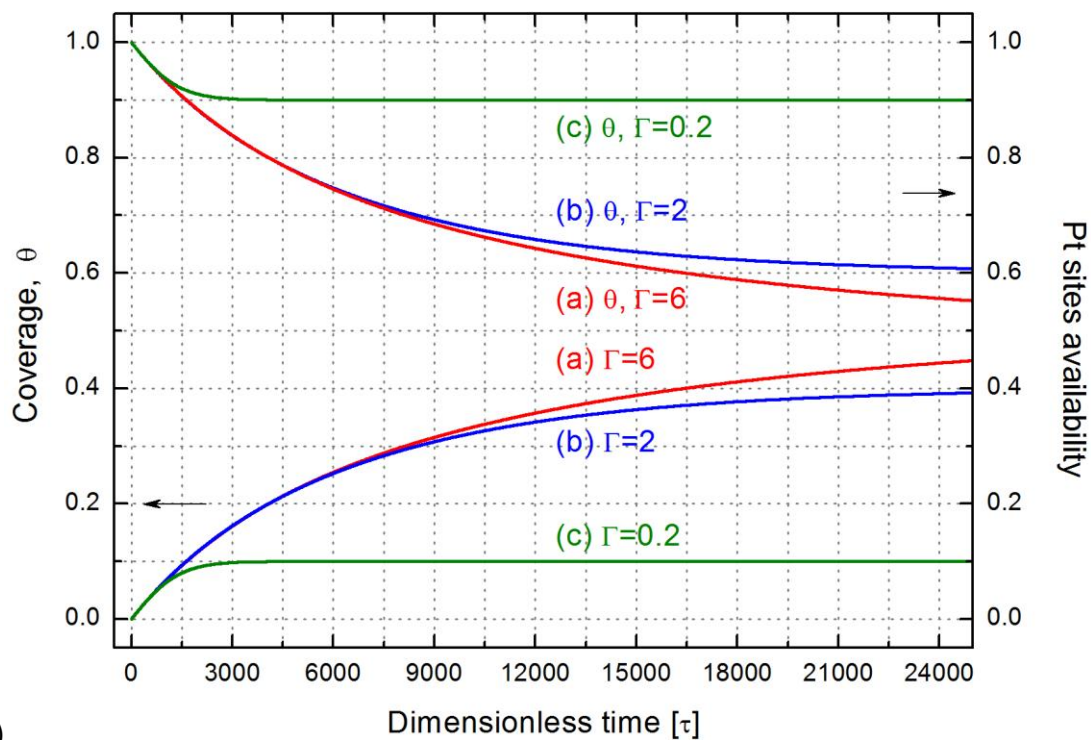


Figure 3.3 a) Dimensionless concentration at the interface (@ $\xi=0$), b) Coverage and Pt availability, c) Voltage changes as varies with Da_1 and Ψ_1 and fixed $\Gamma_1=6.0$ by Pt contamination (a) High/High (b) Low/High & High/Low (c) Low/Low



a)



b)

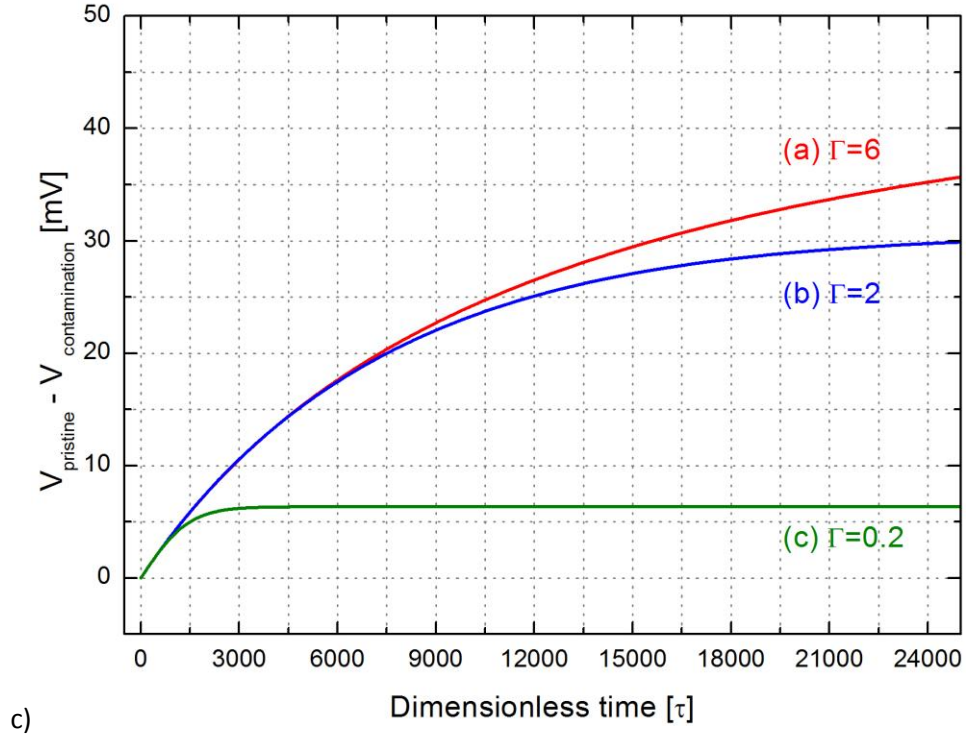
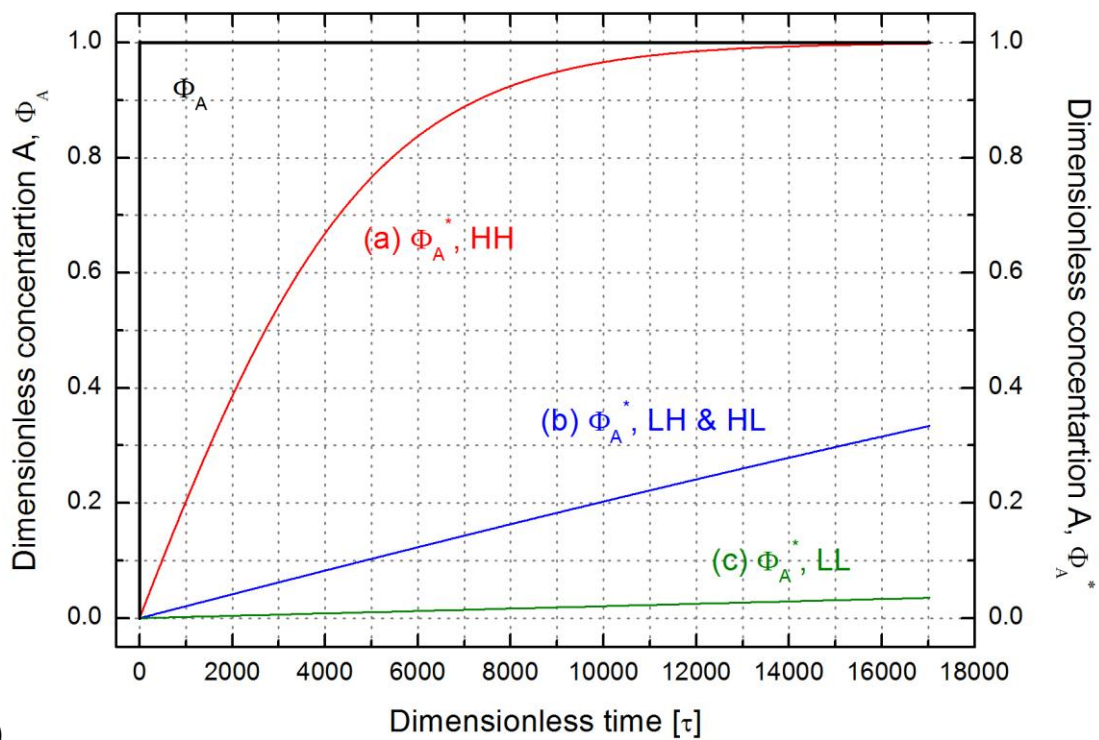


Figure 3.4 a) Dimensionless concentration at the interface (@ $\xi=0$), b) Coverage and Pt availability, c) Voltage changes by Pt contamination as varies with Γ_1 (a) 0.2 (b) 2.0 (c) 6.0 and Da_1 and Ψ_1 are fixed.

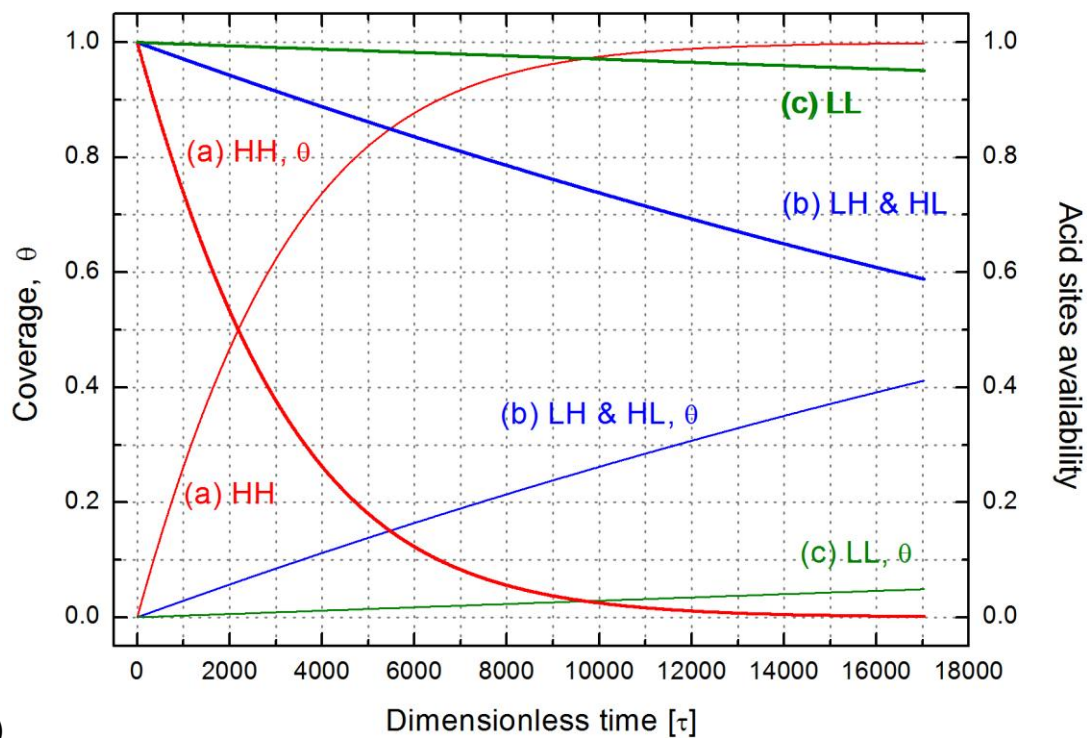
3.3.3 IONOMER CONTAMINATION

Next, we consider ionomer contamination and voltage change resulting from the ion-exchange reaction. Figure 3.5a shows the dimensionless concentration for contaminant at $\xi=0$ in the channel (Φ_A) and at the interface (i.e., GDL and CL) (Φ_A^*) which are predicted by the model for the case where fixed Γ_2 while, Da_2 and Ψ_2 are varies (shown in Table 3.4). Figure 3.5b and 3.5c show predictions for averaged coverage and voltage change at varies of Da_2 and Ψ_2 resulting from the Figure 3.5a. Like the Pt contamination, the greater Da_2 and Ψ_2 yield the significant contamination impact. However, it is interesting to note that the ionomer contamination is more sensitive of voltage to coverage than the Pt contamination because the exponent for H^+ in the ionomer of the electrode is 4. Also, the maximum coverage for the ion-exchange mechanism is 1.0 whereas the maximum Pt coverage is typically less than 1.0. It is also interesting to note that as shown in Figure 6, Γ affects the rate coverage for the membrane and ionomer but affect the final value for Pt coverage (see Figure 3.5). This is because for the maximum coverage value is 1.0 for ion exchange and typically <1.0 for adsorption.

In summary the analysis of dimensionless numbers for the ionomer contamination also reveals that the higher Da_2 , Ψ_2 and the Γ_2 lead fast contamination reaction and the reaction continues until the coverage reached 1.0. For the tolerance point of view, the predictions show that coverage of less than 0.1 is required for the voltage loss to be less than 25mV by ionomer contamination. Another possible ionomer contamination mechanism is absorption of contaminant A into ionomer in electrode. In this case, we can use same design equations and analysis with Pt adsorption cases. That is, the Langmuir absorption isotherms can be used predicting the impacts of ionomer contamination.



a)



b)

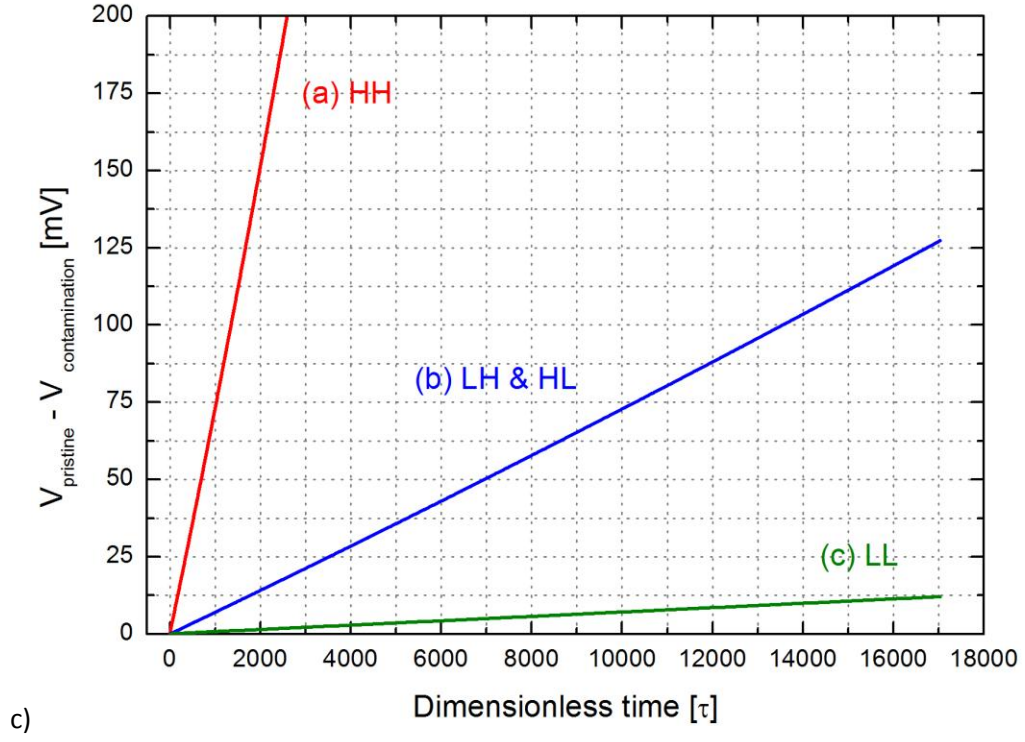
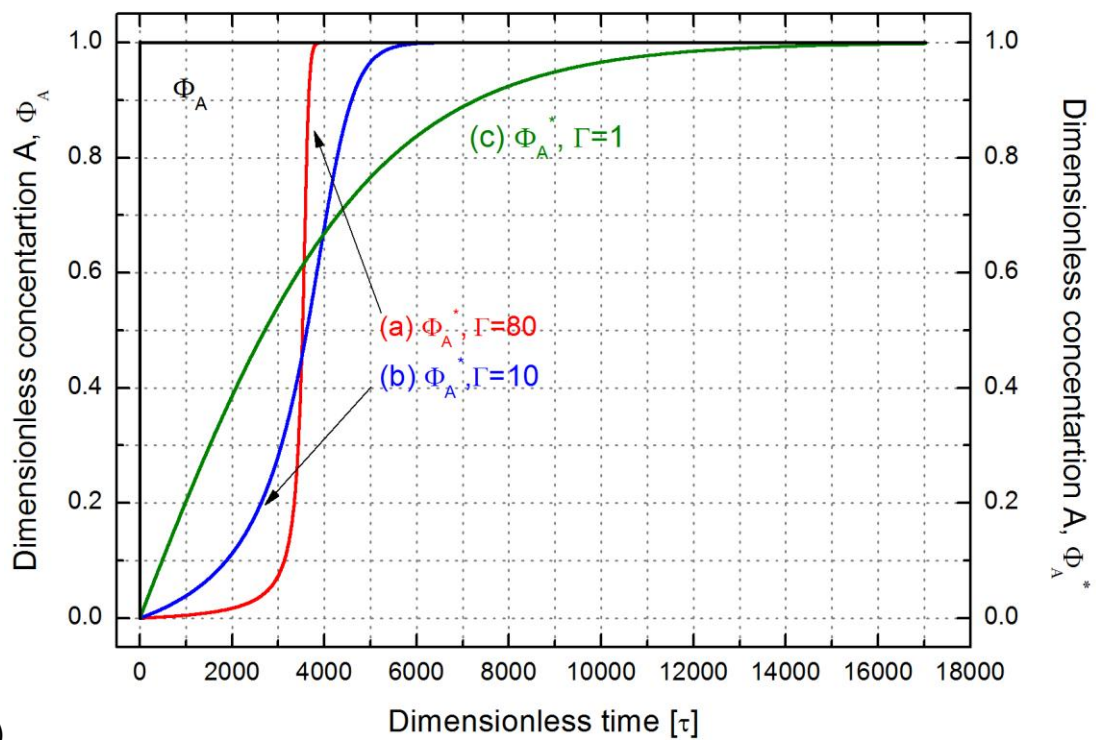
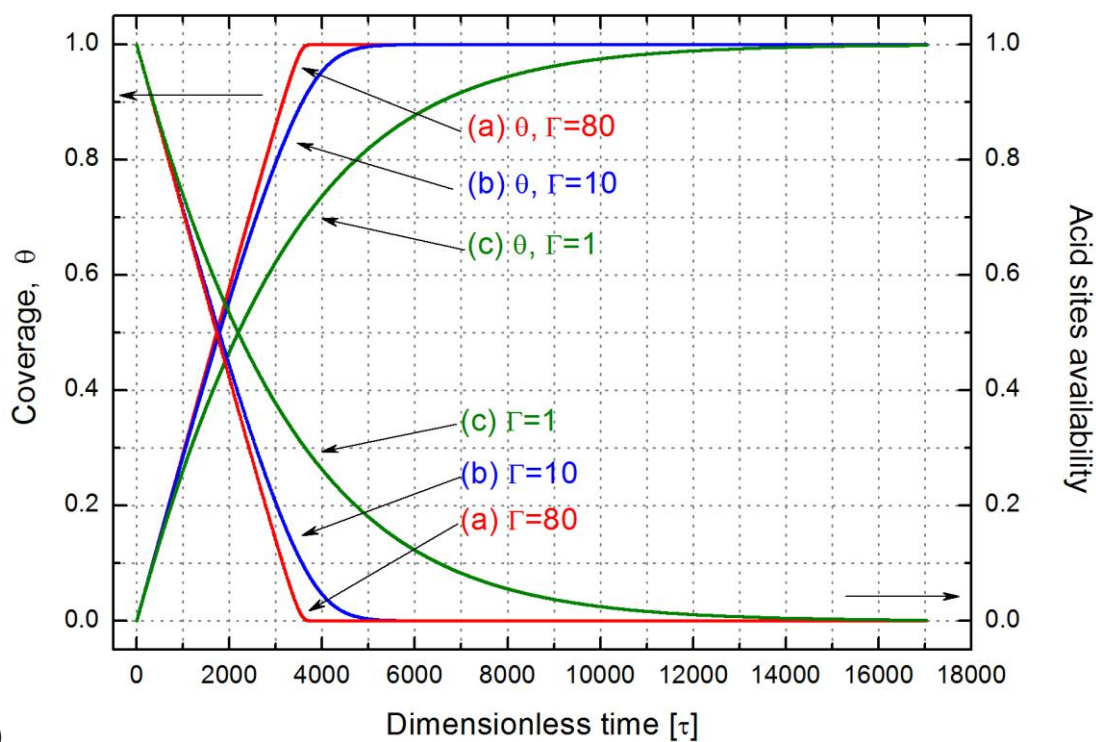


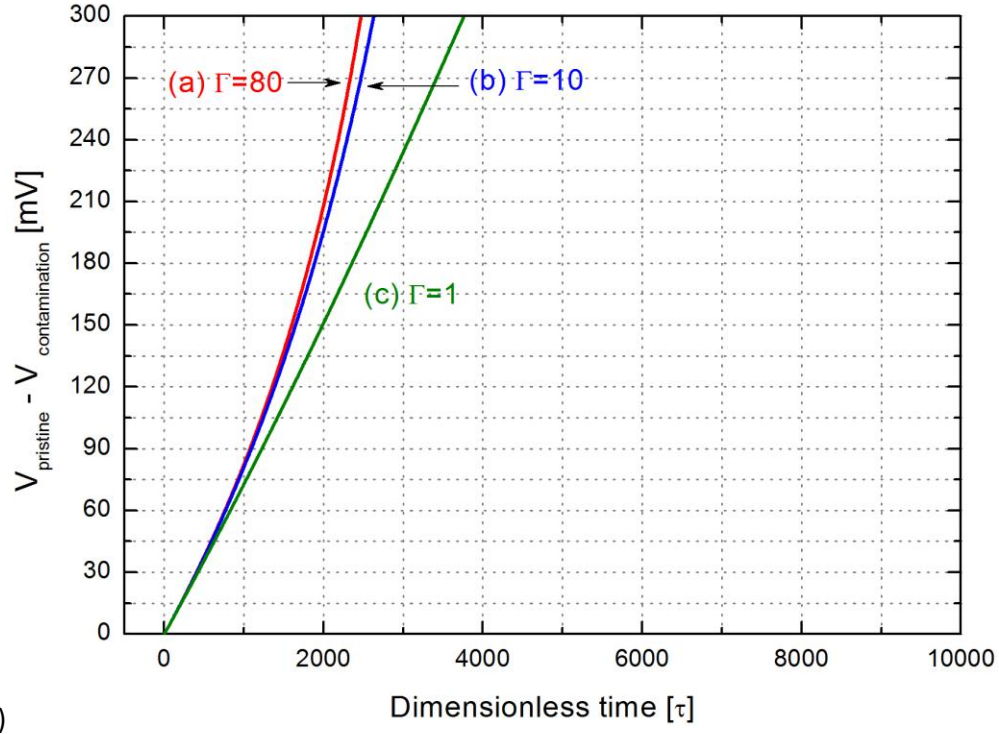
Figure 3.5 a) Dimensionless concentration at the interface ($@ \xi=0$), b) Coverage and acid sites availability, c) Voltage changes as varies with Da_2 and Ψ_2 and fixed $\Gamma_2=1.0$ (a) High/High (b) Low/High & High/Low (c) Low/Low



a)



b)



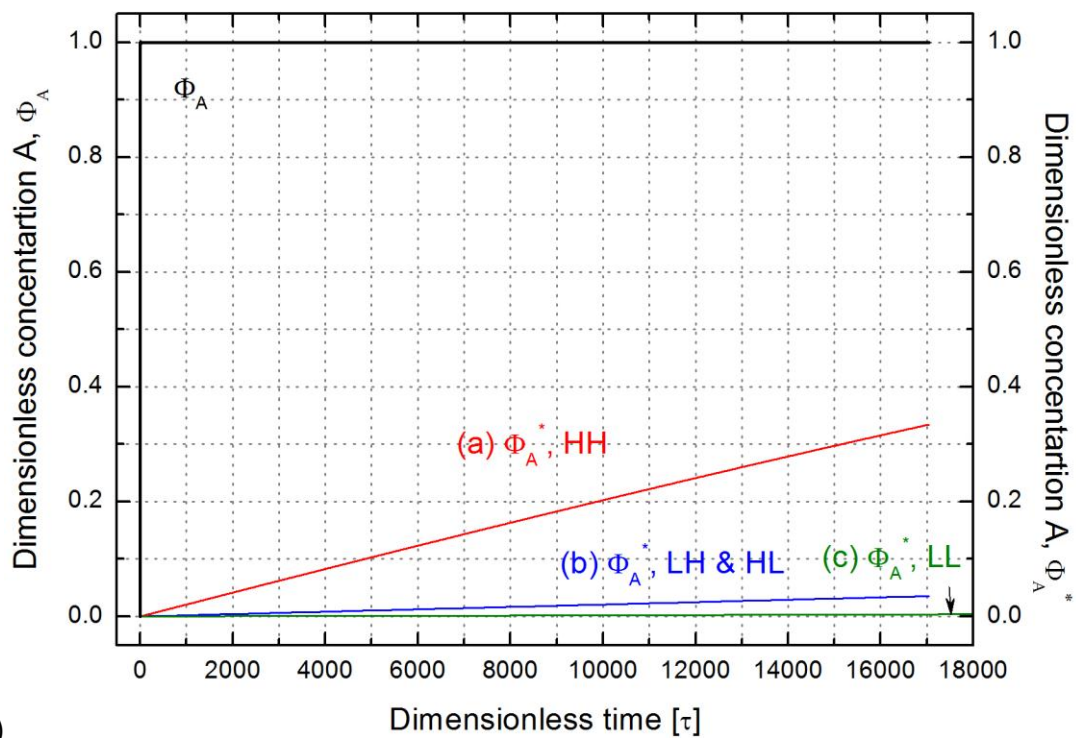
c)

Figure 3.6 a) Dimensionless concentration at the interface ($@ \xi=0$), b) Coverage and acid sites availability, c) Voltage changes by ionomer contamination as varies with Γ_2 (a) 80 (b) 10 (c) 1 and Da_2 and Ψ_2 are fixed.

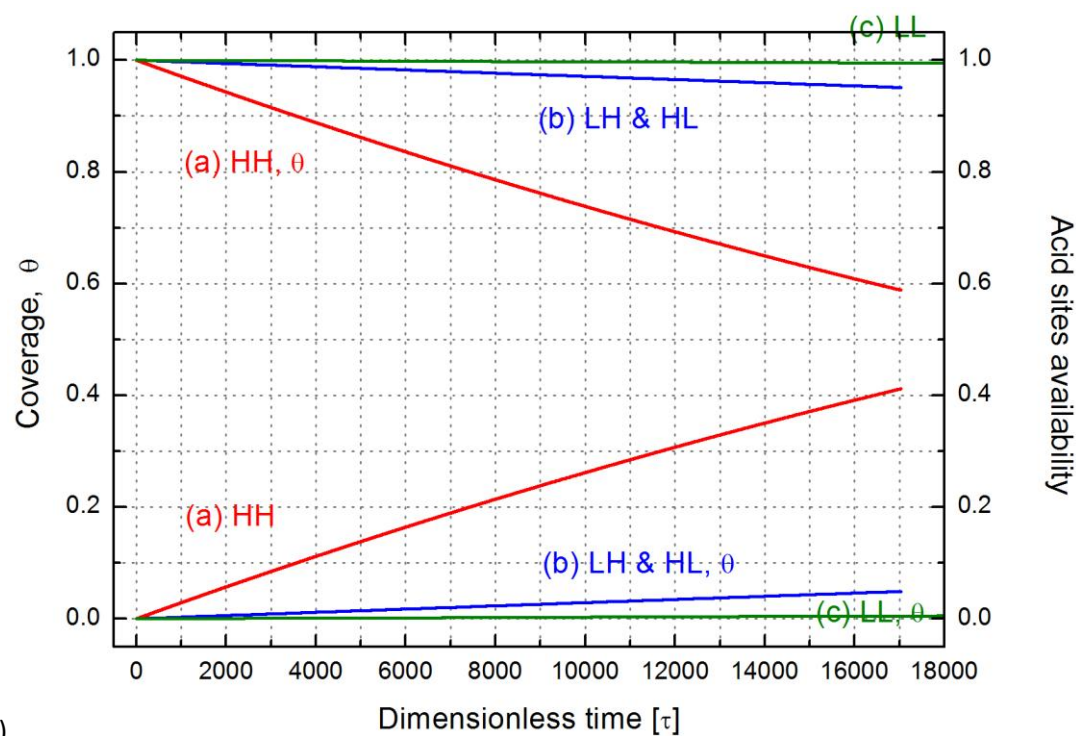
3.3.4 MEMBRANE CONTAMINATION

Similarly, the analysis of dimensionless numbers for the membrane contamination by ion-exchange reaction also show that higher Da_3 , Ψ_3 and Γ_3 yield fastest contamination as shown in Figures 3.7 and 3.8. The interesting aspect of membrane contamination is that Ψ_3 is a small number due to the moles of ionome in a typical membrane. Thus contamination and voltage loss are slower for the membrane than the catalyst or ionomer in the electrode. This is the same explanation as noting that the contamination reaction is significantly slower than electrode contamination since the diffusion lengths are increased as the reaction plane moves toward the center of the membrane (i.e., $Da_{1,2} > Da_3$). The membrane contamination by ion-exchange reaction continues until the acid sites are fully exchanged which lead to the total loss of conductivity.

From a tolerance perspective, the prediction results show that the membrane contamination is more tolerant than the ionomer contamination. However, we believe that both mechanisms are interacted with each other. In other words, the greater capacity in membrane can decrease the steady state contamination by equilibrium the coverage between less capacity (i.e., ionomer) and more capacity (i.e., membrane). Note that the prediction results in Figure 3.3 to 3.8 are prepared by assuming non-interaction between contamination sources (i.e., ionomer and membrane). We will discuss in next section about the interaction of ionomer and membrane contaminations.



a)



b)

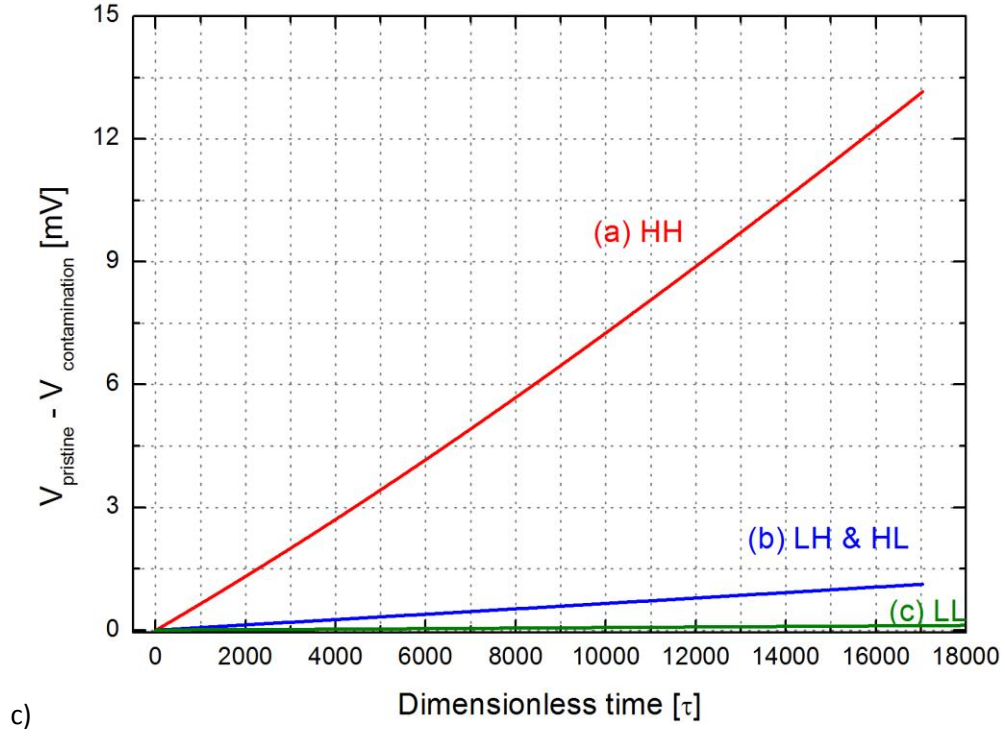
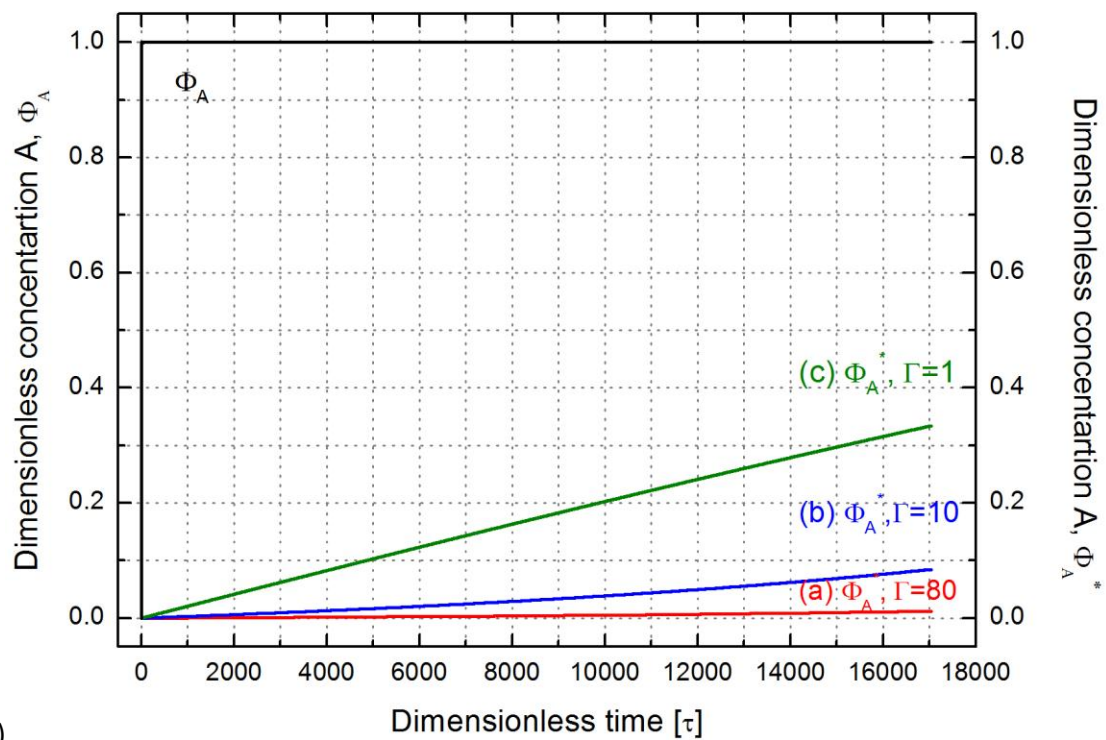
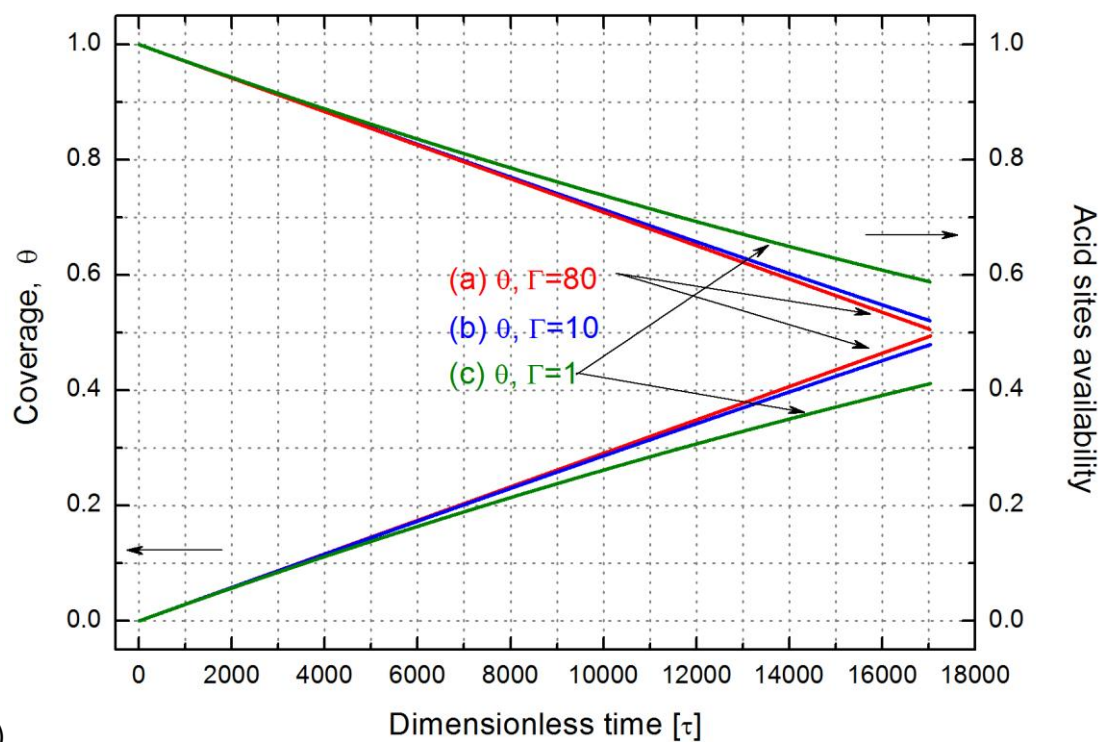


Figure 3.7 a) Dimensionless concentration at the interface (@ $\xi=0$), b) Coverage and acid sites availability, c) Voltage changes by membrane contamination as varies with Da_3 and Ψ_3 and fixed $\Gamma_3=1.0$ (a) High/High (b) Low/High & High/Low (c) Low/Low



a)



b)

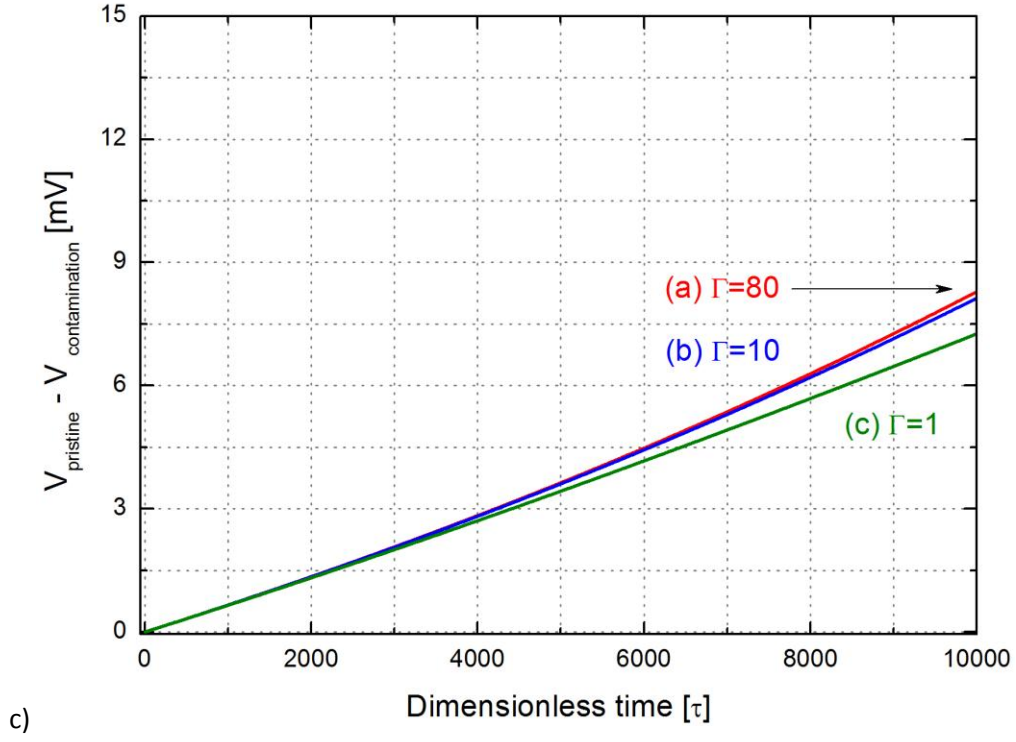


Figure 3.8 a) Dimensionless concentration at the interface (@ $\xi=0$), b) Coverage and acid sites availability c) Voltage changes by membrane contamination as varies with Γ_3 (a) 80 (b) 10 (c) 1 and Da_3 and Ψ_3 are fixed.

3.3.5 DISTRIBUTIONS ALONG THE CHANNEL

Figure 3.9 shows the local coverage and local voltage distributions to the dimensionless length (ξ) for contaminant A as Da increases for each mechanism (i.e., adsorption and ion exchange). Both mechanisms show that the concentration distribution becomes more important with increasing the Da number. Figure 3.10 shows the local coverage and local voltage distributions for contaminant A to the dimensionless length (ξ) as Ψ increases for each mechanism (i.e., adsorption and ion exchange). Like the Da , both mechanisms show that the distribution becomes more important with increasing the Ψ . Note that the local voltage for the ion exchange was predicted from the consideration of ionomer in the electrode.

3.4 COMPARISON TO EXPERIMENTAL DATA

In this section, the contamination model presented above is compared with the *in-situ* experiment data. To make these comparisons, the selections of dimensionless numbers are important. These values could be obtained from the literatures or determined from separate *ex-situ* experiments [49-50,72,73]. To predict the comparisons we chose, an organic compound, diethylene glycol monoethyl ether (DEGEE), which shows multi contamination mechanisms, and sodium (Na^+) which shows only ion-exchange phenomena. That is, the possible mechanisms for the DEGEE contaminant is the adsorption on the Pt surface and the absorption into ionomer and membrane, whereas the Na^+ has only effect on ionomeric components by the ion-exchange reaction.

The calculated Da and Ψ for each mechanism are shown in Table 3.6 (i.e., 1=Pt, 2=ionomer, 3=membrane). For the Ψ calculation, the $ECSA=68.0m^2/g_{pt}$ is used for each

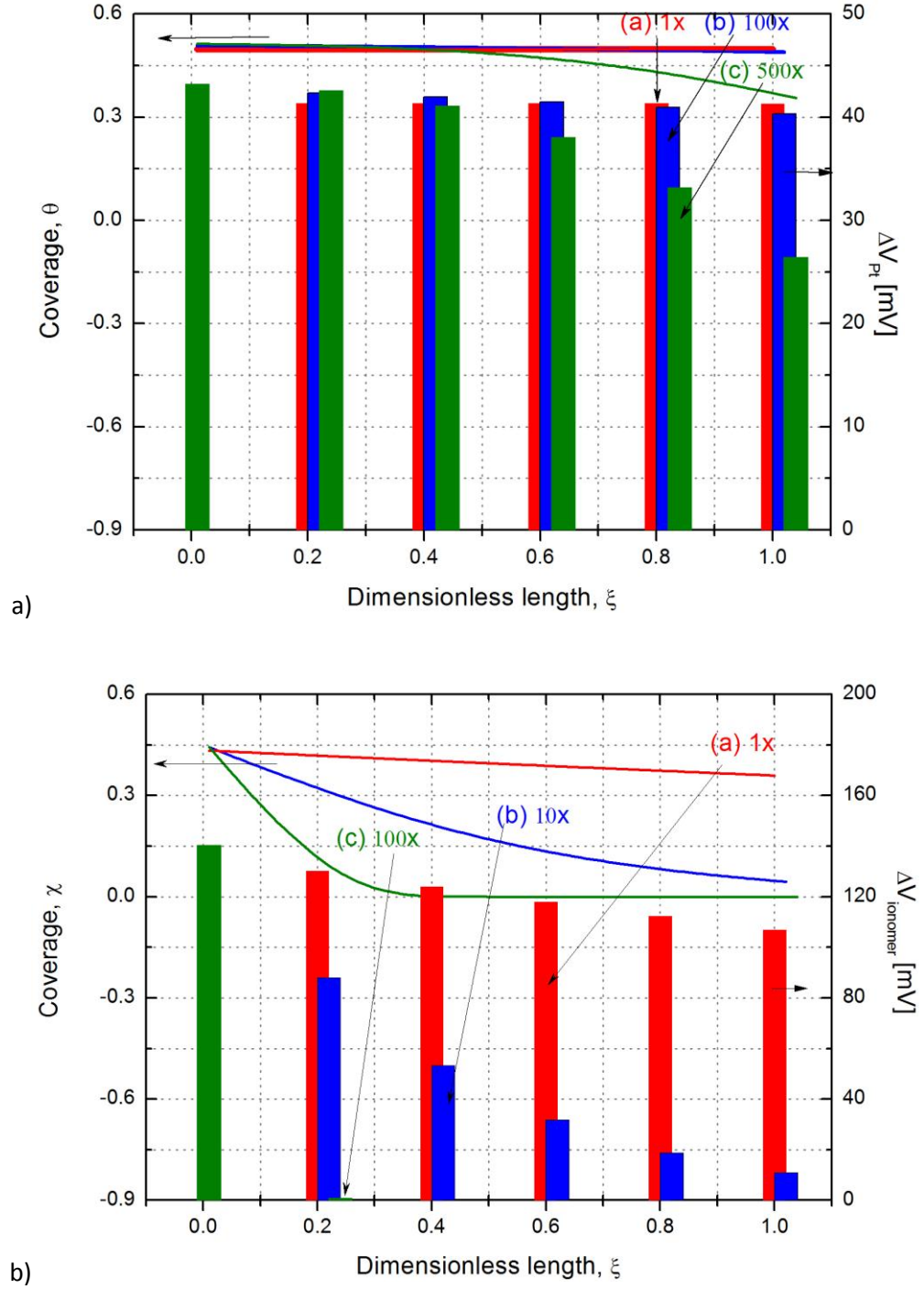
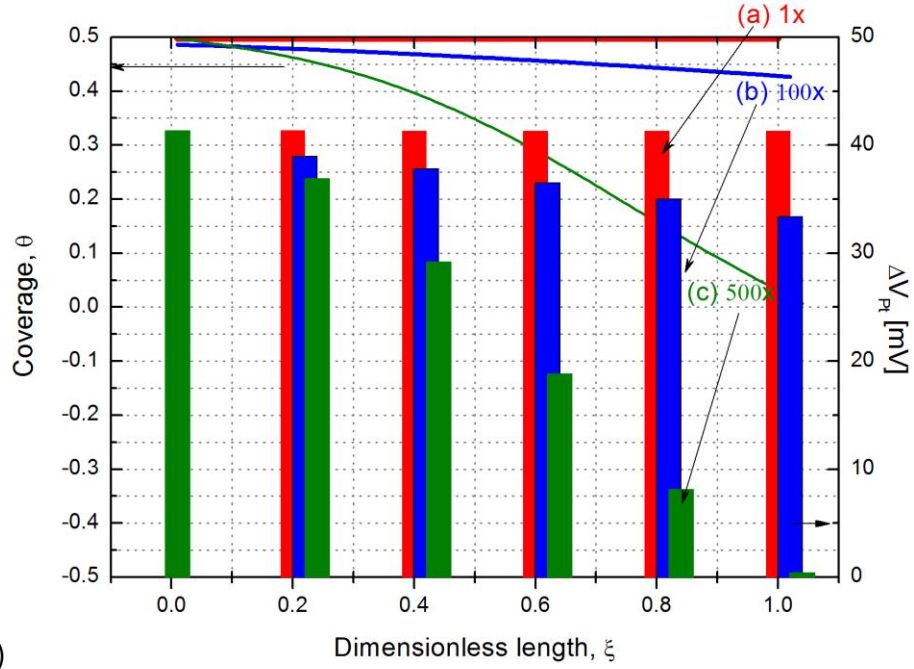
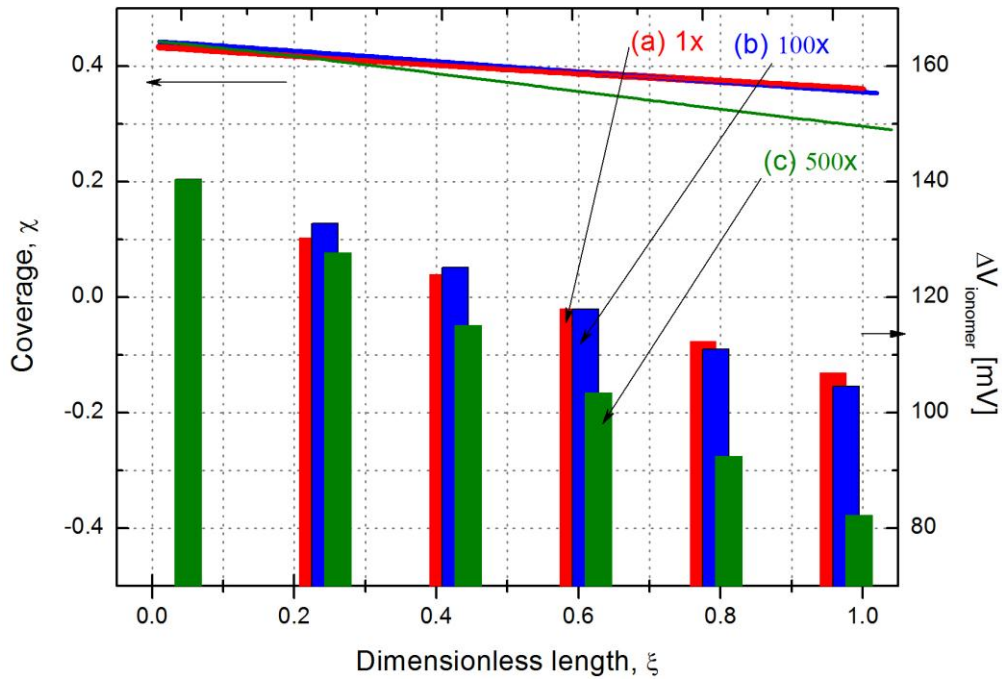


Figure 3.9 Local coverage and ΔV distributions for contaminant A to the dimensionless length as varies of Da , a) adsorption, $1X(Da_1=0.03, \Psi_1=0.14, \Gamma_1=6)$, b) ion-exchange, $1X(Da_2=0.056, \Psi_2=0.003, \Gamma_2=1.0)$



a)



b)

Figure 3.10 Local coverage and ΔV distributions for contaminant A to the dimensionless length as varies of Ψ , a) adsorption, 1X($Da_1=0.03$, $\Psi_1=0.14$, $\Gamma_1=6$), b) ion-exchange, 1X($Da_2=0.056$, $\Psi_2=0.003$, $\Gamma_2=1.0$)

case, the effective diffusion coefficient is obtained from Eq. [3.33] and [3.34] assuming the ionomer thickness as 1 μm of 5 μm of electrode thickness. The diffusion coefficient of methanol and Na^+ in Nafion[®] membrane were used to represent the diffusion of DEGEE and Na^+ in ionomer and membrane respectively [56-61].

3.4.1 SCALE EX-SITU TO IN-SITU

Our goal for the model is to predict in-situ voltage losses using *ex-situ* measurement. For the Pt coverage the ex-situ measurements should be performed on thin-film electrode. As shown in Figure 11, these *ex-situ* Pt coverage data are obtained with contaminants in the liquid phase. However for the *in-situ* cases, transport of contaminants is predominantly through the gas phase. Thus, assumption (16) is useful since the concentrations are low. Further to establish the relationship between the coverage measured with *ex-situ* liquid concentration shown in Figure 11 and the coverage corresponding to gas phase concentration of *in-situ*, we match the capacity ratios as shown in Eq. [3.47].

$$\frac{\Psi_{ex}}{\Psi_{in}} = \frac{C_{A0,ex}}{C_{A0,in}} \frac{h_{ex}(=y)A_{ex}}{h_{in}A_{in}} \frac{C_{S,in}(t=0)}{C_{S,ex}(t=0)} = 1 \quad [3.47]$$

In Eq. [3.47], the *in-situ* available moles are calculated using the volume of the channel which corresponds to the product of the electrode area and the channel length. This corresponds to the available moles for contamination since the gas diffusion coefficients are large and yield well-mixed conditions in the channel. For the *ex-situ* available moles,

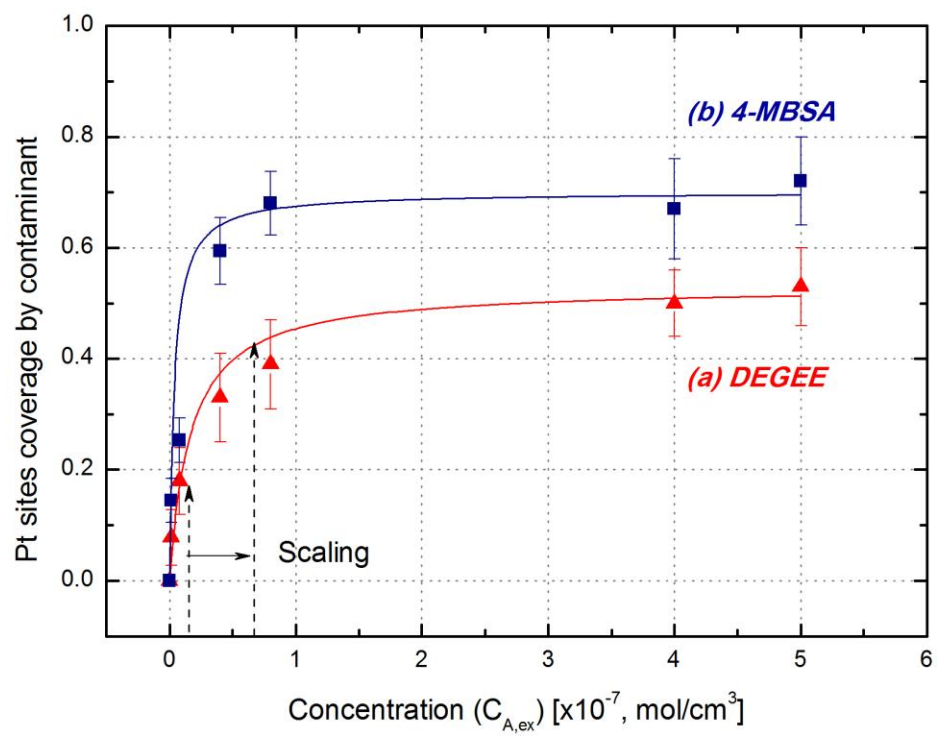


Figure 3.11 *Ex-situ* adsorption isotherm curve of Pt/C for DEGEE and 4-MBSA

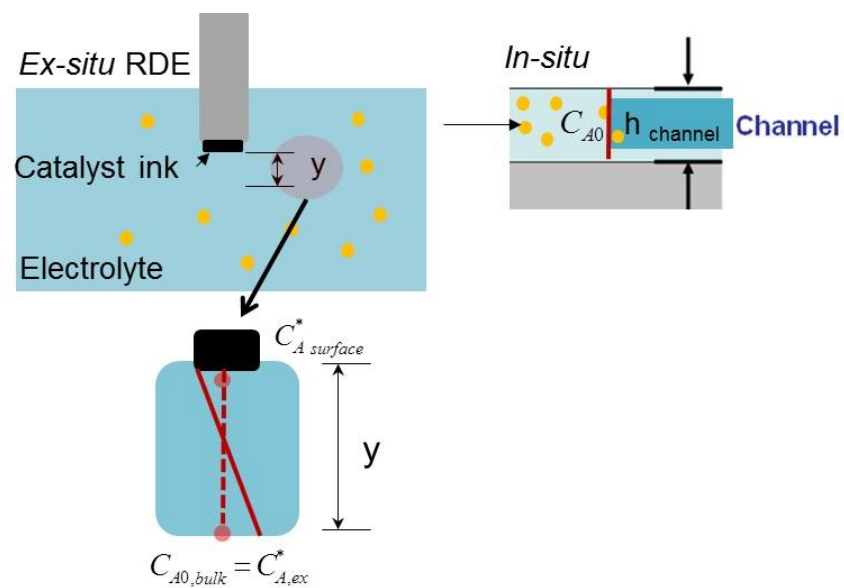


Figure 3.12 Comparison of *ex-situ* and *in-situ* for Pt contamination scaling

we use the product of the liquid phase contaminant concentration, thin film electrode geometric area, and the diffusion boundary layer. Note that since there is a concentration gradient in the diffusion layer, we use $C_{A0,ex}/2$ as shown in Figure 12. Now to determine the boundary layer we use Eq. [3.48].

$$\zeta = y \left(\frac{a \nu}{3D_R} \right)^{1/3} \sqrt{\frac{\Omega}{\nu}} \quad [3.48]$$

where, $a = 0.51$, ζ =dimensionless concentration for boundary layer, ν = kinematic viscosity of water, D_R = diffusion coefficient of reactant, Ω = angular velocity

For the experiments of Figure 3.11, we rotated the electrode at 2400 rpm and these are calculate a boundary layer of 0.087 cm as shown in the Appendix A and Figure 3.11.

Scaling factor for the adsorption mechanism is 40. This scaling factor indicates that the concentrations of adsorption isotherm shown in Figure 3.11 must be divided by the 40 to apply to the *in-situ* data or predictions.

$$C_{A0,in} = C_{A0,ex} / 40 \quad [49]$$

For the ion-exchange mechanism, the scaling factor for the electrode and the membrane can be determined by Eq. [3.50] where the thickness of each membrane section is known.

$$\frac{\Psi_{ex}}{\Psi_{in}} = \frac{C_{A0,ex}}{C_{A0,in}} \frac{A_{ex}}{A_{in}} \frac{C_{HM,in}(t=0)}{C_{HM,ex}(t=0)} \frac{z_{mem,in}}{z_{mem,ex}} = 1 \quad [50]$$

3.4.2 ADSORPTION AND ABSORPTION MECHANISMS

Figure 3.12 shows the prediction results as lines in comparison with *in-situ* experiment results for each three cases in Table 3.5 corresponding to change in the feed concentration and the current. The comparison of the model prediction with *in-situ*

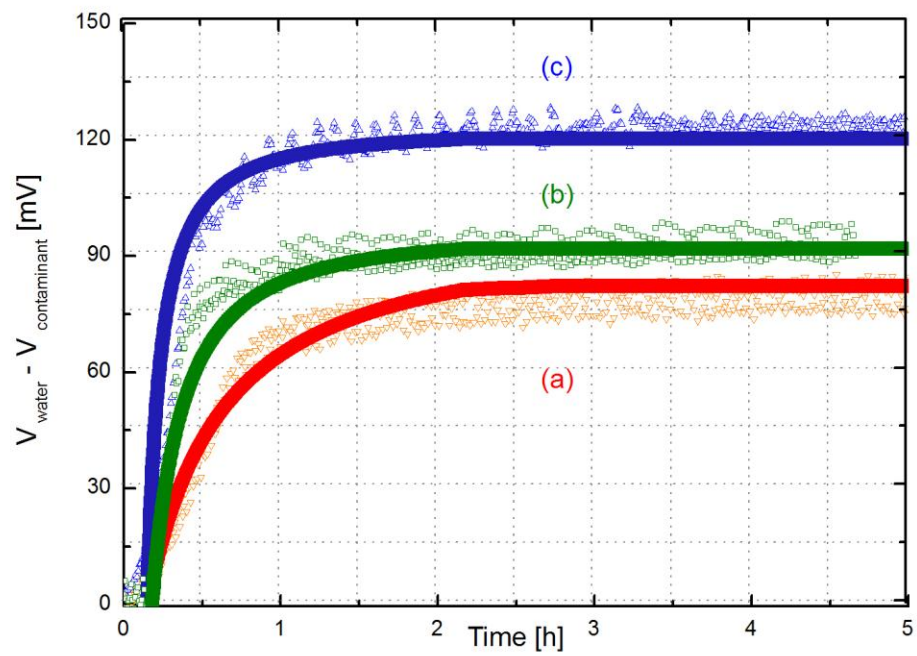


Figure 13. Comparison of model predictions and *in-situ* DEGREE infusion voltage loss (iR corrected)

Table 3.5. Experimental conditions shown in Figure 3.13 and comparison of ΔECSA

Exp. #	T [°C]	RH [%]	i [A/cm ²]	C _{A0} [mol/cm ³]	ΔECSA [%]	
					Measurement	Prediction
a	80	32	1	1.35E-08	-24.1	-20.8
b			0.2	1.33E-08	-26.0	-23.6
c			0.2	6.63E-08	-40.0	-42.3

Table 6. Dimensionless numbers for model prediction in Figure 3.13

Exp. #	Ψ_1	Da ₁	Ψ_2	Da ₂
a	2.01E-03	9.34E-03	1.31E-03	9.13E-03
b	1.97E-03	4.61E-02	6.40E-03	4.08E-02
c	9.84E-03	4.61E-02	1.28E-03	4.08E-02
K _{eq}	6.0E+07 [cm ³ /mol]		8.0E+07 [cm ³ /mol]	
B	0.53		0.32	

experiment data for all cases shows that the predicted coverage (ΔECSA) and voltage loss (iR corrected) are reasonable (see Table 5). Table 3.5 shows that the Ψ_1 and Ψ_2 for case (a) and (b) are almost equal since the feed concentrations at the channel are close and thus the model predicts the same loss of ECSA (i.e., coverage). Prediction results for coverage seems reasonable compared to the experiment measurements (i.e., *in-situ* CV at the end of infusion). Also, the Da_1 and Da_2 for case (b) and (c) in Table 3.6 are equal due to the same species (i.e., D_{eff} is constant) and operating conditions such as RH, i , T , and stoics. Note that for the case of (a) in Table 3.6, the $i=1.0\text{A}/\text{cm}^2$ was higher than that of cases (b) and (c) (i.e., $i=0.2\text{A}/\text{cm}^2$) and for a fixed stoic of 2.0/2.0, the u_f for case (a) is larger than cases (b) and (c). The larger u_f decreases the Da number. Likewise the model predictions with the higher Da and Ψ yield the fast contamination and the higher Γ causes a higher coverage ratio (i.e., the greater voltage loss at the steady state).

For the case of (a) in Figure 3.12, each contribution from different contamination sources (i.e., Pt, ionomer, and membrane) are shown in Figure 3.13. The voltage losses by Pt (15%) and membrane contamination (8%) show relatively small impacts to the total loss whereas the ionomer contamination (77%) shows a significant impact. As we described earlier, the predicting voltage loss for each source were different even though the coverage could be equal (see Figure 3.2). For the tolerance prospective, the 90mV of total voltage loss that occurs within 5 h is unacceptable. However, we can speculate that the ionomer contamination by the absorption of DEGEE can be recoverable since the DEGEE does not have any functional groups and hence there should be no ion exchange with the acid group in the ionomer. Thus, we can speculate that the DEGEE can be easily

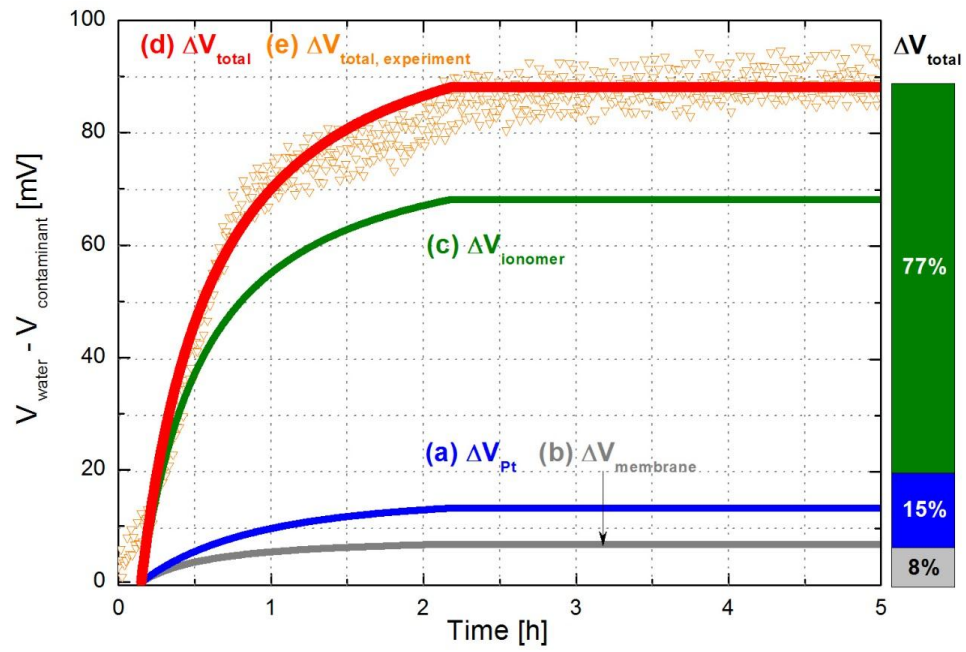


Figure 3.14 Analysis of total voltage loss by contamination sources

Table 3.7. Dimensionless numbers for model prediction in Figures 3.14 and 3.15

	256ppm DEGEE (Figure 14)	30ppm NaOH (Figure 15)
Ψ_1	2.01E-03	-
Ψ_2	1.31E-03	9.76E-05
Ψ_3	1.31E-03	9.76E-05
Da_1	9.34E-03	-
Da_2	9.13E-03	1.06E-03
Da_3	9.13E-03	1.06E-03

removed by contaminate-free gas purges. We observed that the HFR change during contamination and during a recovery experiment supports (see Chapter 5) this explanation.

3.4.2 ION-EXCHANGE MECHANISM

Figure 3.14 shows the prediction results as lines in comparison with experiment results as dots for 30ppm of NaOH infusion. The comparison of the model prediction with *in-situ* experiment data shows that the predicted voltage loss is reasonable for an initial infusion region (i.e., $t=0 - 40$ h). The voltage loss by the ionomer contamination is significantly larger than the other sources (i.e., Pt and membrane). It should be pointed out that the Pt contamination can be neglected for Na^+ contamination. A previous study [8-9] also reported that the cation contamination on electrode did not affect on the Pt catalyst but speculated that there was an effect in the ionomer. *In-situ* cyclic voltammetry (CV) measurements during 80 h of NaOH infusion (see the vertical data at 21 h, 45 h, and 78 h in Figure 3.15) supports no change of available Pt concentration (i.e. negligible ECSA changes <5%) as shown in Figure 3.16. The membrane contamination also shows relatively small impact on PEMFC performance relative to ionomer contamination. However, an over-prediction is observed after 40 h. We believe that the over-prediction results clearly indicate the interaction between ionomer and membrane. The reason for this is that the Da number is decreased with time since the contamination reaction plane moves toward the membrane from the electrode. The effective diffusion length is increased which results in lowering the Da number. Thus, the other line which show lower slope of voltage loss is drawn at 50 h in Figure 3.15 (i.e., solid line=reaction plane

in the electrode, dash line=reaction plane in the membrane). We speculate that the initial contamination is governed by the ionomer contamination and the membrane contamination becomes more important as the contamination continues. In addition, we believe that the contamination by the ion exchange cannot be recoverable since the Na^+ has the strong interaction with the sulfonic acid groups in ionomeric components (e.g., Nafion[®]).

3.5 CONCLUSION

A simple time dependent 2-D model that accounts for the contamination mechanisms in PEMFCs in terms of measureable properties has been provided. The model equations allow prediction of performance loss and distribution (i.e. voltage distribution) for PEMFCs. The contamination phenomena are shown to be controlled by three important dimensionless groups: a Damhköler number for the contamination reaction rate (Da), a capacity ratio (Ψ), and a coverage ratio (Γ) for each mechanism. The experiments and model predictions were compared to evaluate the model and the predictions are shown to be reasonable. A method for scaling a equilibrium constants between liquid phase ex-situ and gas phase in-situ has been presented. The model can be used to provide a tolerance limits for contamination. The model does not predict long term ion exchange because the acid sites in the electrode and membrane are interacted. Future work will address their interaction.

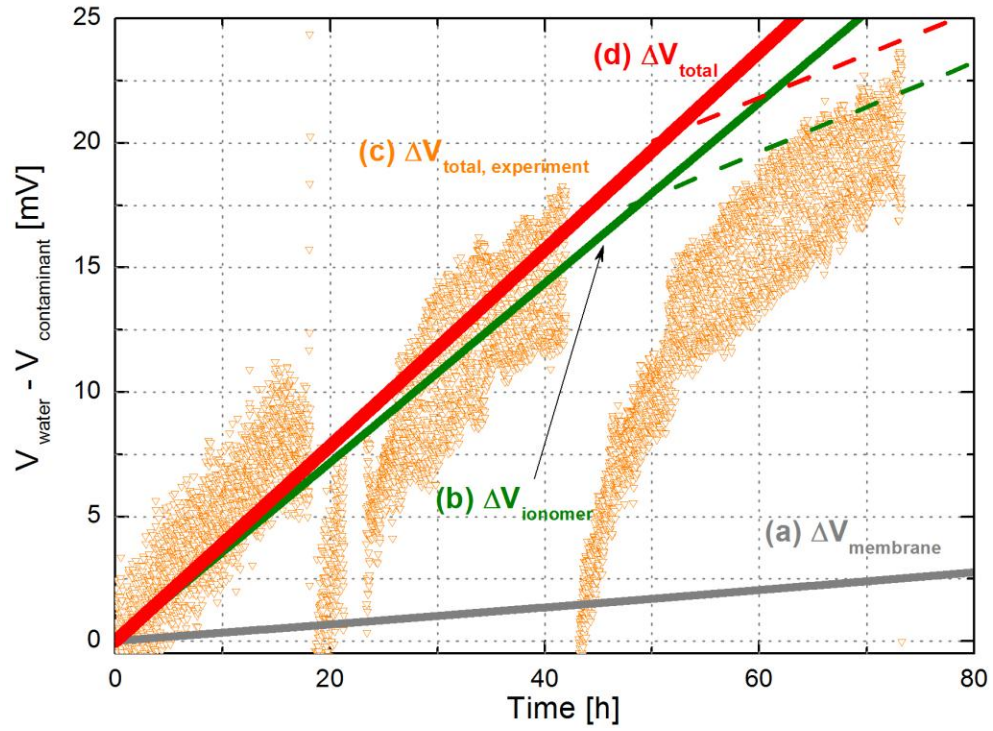


Figure 3.15 Comparison of model predictions and *in-situ* 30ppm of NaOH infusion voltage loss

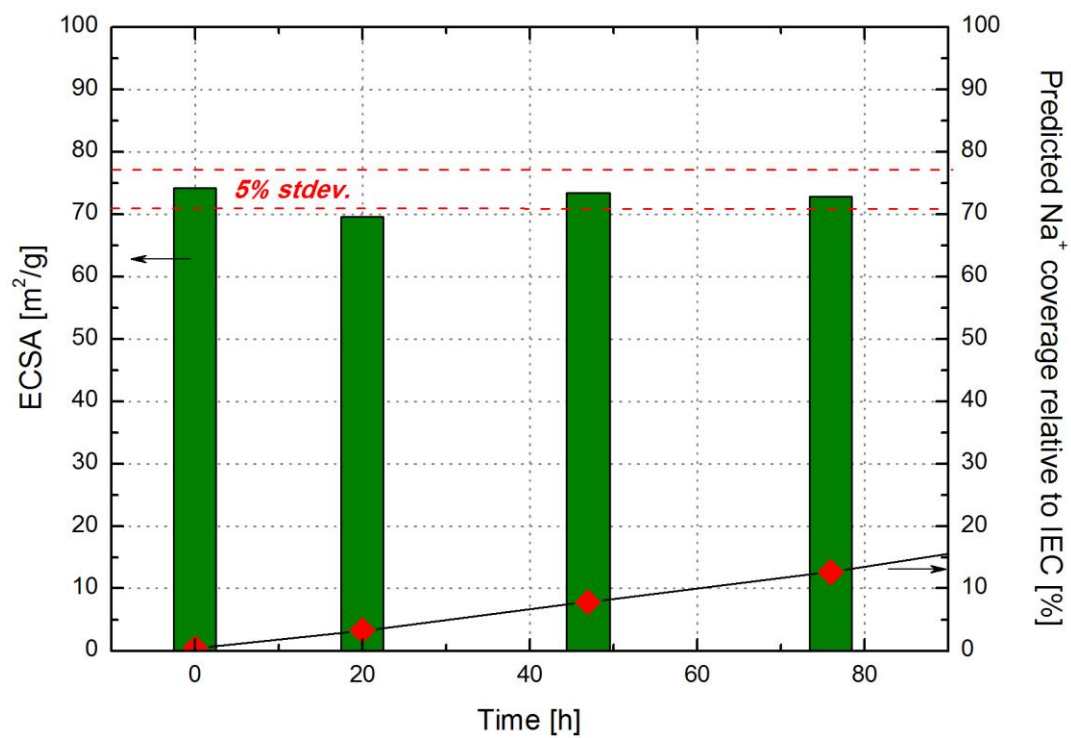


Figure 3.16 *In-situ* measurements of ΔECSA during 30ppm of NaOH infusion for 80 h

CHAPTER 4

UNDERSTANDING THE FUNDAMENTAL MECHANISMS AND PREDICTING PERFORMANCE LOSS IN PEMFCs FROM ANILINE AS A CONTAMINANT

This chapter presents an *ex-situ* study of aniline, a possible contaminant for proton exchange membrane fuel cells (PEMFCs) originating in balance of plant (BOP) components. Three mechanisms are investigated: (1) adsorption on Pt/C catalyst, (2) ion-exchange reaction in membrane, and (3) electrochemical reactions which may compete with the main reactions of the PEMFC. The results show that aniline shows a higher affinity to proton exchange membrane than other monovalent cations, thus indicating greater conductivity loss at the same concentration of contaminant. Conductivity loss for aniline-contaminated NRE211 shows 100 times lower than pristine at RH=50%. The water content measurements show that water expulsion by aniline from the membrane also leads to significant conductivity loss. Electrochemical surface area (ECSA) is lost with aniline adsorption and comparison of Pt/C adsorption isotherms for aniline and benzene shows that this loss provides an understanding the impact is due to the aromatic functional group of aniline.

4.1 INTRODUCTION

In the development of proton exchange membrane fuel cells (PEMFCs), the cost of balance of plant (BOP) materials and their effect on PEMFC durability can retard commercialization and installation. Fuel cell durability can be affected by contaminants from gaskets or seals in the form of metal cations [5-14], and also from organic leachates from stack and BOP components [31-34, 49-50]. These BOP components would cost less if off-the-shelf materials were used, and in this paper we consider an amine-based contaminant that may be present in hoses and tubing materials, especially those colored with dyes. Our long-term goal is to identify compounds that may decrease performance and to suggest that *ex-situ* experiments may provide sufficient data to establish “criteria for avoidance” in BOP components. We seek evidence that aids the preliminary screening of BOP materials and helps us recommend alternative materials to component suppliers, enabling them to minimize contaminant effects while maintaining high performance levels in PEMFCs.

Table 4.1 Properties of aniline in H₂O

Properties	Concentration of aniline in water					Remark
	5mN	1mN	0.5mN	0.2mN	0.1mN	
UV-vis absorbance intensity	-	1.446	0.695	0.28	0.132	@280nm
pH	6.54	5.5	5.3	5.07	4.84	
Conductivity[μs]	4.69	2.51	2.14		1.96	
Vapor pressure of aniline						
Temperature[℃]	20	34.8	69.4	96.7	119.9	
Vapor pressure[mmHg]	0.6	1	10	40	100	

pK_b= 9.3 in acidic solution

Solubility in water : 3.6g/100ml at 20 $^{\circ}$ C

Aniline is one of the oldest commercial organic chemicals used by the synthetic dye [74] industry and is used in the production of colored hoses and packing in the automotive industry. It has been identified in leaching solutions during the screening [33] of possible off-the-shelf BOP materials. Thus, both the anode and cathode might be affected by aniline compounds exposed to water in PEMFCs since the amine group easily dissolves in water and protonates in acidic solutions as shown in Figure 4.1. In this chapter we investigate three mechanisms through which aniline may decrease the fuel cells' performance: (1) chemical adsorption which decreases the active sites of platinum carbon (Pt/C) catalyst, (2) electrochemical reactions which may compete with the main reactions of the PEMFC, and (3) ion exchange reactions between anilinium ion and proton sites of the ionomer in electrode and membrane, decreasing the conductivity of the catalyst layer and proton exchange membrane.

The hydrolysis of aniline ($pK_b=9.3$) [74] results in a cation, anilinium, which is similar to NH_4^+ . We note that NH_3 has drawn recent attention as a fuel contaminant [15, 75]. The adsorption of aniline compounds from a solution onto both carbon and Pt has been reported, with some evidence that the benzene ring induces both steric hindrance and a change in the hydrophilic property [76-77]. For example, Huang et.al, [77] reported that aniline can be adsorbed on the surface of a Pt (111) in the presence of hydrogen gas at 350K as a parallel-positioned aromatic benzene ring (π -bonding). Adsorption resulting from the benzene ring may also occur in the gas diffusion layer (GDL), as well as in the catalyst layer although no data has been reported and we did not observe significant changes in the liquid phase solution through immersion. Only a few studies on the diffusion of aniline through the perfluorosulfuric acid (PFSA) ion exchange membrane

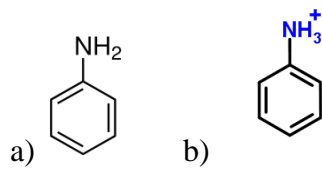


Figure 4.1 Schematics of aniline and hydration form
(a) aniline; (b) hydrated anilinium ion

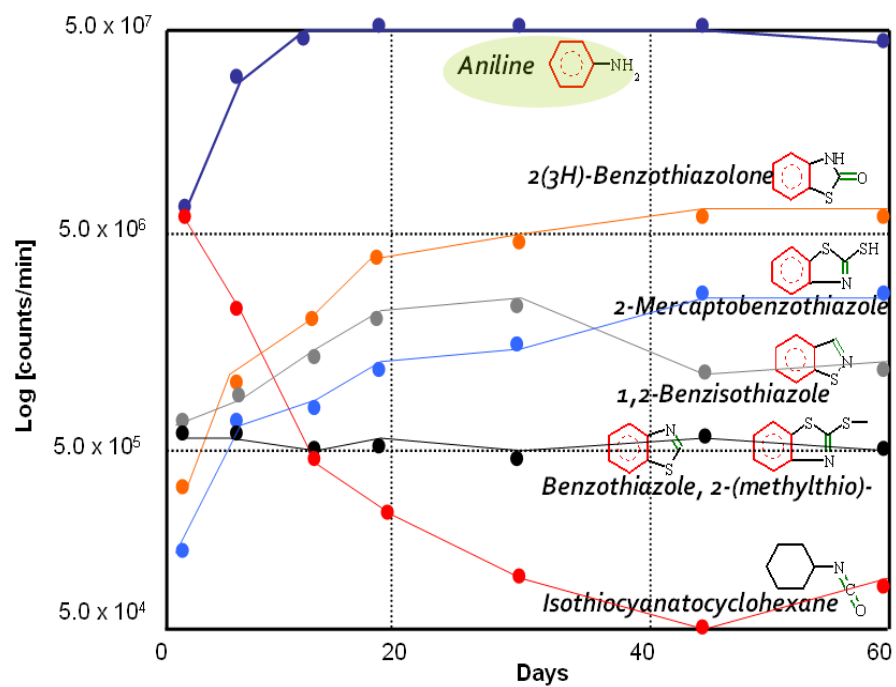


Figure 4.2 Identify model compounds from SBR leachants by GCMS

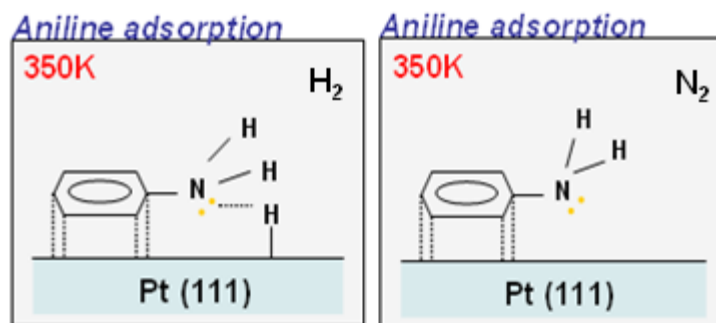


Figure 4.3 Schematic of adsorbed aniline on Pt site [77]

have been reported, and these studies were conducted with the sodium form of the membrane rather than the proton form of the membrane [78-79]. Studies in which PANI film was synthesized by electrochemical potential cycling between 0.0 and 0.8V (vs. RHE) have been also reported [80-82], and PANI polymerization is studied below since it may be a competitive reaction in addition to loss of ECSA in PEMFCs.

In this chapter, three possible aniline contamination mechanisms in PEMFCs are studied. We used a thin-film rotating disk electrode and electrochemical techniques such as cyclic voltammetry (CV) and kinetic current analysis of oxygen reduction reaction (ORR). The isotherms of the MEA and PFSA membrane are also reported by using UV-vis. spectrum analysis to determine change with solution concentrations.

4.2 EXPERIMENTAL

4.2.1 MEMBRANE ISOTHERMS

Several mixtures of sulfuric acid (5mN) solution and aniline (5mN) solutions were prepared with the different molar ratios for the measurement of the absorption isotherm of a N117 ($5.0 \times 2.5 \text{ cm}^2$) at 23°C. Two samples of each cation solution were prepared to check reproducibility.

The isotherm experiments included a pretreatment of the membrane, followed by immersion of the membrane in aniline solution of interest, followed by extract ions.

A pretreatment procedure used one piece of a dry N117 ($5.0 \times 2.5 \text{ cm}^2$) which was weighed prior pretreatment to calculate the IEC and which was then boiled in 2M HCl_2SO_4 for 1 h followed by storage in DI water. The pretreated samples were immersed in each of the mixtures and magnetic stirrer plates were used for mixing for 24

h to allow equilibrium conditions of the ion exchange reaction (or absorption) between the anilinium (or aniline) ions and the proton form of the membrane. Solution concentrations before and after the immersion were measured as discussed below. To confirm the amount of aniline exchanged, the membranes were placed in 2M HCl to extract the previously exchanged aniline.

The concentration of aniline species can be measured by a UV-visible spectrophotometer (Shimadzu UV2101) at a wavelength of 190–290nm. Table 1 shows the UV-vis. relative absorbance for different concentrations of aniline in water. For the UV-vis., 203nm wavelength was chosen for quantification of aniline ions in acid solutions and the calibration curve was linear with intensity at 203nm for the concentration of aniline solutions between 0.05 to 5mM with an accuracy of $\geq \pm 0.05\text{mM}$. ACS reagent grade HCl, H₂SO₄, NaCl, CaCl₂, and NH₄Cl were used as received.

4.2.2 WATER UPTAKE MEASUREMENT

With the objective of comparing water uptake for aniline and Na⁺ 70% exchanged sites, three pieces of N117s (0.9 cm × 4.25 cm) were placed as a sandwich in the Beckktech cell. The cell is equilibrated with a 300 sccm flow of H₂ at 80 °C and 90% RH for 1 h using a Scribner 890E PEMFC test station. The humidity was changed from low (20%) RH to high (95%) RH. After hold of 2 h for each RH to assure equilibrium conditions, we disassembled the cell, weighed the 3 piece sandwich, and calculated the mass of water uptake. Finally, the exchanged acid sites by aniline were measured by the back titration method.

4.2.3 MEMBRANE CONDUCTIVITY MEASUREMENT

For the conductivity measurements, NRE 211 was used to minimize the time to reach equilibrium. Membrane conductivities for pristine and aniline exchanged NRE211 membranes were determined at ten values of constant relative humidity (RH) (i.e., 10, 20, 30, 40, 50, 60, 70, 80, 90, 95%) by applying DC currents at the cell temperature of 80 °C. The potentiostat (model PAR273) was used with a four-probe conductivity Teflon-based cell (model BT-112) made by Beckktech LLC. The cell is equilibrated with a 300 sccm flow of N₂ at 80 °C and 90% RH for 1 h using a Scribner 890E PEMFC test station that was calibrated for both flow and humidity. The humidity was changed from low (20%) RH to high (95%) RH while the membrane conductivity was measured with a hold of 1 h for each RH to assure equilibrium conditions. A VAISALA dew point chamber was attached at the outlet of the conductivity cell to confirm dew point temperature of outgases relative to those set by the test station. No conductivity change were observed over three cycles of RH change and thus we conclude that the % exchange did not change during the conductivity measurements.

4.2.4 ATR-IR SPECTRUM ANALYSIS

Fresh samples of aniline exchanged membrane, NRE211 (0.9 cm × 4.25 cm) were prepared by soaking in mixture of 5mN of aniline and 5mN H₂SO₄ (1:1). The % exchange of proton sites was expected about 90% of IEC. The sample was rinsed with DI water to remove surface aniline and then, dried with nitrogen gas purging at room temperature for 30 min. ATR-IR spectra were collected on a spectrometer (Nicolet 670)

equipped with a detector (Spectratech). The average number of scans per spectrum was 100. Each spectrum was recorded from 4000 to 800 cm^{-1} .

4.2.5 RDE MEASUREMENT

Two electrodes, one with Pt and one without Pt catalyst, were prepared. Carbon-supported 45.5wt% Pt (Tanaka, Pt loading $0.02\text{mg}/\text{cm}^2$) was dispersed in isopropyl alcohol (IPA) and DI water in the presence of a 20wt% Nafion[®] (vs. Pt). The Pt catalyst ink was mixed and ultrasonically dispersed for approximately 20 minutes. Mixture of carbon and a Nafion[®] binder for the electrode without Pt were also prepared for comparison. Vulcan XC-72R powder was mixed with distilled water and IPA, followed by sonication for 30 min with cooling to maintain temperature. For each electrode, the ink was dropped onto a glassy carbon ring disk electrode (0.2475cm^2), and electrochemical analysis was performed with a PAR model 263A potentiostat. Only the RDE part of the electrode was used. A 0.1M perchloric acid solution (HClO_4) and mercury sulfate electrode were used as the electrolyte and reference electrode, respectively.

The electrochemical surface area (ECSA) was determined from CV experiments using the hydrogen adsorption/desorption peak according to equation (1) and found to range from $68 - 72\text{m}^2/\text{g}_{\text{pt}}$ for pristine Pt/C electrode (Pt loading= $0.02\text{mg}/\text{cm}^2$). The q (C/cm^2) is the atomic hydrogen adsorption charge density, L ($\text{g Pt}/\text{cm}^2$) is the Pt loading in the electrode, Γ ($= 210\text{ }\mu\text{C}/\text{cm}^2$) is the well-established quantity for the charge to reduce a monolayer of protons on Pt, i (A/cm^2) is the current density collected during CV scan, and f (V/sec) is the scan rate [85].

$$ECSA = \frac{q}{210 \cdot L} = \frac{\int \frac{i}{f} dV}{210 \cdot L} \quad [4.1]$$

The calculation for a double layer capacitance, C_{dl} (F/cm²) was made based on Eq. [4.2], the following equation where [86] in double layer regime of voltammogram. Cathodic and anodic current densities (i.e. i_c and i_a (mA/cm²)) were chosen at 0.4V (vs. RHE) of the CV voltammograms 25, 50, and 100 mV/s.

$$C_{dl} = \frac{\Delta i}{(dE/dt)} = \frac{\Delta i}{Scan\ rate} \quad [4.2]$$

4.3 RESULTS AND DISCUSSION

4.3.1 ION-EXCHANGE

In general, PFSA membranes must be well-hydrated to obtain optimal proton conductivity because the membrane's conduction mechanism relies on the dissociation of protons from the ion-exchange group in the presence of liquid water and available proton sites. If the cation contaminants occupy the available proton sites of the PFSA ion exchange membrane, or if they shield water from those sites [87-89], proton conductivity will decrease. The contaminants may also exchange with ionomers in the binder of the catalyst layer.

Measurements of aniline concentration in the solution before and after PFSA membrane immersion show that an ion exchange^{*} reaction occur in a Nafion[®] 117 (N117) membrane. Aniline can absorb into the PFSA membrane and interact with sulfonic acid sites due to hydrolysis ($pK_b=9.30$) in acidic solutions, as shown in the chemical structure of the anilinium ion in Figure 1. The UV-visible spectrums of aqueous aniline solutions at 280nm and acid solutions (0.1M HClO₄) at 203nm decreased upon exposure to N117

after immersion of the membrane in 1mN aniline (H₂O or 0.1M HClO₄). The measured capacity of the membrane was 6.0 ± 0.3 [$\mu\text{mol}/\text{cm}^2$], which is more than the sodium ion-exchange capacity of 5.0 ± 0.4 [$\mu\text{mol}/\text{cm}^2$]. The over-absorption of aniline compared to the ion exchange capacity can be explained by the hydrolysis of amine. The capacity of MEA was also measured to be 7.0 ± 0.4 [$\mu\text{mol}/\text{cm}^2$], which is also more than the sodium ion exchange capacity of 5.6 ± 0.3 [$\mu\text{mol}/\text{cm}^2$].

*Here we use ion exchange rather than absorption to describe the accumulation of aniline in the membrane because we observed a shift in the O=S=O stretching peak with ATR-IR measurements.

That is, the ion exchange by the anilinium ion and the absorption by aniline can be considered in the water cluster of the membrane. Note that aniline can exist in acidic conditions as aniline or as an anilinium ion. In PEMFCs, the silicon rubber gasket and the gas diffusion layer may be treated with a PTFE solution and thus we immersed these in aniline solutions to test the affinity of aniline for these materials. Our experiments did not reveal measurable absorption of aniline and even though the aniline might be absorbed into the micro-pores in carbon cloth GDL and micro-porous layers of the GDL due to hydrophobicity, it was not observed in our experiments.

The partition coefficient for ion exchange can be written for the following ion exchange reaction: $M^{n+} + n\text{HSO}_3 - R \Leftrightarrow M(\text{SO}_3 - R)_n + n\text{H}^+$, where M is the cation, HSO_3^- is the sulfonic acid group of the PFSA membrane, $\text{HSO}_3 - R$ is the PFSA membrane, n is the number of electrons participating in the ion-exchange reaction [19]. Thus,

$$K_{eq} = \frac{M_{M+}^{|z|} \cdot X_{H+}^{|z|}}{M_{H+}^{|z|} \cdot X_{M+}^{|z|}} \quad [4.3]$$

, where X_{M+} is the mole fraction of cations for ion-exchange capacity in an external solution, X_{H+} is the mole fraction of protons for the ion-exchange capacity in an external solution, M_{M+} is the mole ratio of exchanged cations in the membrane, M_{H+} is the mole ratio of protons in the membrane, and z is the charge number of the ions.

The partition coefficient for aniline was calculated with Eq. [4.3] to be 72 ± 5 , and it can be compared to the coefficients of 1.5 ± 0.3 for ammonium (NH_4^+), 1.2 ± 0.3 for sodium (Na^+), 5.1 ± 0.5 for potassium (K^+), and 230 ± 10 for calcium (Ca^{2+}). Our value for aniline is very similar to previously reported data (which gives a selectivity of 69 for aniline in Nafion[®]) by Ogumi et.al, [78]. The fact that aniline's partition coefficient is larger than ammonium's constant may indicate the effect of the ring structure or other electrostatic interactions between sulfonic acid and ether groups of Nafion[®]. The isotherms shown in Figure 4.4 also reveals that aniline is more favorably absorbed and exchanged in an N117 membrane than monovalent cations such as sodium, potassium and ammonium, but less favorably absorbed than a bivalent cation such as calcium ions.

We hypothesize that an aniline exchanged membrane may show much higher hydrophobicity than other metal cation-exchange membranes even though anilinium is monovalent cation. Reported values of the water content (λ) measured in the liquid phase for various cation exchanged PFSA membranes are shown in Table 3. The water content (λ) represents the number of water molecules (nH_2O) per proton site within the PFSA membrane (nSO_3^-). The λ of aniline-form Nafion[®] is higher than the λ of hydrophilic cations such as the Na^+ - or the Ca^{2+} -form Nafion[®]. The water content of N117s

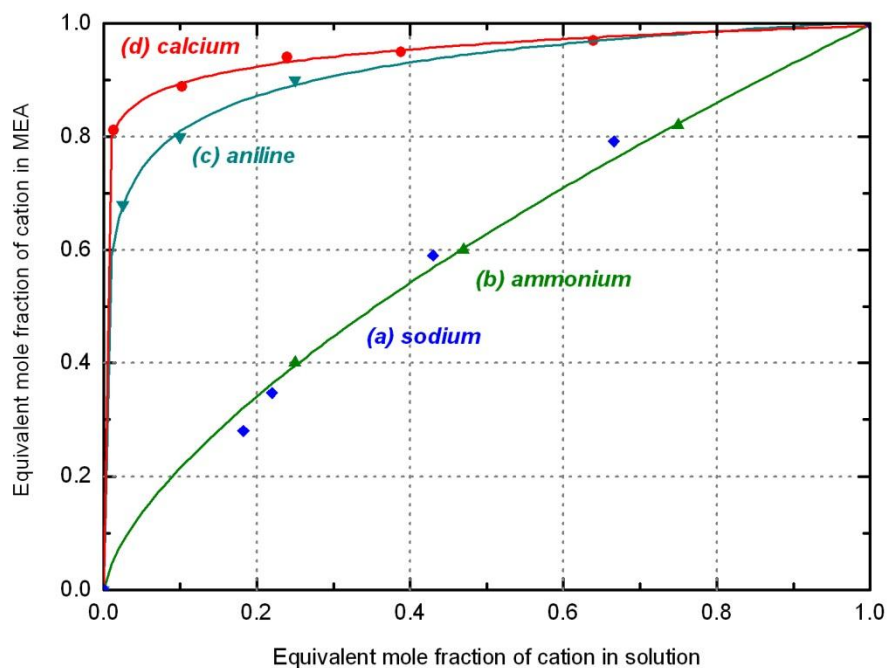


Figure 4.4 Ion-exchange isotherms of MEA (Pt loading 0.4/0.4 mg/cm²) for different cations (a) sodium (b) ammonium (c) aniline (anilinium) (d) calcium at T=23°C

Table 4.2 Measured capacities of membranes and MEA by different cations

Ion	Nafion117 [®]	GORE PRIMEA [®] 57	Method
Na ⁺	5.0±0.4 μmol/cm ²	5.6±0.3 μmol/cm ²	Back titration
NH ₄ ⁺	4.9±0.4 μmol/cm ²	5.4±0.3 μmol/cm ²	Titration/ ISE*
C ₆ H ₈ N ⁺	6.0±0.3 μmol/cm ²	7.0±0.3 μmol/cm ²	Titration/ UV-vis.

* Ion selective electrode for ammonia

Table 4.3 Equilibrium constants for N117 different cations

Ion	K _{eq}	Method	*λ(H ₂ O/SO ₃ ⁻)
Na ⁺	1.2±0.3	Back titration	18.4
K ⁺	5.1±0.5	Back titration	13.3
Ca ²⁺	230±10	Back titration	17.2
NH ₄ ⁺	1.5±0.3	Titration / Ion selective electrode	13.2
C ₆ H ₈ N ⁺	72±5	Titration / UV-vis.	10-11.5
H ⁺			20-22

* Water content in N117 equilibrated in solutions containing various cations

equilibrated at different RHs shown in Figure 4.5a also supports the hypothesis of lower water content for 70% aniline exchanged N117 relative to pristine and 70% sodium exchanged N117s. As shown in Figure 4.5b, we observed a logarithmic relation between available proton acid sites and membrane conductivity rather than a linear relation, which is generally expressed in sodium- and calcium-form membranes

Figure 4.6 compares membrane conductivity data for different cation forms of the NE211 membrane. The ammonium-form NRE211 (line (c) in Figure 4.6) shows similar conductivity loss to the sodium-form NRE211 (line (b) in Figure 4.6). However, the anilinium-form NRE211 (line (g) in Figure 4.6) indicates 10X lower conductivity. The conductivity for potassium- and sodium-form membranes are different, confirming previous reported lower water content [90] for the potassium-form membrane compared to the sodium-form membrane. This is due to a different hydrated radius of cations. The larger the radius of the potassium, the less it attracts water molecules since its electric charge needs to diffuse over a large distance. Interestingly, the 50% exchange of acid sites with aniline (line (e) in Figure 4.6) followed by the 99% of ammonium or sodium form of membranes (lines (b) and (c) in Figure 4.6).

Therefore, we can conclude that aniline-membrane conductivity is affected by not only electrostatic attractions (ion-exchange, hydrogen bonding) but also water expulsion due to its functionality, size, and hydrolysis. In our opinion, this hydrophilic/hydrophobic effect may also support the slightly higher affinity of the PFSA-membrane for aniline compared with sodium and ammonia (shown in Table 4.2). Ogumi et.al, [78] and Okada et.al, [96] also reported that hydrophobic cations such as ruthenium bipyridine complex, Cs, and Ba have larger exchange selectivity than hydrophilic cations such as Na and Li.

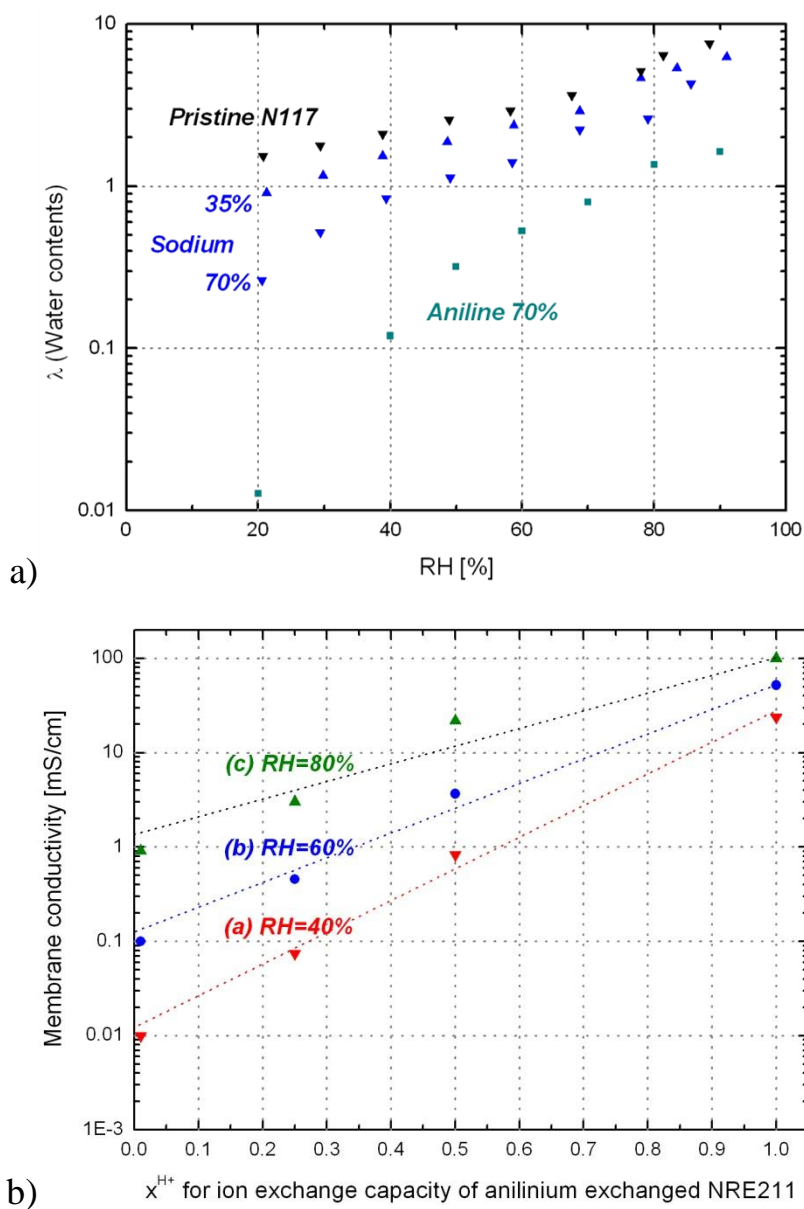


Figure 4.5 a) Comparison of water uptake of pristine, sodium, aniline exchanged N117s at different RHs b) Membrane conductivity of anilinium exchanged NRE211 membranes as a function of proton mole fraction of NRE211 and RH

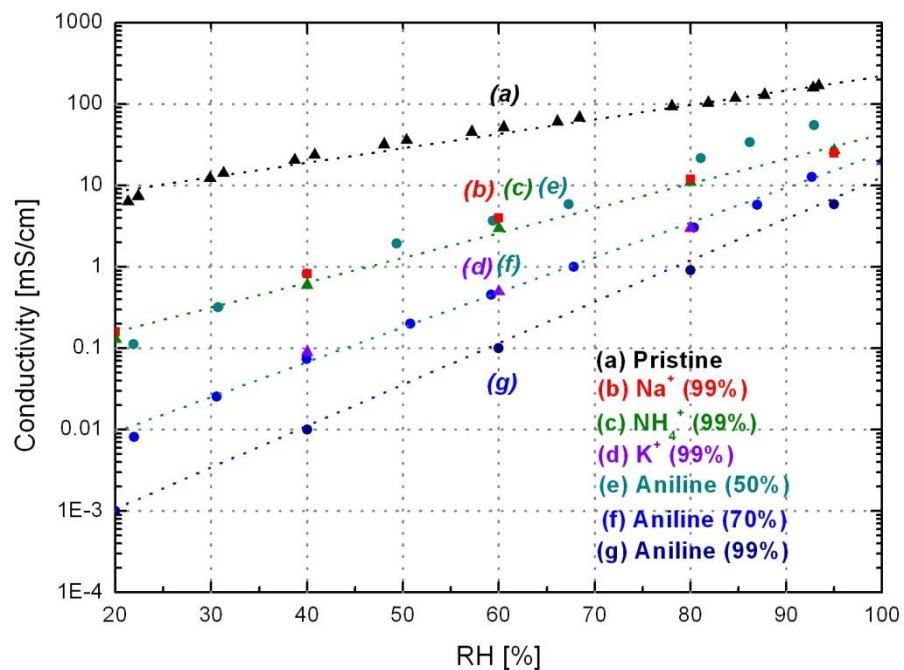


Figure 4.6 In-plane membrane conductivity of NRE211 membranes as a function of RH and concentration of contaminants (a) pristine (b) 99% of sodium (c) 99% of ammonium (d) 99% of potassium (e) 50% of aniline (f) 70% of aniline (g) 99% of aniline

They also reported that hydrophobic cations were confirmed at the intermediate region of the PFSA membrane.

Figure 4.7 represents ATR-IR spectrums for aniline and sodium-form membranes. The sodium-form membrane shows a shift of O=S=O stretching peak (i.e., 1058cm^{-1} to 1064cm^{-1}), which indicates the interaction between sodium cation and the sulfonic acid group of membrane. The aniline-form membrane also shows the shift of O=S=O stretching peak. Also, it is interesting to note that the C-O-C stretching vibration bands also shift (i.e., 1058cm^{-1} to 1064cm^{-1}) and disappearance (i.e., for Na^+ and aniline together) which may indicate additional complexation and dehydration corresponding to aniline. The disappearance of the peak may indicate that the anilinium interacted with the perfluoroether side chain ($\text{CF}_2\text{-O-CF}_2$) of the Nafion[®] (i.e., the hydrogen bond between a lone oxygen molecule and an anilinium), and it may induce a conformational change of the perfluoroether side chains.

4.3.2 ANILINE INTERACTIONS WITH THE Pt/C CATALYST ELECTRODE

The CVs of Figure 4.8a show that the peaks for desorption and adsorption of protons (0 - 0.25V) decreased, indicating that the available proton sites of platinum for electrochemical reactions decrease when aniline is added to the HClO_4 electrolyte of the RDE system. This adsorption of aniline on the Pt/C catalyst electrode may be a result of the nitrogen atom of the amine group or the aromatic ring of parallel-oriented aniline [77] reaching the platinum catalyst's electrode sites. This may possibly be due to the strong electronegativity and interaction between the aromatic ring and the platinum. Since the interface between bare Pt and ionomer is hydrophobic [91], aniline may easily come into

contact with the interface between Pt and Nafion® through adsorption, absorption, or an ion-exchange reaction (Recall the hydrophobic nature of the aromatic ring of aniline discussed above).

Figure 4.9 shows a comparison of partial CV graphs (0-0.55V vs. RHE) of the Pt/C in the presence of benzene and aniline. Both show similar ECSA change as the concentration of each contaminant changes and this is reflected in the adsorption isotherms (Figure 4.10) for the Pt/C catalyst. In Figure 4.10, Langmuir adsorption behavior is shown for both benzene and aniline and maximum coverages (i.e., coverage 0.55-0.65) were equal within the accuracy of these data.

Figure 4.8a and 4.8b imply that several unknown reactions occur during the cycling of the voltage since there are peaks at 0.6 – 0.8V and the current increases around 0.9 – 1.2V. This may be associated with the coupling of quinone (Q) and hydroquinone (H₂Q) formed in the carbon support surface, as in the following redox process: . There are changes also observed for a Carbon (Vulcan XC-72R)-coated Nafion® binder electrode without Pt (shown in Figure 4.8b) with the addition of aniline. The CV peak at a voltage of the Q-HQ redox couple cannot increase through potential cycles on a carbon surface if there are no other sources (e.g., aniline). However, the peak around 0.6 – 0.7V shown in Figures 4.8a and 4.8b keeps increasing through potential cycles with aniline. Thus, the peak increase shown in Figures 6a and 6b around 0.6 – 0.7V may be evidence of PANI film growth or other oxidant products. Previous studies reported that multi-layers PANI can be synthesized on the carbon electrodes from aniline molecules adsorbed by electrochemical load cycling in an acidic solution (H₂SO₄) [80-84]. Hence, in the case of PANI film growth on a Nafion®-coated Pt/C electrode, PANI can affect the

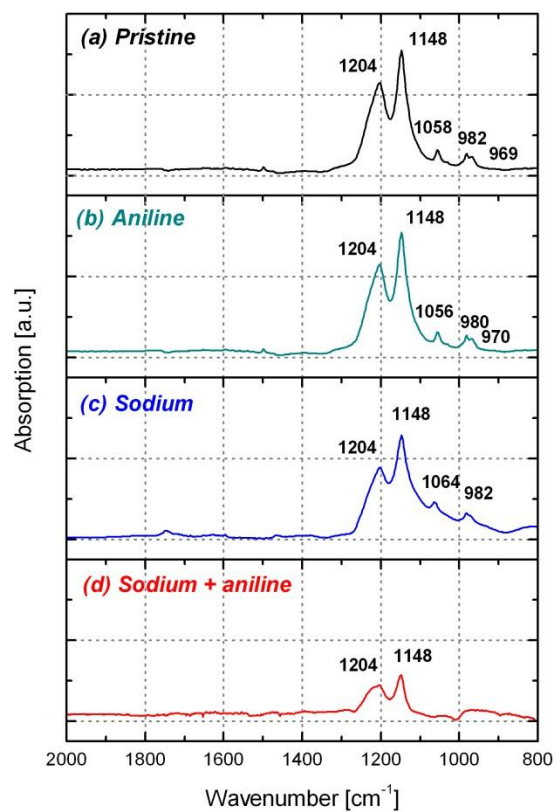
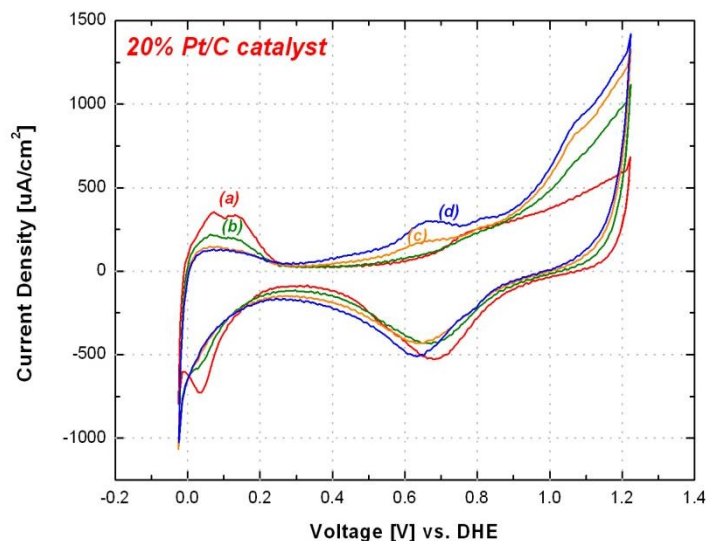
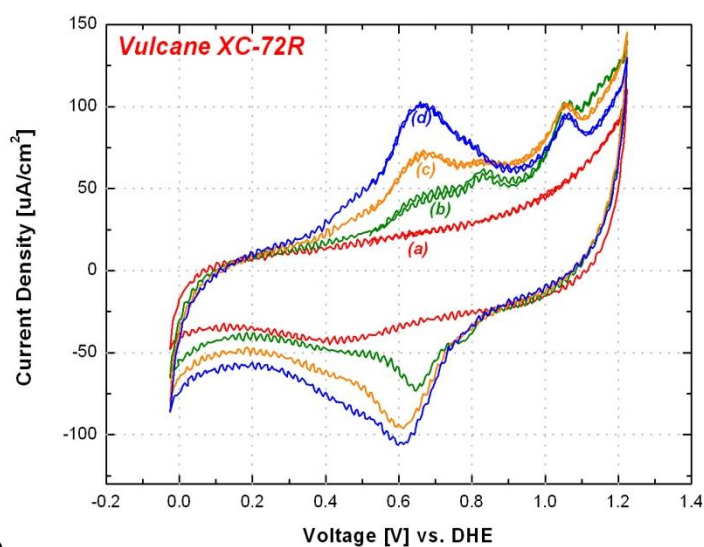


Figure 4.7 ATR-IR spectrums of (a) pristine (b) aniline (c) sodium (d) sodium and aniline absorbed N117



a)



b)

Figure 4.8 a) Cyclic voltammograms of aniline contaminated carbon supported 20% Pt catalyst (a) 0.0 mM (b) 0.04 mM (c) 0.10 mM (d) 0.19 mM of aniline in 0.1M HClO_4 solution. b) Cyclic voltammograms of aniline contaminated (0.04 mM) Vulcan XC-72R and growth of electrochemically synthesized PANI after (a) 5 (b) 10 (c) 30 (d) 100 CV cycles. The electrode had an area of 0.24 cm^2 , the temperature was 23°C , and the scan rate was 25 mV/s .

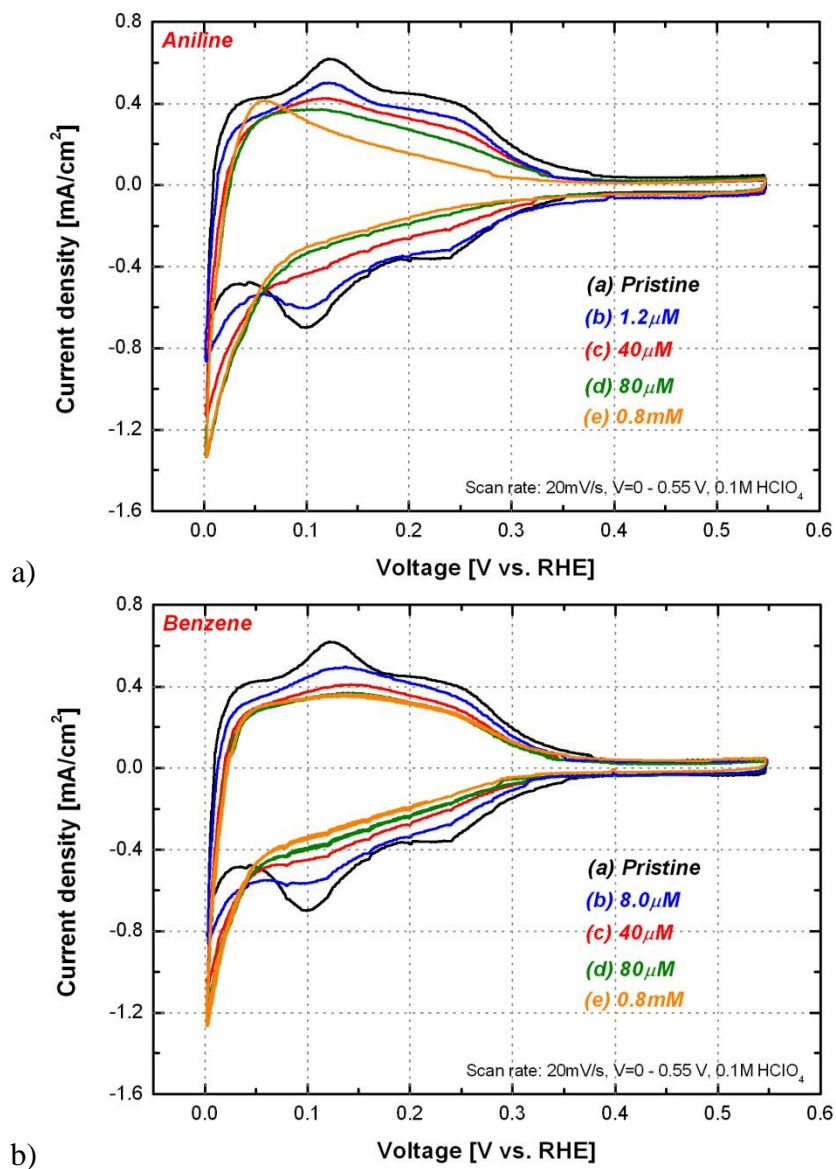


Figure 4.9 a) Partial cyclic voltammograms scan of aniline contaminated carbon supported 45.5% platinum catalyst (a) 0.0 mM (b) 1.2 μM (c) 0.04 mM (d) 0.08 mM (e) 0.8 mM of aniline in 0.1M HClO₄ solution. b) Partial cyclic voltammograms scan of benzene contaminated carbon supported 45.5% platinum catalyst (a) 0.0 mM (b) 1.2 μM (c) 0.04 mM (d) 0.08 mM (e) 0.8 mM of aniline in 0.1M HClO₄ solution.

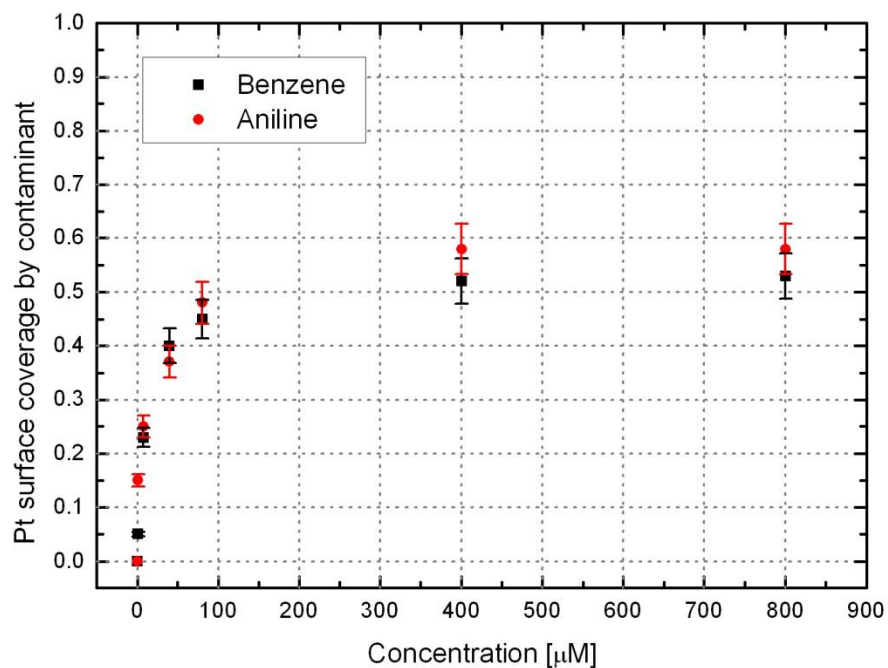


Figure 4.10 Adsorption isotherms of aniline and benzene for 45.5 wt% Pt/C electrode at 0.4V vs. RHE, $T=23^{\circ}\text{C}$, Pt loading= $0.02\text{mg}/\text{cm}^2$

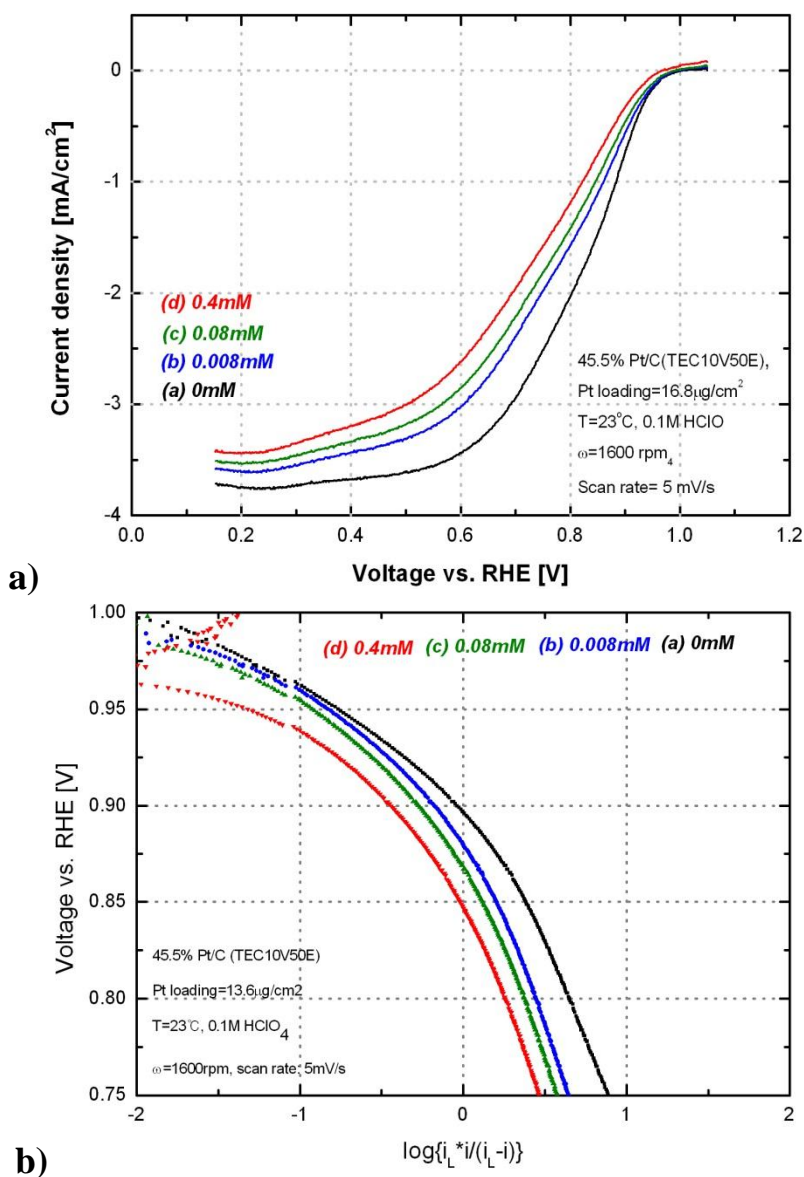


Figure 4.11 a) Aniline contamination effect of ORR current for a 45.5% Pt supported on carbon catalyst in 0.1M HClO₄ at 5mV/s with O₂ purge: (a) 0mM; (b) 0.008mM; (c) 0.08mM; (d) 0.4mM ; ω=1600rpm. b) Tafel slopes of a) (a) 0mM; (b) 0.008mM; (c) 0.08mM; (d) 0.4mM

conformational change of the ionomer at the interface between the Pt/C and the ionomer by changing the conformation of the ionomer. Although PANI is a conducting polymer, it may negatively affect the performance of the PEMFC since the grown film of PANI onto a Pt/C catalyst electrode may interfere with the catalyst's activities and the adsorption of hydrogen and oxygen gases. Future work may wish to consider measurements of O₂ diffusion through the PANI/Nafion[®] films.

In Table 4, the ECSA loss and the double layer capacitance are shown after 200 potential cycles for the Pt electrode with binder or not. Various sparging gases (Ar, H₂, and O₂) were used to understand contamination effects in the anode and cathode environments of a PEMFC. The result indicates that the Nafion[®] binder in the electrode helped adsorb aniline since the ECSA loss is higher when the binder is present in the Pt/C electrode. As is the case with ion exchange in the membrane structure, the hydrophobicity of aniline may facilitate adsorption on the Pt/C electrode since the Nafion[®] binder has a hydrophobic backbone at the intermediate regions (hydrophobic and hydrophilic) of Nafion[®], and the hydrophobic interface between the Pt/C and the Nafion[®] binder has been observed. Thus the protonation of the amine group may facilitate ion exchange with the Nafion[®] binder. The O₂ gas sparging case showed greatest ECSA loss.

The measurement of the ORR currents in Figure 4.11 shows a decrease of the limiting current with aniline contamination. This decrease of limiting current is consistent with the loss of ECSA shown in Figure 4.11. Analysis of Tafel slopes also shows a 60% (almost 0.6 order of difference in the logarithm graph) of kinetic current decrease (i.e., the graphs shift on left side). This decrease is consistent with a 65% loss of ECSA, and it may be accounted for by the growth of PANI interfering with the mass transfer of oxygen

gas onto the Pt/C electrode. However, the Tafel slopes did not change significantly; -60 ± 3 mV/decade and -120 ± 5 mV/decade were calculated for Tafel slopes.

The decrease of ECSA by aniline contamination appears to be irreversible, in contrast to the ECSA decrease caused by ammonia [15] which can be reversed by increasing the humidity. Also, this decrease is in contrast to carbon monoxide contamination, which can be electrochemically oxidized during subsequent CV cycles. We might speculate that the aniline contamination of the Pt/C catalyst electrode would be greater on the anode side of PEMFC due to the lack of PtO in the presence of hydrogen. The loss of ECSA was not reversible by electro-oxidation at certain high-potential conditions experiments. However, we found that we could recover the activity of the Pt/C electrode after aniline contamination by cleaning it with an acid solution (in this experiment 0.1M HClO₄) which appears to partially remove anilinium or the aniline ion from the Nafion[®] binder and the Pt/C active surface. The ECSA was recovered to around 90% after flushing the electrode with a 0.1M HClO₄ solution followed by applying a potential cycle into a high potential region (i.e., 1.2V vs. RHE). This may indicate that excessive aniline absorption into the Nafion[®] binder and onto the Pt/C can be removed by cleaning with HClO₄.

Table 4.4 Comparison electrode properties for various experiment conditions after 200 potential cycles (0-0.6V vs. RHE) in 0.04mN aniline solution (HClO₄)

Sparging gas	Ar		O ₂	H ₂
Binder(Nafion [®])	with	without	with	with
ECSA [%]	-65.3	-65.7	-92.3	-42.8
C _{dl} [%]	84.1	32.5	104	16

4.3.3 PREDICTING THE VOLTAGE LOSS

To assess and develop a model prediction [see Chapter 3] that relates aniline Pt coverage with voltage loss, we can use Ohm's law and the Tafel equation. With an assumption of no ΔV_{OCV} and negligible anodic overpotential ($\Delta \eta_a$), the total voltage change can be written:

$$\Delta V = -i_p(R_p - R_c) + \Delta \eta_c, \text{ where p=pristine, c=contamination} \quad [4.3]$$

The resistance is related to the membrane conductivity (κ) which can be determined from the *ex-situ* membrane conductivity results shown in Figure 3b. The conductivity (κ) and coverage (χ) have the following exponential relation at constant RH conditions.

$$\ln \kappa = a\chi + b, \text{ where } a=-6.37 \text{ and } b=4.11 \text{ for aniline at RH=60\%} \quad [4.4]$$

The constants a and b at different RHs are listed in Table 5.

Thus, the iR loss can be written in terms of coverage (χ) by contaminant in the membrane for a specified RH condition:

$$\Delta V_{iR} = -\Delta \left(\frac{i_{z_{mem}}}{\kappa} \right) = -\Delta \left(\frac{i_{z_{mem}}}{e^{a\chi+b}} \right) \quad [4.5]$$

For the cathodic overpotential ($\Delta \eta_c$), the Butler-Volmer equation can be simplified to a Tafel expression of large cathodic over-potentials of the oxygen reduction reactions (ORR) in PEMFCs and can be written according to the notation in Ref. [26].

$$-i = i_{0,j} \left[\Pi \left(\frac{C_j}{C_{j,ref}} \right)^{q_{ij}} \exp \left(\frac{-\alpha_c F \eta_s}{RT} \right) \right] \quad [4.6]$$

Eq. [4.6] can be rearranged to show the explicitly:

$$\eta = -\frac{RT}{\alpha_c F} \ln \left\{ -\left(\frac{i}{i_0} \right) \cdot \Pi \left(\frac{C_j}{C_{j,ref}} \right)^{1/q_{ij}} \right\} \quad [4.7]$$

For the ORR, (i.e., $2H_2O \leftrightarrow O_2 + 4H^+ + 4e^-$) Eq. [4.6] can be written for pristine and contamination electrode, and through subtraction, the voltage change by contamination can be expressed:

$$\Delta V = \eta_{contamination} - \eta_{pristine} = -\frac{RT}{\alpha_c F} \ln \left\{ \left(\frac{C_{H^+, pristine}}{C_{H^+, contamination}} \right)^4 \left(\frac{C_{Pt, pristine}}{C_{Pt, contamination}} \right) \right\} \quad [4.8]$$

Figure 4.12 shows the voltage loss that might be expected in a PEMFC corresponding to the total voltage change can be predicted from the Pt, ionomer and, membrane contamination which can quantify the ECSA change and conductivity loss of membrane. Note that here we used the stoichiometry numbers (e.g., $q_{ij}=1$ for Pt contamination, $q_{ij}=4$ for ionomer contamination) of ORR for the q_{ij} , which assumes the reaction follows stoichiometry for each contamination mechanism in Eq. [4.7]. Also, the ratio of proton and Pt concentration of pristine and contamination in Eq. [4.8] represent coverage by contaminant on the Pt sites or in the proton sites of ionomer in the electrode. Thus, we can speculate from the Eq. [4.8], the voltage loss arising from the electrode have two contributions from the Pt and ionomer and to predict the voltage loss by the electrode contamination, the coverage change on the Pt sites and in the proton sites of ionomer are required. To obtain those values, we can use adsorption and ion exchange isotherms shown in Figures 4.4 and 4.10. For the Pt contamination, we can obtain the coverage from Figure 4.4 as a function of concentration. Also, for the ionomer contamination, we can predict the coverage as a function of mole fraction of proton and aniline from the Figure 4.4.

The voltage change by membrane contamination depends on RH at the channel, and the lower RH is the more effect of aniline. Note that, in contrast to sodium contamination

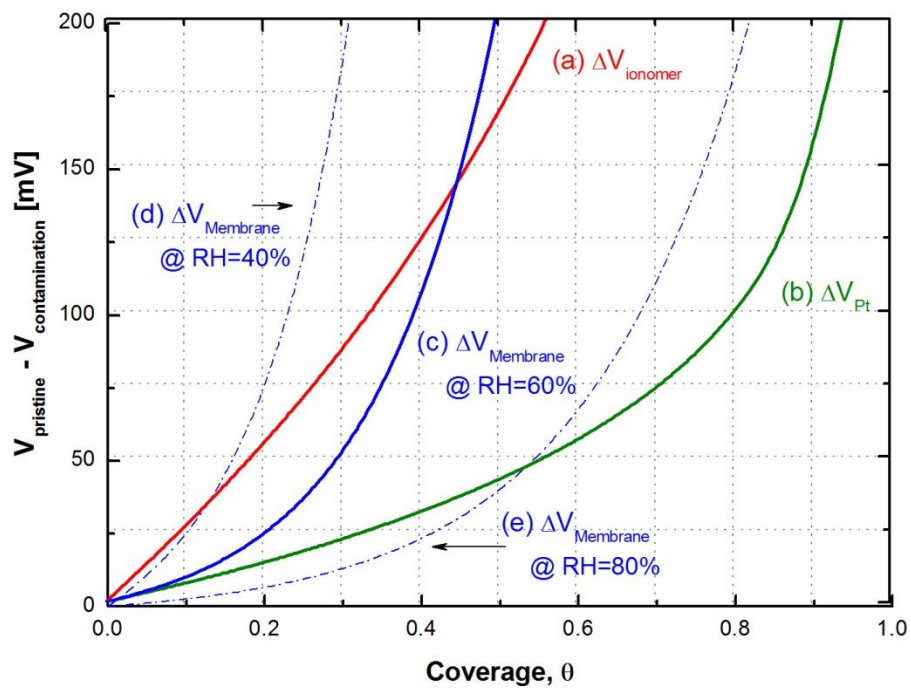


Figure 4.12 Predicting voltage change depends on coverage for each contamination source (a) ionomer (b) Pt (c) membrane at RH=60%, (d) membrane at RH=40%, (e) membrane at RH=80%

[21], aniline contamination yields voltage losses greater than 50mV with a RH=60% coverage of 0.3 to 0.4. This is an average RH on the cathode using 32% of the inlet RH with 10A operating conditions (i.e., 0.2A/cm² in a 50cm² lab PEMFC cell). This voltage loss depends on three different contamination sources, the electrode ionomer, the Pt/C coverage and the membrane, as shown in Figure 4.12. This figure shows that the contamination effect of the ionomer and membrane are dominant relative to Pt contamination. For a small coverage by aniline, the contamination impact on ionomer is more critical than membrane but the impact on membrane contamination becomes more important as the coverage increases (i.e., contamination continues).

4.4 CONCLUSIONS

The possible contamination mechanisms of aniline and then effect on PEMFCs were studied. The ion exchange reaction that occurred in the PFSA membrane and Nafion[®] ionomer in the Pt/C catalyst electrode caused significantly create voltage loss through a decrease of the number of available proton sites on the PFSA membrane. Aniline is also adsorbed on the platinum catalyst and carbon support and this may be a result of the nitrogen atom of the amine group of aniline and of interactions between the aromatic ring and the platinum metal. The ECSA and kinetic current for the ORR of the Pt/C catalyst were reported and shown to decrease by contamination from aniline adsorption/absorption. The isotherms for each contamination mechanism enables to the quantification of coverage by aniline as a function of concentration. Finally, a simple estimate of voltage loss was for each contamination mechanism by using the *ex-situ* data in Tafel equation, membrane conductivity experiments. The voltage loss for the ionomer

and membrane through an ion-exchange mechanism showed the significant performance loss relative to Pt contamination by adsorption.

CHAPTER 5

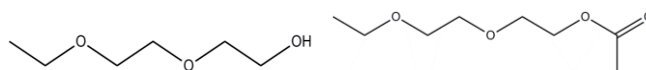
THE CONTAMINATION BEHAVIOR OF ORGANIC MODEL COMPOUNDS ON PEMFC BASED UPON FUNCTIONALITIES: URETHAND BASED ASSEMBLY AIDS

In this chapter, we investigate the contamination effect of some organic model compounds on PEMFC based upon functional groups. Results for each compound are compared by fundamental contamination mechanisms such as ion-exchange, adsorption, and electrochemical reaction. Diethyleneglycol monoethyl ether acetate (DEGMEA), Diethyleneglycol monoethyl ether (DEGEE) Benzyl alcohol (BzOH), 4-Methyl benzenesulfonamide (4-MBSA), and 2,6-Diaminotoluene (2,6-DAT) are chosen as model compounds from urethane based assembly aids materials. Ex-situ studies such as rotating disk electrode (RDE), ion-exchange isotherms, membrane conductivity and *in-situ* infusion single cell test are performed to understand and correlate the contamination mechanisms and functionalities of compounds. The aromatic compounds (i.e., 2,6-DAT, BzOH, 4-MBSA) show severe impacts on Pt contamination. The N-H containing compound (i.e., 2,6-DAT) results in drastic conductivity loss by ion-exchange reaction with ionomeric components. The aliphatic compounds (DEGEE, DEGMEA) also show ionomer contamination but not significant relative to the 2,6-DAT. Finally, the *ex-situ* and *in-situ* results are correlated by simple Butler-Volmer equation to understand contribution from each mechanism.

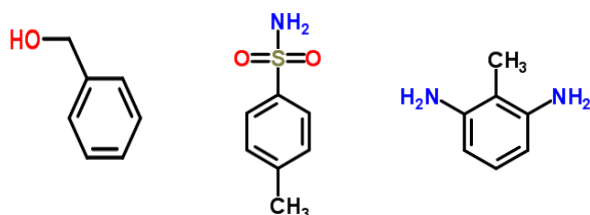
5.1 INTRODUCTION

Much interest has been aroused in contamination study on proton exchange membrane fuel cells (PEMFCs) for durability and cost needs [32-34]. Generally, organic contaminants have received relatively little attention than metal cation, air, and fuel contamination studies [6-26]. The question has been raised as to whether the cheaper plastic materials can be applicable for PEMFCs as a structural materials or assembly aids in acceptable performance change. The cheaper off-the-shelf materials can reduce the cost of PEMFCs but contamination impacts may be increased. Contaminants leached from BOP materials are being systematically studied [31-34, 49-50, 73,] and one aspect of this study is the selection of model compounds based on functional groups. Our long-term goal is to quantify the effect of these model compounds and suggest *ex-situ* experiments that provide sufficient data to establish “criteria for avoidance” in the selection of plastic materials for BOP components. These ex-situ results will also use for the model predictions.

In an analytical study from Clay et al., [33-34] many organic compounds were identified in leachate of urethane based assembly aids materials through GC-MS. Clay also measured pH, total organic carbon (TOC), and conductivity of solutions for 6 week to track the amount of organic and inorganic compounds in leachate. In this chapter, we pay attention to selected organic model compounds impacts on PEMFCs performance based upon their functionalities. The chemical structures for model compounds show in Figure 5.1.



DEGEE / DEGMEA



BzOH / 4-MBSA / 2,6-DAT

Figure 5.1 Chemical structures of model compounds chosen for study

The criteria for selection are aromatic or aliphatic, and containing amine group or not. Both 2, 6-DAT and 4-MBSA have an aromatic benzene ring and an amine ($-NH_2$) group. In previous study [see Chapter 4], the aniline which has a benzene ring and amine group showed three different contamination mechanisms such as ion-exchange by protonated amine group, adsorption by benzene ring, and side electrochemical reaction to produce polymer film on Pt electrode. The contamination study for ϵ -caprolactam [will show in Chapter 6] also confirmed acid catalyzed open ring reaction of ϵ -caprolactam followed by the ion-exchange reaction. Thus, we believe that N-H containing organic compounds could influence on proton conductivity of membrane by the electrostatic interaction of protonated amine and sulfonic group. The BzOH also has an aromatic ring but no amine group. Thus, it is not hard to guess no ion-exchange but adsorption on the Pt catalyst. Finally, the DEGEE and DEGMEA are chosen for representing aliphatic model compounds which do not have aromatic benzene ring structure and amine groups.

Again, all model compounds which selected for the study have been identified through GC-MS analysis in leachate solutions from the urethane based assemble aid materials. Hydrolyzed residual monomer (2,6-DAT), water scavenger (4-MBSA), anti-oxidant product (BzOH) and industrial solvent (DEGEE and DEGMEA) are investigated for the origin of leachate solutions [34]. Consideration of these organic model compounds and their effect on performance can allow for a correlation between chemical species, functional groups, and contamination mechanisms. Furthermore, we can predict impact on the PEMFCs with breaking down by contamination mechanisms and sources. Since the discussion for GDL contamination is beyond the scope, we mainly focused on contamination effects on membrane and Pt/C catalyst.

The ion-exchange isotherm curves for PEM of the model compounds have been prepared for the 2,6-DAT and other model compounds (i.e., BzOH, DEGEE, DEGMEA, 4-MBSA) which only show absorption behavior. The membrane conductivity (σ) is obtained from the measurement of resistivity of the PEM using direct current (DC) four probe methods. RDE experiments are performed to evaluate the loss of Pt catalyst activity and other possible electrochemical reaction. The Pt isotherm are prepared for the model prediction. Under certain potentials, the effects on the kinetics of Pt/C catalyst have been observed as the change of electrochemical surface area (ECSA) and parallel redox reaction for the 2,6-DAT. Finally, *in-situ* infusion data for selected model compound (i.e., DEGEE) is compared with the prediction which obtains from ex-situ studies on electrode and membrane separately.

5.2 EXPERIMENTAL

5.2.1 NAFIOIN MEMBRANE ISOTHERMS BY UV-VIS MEASUREMENT

Each of the Nafion® membrane (e.g., N115, $2.5 \times 2.5\text{cm}^2$) samples for spectroscopy analyses were prepared by soaking in 5mN of organic solution (e.g., 2,6-DAT, 4-MBSA, BzOH, DEGMEA) in 5mN H_2SO_4 (concentration of solution can change). The pH of the mixture solution of each 5mN organic solution and 5mN H_2SO_4 was decided based on a pKa of organic species (e.g., $8 < \text{pKa for amine} < 11$) to allow hydrolysis of amine group ($-\text{NH}_2$). In other words, the amine group of organic species can be hydrolyzed in the acid condition of $\text{pKa} > \text{pH}$ of solution due to its weak base property [105]. Therefore, the pHs of all solution prepared were less than $\text{pH}=4$. The absorption of organic species was estimated by UV-vis peak change of solution before and after soaking of Nafion®

membrane, around wavelength 250-260nm which indicates benzene ring. To check consist of organic absorption, the organic compound absorbed Nafion[®] sample was rinsed with DI water to get rid of over-absorption, and then soaked again into 2M H₂SO₄ solution to expect fully proton exchange acid sites in Nafion[®] so as to organic compound can be extracted by 2M H₂SO₄. The extracted organic compound in 2M H₂SO₄ was also quantified by a calibration curve (e.g., organic species concentration vs. UV-vis intensity at 250-260nm) in UV-vis spectrum. The calibration curve indicated a linear relation between absorption intensity and concentration. Three replicates of UV-vis measurement showed negligible discrepancy. Each spectrum was recorded from 800 to 190 nm. The membranes were pretreated by boiling in H₂SO₄ (1M) and stored in DI water.

5.2.2 IN-PLANE MEMBRANE CONDUCTIVITY MEASUREMENT

One piece of NRE211 membrane (4 cm × 5 cm) for the conductivity measurement was prepared by soaking into the model compound solution (e.g., 5mM and 50mM) and then, the membrane was cut by 5 piece samples to measure. After rinsing the residual on the surface of membrane by DI water, membrane conductivities were determined at ten values of constant relative humidity (RH) (i.e., 10, 20, 30, 40, 50, 60, 70, 80, 90, 95%) by applying DC currents at the cell temperature of 80 °C. The potentiostat, a model PAR273, was used with a four-probe conductivity Teflon-based cell; model BT-112, made from Beckktech LLC. The cell is pre-equilibrated with a 300 sccm flow of N₂ at T_{cell}=80 °C and RH =90% for 1 hr. The humidity was changed from 20% RH to 95% RH to measure the membrane conductivity with a hold of 30 min between the various RH conditions to assure equilibration at the next RH. The reported values of the membrane conductivity

were obtained by two continuous RH changes. The deviation between continuous results was negligible. A VAISALA dew point chamber was also attached at the outlet of the conductivity cell to correct dew point temperature of outgases (e.g., RH presented was measured by the dew point measurement in outlet).

5.2.3 RDE MEASUREMENT

Electrode catalysts inks were made with a carbon-supported 45.5% Pt (Tanaka) catalyst to achieve a Pt loading of 0.02 mg/cm^2 . The catalysts were dispersed in DI water and isopropyl alcohol (IPA) in the presence of a Nafion[®] ionomer solution. The platinum catalyst ink was mixed and dispersed by ultrasonic for approximately 20 minutes and dropped on a glassy carbon disk electrode (0.2475 cm^2). The cyclic voltammetry was performed with a Model E7R9 RRDE from Pine Instruments in connection with a potentiostat, model PAR 263A. Only the RDE part of the electrode was used. A 0.1M perchloric acid solution (HClO_4) and mercury sulfate electrode were used as an electrolyte and reference electrode, respectively. For the cleaning, the potential cycles from 0.05 to 1.25V (vs. RHE) were applied with 5000 cycles at scan rate of 500mV/s. Each 3 cycles of CV was measured without rotating after adding each model compound to the electrolyte followed by mixing at 1600 rpm for 5min. During the injection of contaminant, the voltage was hold at 0.4 V (vs. RHE) to prevent oxidation of contaminant. The ECSA calculation was used hydrogen desorption area which generally considered integrating the area from 0.07 to 0.4 V.

5.2.4 IN-SITU SINGLE CELL TEST

GM provided MEA (50cm²) was used for a single cell test. RH was set at 32% on both and a constant current (i.e., 0.2 A/cm²) operation mode was applied to get rid of water effect for Nafion® membrane. Each model compounds solution was introduced on the cathode with air by micro syringe pump through a nebulizer while voltage and HFR were recording at constant current density (i.e., 0.2 A/cm²). CV was also recorded at beginning of test (BOT), end of infusion (EOI), and end of test (EOT) to see the contamination effect on Nafion® membrane (or ionomer) and Pt/C catalyst activity respectively.

5.3 RESULTS AND DISCUSSION

5.3.1 CONTAMINATION IMPACT ON PEM

Figure 5.2 presents ion-exchange isotherms for membrane (i.e., N115) of 2, 6-DAT in relative to other cations. The ammonia (NH₄⁺ in acid), aniline (C₆H₅NH₃⁺ in acid), and phenylenediamine (C₆H₄(NH₃)²⁺ in acid) are compared to explain the effect of functionality on absorption compared with the metal cations such as sodium (Na⁺), calcium (Ca²⁺). Recall that pKa of amine (-NH₂) is generally pKa = 8 ~ 11 which allows hydrolysis of amine group (-NH₃⁺ in acid) [105]. The isotherms represent the ionic composition of the membrane as a function of the equivalent cationic mole fraction of contaminant in solution (i.e., proton vs. cation). The isotherms for Na⁺ and Ca²⁺ are curved above diagonal solid line which explains a higher affinity to PEM than proton. Note that most of metal cations reported higher affinity to the PEM except Li [11, 26, 102]. Likewise, ammonia, aniline, phenylenediamine, and 2,6-DAT also show higher affinity. In other words, they can replace acid sites (e.g., -SO₃⁻ H⁺) in membrane, to great

extent, if they are compete with proton. Again, the pKa of amine (-NH_2) groups in 2,6-DAT are close to 9 [105]. For that reason, the amine (-NH_2) groups of 2,6-DAT can be protonated (i.e., hydrolyzed) in acid condition ($\text{pH} < 4$) due to its weak base property. The absorption of 2,6-DAT is strongly depends on pH of solution. Note that the protonation of amine group (-NH_3^+) of 2,6-DAT is very important for the interaction with sulfonic group (-SO_3) in PEM. Thus, it is the condition for electrostatic interaction between amine group (-NH_2) and sulfonic group (-SO_3) to be less pH of solution than the pKa of amine groups (-NH_2).

As we reported earlier [see Chapter 3], the protonated amine group of aniline ($\text{C}_6\text{H}_5\text{NH}_2$) can interact electrostatically with sulfonic group (-SO_3) of membrane. We believe that the protonated amine (-NH_3^+) of aniline act like a monovalent charge of cation. Accordingly, phenylenediamine and 2,6-DAT also can be allowed to absorb into membrane by the ion-exchange reaction in acid condition. It is note that the pH in PEMFCs speculates around 3 to 4 in which weak acid condition. Similar to metal cations of Na^+ and Ca^{2+} , ammonia (NH_4^+ in acid) also favor to membrane but less affinity than 2,6-DAT and phenylenediamine. It seems reasonable to assume that diprotic 2,6-DAT and phenylenediamine may act like a divalent calcium ion. Besides, phenylenediamine also shows higher affinity than aniline and other diprotic (e.g., two amine groups) compound, 2,6-DAT. However, 2,6-DAT shows less favor than aniline and phenylenediamine. The reason for less affinity of 2,6-DAT to PEM may have relevance to the steric hindrance of methyl (-CH_3) group of 2,6-DAT. The location of methyl (-CH_3) group may interfere the interaction between sulfonic group and amine groups. In sum, N-

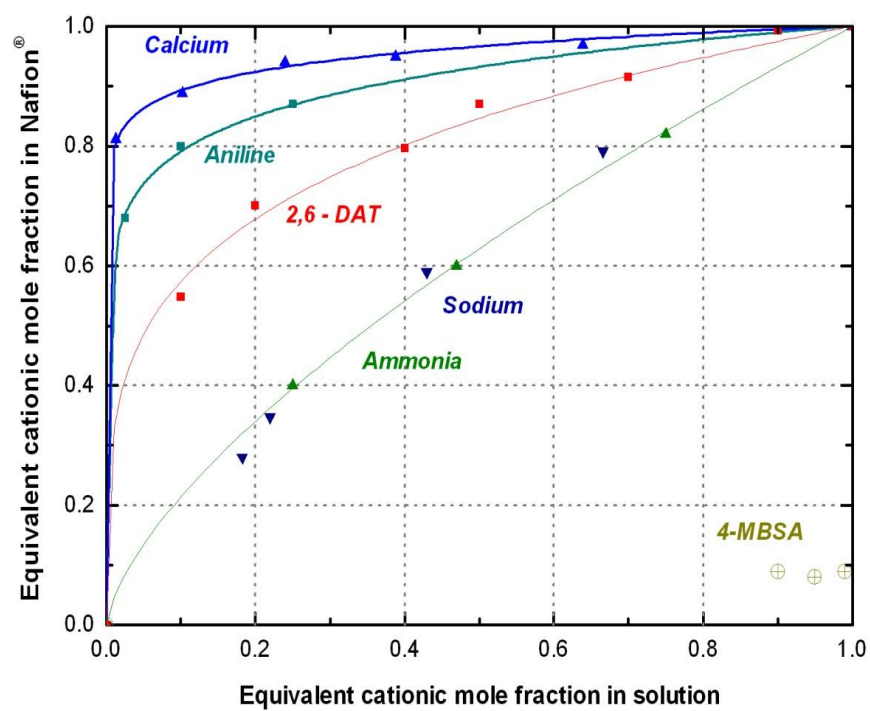


Figure 5.2 Ion-exchange isotherm for N-H containing organic model compounds

H containing organic compound, 2,6-DAT, significantly shows higher affinity to PEM and it gives a higher resistance to proton conductivity of PEM which is clearly showed on conductivity result as we will discuss next.

The conductivity data for NE211 of model compounds form, studied to date, that contaminate a PEM are present in Figure 5.3. Percentage indicates the ratio of exchanged acid sites by each compound. It is not difficult to see that all results show logarithm linear relation with RH change ($\log \sigma = aRH + b$, a and b are constant) and the great conductivity loss by the ability to ion-exchange of N-H containing compounds with the PEM are observed. Notably, the conductivity loss of 2,6-DAT is greater than ammonia and aniline at same extent of exchange concentration of acid sites. We speculate that the water expulsion due to the size of molecules or hydrophobic benzene structure can be a possible explanation to support the greater conductivity loss. The conductivity losses for 50% exchange concentration of aniline and 99% concentration of ammonium showed similar extent of loss (e.g., compare (c) and (d) in Figure 5.3) which also indicate the water expulsion effect by aniline [see Chapter 3]. We reported on earlier study about water content in aniline absorbed N117 which showed significantly less than sodium form of N117 [see Chapter 3]. Besides, the number of water tightly bounded into hydrocarbon molecules generally reported as lower than ammonia or ammonium [90]. The water expulsion for aniline absorbed membrane also observed on the proton concentration and conductivity relation. They showed logarithm relation (e.g., compare (d), (e), (f) in Figure 5.3 at same RH) while metal cation exchanged membrane showed linear relation [89]. In sum, we can conclude that the severe conductivity loss for N-H containing model compounds relative to alkali metals caused by the water expulsion effect. Note that the

other study [87] mentioned that Nafion[®] membrane lose great extent of conductivity once water contents (e.g., λ =moles of SO_3^- vs. moles of water in membrane) has been about 2 which is a threshold for the cluster-channel formation by water in membrane.

Given UV-vis analysis, we observed no significant intensity peak changes before and after soaking PEM into organic compounds solutions which indicate no notable ion-exchange reaction by BzOH, DEGMEA, DEGEE, and 4-MBSA with PEM. Except 4-MBSA, other compounds such as BzOH, DEGEE and DEGMEA, have not protonated functionalities in chemical structures. It would be interesting to see that there is no significant ion-exchange reaction by 4-MBSA even though the pK_a of amine is 10.2 [105]. We speculate the big molecular size may interfere absorption of 4-MBSA into the water cluster in PEM (or very slow reaction). The other study [106] also reported no high frequency resistance (HFR) change with toluene contamination on *in-situ* single cell test of PEMFCs. It is note that the toluene does not have protonated amine functional group.

However, BzOH, DEGEE, DEGMEA, and 4-MBSA can still absorb into PEM by concentration gradient as well as their structural analogy of hydrocarbon. From the results of the membrane conductivity as shown in Figure 5.3, the 10 – 60% of conductivity loss is observed depends on RH. The conductivity loss shows greater at dryer condition (e.g., lower RH). Again, as in the case of aniline and 2,6-DAT, the water expulsion effect showed notably at lower RH region. Note that for the non-electrostatic interactive model compounds such as DEGMEA, DEGEE, BzOH, and 4-MBSA show 1 – 2 orders of magnitude less for conductivity loss than ion-exchangeable N-H containing compounds such as aniline, ammonium, 2,6-DAT etc.

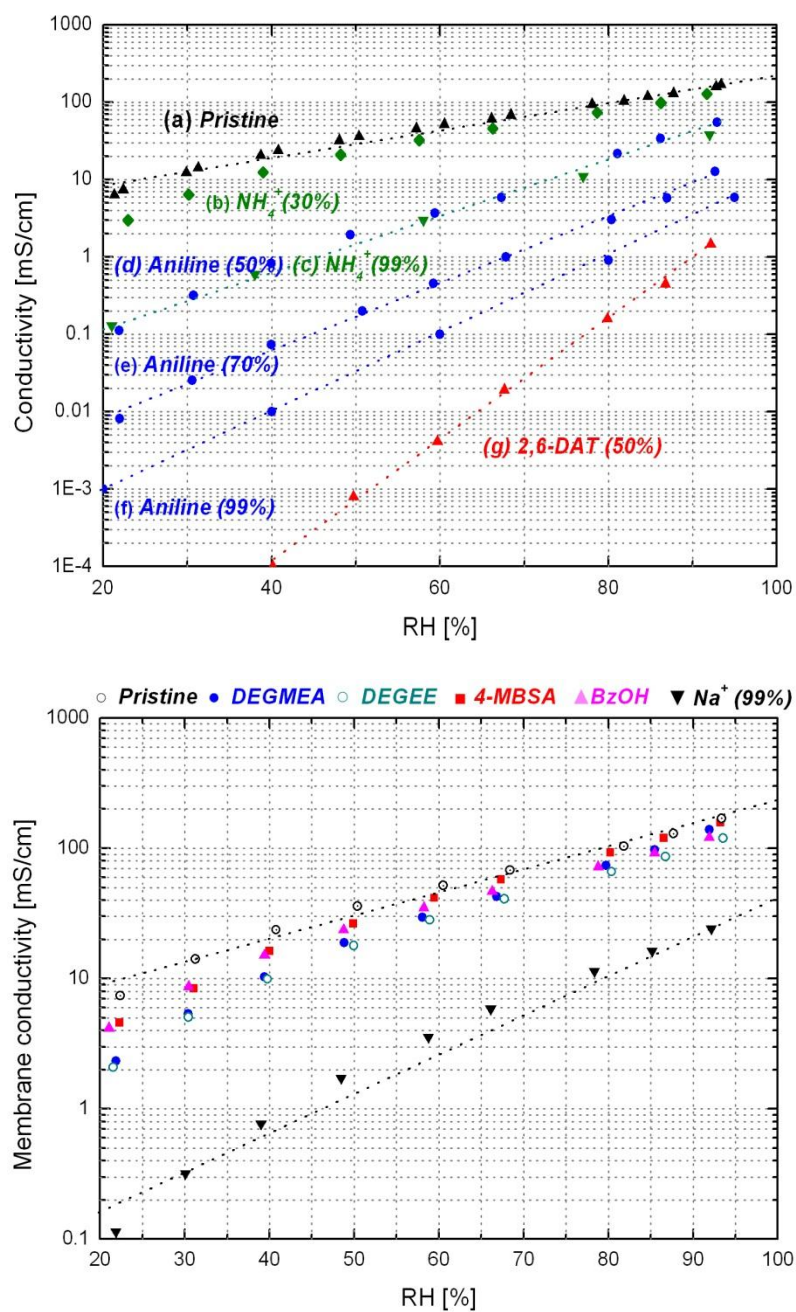


Figure 5.3 Comparison of membrane conductivity for model compounds: ion-exchange and absorption

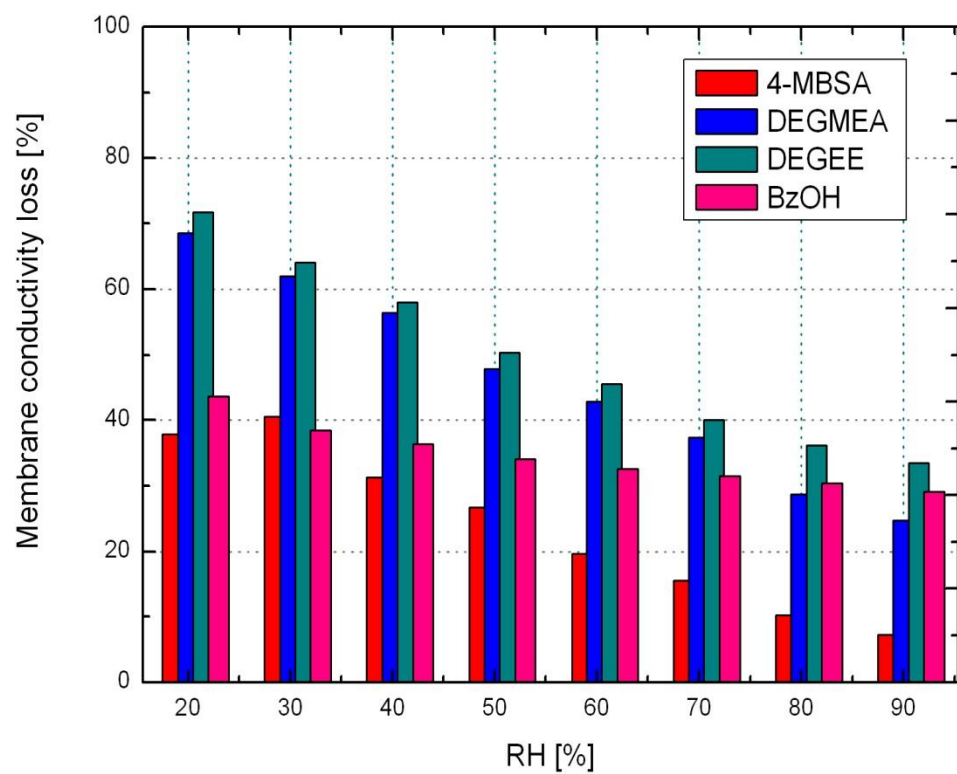


Figure 5.4 Comparison of membrane conductivity for model compounds

Figure 5.4 presents comparison of conductivity loss for 4-MBSA, DEGMEA, DEGEE, and BzOH. Again, the certain conductivity loss around 30 – 65% are observed but still less than 2,6-DAT (e.g., >99%) contamination. At the same time, it would be interesting to see that aliphatic structured compounds such as DEGEE and DEGMEA show greater conductivity loss than aromatic ring structured compounds such as 4-MBSA and BzOH. The reason for this may be the hindrance from the bigger size of molecules or functionality which interfering penetration of compounds into water clusters in PEM.

In sum, we can conclude that the 2,6-DAT would be most undesirable compound in PEMFCs which showed 0.5 coverage of acid sites (y-axis in Figure 5.2) at 0.1 mole fraction of 2,6-DAT relative to proton (x-axis in Figure 5.2) as well as over 99% conductivity loss at coverage 0.5 as shown in Figure 5.3.

5.3.2 CONTAMINATION IMPACT ON Pt/C CATALYST

CVs of 45.5% Pt/C catalyst are obtained for different concentration of contaminants in Figure 5.5. All contaminants affect on hydrogen adsorption and desorption and Pt oxidation and PtOx reduction regions. The extent of ECSA loss strongly depends on their functionality. Aromatic ring structural compounds such as BzOH, 4-MBSA, and 2,6-DAT show over 50% ECSA loss while aliphatic structural DEGMEA only show 30-40% at saturation coverage. The benzene ring has been known as the parallel orientated adsorption mechanism onto a surface of Pt [77, 107-108]. The aliphatic DEGMEA and DEGEE, possibly, can adsorb onto the Pt surface by an interaction between acetate group or hydroxyl group and Pt. Therefore, it seems reasonable to assume that the impacts from the aromatic compounds are more significant than the aliphatic compounds. Note that

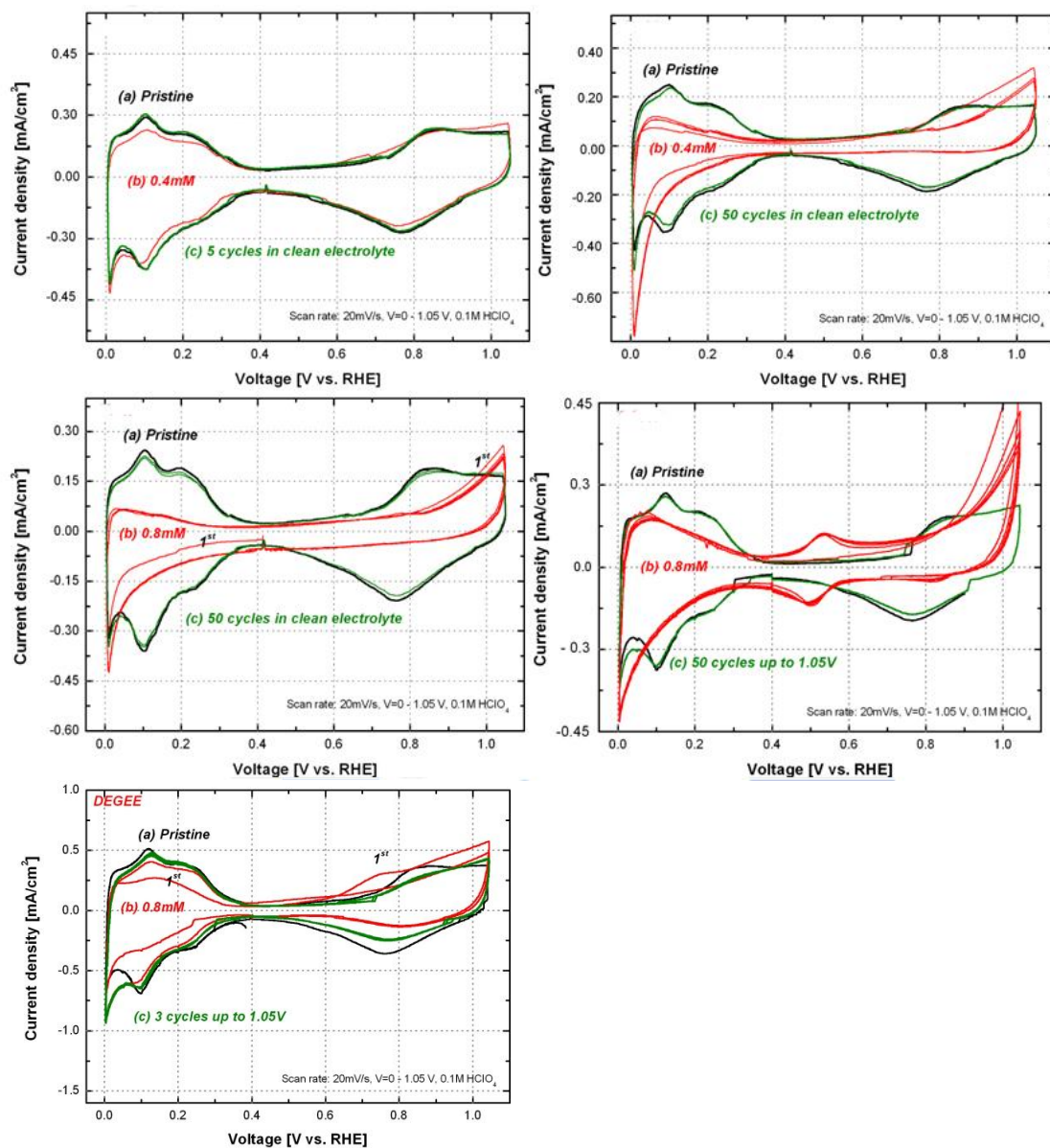


Figure 5.5 Cyclic votammograms for contaminated Pt/C catalyst: T=23 °C, 0.1M HClO₄, scan rate=20mv/s, 0.0 – 1.05V, Pt loading=0.02mg/cm²

parallel oriented adsorption behavior are known for the aromatic ring compounds.

For a recovery point of view, few potential cycles upon 1.05V vs. RHE apply to see change of Pt active sites (e.g., Δ ECSA and other oxidation peaks). The recovery also has a strong association which underlines the connection between the adsorption mechanism (parallel oriented adsorption) for aromatic and aliphatic. In other words, the aromatic compounds were harder to get rid of them (e.g., desorption) on the Pt surface during the potential cycles. To reach over 80% recovery for ECSA, we need to apply 50 times of potential cycles for aromatic compounds such as 2,6-DAT, BzOH, and 4-MBSA while, 5 cycles for aliphatic DEGEE and DEGMEA was need to get fully recovery.

Supposedly, the fully recovery for aromatic compounds may indicate the reduction of benzene (e.g., hydrogenation at 0.05 to 0.1V vs. RHE) and oxidation of other functional groups (methyl, amine, acetate etc.) occurred over 0.9V vs. RHE for all model compounds. In a real PEMFC system, the high voltage operating can help to oxidize organic species to some extent but still aromatic benzene is hard to eliminate from the Pt due to its need for low reduction potential (0.05 to 0.1V vs. RHE). Only for the 2,6-DAT CV shows unknown oxidation and reduction peak around 0.5V vs. RHE which may indicate the production of oxidants such as benzidine, p-aminodiphenylamine, quinone, hydroquinone etc. by radical reaction of head to tail or tail to tail coupling [80-81]. Note that the redox peak does not grow by potential cycles not like aniline [80-84].

The isotherms for adsorption are compared in Figure 5.5 and all data can be applicable for Langmuir adsorption model. Based on isotherms, we can rank model compounds as coverage on Pt active sites: 4-MBSA, BzOH (coverage>60%) > 2,6-DAT (coverage 45 – 60%) > DEGMEA (coverage <30%). To see the functionality impact on

adsorption, other compounds such as aniline, benzene are compared together. Obviously, all aromatic compounds show more coverage (i.e., over 50%) than aliphatic compounds. We believe that its higher coverage is due to the adsorption behavior of benzene ring on the Pt. Recall the parallel oriented adsorption behavior.

Note that the 4-MBSA and BzOH are highest coverage than other aromatic compounds. The higher carbon number of 4-MBSA and BzOH may result in higher coverage on Pt. In addition to the cleavage of C-S bond of 4-MBSA and C-C bond of BzOH may be probable to explain for highest coverage as well. For example, the C-S cleavage of 4-MBSA produce benzene and SO_2NH_2^- which both are possibly absorbed onto the Pt [107-108]. The BzOH may also have the reductive cleavage due to the electro reduction reaction to produce benzene and methanol (CH_3OH) in the presence of hydroxyl group ($-\text{OH}$).

5.3.3 *IN-SITU* INFUSION TEST

Figure 5.7 shows that at same infusion conditions (e.g., $T=80^\circ\text{C}$, $\text{RH}=32/32\%$, stoich.=2.0/2.0, back pressure=150/150kPa, infusion rate=0.03cc/min, contaminant concentration in bottle shown in graph) the voltage changes sensitive to the type of model compounds. Note that water infusion represents baseline on this experiment. All compounds infusion show voltage loss with HFR increase but once in recovery the behavior is different depends on chemical functionalities and size of compounds. The faster and slower response on contamination until reach steady state may correlates with the diffusion of contaminant through the ionomer to reach on Pt surface.

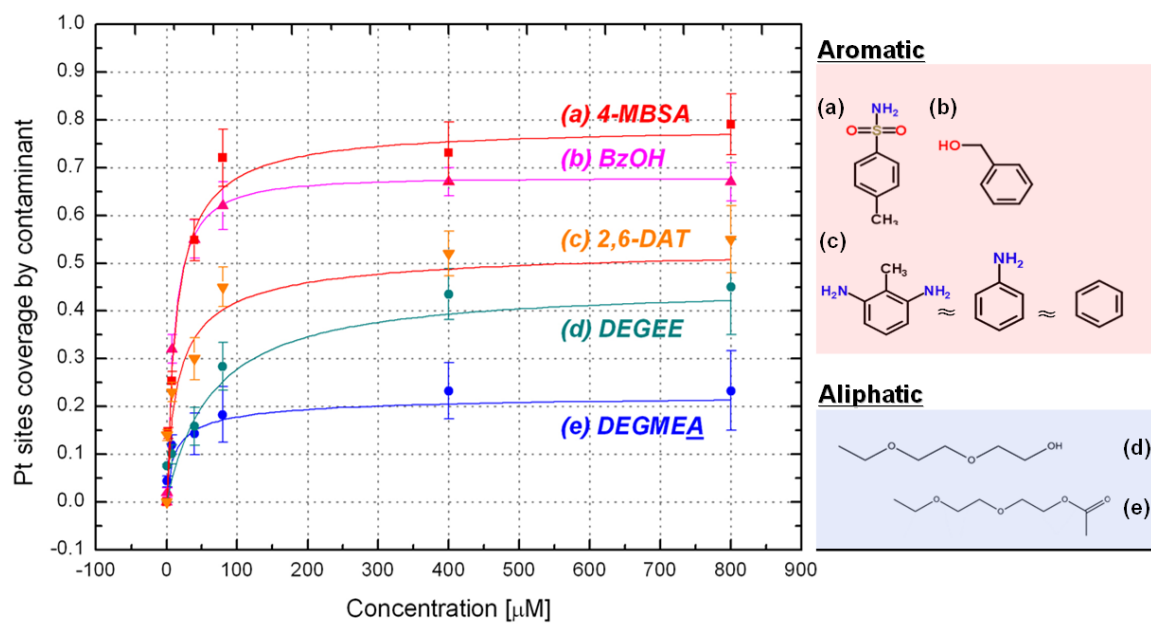


Figure 5.6 Adsorption isotherm of Pt/C electrode at 0.4V for model compounds

Thus, the dynamics of contamination can depend on the size of molecules as well as the affinity to ionomer. In other words, the dynamics of voltage response follows how fast contaminant can absorb into the ionomer and diffuse through. The smaller aliphatic structured DEGEE shows fast response (e.g., fast contamination impact) than bigger aromatic structured compounds (e.g., 4-MBSA and 2,6-DAT) and the chemical similarity of DEGEE (e.g., linear chain and ethoxy bond etc.) with ionomer can also explain the fast contamination impact. The higher affinity to ionomer from 2,6-DAT than 4-MBSA may a possible explanation for fast response on voltage change. Again, likewise *ex-situ* result, the concentration effect ((b) and (c) in Figure 5.7) also proved by *in-situ*.

Different responses at recovery region are also observed during water infusion. Recovery region indicates the infusion of DI water without contaminant at normal operating condition. For the fast recovery and fully (i.e., > 96% on base) on DEGEE, it seems reasonable because the previous *ex-situ* result supported no ion-exchange reaction but only possible for absorption by concentration gradient. In other words, the contamination effect by DEGEE infusion shows quickly by absorption and adsorption but the ionomer contamination can be easily removed by cut-off the DEGEE due to non-interaction with ionomer (i.e., ion-exchange reaction). Thus, the ionomer contamination can be easily recovered and only the contribution from Pt contamination can remain to show voltage change at the recovery region. However, for the 2,6-DAT which proved ion-exchange reaction in PEM (e.g., higher affinity) and for the 4-MBSA compound which may show size effect into PEM, the no recovery during normal operation without contaminant have been observed. Again, given the HFR response during infusion, the explanation seems reasonable.

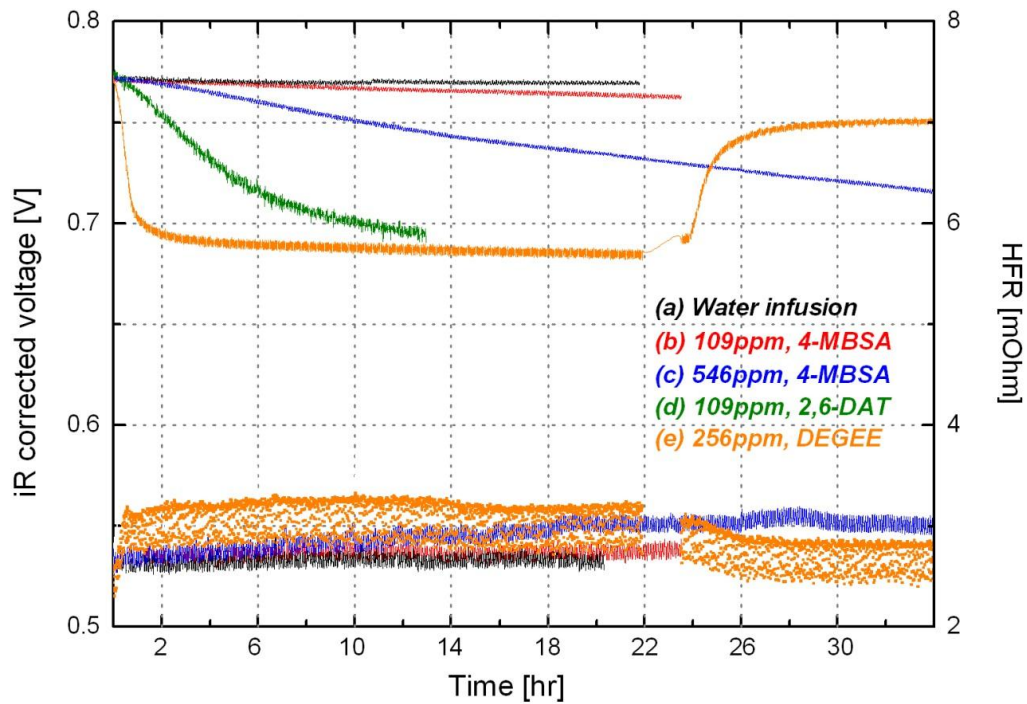


Figure 5.7 In-situ voltage response for model compound infusion: Infusion on cathode
 $T_{\text{cell}} = 80\text{ }^{\circ}\text{C}$, $\text{RH} = 32/32\%$, $\text{stoich.} = 2.0/2.0$, back pressure = 150/150 kPa

5.3.4 CONTRIBUTIONS ON VOLTAGE CHANGE FROM MECHANISMS

SEE CHAPTER 3 AND 4 MORE DETAILS

5.3.5 ΔV ANALYSIS FOR DEGEE CONTAMINATION FROM EX-SITU RESULTS

Figure 5.8 presents voltage response for DEGEE infusion on cathode at different concentration. Note that the voltage change for contamination defines as subtraction from water infusion and here the feed concentration of contaminant has been calculated in assumption of vapor phase infusion as below and the plug flow reactor (PFR) which is well known concept for chemical engineer has used to define concentration. The molar flow rate of contaminant has decided by multiple of concentration in the contaminant solution prepared in bottle and infusion rate (e.g., pumping rate into the cell). Total volumetric flow rate obtains from ideal gas law.

$$C_{cont.} = \frac{n_{cont.}}{v_T} \quad [5.6]$$

$$v_T = \frac{n_T RT}{P} \quad [5.7]$$

$$n_T = n_{feed} + n_{cont.} = n_{Air} + n_{water} + n_{cont.} \quad [5.8]$$

where, n_T = total molar flow rate, n_{feed} = molar flow rate for humidified air, n_{Air} = molar flow rate for air, n_{water} = molar flow rate for water vapor, $n_{cont.}$ = molar flow rate for contaminant. Note that the molar flow rate of contaminant is negligible in relative to air flow rate. Thus, it is probable that aerosol of contaminant nebulized into the cell can be assumed as a vapor at lower RH (32%). More details of experimental conditions are listed in Table 5.1.

To obtain the predictive coverage for *in-situ* experiment, we brought the corrected *ex-situ* adsorption isotherm, which obtained by film electrode experiment in liquid phase, on the area (0.2475 vs. 50 [cm²]) and then, the x-axis changed to the mole fraction rather than concentration considering assumption of vapor phase infusion. Figure 5.9 shows corrected adsorption isotherm originally shown in Figure 5.6. The predictive coverage compared with *in-situ* CV measurement at the end of infusion (e.g., time=7 hr for (a), 23 hr for (b), 6 hr for (c) in graph). Results show good agreement in consideration of 5% error. Based on the prediction curve in Figure 5.8, we can predict voltage change by Pt contamination only on each condition as listed in Table 5.1.

Again, the DEGEE infusion shows fast contamination effect but easy recovery on normal operating condition. Likewise *ex-situ* isotherms result, the concentration effect clearly shows in comparison between (a) and (b). However, all the same for ECSA loss, it is interesting to point out the deviation between (b) and (c) for the voltage changes at the steady state. Given the two different contamination mechanisms, the deviation can be resulted from ionomer contamination. Namely, the operating condition is different between (b) and (c). For the (c), RH and current density (i) are higher 80 vs. 32 [%] and 1.0 vs. 0.2 [V/cm²] respectively. More water generation at higher current density by ORR and higher RH feed in can wash out more contaminant in the electrode, which brings weak ionomer contamination impact. Recall that DEGEE absorption depends on concentration gradient in electrode between channel and ionomer and DEGEE is very soluble in water.

Table 5.1 Prediction of voltage change (ΔV_{pt}) by Pt contamination

Experiment*	C_{bottle}	Infusion rate	$C_{cont.}$	$\Delta ECSA$		Prediction
				<i>ex-situ</i>	<i>in-situ</i>	ΔV_{pt}
	[ppm]	[cm ³ /min]	$\times 10^{-9}$ [mol/cm ³]	[%]		[mV]
(a)	1280	0.03	1.673	-32.0 ± 4.0	-40.0	23.0 ± 4.0
(b)	256	0.03	0.329	-22.0 ± 5.0	-26.0	15.0 ± 5.0
(c)	84	0.465	0.334	-22.0 ± 5.0	-25.0	15.0 ± 5.0

*(a), (b) T=80 °C, RH=32/32%, i=0.2A/cm², P=150/150 kPa, stoich.=2.0/2.0

(c) T=80 °C, RH=80/80%, i=1.0A/cm², P=150/150 kPa, stoich.=2.0/2.0

Table 5.2 Prediction of voltage change ($\Delta V_{ionomer}$) by ionomer contamination

Experiment	$\Delta \kappa$	ΔHFR	Prediction
	<i>ex-situ</i>	<i>in-situ</i>	$\Delta V_{ionomer}$
	[%]		[mV]
(a)	-43.0	-30.5	130 ± 7.0
(b)	-25.0	-22.2	78.0 ± 7.0
(c)	-17.0	-14.9	44.0 ± 7.0

Table 5.3 Comparison of prediction and measured total voltage change by contamination

Experiment	Prediction			Measrued
	ΔV_{pt}	$\Delta V_{ionomer}$	ΔV_{total}	ΔV_{total}
	[mV]			
(a)	23.0 ± 4.0	130.0 ± 7.0	153.0 ± 7.0	125
(b)	15.0 ± 5.0	78.0 ± 7.0	93.0 ± 7.0	91
(c)	15.0 ± 5.0	44.0 ± 7.0	59.0 ± 7.0	45

To consider ionomer contamination impact, we need to close look at *ex-situ* membrane isotherms and conductivity data together. For the isotherm for 2,6-DAT which showed ion-exchange reaction with membrane (or ionomer), can be used for the prediction on voltage change. The mole fraction between 2,6-DAT and proton in membrane gives the prediction of coverage of acid sites in membrane (or ionomer) so that we can predict the voltage change. However, here for DEGEE infusion which did not have ion-exchange isotherm, we have to look at conductivity measurement data as changing of RH. Note that, the result in Figure 5.4 represents experimental condition (a) in Figure 5.9. First, we assume that conductivity change by DEGEE absorption in ionomer would be same as conductivity change of membrane due to the difficulty to measure membrane conductivity of ionomer by *ex-situ*. Furthermore, RH on cathode can calculate 32 to 80% in the consideration of $i=0.2\text{A}/\text{cm}^2$, 32% RH feed, and the assumption of no water transport from anode to cathode. Thus, we simply choose conductivity data at RH equal to 60% over the *in-situ* cathode for prediction. The *in-situ* measured HFR incremental during infusion of contaminant is also comparable with *ex-situ* conductivity data. Finally, the predicted and observed total voltage change which contribute from two different mechanisms, Pt and ionomer contamination are shown in Table 5.3. The over-prediction (e.g., 10 – 30mV) are shown but can be explained from the assumption for exponent (q_{ij}) in Butler-Volmer equation, which we assume stoichiometry ($q_{ij}=4$) on ORR. Further *ex-situ* experiments will be designed to specify the exponent in Butler-Volmer equation. More details of the prediction results for DEGEE infusion with the developed model is introduced in the section of ‘Comparison to the experimental’ section in Chapter 3.

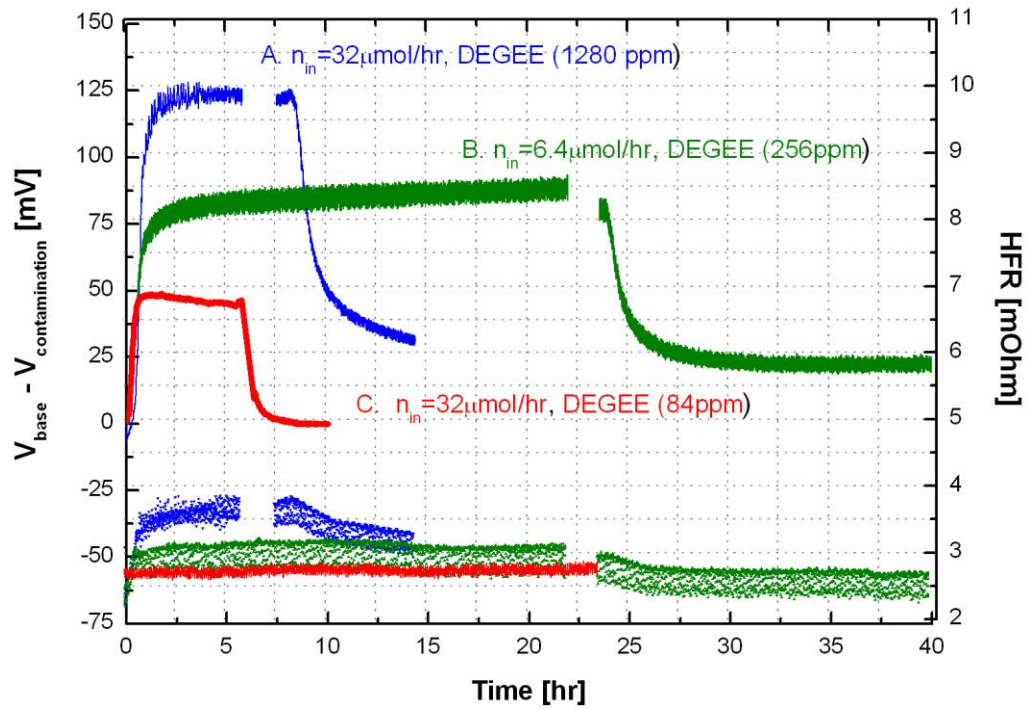


Figure 5.8. *In-situ* voltage response for DEGEE: Infusion on cathode: $T = 80^{\circ}\text{C}$, $\text{RH} = 32/32\%$, $\text{stoich.} = 2.0/2.0$, back pressure = 150/150 kPa

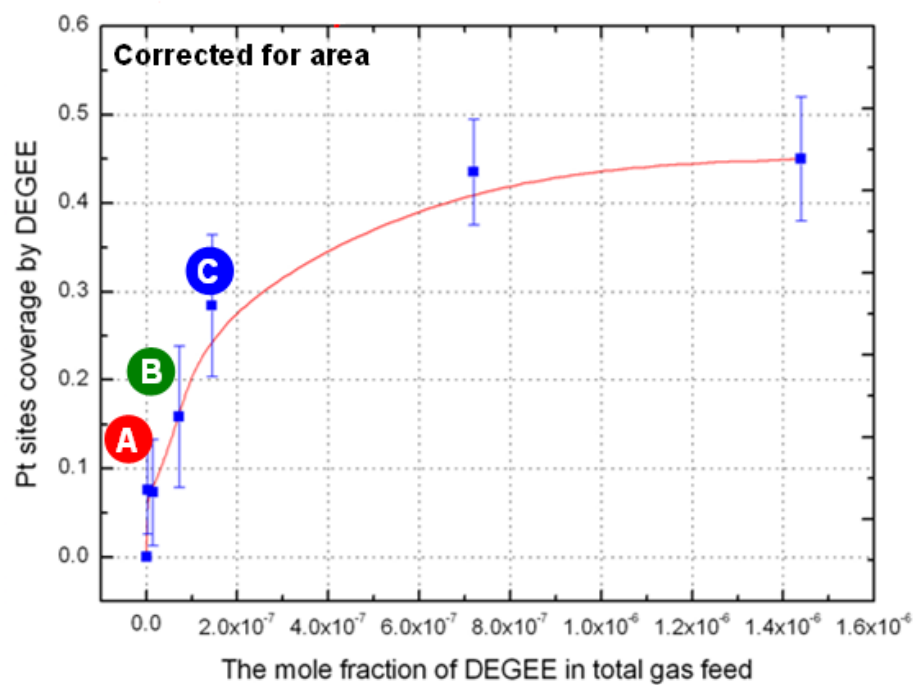


Figure 5. 9 Prediction for the coverage by ex-situ adsorption isotherm for DEGEE (Note: Please see Chapter 3 about the scaling of *ex-situ* concentration to *in-situ* or predictions.)

5.3.6 COMPARISON TO THE PREDICTING RESULTS OF 2, 6-DAT CONTAMINATION

In this section, *in-situ* infusion results of 2,6-DAT (e.g., 109ppm ($C_{leachate}$) of 2,6-DAT infused on cathode at $T=80^{\circ}\text{C}$, $RH=32/32\%$, $stoics=2.0/2.0$, back pressure=150/150kPa with feed rate of 0.03ccm) are compared with the prediction results. MEAs which have different loading of Pt as 0.1, 0.2 and $0.4\text{mg}/\text{cm}^2$ are tested and predictions are made by the developed model in Chapter 3.

Figure 5.10 shows results of the comparison. Parameters for the prediction for each mechanism (i.e., Pt and ionomer) are listed in Table 5.4. The prediction seems reasonable until the short period of time however, deviation shows after 8 to 10 hours. To understand the reason for the deviation, we have to analyze by each source. For the Pt contamination, *in-situ* CV results (i.e., ΔECSA) which measured at the end of infusion are compared with the prediction results of the coverage and seem reasonable. For the ionomer contamination, prediction results presents that the voltage loss increase linearly. As we discussed earlier in Chapter 3, it seems reasonable since change of mole fraction of contaminant and proton in ionomer will lead to the total loss of conductivity (i.e., voltage loss). However, we should consider the interaction between ionomer and membrane since the contaminant can diffuse from the ionomer to the membrane. Thus, we can speculate that the diffusion length will be changed as contamination continues. In other words, the effective diffusion coefficient will be changed due to the change of reaction plane for ion-exchange reaction from the surface of the ionomer to the inside of the

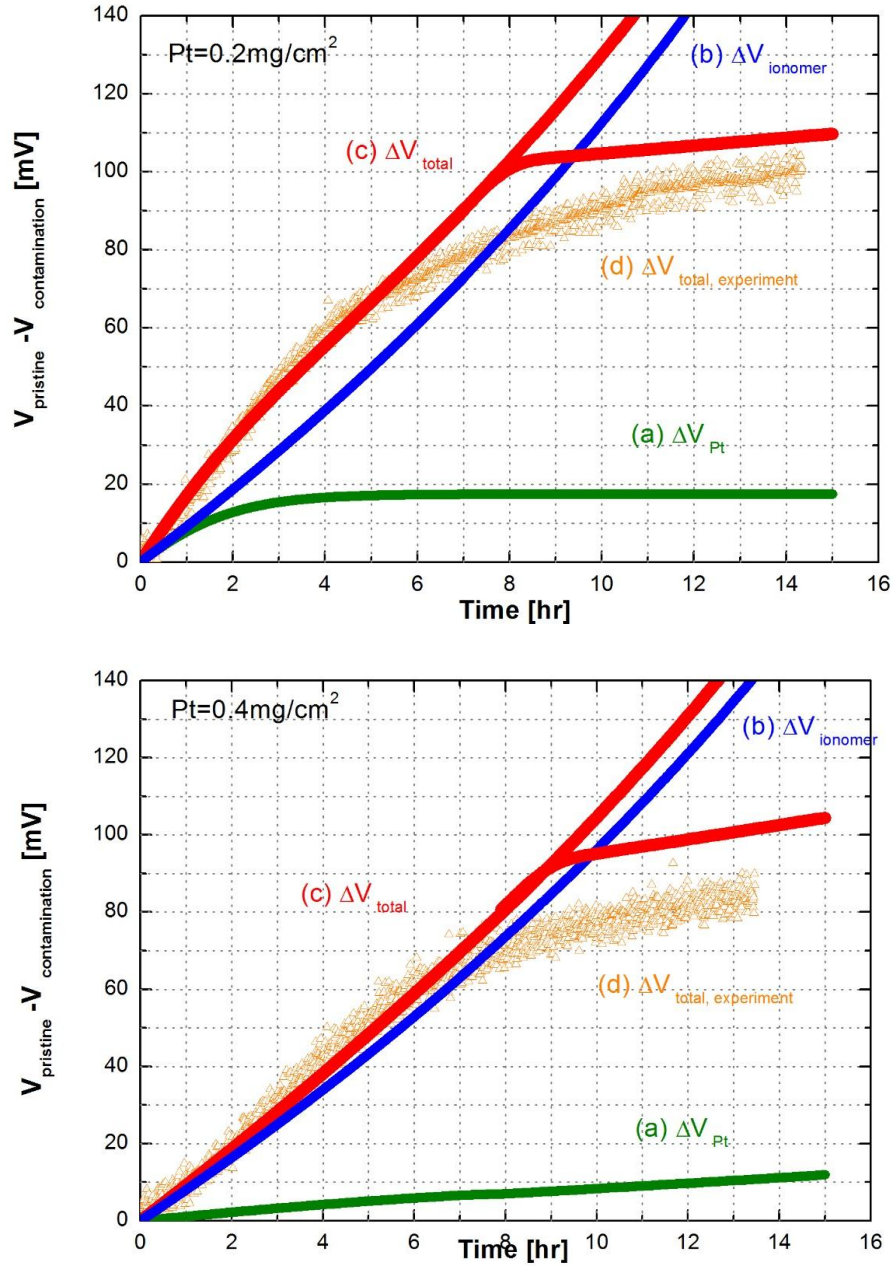


Figure 5. 10 Comparison of predictions to the experiment results of 2, 6-DAT infusion

Table 5.4 Dimensionless numbers to use for prediction in Figure 5.10

Ψ_1	Da_1
(a) 2.88E-03	3.69E-02
(b) 5.76E-03	7.37E-02
Ψ_2	Da_2
(a) 7.15E-04	3.69E-02
(b) 7.00E-04	7.37E-02

Table 5.5 Comparison predicted $\Delta ECSA$ to in-situ CV measurements

	$\Delta ECSA$ [%], measurement	$\Delta ECSA$ [%], prediction
a)	-23.0	-25.2
b)	-37.0	-35.5

membrane. This change of reaction plane leads to decreasing of Da number for ionome contamination. The decrease of the Da number represents the slope change of the voltage loss curve. Therefore, the plots for voltage loss by ionomer contamination are prepared two different linear lines after 8-10 hours. The reason why chose the 8-10 hours as reflection points is that the coverage for acid sites are 0.2 -0.3 at that time which may enough amount of exchanged capacity for the ionomer. We assume that the contaminant exchanged ionomer first and diffuses to the membrane. More experiments to determine the threshold for the slope change which result from the interaction between ionomer and membrane are need to be designed.

5.4 CONCLUSION

In this chapter, few organic model compounds such as aromatic 2,6-DAT, 4-MBSA, BzOH and aliphatic DEGEE, DEGMEA have been to study the impact in PEMFCs by mechanisms and functionality. Those model compounds have been identified in leachant which prepared in soaking of plastic materials, which can possibly use for the assembly in PEMFCs.

The comparison between model compounds study shows that the contamination by aromatic compounds results in more severe impact on Pt contamination and N-H containing compound shows is worst case for ionomer contamination due to N-H hydrolysis in acid condition. The aliphatic compound without N-H containing group (e.g., DEGEE and DEGMEA) shows faster contamination impact than other aromatic compounds and easy recovery.

Finally, to account for the contamination mechanisms, we conduct several *ex-situ* studies such as isotherms for Pt and membrane, membrane conductivity, and also *in-situ* infusion test. Two contamination mechanisms, Pt and ionomer contamination in electrode are investigated from *ex-situ* study. The ion-exchange isotherm and conductivity loss for membrane contamination, Pt adsorption isotherm for Pt contamination are prepared. The prediction of voltage change for each contamination contribution at steady state has been made as shown in Figure 5.11 by Butler-Volmer equation from *ex-situ* results.

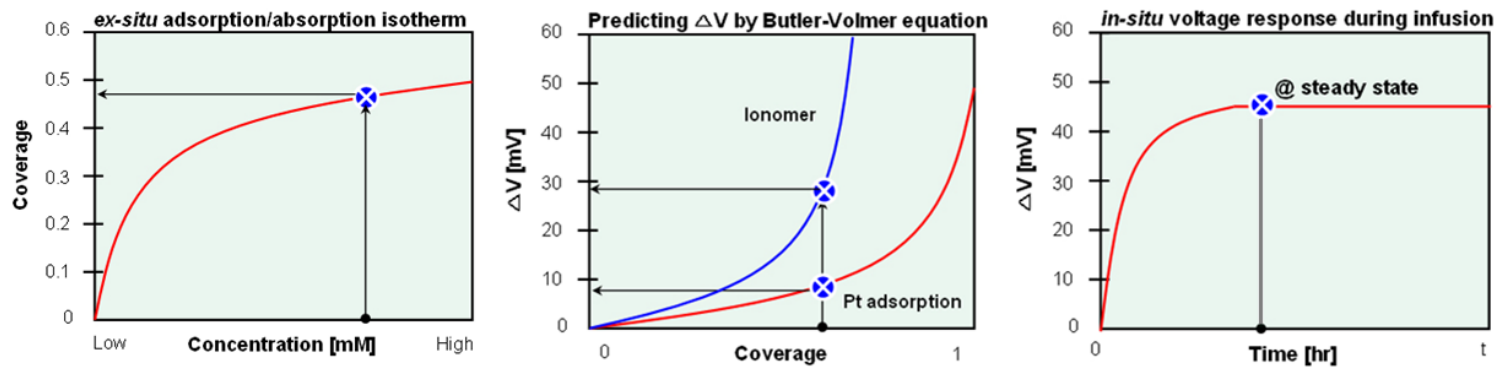


Figure 5.11 Schematic for the prediction of voltage change: correlation between *ex-situ* and *in-situ*

CHAPTER 6

THE CONTAMINATION MECHANISM AND BEHAVIOR OF AMIDE BOND CONTAINING ORGANIC CONTAMINANT ON PEMFC: PPA

In this chapter, we investigate the effect of amide bond (-CONH-) containing organic contaminant on PEMFC where contamination is compared with well-known contaminants, inorganic contaminants and ammonia. ϵ -caprolactam chose as a model compound which has been detected in leachate solutions from Polyphthalamide (PPA) materials that may be used in PEMFC system components. ϵ -caprolactam absorption into Nafion[®] membrane investigated and proved by UV-vis. spectrometry and ATR-IR analyses. The results show temperature effect on the absorption/ion-exchange which represents acid catalyzed hydrolysis mechanism of ϵ -caprolactam. In-plane membrane conductivity data also supports the temperature effect on the absorption/ion-exchange. The acid catalyzed hydrolysis of ϵ -caprolactam could produce ϵ -caproic acid and its amine group easily protonated in acid condition due to the pKa value of 9 for amine group.

The ϵ -caprolactam also affected the hydrogen adsorption/desorption and oxygen reduction reaction on a Pt/C and a polycrystalline Pt. They also reduce the peak associated with the Pt oxidation and PtOx reduction. The oxidation peak showed around 0.25V vs. RHE which is consistent with redox peak shown in a CV after injection of acetic acid (CH₃COOH) which supports a hypothesis that carboxylic acid adsorption and

electro-oxidation reaction occur to produce proton and electron on Pt surface: $\text{-COOH} + \text{Pt} \rightarrow \text{-COO-Pt} + \text{H}^+ + \text{e}^-$. In-situ results at different temperature (i.e., 50 and 80 °C) also support the endothermic ring opening of ϵ -caprolactam. Additional supporting work for this chapter is provided in Appendix C. In this appendix, the calculation of amounts of feed of ammonia gas into electrolyte is shown.

6.1 INTRODUCTION

Proton exchange membrane fuel cells (PEMFCs) have been receiving much attention due to high efficiency, low operating temperatures (70 – 90 °C), and clean byproduct (H_2O). However, there are still major remaining obstacles, cost and durability, for the wider commercialization of PEMFCs. Note that the cost of Balance of Plant (BOP) materials in PEMFCs recently needs to be more reduced rather than stack cost [110]. We are focused on system-derived contaminants out of off-the-shelf materials which can be alternatives for cost reduction in PEMFCs, but have studied for possible contamination mechanisms. To gain a fundamental understanding around the effect of organic contaminants on PEMFCs, the model compound, ϵ -caprolactam as shown in Figure 6.1 which represent effect of functional groups ketone ($=\text{CO}$), amine ($-\text{NH}_2$), amide ($-\text{NH}$), and carboxylic acid ($-\text{COOH}$). The ϵ -caprolactam chose based on GC-MS analysis of leachate [111] from possible plastic materials, PPA, may use in PEMFCs. 1,8-diaza cyclotetradecane-2,7-dione (DCDD) also confirmed as major species leached out of PPA materials. The result of ϵ -caprolactam compared with well studied contaminants on PEMFCs such as alkali, alkali earth metals, and ammonia, based on fundamental contamination mechanisms such as ion-exchange reactions, adsorption, and absorption.

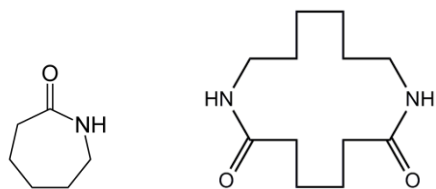


Figure 6.1 (a) ϵ -caprolactam (b) 1,8-diaza cyclotetradecane-2,7-dione (DCDD)

Based on previous ammonia (NH_3) [112] and aniline ($\text{C}_6\text{H}_5\text{NH}_2$) [113] contamination studies, we want to extend more N-H containing organic contaminant studies based on functional groups and contamination mechanisms. For the ion-exchange contamination mechanism, the effects of alkali and alkaline earth metal or transitional cations such as Li^+ , Na^+ , K^+ , Cs^+ , Ni^+ , NH_4^+ , Cu^{2+} , Ca^{2+} , Fe^{3+} etc on PFSA cation exchange membrane were well known [5-17,75, 86-89]. Oxygen reduction reaction kinetics at Pt electrode covered with Nafion[®] ionomer [7, 9] were also reported previously. Once cationic contaminants have been replaced with proton sites of sulfonic acid groups, not only a resistance of proton exchange membrane (PEM) was increased but also a structural change of ionomer appeared to be related with degradation on Pt/C catalyst activity. The structural change of Pt/ionomer interface by ion-exchange reaction of cationic contaminants could affect the kinetics of the Pt/C catalyst electrode for the Hydrogen Evolution Reaction (HER) and Oxygen Reduction Reaction (ORR) [7, 9]. The ammonia (NH_3) has amine group and the aniline has a benzene ring, as well as amine group ($-\text{NH}_2$). Both amine groups can fully protonate in acid condition ($\text{pH} < 4$) due to their acid dissociation constant ($\text{pK}_a \approx 9$) so that electrostatic interaction between the protonated amine and sulfonic group of Nafion[®] membrane is possible followed by conductivity loss. The interaction of protonated amine and sulfonic group or lone pairs of oxygen of $-\text{C}-\text{O}-\text{C}-$, may lead the structural change of PFSA ionomer on electrode and loss of the proton conductivity. For the adsorption contamination mechanism, CO [21], SO_2 [18-19], and H_2S [20] in the feed gas are well known contaminants on the Pt/C electrode. Organic species, the aniline also interacts with the Pt/C electrode due to its chemical structure containing an aromatic ring and a nitrogen atom from the amine

group. Also, the aniline contamination effect during potential cycles was reported to grow PANI film on a Pt/C electrode as parallel electrochemical reaction on PEMFC [see Chapter 3].

In present study, the cyclic amide structure of ϵ -caprolactam is interested to see their impacts on PEMFC performance. The ϵ -caprolactam was identified as a major chemical species which leached from the PPA materials, which categorized as a nylon type polymer [115]. Consideration of the ϵ -caprolactam compared to previous studies such as aniline, ammonia (NH_3), and cationic metal ions may allow for a correlation between chemical species, functional groups, and *in-situ* PEMFC response. To quantify the effect of these model compounds based on functional groups may provide sufficient data to establish “criteria for avoidance” in the selection of BOP components materials.

6.2 EXPERIMENTAL

6.2.1 MEMBRANE CONDUCTIVITY MEASUREMENT

Membrane conductivities were determined at ten values of constant relative humidity (RH) (i.e., 10, 20, 30, 40, 50, 60, 70, 80, 90, and 95%) by applying DC currents at the cell temperature of 80 °C. The potentiostat, a model PAR273, was used with a four-probe conductivity Teflon-based cell, a model BT-112, made from Beckktech LLC. The cell is pre-equilibrated with a 300 sccm flow of N_2 at $T_{\text{cell}}=80\text{ }^\circ\text{C}$ and $\text{RH}=90\%$ for 1 hr to condition the sample. The humidity was changed from 20% RH to 95% RH to measure the membrane conductivity with a hold of 30 min between the various RH conditions to assure equilibration at the next RH. The reported values of the membrane conductivity were obtained from and the DC resistance data and there was minimal variation between

the two values. VAISALA dew point chamber also attached outlet of the conductivity cell to correct dew point temperature of outgases.

6.2.2 RDE MEASUREMENT

Electrode catalysts inks were made with a carbon-supported 45.5% Pt (Tanaka) catalyst to achieve a Pt loading of 0.02 mg/cm^2 . The catalysts were dispersed in DI water and isopropyl alcohol (IPA) in the presence of a Nafion[®] ionomer solution. The platinum catalyst ink was mixed and dispersed by ultrasonic for approximately 20 minutes and dropped on a glassy carbon disk electrode (0.2475 cm^2). The electrochemical analyses, (i.e., cyclic voltammetry, and kinetic currents for the oxygen reduction reaction), was performed with a Model E7R9 RRDE from Pine Instruments in connection with potentiostat, a model of PAR 263A. Only the RDE part of the electrode was used. A 0.1M perchloric acid solution (HClO_4) and mercury sulfate electrode were used as an electrolyte and reference electrode, respectively. For the high temperature (73°C) RDE experiment, a heat jacket was wrapped surround in 3-neck flask including electrolyte and a special RDE tip for high temperature: The tip for high temperature to be stable at 80°C was provided by Pine Instrument. For ammonia gas infusion RDE experiment, 997 ppm ammonia gas in balanced with nitrogen exposure into electrolyte in RDE system through mass flow controller (MFC).

6.2.3 MEMBRANE ISOTHERMS

Concentration of ϵ -caprolactam and ϵ -amino caproic acid can be measured by a UV-visible spectrophotometer at 190 – 400nm wavelengths. Several mixtures of 5mN sulfuric

acid (H_2SO_4) solution and 5mN ϵ -caprolactam solutions were prepared with the different molar ratios for the measurement of absorption isotherm in a N117 at 90°C . All mixture solutions were controlled $\text{pH} < 5$ thus, amine group of ϵ -caprolactam expected to be protonated due to the pK_a of amine group closed to 9. Two samples for ϵ -caprolactam solution were prepared to check reproducibility. One piece of membrane ($3.0 \times 3.0 \text{ cm}^2$) was immersed in each of the mixtures. Magnetic stirrer plates were used for mixing to allow the ion exchange reaction between the protonated form of ϵ -caprolactam and proton form of the membrane. The subsequent ϵ -caprolactam concentrations remaining in the solution and 2M HCl after extraction of ϵ -caprolactam out of membrane were measured by UV-visible spectrometer (Shimadzu UV2101) at 190–400 nm wavelengths (calibrated over a concentration range).

6.2.4 ATR-IR AND UV-VIS. ANALYSIS

Each NRE211 ($0.9 \times 4.25 \text{ cm}^2$) samples for spectroscopy analyses was prepared by soaking in 5mM of ϵ -caprolactam in 10mM H_2SO_4 . The replacement expectation of proton sites in NRE211 was less than 35% for IEC. The sample was rinsed with DI water to get rid of over-absorption, and dried with nitrogen gas purging at room temperature for 30min. ATR-IR spectra were collected on a spectrometer equipped with a detector. A total of 100 scans were averaged per spectrum. Each spectrum was recorded from 4000 to 800 cm^{-1} . Extraction solutions with 99.8wt% of methanol out of ϵ -caprolactam and ϵ -caproic acid absorbed N115 were also measured to confirm their chemical structure in

Nafion[®] membrane. The ATR-IR data of ϵ -caprolactam and ϵ -caproic acid in methanol also compared as references.

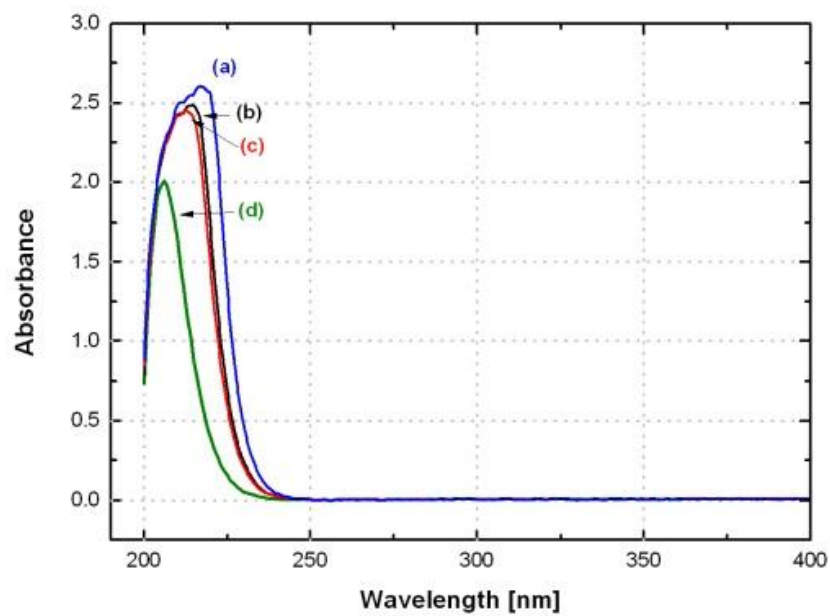
6.2.5 *IN-SITU* SINGLE CELL TEST

GM provided MEA (50cm²) was used for a single cell test. RH was set at 50% on both and a constant current operation mode was applied to get rid of water effect for Nafion[®] membrane. Again, water generation and contents of MEA were estimated to be equal at different temperatures but the same RH 50%. Same mole flux (i.e., 11 μ mol/hr) of ϵ -caprolactam solution was introduced on the cathode side with air of the single cell by a micro syringe pump and nebulizer while voltage was recorded at constant current density (i.e., 0.2A/cm²). HFR and CV were also recorded before and after contamination to see the contamination effect on Nafion[®] membrane and Pt/C electrode activity respectively.

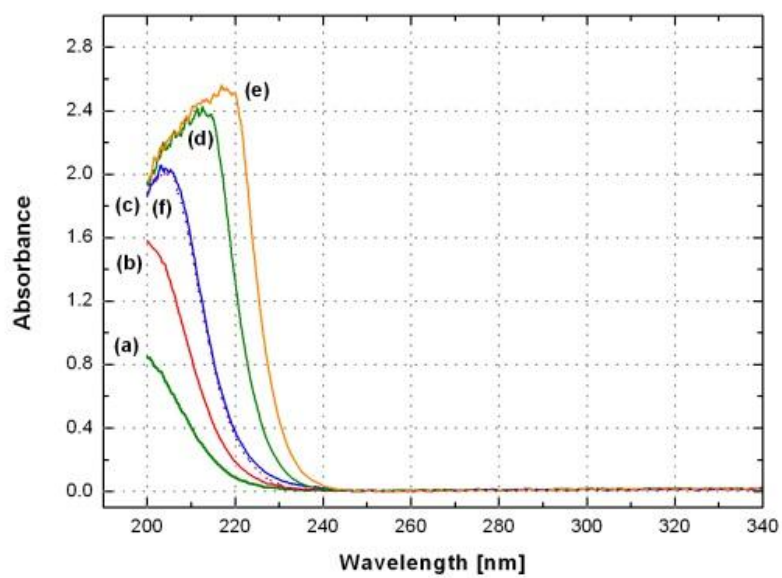
6.3 RESULTS AND DISCUSSION

6.3.1 THE EFFECT OF TEMPERATURE ON THE ION-EXCHANGE

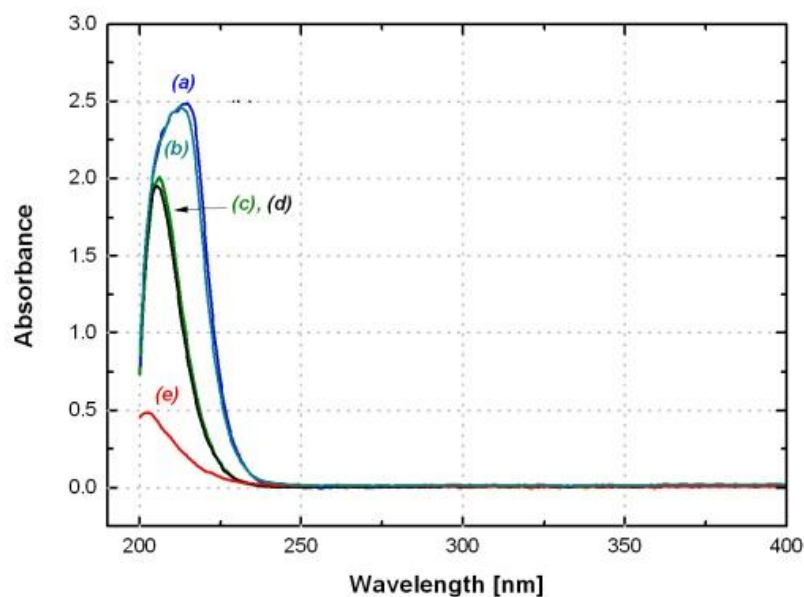
Figure 6.2 shows UV-vis. analysis results whether ϵ -caprolactam shows absorption behavior into Nafion[®] membrane. Figure 6.2a shows that there is no significant maximum peak change with soaking of N117 in 5mN caprolactam with 0.1M HCl(aq) (with acid as a source for the protonation) at room temperature (i.e., compare lines (b) and (c)). Figure 2b also shows non-effect in 1 mN (i.e., compare lines (c) and (f)) albeit without acid as a source for the protonation. The non-effect on the GDL was also shown in Figure 2c in 10mM HCl by lines (c) and (d). However, the temperature effect was



a)



b)



c)

Figure 6.2 **a)** UV-vis spectrum of various concentration of ϵ -caprolactam solutions in 0.1M HCl(aq) (a)10mN (b)5mN (c)5mN after soaking a piece of N117 ($3 \times 3 \text{ cm}^2$) soak (d)1mN **b)** various concentration aqueous ϵ -caprolactam solutions (a)0.25mN (b)0.50mN (c)1.0mN (d)5.0mN (e)10mN (f)1.0mN after soaking of a piece of NR211($3 \times 3 \text{ cm}^2$) **c)** various concentration of ϵ -caprolactam solutions in 10mM HCl(aq) (a)5mN (b)5mN after soaking of N117 ($3 \text{ cm} \times 3 \text{ cm}$) at RT (c)1mN (d)1mN after soaking of SGL 35 BC (e)5mN after soaking a piece of N117 ($3 \times 3 \text{ cm}^2$) at 90°C

shown by line (e) where the maximum intensity peak of UV-vis. spectrum of ϵ -caprolactam was dramatically decreased where N117 was soaked in ϵ -caprolactam solution with acid sources for the protonation at $T=90^{\circ}\text{C}$. We hypothesize that there is an open ring reaction of lactam ($-\text{NH}-\text{C}=\text{O}-$) which is more favorable due to the endothermic reaction similar to the ring opening reaction of lacton which has a similar molecular structure ($-\text{O}-\text{C}=\text{O}-$) and those reactions are favored among increasing temperatures. The acid-catalyzed hydrolysis of amides has been extensively investigated and reviewed [116-118]. Therefore, after the ring opening reaction, ϵ -caprolactam would become ϵ -amino caproic acid if it were hydrolyzed in acid solution due to the hydrolysis of the amide bond. In other words, each ϵ -caprolactam molecule would be broken by acid-catalyzed hydrolysis of amide. Hence, in the case of a higher temperature environment, the ϵ -amino caproic acid can be produced more and protonated quarternary amine group of ϵ -amino caproic acid can generate as ammonium ion, NH_3^+ in acid condition. Figure 6.3 shows the schematic of ϵ -caprolactam and possible electrostatic interaction between protonated form of ϵ -amino caproic acid and sulfonic group of Nafion[®] membrane. The ion-exchange reaction between the protonated quarternary amine group, NH_3^+ of ϵ -amino caproic acid and sulfonic acid group in Nafion[®] membrane increased the membrane resistance and the proton conductivity decreased. However, we believe that the ion exchange reaction may be more difficult for organic species than other metal cations such as K^+ , Na^+ , Ca^{2+} and Fe^{3+} due to steric hindrance from chemical structure: bulky and longer chain, compared to others. However, they still lead serious contamination effects even though exchanged concentration for IEC is less than other inorganic contaminants: the steric hindrance interfere to conduct protons in PEM. The protonated form of closed

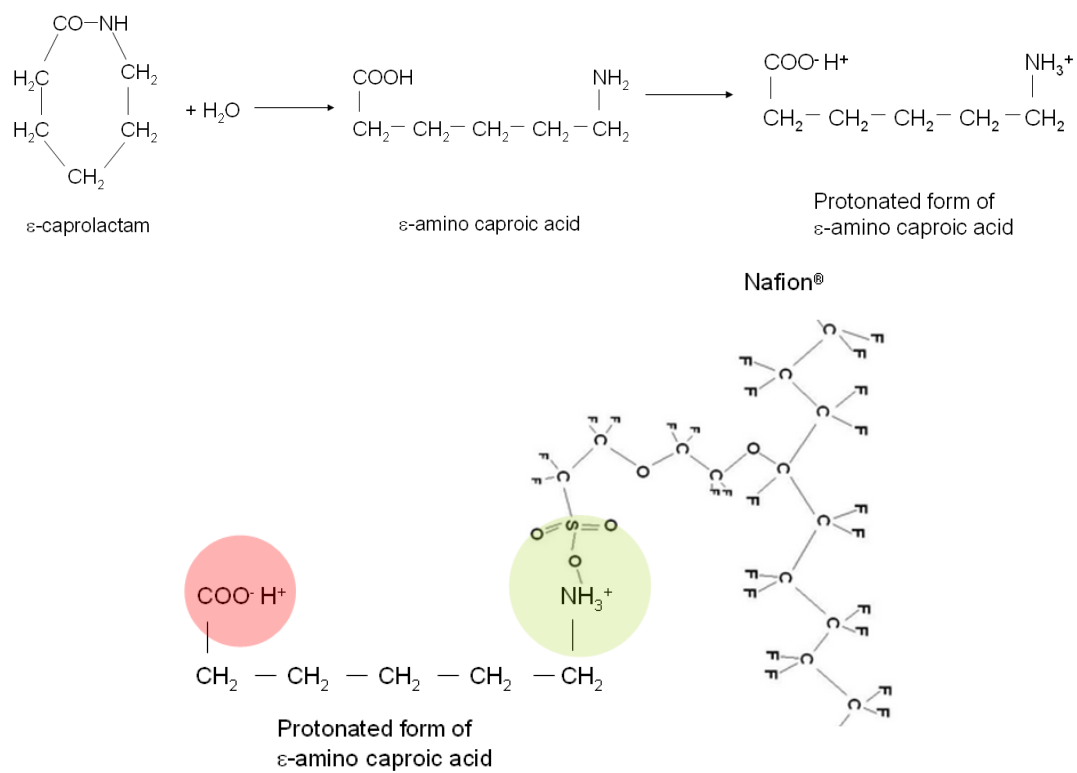


Figure 6.3 Schematic of protonated ϵ -caprolactam by acid-catalyzed hydrolysis mechanism and possible electrostatic interaction with sulfonic group

structure of ϵ -caprolactam may also possible to interact with sulfonic group by electrostatic interaction after absorbing into Nafion[®] membrane. Thus, there would be partition between closed ring structure and open ring structure species in Nafion[®] membrane depends on their thermodynamic properties. However, the temperature effect on absorption could explain with acid catalyzed hydrolysis of ϵ -caprolactam to open ring structure.

In-plane membrane conductivities for NRE211s, which were soaked in 0.1M ϵ -caprolactam solutions at different temperatures, room temperature and 90°C, were measured to verify the temperature effect of ϵ -caprolactam on Nafion[®] membrane. Figure 6.4 shows the effect of relative humidity on the membrane conductivity for various species. The NRE211 sample (0.9 cm×4.5 cm) soaked in ϵ -caprolactam solution at 90°C (line (f) in Figure 6.4) showed two factors lower for conductivity compared to it being soaked in ϵ -caprolactam solution at 25°C (line (e) in Figure 6.4) while, available acid sites in ϵ -caprolactam exchanged Nafion[®] membrane was 30%. The lower membrane conductivity in lower concentration exchanged Nafion[®] membrane may cause from the steric hindrance of ϵ -amino caproic acid or protonated ϵ -caprolactam to reduce proton conductivity and water contents. Note that the all NRE211s fully exchanged with cationic form of contaminants (i.e., Na⁺, NH₃⁺, C₆H₅NH₃⁺) except ϵ -caprolactam replaced NRE211 (i.e., 30% exchange of acid sites) and 100 times lower membrane conductivity for ϵ -caprolactam at RH=50%. The in-plane membrane conductivity for NRE211s exchanged with contaminants have a log-linear proportionality with the relative humidity (RH): $\log(\sigma)=aRH+b$ (a and b are constant). Table 6.1 shows that the slope (large slope

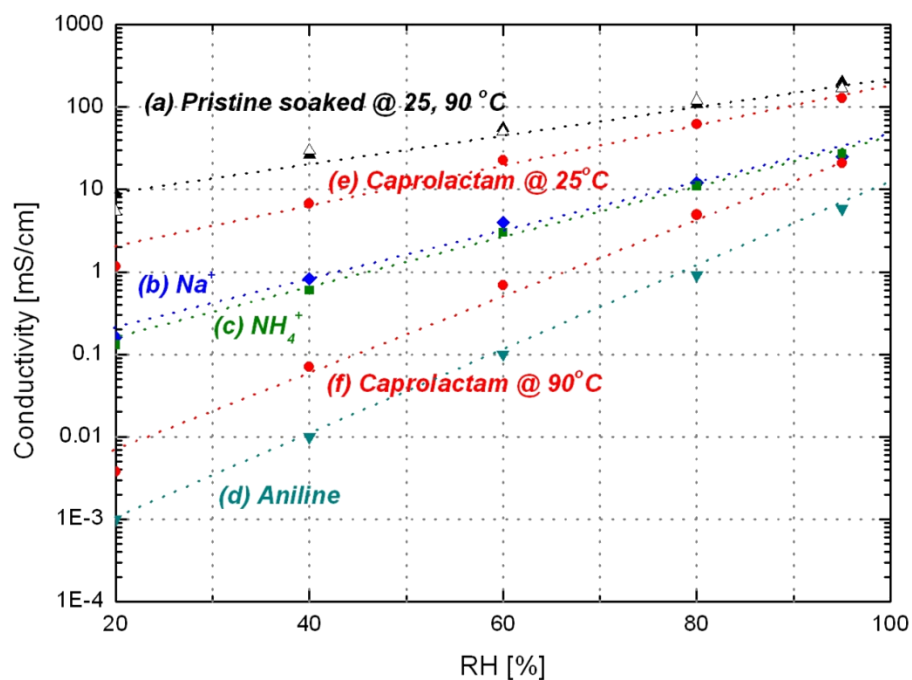


Figure 6.4 Conductivity of NE211 and comparison of various contaminants for the effect of RH and contaminant (% ion-exchanged) concentration

indicates more dependence of membrane conductivity on RH) of each species exchanged form of NRE211. For the temperature effect, one can use the data in Table 6.2 to calculate the equilibrium constants for the partition between the closed ring and open ring of ϵ -calprolactam. Thus, as shown in Table 6.3, the equilibrium constant ($K_{90^\circ\text{C}}$) for ring opening reaction of caprolactam to ϵ -amino caproic acid is twice as large as $K_{25^\circ\text{C}}$. (i.e., pK changed from 3.27 to 3.00) Note that ΔH_{rxn} for ring opening reaction of caprolactam is calculated 8.85 kJ/mol (greater than 0, endothermic reaction) based on the values in Table 6.3. The ratio of $K_{90^\circ\text{C}}/K_{25^\circ\text{C}} = 2.0$ for ϵ -amino caproic acid are calculated by Van't Hoff equation as follows. Gibbs free energy in Table 6.3 showed positive for both temperatures since $\Delta H > 0$, $-T\Delta S < 0$ which are unfavorable enthalpy change (endothermic) and favorable entropy change (disorder increases due to open ring reaction).

$$\ln\left(\frac{K_2}{K_1}\right) = -\frac{\Delta H_{\text{rxn}}}{R}\left(\frac{1}{T_2} - \frac{1}{T_1}\right) \quad [6.1]$$

$$K = \exp\left(\frac{-G}{RT}\right) = \exp\left[\frac{\left(S - \frac{H}{T}\right)}{R}\right] \quad [6.2]$$

$$pK = -\log[K] \quad [6.3]$$

Table 6.1 The slope of cation exchanged NRE211 membrane conductivity

(a) Pristine	(b) Na	(c) NH ₃
0.0188 ± 0.002	0.0277	0.0311
(d) Aniline	(e) ε-caprolactam (25 °C)	(f) ε-caprolactam (90 °C)
0.0520 ± 0.003	0.0267	0.0493

$$\log(\sigma)=aRH+b$$

Table 6.2 Kinetic constants of caprolactam for ring opening reaction

Reaction	Kinetic constants of the rate equation				G [kJ/mol]	
	A [kg/mol ² ·hr]	E [kJ/mol]	H [kJ/mol]	S [kJ/mol·K]	25 °C	90 °C
Ring opening	1.69E+06	88.09	8.85	-0.033	18.59	20.83

Table 6.3 pK value for ring opening reaction of ε-caprolactam at different temperatures

T	25 °C	90 °C
pK	3.27	3.00

The isotherm of Nafion[®] membrane for ϵ -caprolactam prepared in 80 °C showed higher affinity in relative to the single charged cation exchanged Nafion[®] membrane: Na⁺ and NH₃⁺ (i.e., lines (a), (b), and (d) in Figure 6.5). The higher affinity may due to the similarity between acid condition of Nafion[®] membrane and carboxylic acid (-COOH) of ϵ -amino caproic acid. The bigger size of ϵ -caprolactam also can be evidence, which reported for potassium has higher affinity to PEM than sodium due to small hydration radius of potassium caused by large radius of potassium than sodium [122].

6.3.2 COMPARISON OF THE EFFECT OF N-H CONTAINING CONTAMINANTS ON MEMBRANE

In an effort to understand the effect of ϵ -caprolactam (CH₂C(O)NH), ammonia (NH₃), and aniline (C₆H₅NH₂), which are representative of the N-H containing compounds, studied to date, that may contaminate Nafion[®] membrane which were compared in Figures 6.4 and 6.5. Studies of NH₃ have shown that it hydrolyzed and ion-exchanges with Nafion[®] membrane and ionomer in the electrodes in PEMFCs [67, 75, 112]. The ammonium ion (NH₄⁺) exchanged acid sites of Nafion[®] membrane showed similar reduction of membrane proton conductivity with Na⁺ exchanged Nafion[®] membrane, while single charged anilinium (C₆H₅NH₃⁺) and ϵ -caprolactam exchanged Nafion[®] membranes were show relatively lower conductivity: Recall ion-exchange isotherm with sodium, ammonium, aniline, and ϵ -caprolactam exchanged showed different affinity to PEM. In previous aniline studies, the anilinium exchanged Nafion[®] showed membrane conductivity loss seriously at low RH than at 100% RH due to the expulsion of water by the hydrophobic aromatic ring of aniline [See Chapter 4]. The previous study were also compared water contents in N117 at same exchanged acid sites with anilinium and sodium

as change of RH which showed lower water contents for anilinium exchanged N117 [See Chapter 4]. To summarize these results, functional groups of aniline and ϵ -caprolactam have affected on the ion exchange reaction/absorption in Nafion[®] membrane as well as water contents due to the interaction with water. Again organic contaminants which have hydrophobic benzene ring can increase the resistance of membrane conductivity severely due to water expulsion. The steric hindrance effect by ion size can be another possible reason for lower membrane conductivity.

6.3.3 INTERACTIONS WITH THE Pt/C CATALYST ELECTRODE

Cyclic voltammograms of polycrystalline and the carbon supported Pt electrode (loading=0.02mg/cm²) were obtained for different concentrations of ϵ -caprolactam solutions in 0.1M HClO₄ electrolyte to investigate the Pt contamination effects. Figure 6.6 shows the effects of ϵ -caprolactam on hydrogen desorption/adsorption at room temperature. The results show no significant loss of ECSA (e.g. ECSA reduced about 10% in 0.4mM of ϵ -caprolactam in 125mL). However, the more loss of ECSA for polycrystalline Pt electrode would lead us to assume that the three phase carbon supported nano particle size of Pt catalyst would robust contamination effect than plain Pt catalyst. We speculated that the carbon support acted as a filter due to its higher PZC compared to pH of electrolyte. For the Vulcan XC-72R carbon support, the point of zero charge (PZC) is 8.6 and RDE experiment conducted at pH 1 (i.e. 0.1M HClO₄) so that the anion, carboxylic acid (-COOH) can be adsorbed onto the surface of carbon. The anion (-COO⁻) of ϵ -amino caproic acid could adsorb onto the surface of Pt as well as carbon

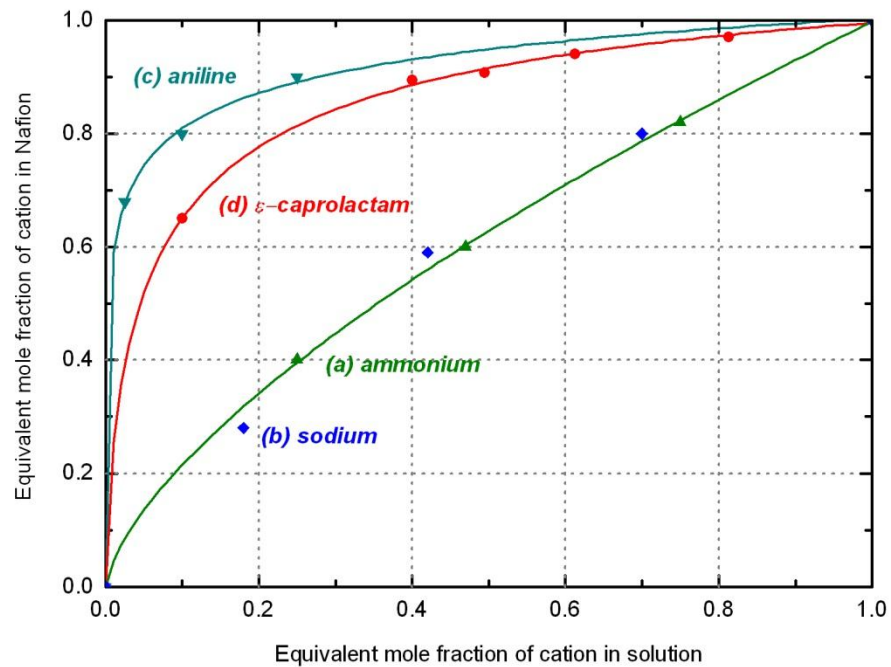


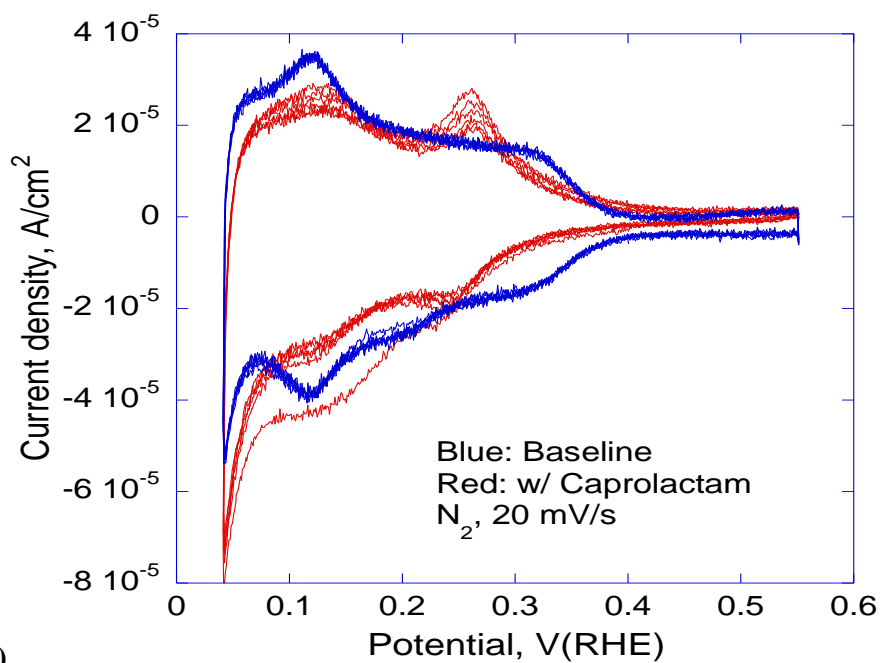
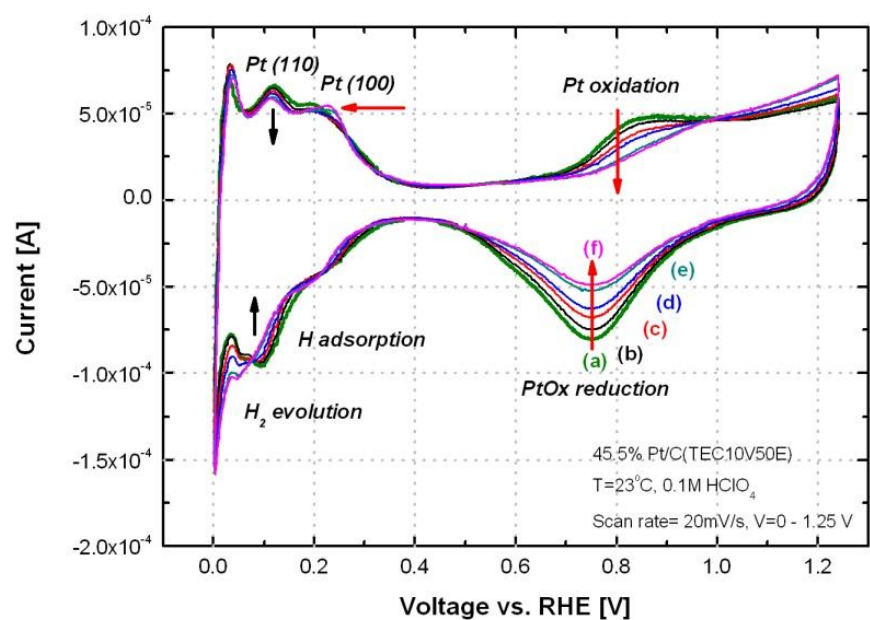
Figure 6.5 Comparison of ion-exchange isotherm of Nafion[®] membrane for (a) ammonium (b) sodium (c) aniline (d) ϵ -caprolactam

support so that polycrystalline Pt electrode showed more loss of ECSA than Pt/C electrode system. The Nafion[®] ionomer used for Pt/C electrode RDE experiment may be other reason to show lower loss of ECSA since contaminants should penetrate through Nafion[®] ionomer to adsorb on the surface of Pt active sites.

The Pt oxidation and PtOx reduction peaks are decreased as ϵ -caprolactam is increased and the oxidation shoulder peak was observed around 0.25V (vs. RHE). The reduction of Pt oxidation and PtOx reduction peak may be explained due to the adsorption of carboxylic acid (-COOH) of ϵ -amino caproic acid onto PtOx surface. Whether the oxidation shoulder peak shown around 0.25V (vs. RHE) comes from the adsorption of ϵ -amino caproic acid on the Pt surface or another electro-organic reaction from the increase of current density from 1.0V to 1.2V (vs. RHE), the oxidation shoulder peak at 0.25V (vs. RHE) was more clearly observed with CV measured at higher temperature $T=73\text{ }^{\circ}\text{C}$ as shown in Figure 6.6b. Therefore, we can assume that the oxidation peak around 0.25V vs. RHE is related with ϵ -amino caproic acid.

As noted above, we also expected significant Pt loss by the ion-exchange of protonated ϵ -amino caproic acid with the acid sites in the Pt/C electrode at $73\text{ }^{\circ}\text{C}$. However, our experimental data did not show much loss of ECSA in *ex-situ* RDE experiment. One possible explanation of this CV result in Figure 6.6 is that the pKa (2~3) of carboxylic acid group.

We conducted RDE experiment pH=1 condition, in other words, the carboxylic acid of ϵ -amino caproic acid did not dissociate at pH=1 ($\text{pH} < \text{pKa}$ of -COOH). Thus, there would be relatively difficulty of carboxylic acid (-COOH) to adsorb onto the surface of Pt electrode than carboxylate (-COO⁻) which is dissociate anion.



(a)

(b)

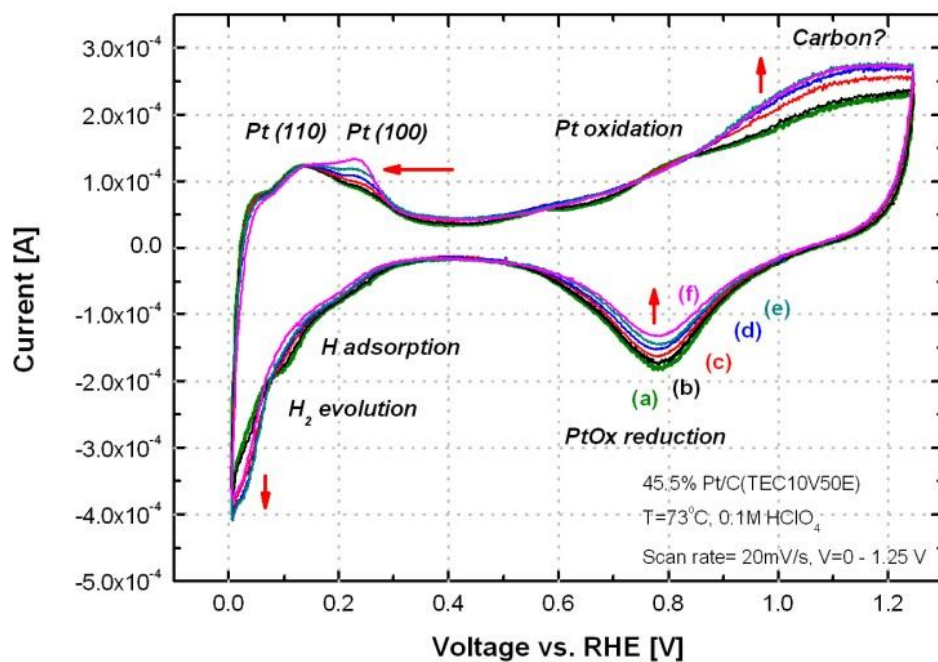


Figure 6.6 (a) Cyclic voltammograms of 45.5% Pt/C and polycrystalline Pt catalyst as concentration of caprolactam increasing a) 0μM b) 8μM (\cong 100ML) c) 40μM (\cong 500ML) d) 80μM (\cong 1000ML) e) 0.4mM (\cong 5000ML) f) 0.8mM (\cong 10000ML)
 (b) Caprolactam effect on cyclic voltammograms of Pt/C catalyst electrode at 73 °C (a) 0 (b) 8μM (c) 16μM (d) 40μM (e) 80μM (f) 0.4mM

The other RDE experiment conducted at pH=2 showed more loss of ECSA (30%) compared to that loss (17%) conducted at pH=1 as shown in Figure 6.7. Note that CV at pH=2 did not show oxidation shoulder peak. In other words, carboxylate anion (-COO^-) adsorbed onto the surface of Pt rather than carboxylic acid (-COOH). The other possible explanation is that the protonated ϵ -amino caproic acid can be regarded as a proton conductor ($\text{-COO}^- \text{H}^+$) even though proton conductivity is less than sulfonic acid group ($\text{-SO}_3^- \text{H}^+$). As a consequence, ϵ -amino caproic acid might be acting as another proton conductor at the ionomer/PFSA membrane thus, ϵ -caprolactam could not affect on Pt active site by adsorption but ion exchange with ionomer.

The oxidation shoulder peak at 0.25V vs. RHE can explain with the oxidation of carboxylic acid (-COOH) onto Pt/C surface. Once the carboxylic acid (-COOH) adsorbed onto the Pt/C, the Pt catalyst may aid to oxidize carboxylic acid at relatively low electro-potential so as to produce proton from the oxidation of carboxylic acid: $\text{-COOH} + \text{Pt} \rightarrow \text{-COO-Pt} + \text{H}^+ + \text{e}^-$. The oxidation shoulder peak increased more at a higher temperature (73°C as shown in Figure 6.6) compared to that results at room temperature (23°C as shown in Figure 6.6). The above reaction scheme, carboxylic acid adsorption and electro-organic oxidation, may be possible to support an oxidation peak. The increase of current density about 1.0V to 1.2V also can be explained by the oxidation of carboxylic acid to produce carbon dioxide: $\text{-COO-Pt} \rightarrow \text{CO}_2 + \text{e}^-$.

The kinetic current of oxygen reduction reaction (ORR) of Pt/C electrode was also measured as increasing of ϵ -caprolactam concentration into solution as shown in Figure 6. 8a. The limiting current and Tafel slopes of 45.5% Pt/C catalyst electrode showed that there were no significant change by adding ϵ -caprolactam. The Tafel slopes were

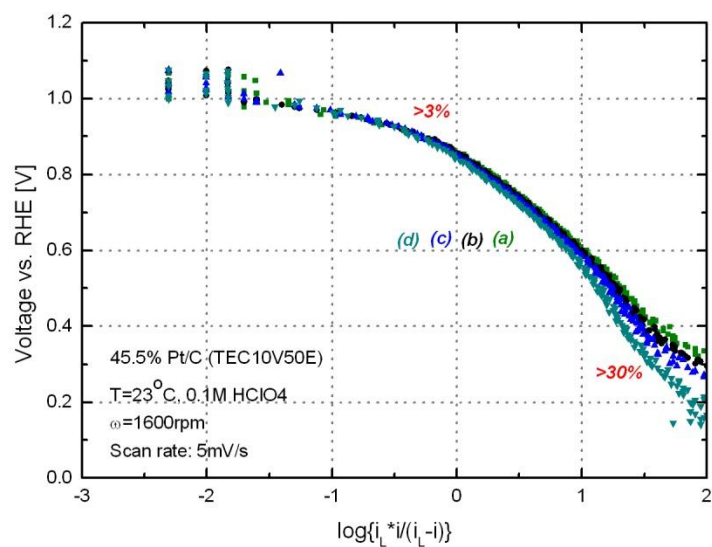
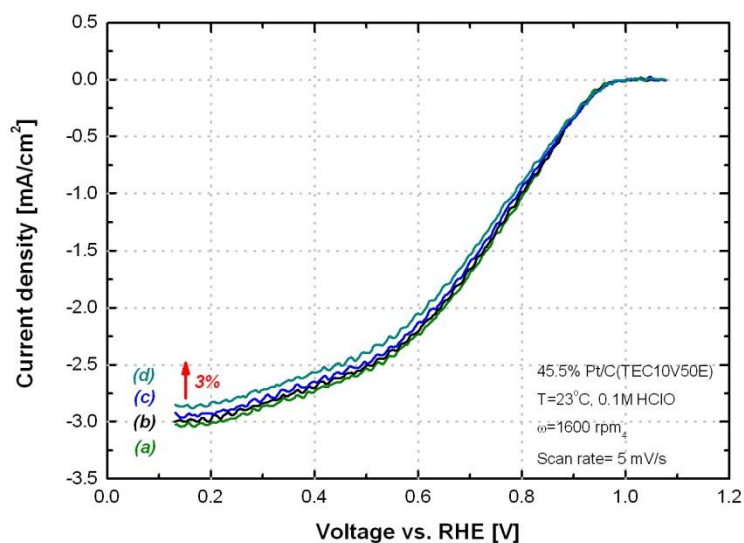
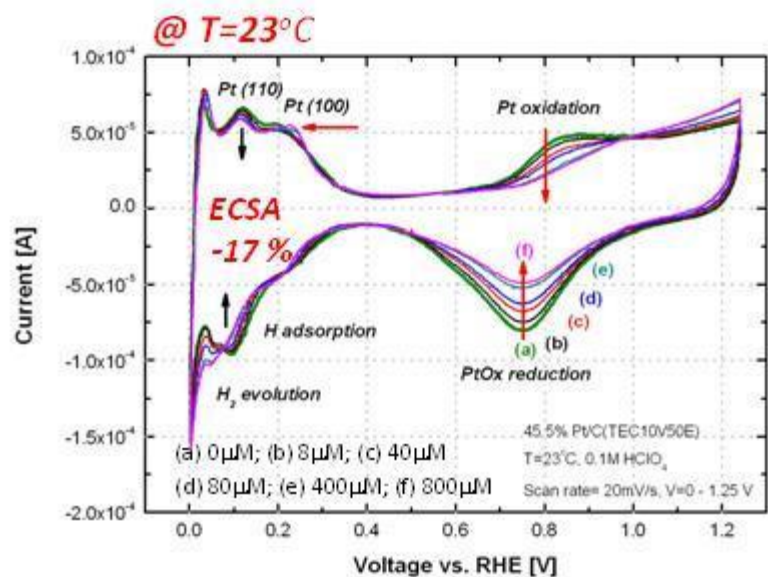
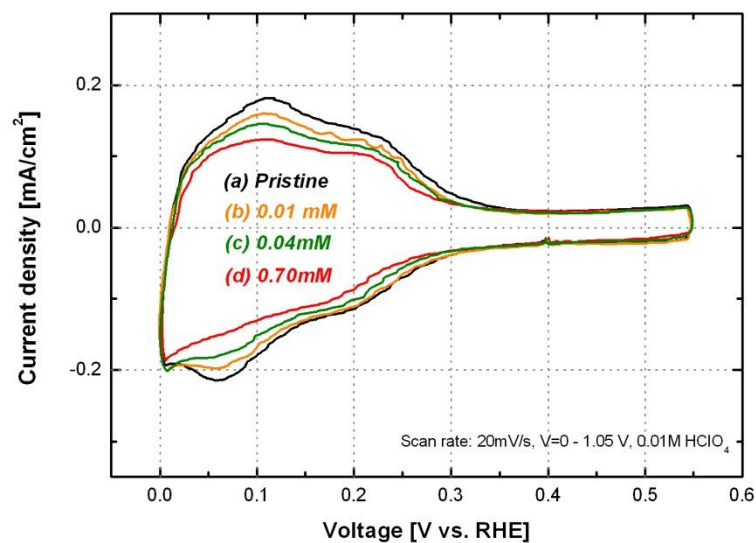


Figure 6.7 ORR kinetic current density and Tafel slopes of 45.5% Pt/C catalyst as concentration of ϵ -caprolactam is increasing; ORR at pH=1; a) 0 b) 8 μ M c) 80 μ M d) 0.4mM



a)



b)

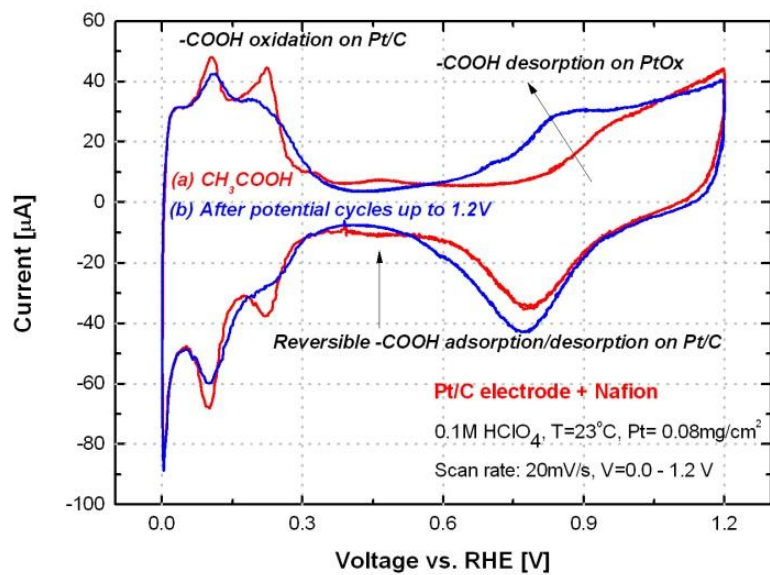
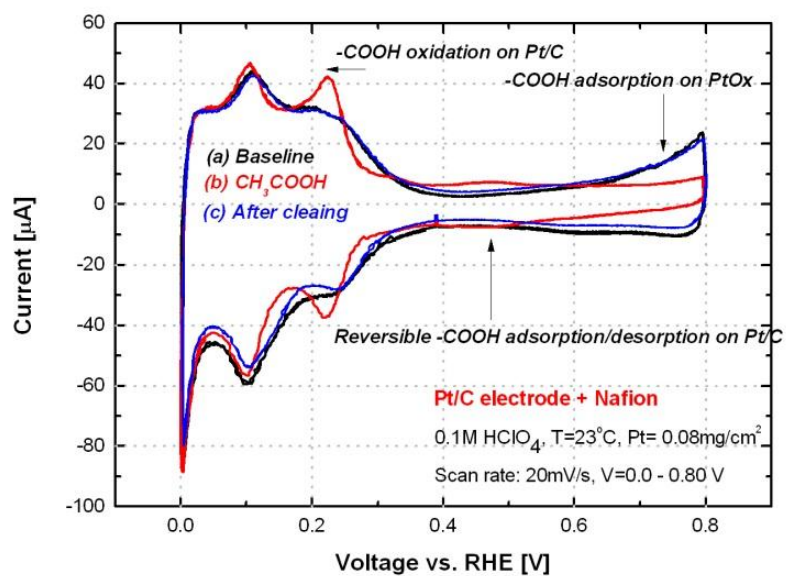
Figure 6.8 pH effect on ECSA loss of Pt/C electrode in the presence of ϵ -caprolactam at T=23°C (a) pH=1 (b) pH=2

changed less than 5% by adding 5000ML (0.4mM) of ϵ -caprolactam into electrolyte. Again, the contamination effect on ORR by ϵ -caprolactam may be significant at higher pH likewise CV results. In sum, the open ring structure of ϵ -caprolactam from the acid-catalyzed hydrolysis can lead the loss of Pt activity due to the adsorption of carboxylate anion ($-\text{COO}^-$). Their impact also depends on the pH. Likewise the conductivity loss by the open ring reaction of ϵ -caprolactam, the temperature impacts on Pt contamination are also shown.

6.3.3 THE STUDY OF FUNCTIONAL GROUPS EFFECT OF ϵ -CAPROLACTAM ON Pt/C

To understand the effect of ϵ -amino caproic acid on Pt/C electrode based on functional groups, we studied two model chemicals, which have same functional group, on Pt/C electrode; ammonia (NH_3) and acetic acid (CH_3COOH) to represent amide ($-\text{NH}_2$) group and carboxylic acid group of ϵ -amino caproic acid. The CVs data in Figure 6.9 showed a redox peak at 0.25V vs. RHE after acetic acid solution was introduced into the RDE system, while the hydrogen adsorption peak of Pt/C electrode reduced. (ECSA loss was less than 10%). This CV result indicates that carboxylic acid groups can adsorb on the surface of Pt/C electrode and electro-organic oxidation can be possible with the aid of a Pt/C catalyst at 0.25V vs. RHE (compared Figures 6.6 and 6.9). These redox couples may be an evidence of carboxylic acid adsorption on Pt since the acid itself cannot be oxidized at this relative low potential (0.25V vs. RHE), and consequently, the carboxylic acid oxidation must be aid by catalyst. Hence, the carboxylic acid adsorption is more possible on a Pt surface. Likewise the loss of ECSA for hydrogen adsorption on Pt, Pt oxidation and PtOx reduction peak is reduced with the carboxylic acid adsorption on their

surface however, it could be mostly recovered after cleaning by a clean electrolyte or potential cycles up to 1.20V vs. RHE. We can conclude that the oxidation peak shown in Figure 6.6 with ϵ -caprolactam was consistent with following mechanisms: the carboxylic acid adsorption and electro-organic oxidation on Pt to produce a proton ($-\text{COOH} + \text{Pt} \rightarrow -\text{COO-Pt} + \text{H}^+ + \text{e}^-$) after acid-catalyzed hydrolysis of ϵ -caprolactam. The CV data with exposure of ammonia gas into RDE system showed that ammonium (NH_4^+) interaction with acid sites of Nafion[®] ionomer in Pt/C electrode thus, the structural change of Nafion[®] ionomer and the loss of proton conductivity may cause of the loss of ECSA by ammonium (NH_4^+) contamination. The CV of Nafion[®] coated on Pt/C electrode for ammonia exposure showed the 20% loss of ECSA for hydrogen adsorption/desorption with 5000ML of ammonia gas exposure. Note that there was no more loss of ECSA after fully saturated the electrolyte with ammonia gas ($\approx 10^5 \text{ML}$). No more loss of ECSA for Pt/C electrode indicated that ammonium (NH_4^+) replaced proton sites of Nafion[®] ionomer in Pt/C electrode so that “blockage secondary effect” of proton pathway may happen, otherwise other electrochemical interaction between the Pt/C catalyst and ammonia were not observed in this CV result. Thus, the “blockage effect” of ammonium in Nafion[®] ionomer comes to the result of ECSA loss. Furthermore, ECSA was fully recovered after cleaning the Pt/C electrode with potential cycles up to 1.2V vs. RHE in clean 0.1M HClO_4 electrolyte. Thus, summarizing the information described in this section on acetic acid and ammonia CV studies, we can conclude that amine group of ϵ -amino caproic acid affected the activity of Pt/C catalyst by ion-exchange reaction with Nafion[®] ionomer and carboxylic acid ($-\text{COOH}$) group of ϵ -amino caproic acid directly affect the loss of ECSA due to the adsorption and electro-organic oxidation depends on pH of system.



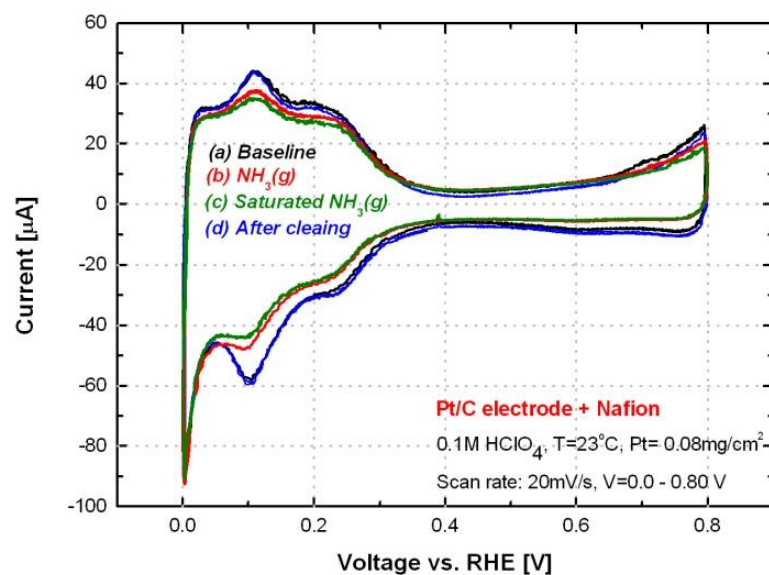


Figure 6.9 a) CV of Nafion[®] coated on Pt/C electrode (a) pristine (b) CH_3COOH (c) After potential cycles up to 1.2V with clean electrolyte b) (a) pristine (b) 5000ML $\text{NH}_3(\text{g})$ (c) saturated $\text{NH}_3(\text{g})$ (d) after potential cycles to 1.2V in clean 0.1M HClO_4

6.3.4 THE ATR-IR STUDY OF NAFION[®] MEMBRANE

ϵ -caprolactam absorbed Nafion[®] membrane showed the shift of SO_3^- stretching peak at 983 cm^{-1} due to electrostatic interaction of protonated amine group and sulfonic group. This behavior attributed to decrease polarization of the sulfonic group (SO_3^-) by protonated ϵ -caprolactam or ϵ -amino caproic acid [121-126]. Wavelength $1600\text{--}1700\text{ cm}^{-1}$ region showed broad overlapped C=O stretching peaks of ketone ($1750\text{--}1680\text{ cm}^{-1}$), carboxylic acid ($1780\text{--}1710\text{ cm}^{-1}$), amide ($1670\text{--}1650\text{ cm}^{-1}$), and asymmetric carbonyl vibration (1655 cm^{-1}) to represent protonated ϵ -caprolactam or ϵ -amino caproic acid. Note that the spectra of aliphatic long-chain carboxylic acid exhibited bands in the range $1345 - 1180\text{ cm}^{-1}$ and the number of weak bands was related to the length of the chain [126]. Three peaks showed in ϵ -caprolactam absorbed Nafion[®] membrane ($1300\text{--}1100\text{ cm}^{-1}$) which represents 6 carbon atoms of aliphatic ϵ -amino carboxylic acid. For acids with an even number of carbon atoms, the number of bands observed equals half the number of carbon atoms (ϵ -amino caproic acid = 6 carbon, 3 weak peaks) [121-126]. Thus, the ATR-IR analysis confirmed that the protonated ϵ -amino caprolactam and ϵ -amino caproic acid were existed in Nafion[®] membrane by electrostatic interaction (ion-exchange) with acid sites.

ATR-IR spectrums of ϵ -caprolactam (line (a) in Figure 6.10b), ϵ -amino caproic acid (line (b) in Figure 6.10b) solutions dissolved in methanol and ϵ -caprolactam (line (d) in Figure 6.10b), ϵ -amino caproic acid (line (c) in Figure 6.10b) extract solutions out of

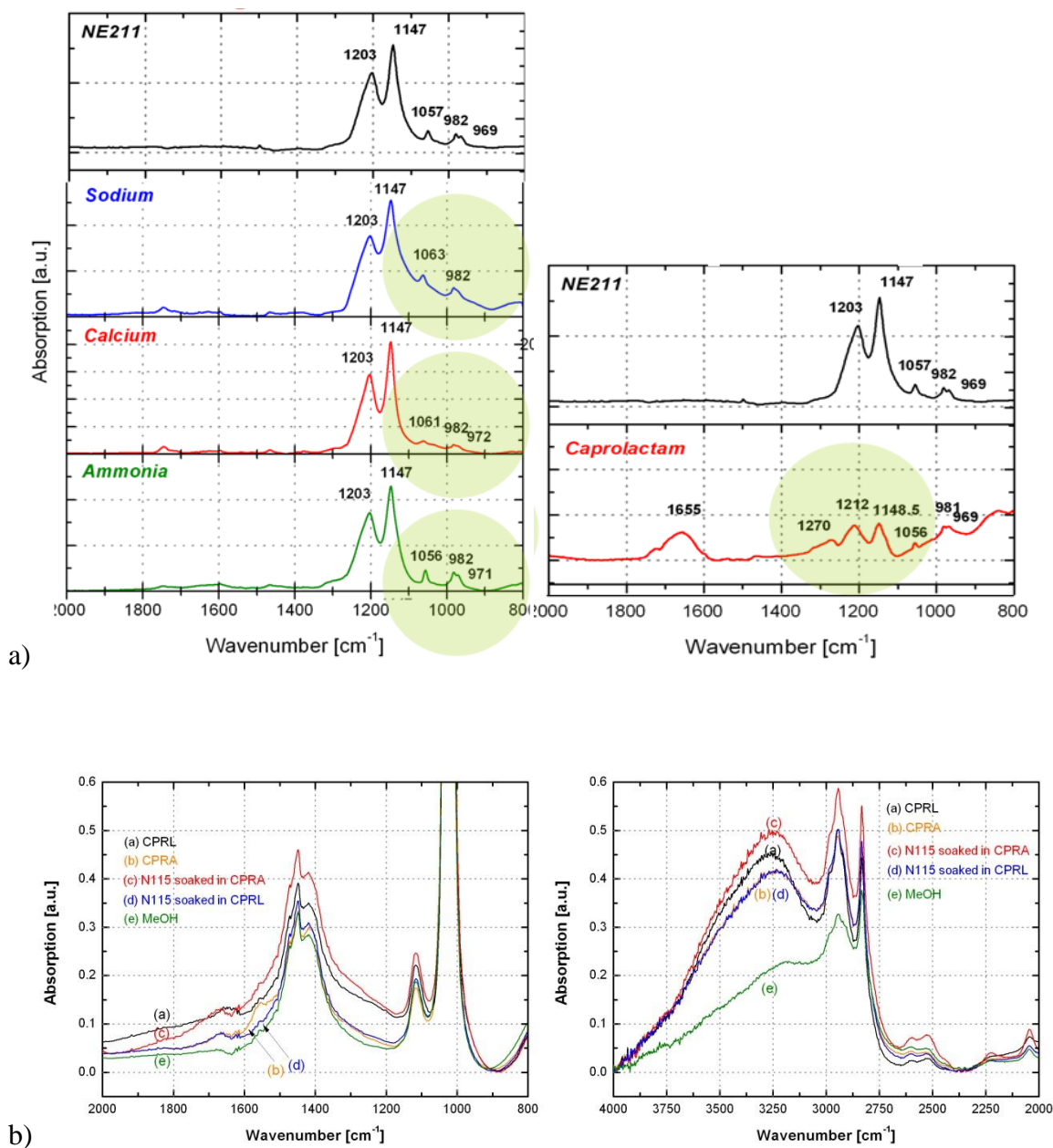


Figure 6.10 a) ATR-IR analysis of various exchanged form of Nafion[®] b) ATR-IR analysis of methanol solutions (a) ϵ -caprolactam (b) ϵ -amino caproic acid (c) extract solution of ϵ -caprolactam out of N115 (d) extract solution of ϵ -amino caproic acid out of N115 (e) methanol

Table 6.4 Assignments of ATR-IR peaks of ϵ -caprolactam exchanged form Nafion[®]

Assignments	Peak for each Nafion [®] form [cm ⁻¹]		Remark
	Pristine	ϵ -caprolactam	
Symmetric C-O-C stretching vibration	969	969 (w)	
Asymmetric C-O-C stretching vibration	982	981	
Symmetric -SO ₃ ⁻ stretching	1057	1056	
Asymmetric carbonyl vibration	-	1655	
Symmetric CF ₂ band	1147	1149	
Asymmetric CF ₂ band	1203	1212	
Keton C=O stretching	1750 – 1680		
Carboxylic acid C=O stretching	1780 – 1710		
Primary amide C=O stretching	1670 – 1650		
Alkyl C-H stretching	2950 – 2850		
Primary aliphatic amide deformation vibration	850 – 810		
	2960 – 2900		Asym CH ₂ str.
	2920 – 2800		Sym CH ₂ str.
-CH ₂ NH ₃ ⁺ , N-H ⁺ deformation and vibration	1635 – 1585, 1615 – 1565		Asym NH ₃ ⁺ def vib.
	1520 – 1480		Sym NH ₃ ⁺ def vib.
	1280 – 1150, 1135 – 1005, 1100 – 930		NH ₃ ⁺ rocking vib., CN str vib.
Aliphatic long-chain carboxylic acids (-COOH)	1345 – 1180		In the solid phase, CH ₂ def. vib., number of bands determined by aliphatic chain length

N115 with methanol were also compared to confirm the chemical structure of ϵ -caprolactam in Nafion[®] membrane whether the ring structure of amide bond of ϵ -caprolactam opened or closed. Broad peak showed 3750-3200 cm^{-1} of the region which superimposed many possible band peaks such as the symmetry and asymmetry amine N-H stretching bands, the amide N-H stretching, the O-H stretching vibration, the C-H stretching vibration of carboxylic acid etc. They showed for all samples (lines (a) through (d) in Figure 6.10b) except methanol peak (line (e) in Figure 6.10b) which indicated the absorption of ϵ -caprolactam and ϵ -amino caproic acid. In the region 1650-1630 cm^{-1} , the ϵ -caprolactam solution dissolved in methanol (line (a) in Figure 6.10b) have the N-H and C=O stretching vibration peak. The shift of band peaks to the 1690 - 1655 cm^{-1} gave rise to solutions (line (b), (c), (d) in Figure 6.10b) which exhibited the C=O stretching vibration of carboxylic acid. Again, it is note that the peak shift in the region of 1690 – 1630 cm^{-1} showed all sample solutions (line (b), (c), (d) in Figure 6.10b) except ϵ -caprolactam solution in methanol (line (a) in Figure 6.10b). We believe that the peak shift in the region of 1690 – 1630 cm^{-1} in Figure 6.10b may support the absorption of the ϵ -caprolactam into Nafion[®] membrane as the open ring structure which is the ϵ -amino caproic acid due to the acid-catalyzed hydrolysis (recall that the schematic of open ring hydrolysis showed in Figure 6.3). The protonation of amine group of ϵ -amino caproic acid electro-statically could interact with sulfonic group in Nafion[®] membrane.

6.3.5 *IN-SITU* RESPONSE OF ϵ -CAPROLACTAM CONTAMINATION

Figure 6.11 shows that *in-situ* voltage (iR corrected) responses for caprolactam infusion at different temperatures. The voltage recorded at constant current density

($0.2\text{A}/\text{cm}^2$) at different temperatures 50 and 80°C but same $\text{RH} = 50\%$. The voltage and HFR was normalized with each baseline to compare with different temperatures. As shown in Figure 6.12, the water contents in Nafion[®] membrane could change at different temperatures even though they contained at same RH condition ($>50\%$). Thus, we chose $\text{RH}=50\%$ to control the same water contents in Nafion[®] membrane. The constant current density expected to produce same amounts of water in a single cell. More inlet water can be expected at a high temperature (80°C) so as to rinse contamination more. However, the voltage drop at high temperature (80°C) showed more in more water produced system (line (b) in Figure 6.11). Therefore, we could ignore the rinsing effect of the contaminant by water. Actually the more water generation in a single cell may lead greater performance losses with ϵ -caprolactam. Recall the acid-catalyzed hydrolysis of ϵ -caprolactam. The open ring reaction happened in the presence of water in acid condition (normally pH in PEMFC estimated around 3 to 4) at a higher temperature (80°C). The HFR was increased 2 times more at 80°C than 50°C and the voltage also dropped more (0.7 compared to a pristine single cell) at the same molar feeds of ϵ -caprolactam into the cell. ECSA loss was measured as -67% (i.e., 43.5 to $11.9\text{ m}^2/\text{g}_{\text{Pt}}$ at 80°C) at the total

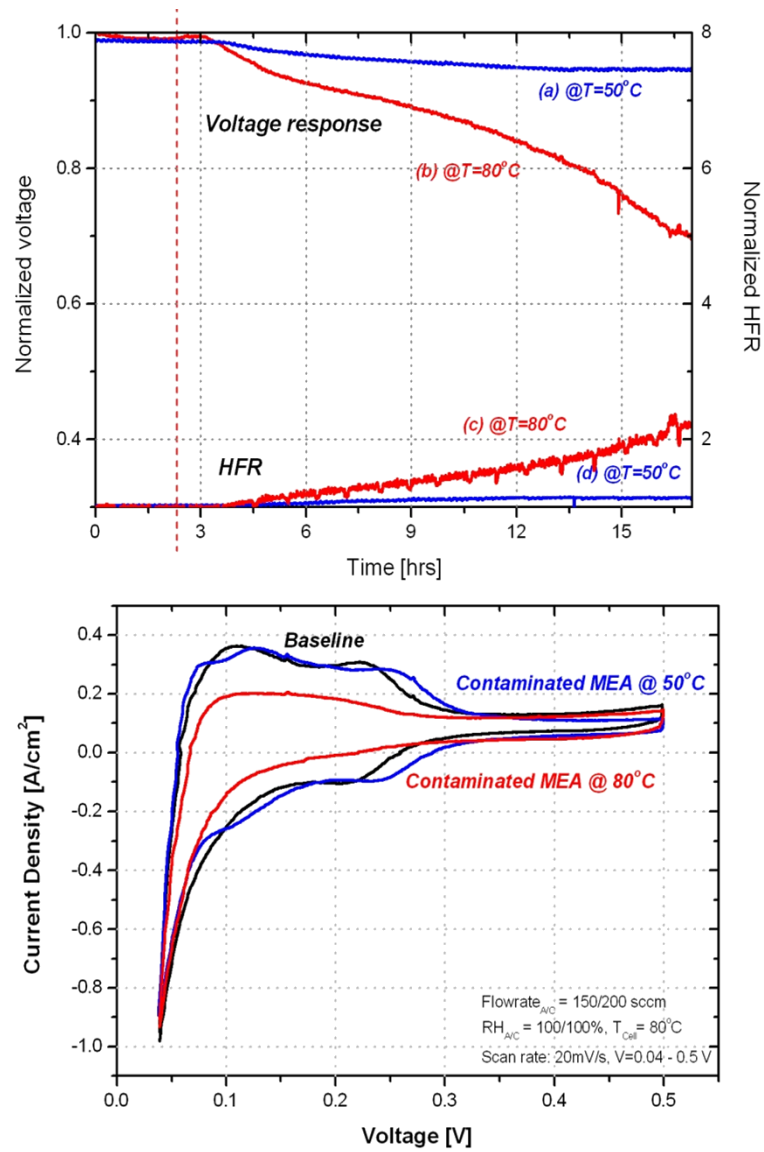


Figure 6.11 *in-situ* response for ϵ -caprolactam at different temperatures on a single cell in PEMFCs (a) voltage response (a) $T=50^\circ\text{C}$ (b) $T=80^\circ\text{C}$ (b) CV graphs (a) $T=50^\circ\text{C}$ (b) $T=80^\circ\text{C}$

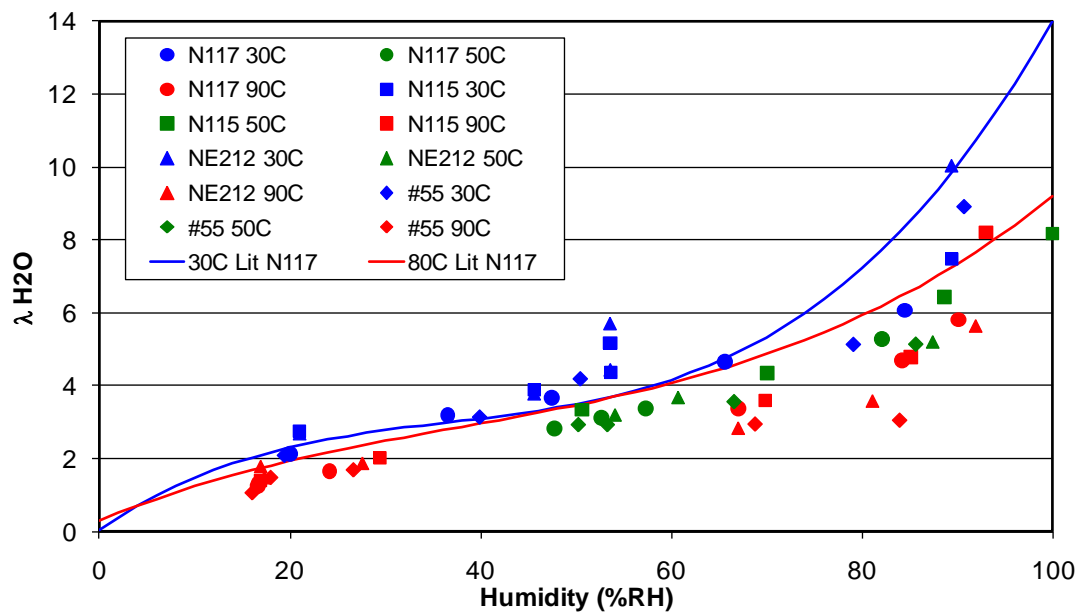


Figure 6.12 Hydration of Nafion® membrane at various temperatures and humidity [128-129]

feeds is equal to 140 μmol which is 50% compared to IEC (270 μmol) of MEA. However, if we considered the partition coefficient between ϵ -caprolactam and the proton in the system based on isotherm curves of Nafion[®] in Figure 6.5, we can estimate 30% of IEC of Nafion[®] filled up with the protonated ϵ -caprolactam or ϵ -amino caproic acid at 80 °C since the molar ratio of ϵ -caprolactam in the solution is close to 0.01 - 0.1 considering feed rate of 11 mmol/hr of ϵ -caprolactam.

Interestingly, in-situ CV results showed greater ECSA loss compared to the loss from the ex-situ CV. The pH dependency on ECSA loss can supports this deviation between *ex-situ* RDE and *in-situ*. Also, gas and liquid phase, GDL, inert gas and air with contaminant may also be considered for differences.

6.4 CONCLUSION

In this chapter, the contamination impacts from ϵ -caprolactam are investigated. on PEMFC based on fundamental contamination mechanisms. The ion-exchange isotherms shows higher affinity to PEM but it also showed the dependency on the temperature. The membrane conductivity (σ) data also supports the temperature effect. At 70-90 °C, it has been confirmed that ϵ -caprolactam absorbed more into Nafion[®] membrane than room temperature. The possible explanation is endothermic open ring reaction of ϵ -caprolactam from acid-catalyzed hydrolysis of amide bond. The ion-exchange reaction of ϵ -caprolactam may occur in the Nafion[®] membrane as well as ionomer in the electrode which reduced the number of available acid sites.

The ECSA loss is more significant on Pt crystalline electrode than Pt/C electrode. The loss of ECSA and the ORR kinetic current density on a Pt/C electrode also depends

on pH of system due to the pKa of carboxylic acid group of ϵ -caproic acid. Nevertheless, it affects the peaks associated with the Pt oxidation and PtOx reduction reactions and tends to decrease these reactions. Oxidation shoulder peak observed around 0.25V vs. RHE consisted with carboxylic acid ($-\text{COOH}$) adsorption and electro-oxidation to produce a carboxylate and a proton. The ϵ -caprolactam effect on electrode is more severe for in-situ than ex-situ, which may be supported by the dissociation of carboxylate anion ($-\text{COO}^-$) from carboxylic acid ($-\text{COOH}$) at lower pH.

In-situ voltage responses for ϵ -caprolactam contamination also show the temperature effect (e.g, higher temperature condition showed greater voltage losses).

CHAPTER 7

ABSORPTION BEHAVIOR OF VANADIUM IN NAFION[®] MEMBRANE

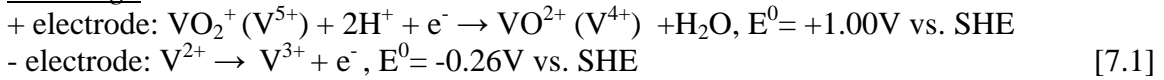
In this chapter, The absorption behavior of vanadium in Nafion[®] was investigated through ex-situ isotherm and conductivity measurements at 23 °C. The data show a maximum of 30% loss of IEC for all four oxidation state of vanadium. The affinity of vanadium to N115 as measured by back titration and AA and characterized by isotherms at 23 °C is highest for the divalent and lowest for the pentavalent species:s $VO_2^+ (V^{5+}) < VO^{2+} (V^{4+}) < V^{3+} < V^{2+}$. Steric hindrance of the associated water complex may explain the lower absorption compared to alkali metals. The conductivity for a VO_2^+ (minimum affinity) exchanged membrane was two to three times lower than a sodium-exchange membrane at RH=100%. Supporting raw data for vanadium absorption measured by AA and ICP are shown in Appendix E.

7.1 INTRODUCTION

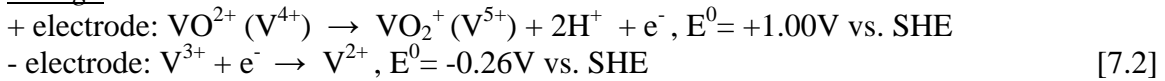
The vanadium redox flow battery (VRFB) has been regarded as the one of the promising large scale energy storage systems. The active species, V^{2+}/V^{3+} and V^{4+}/V^{5+} , are used for negative and positive electrolyte, respectively in 2- 5 M H_2SO_4 solutions in the VRFB applications. The redox reactions during the charge and discharge of a VRFB are shown in Equations 1 and 2 below. As in most flow batteries, the optimum separator

in VRFB would minimize ohmic losses (i.e. maximum conductivity) while preventing cross-over between negative and positive electrolytes which decreases the open circuit voltage, increase coulombic losses and causes a mix-potential to reduce performance of VRFB (self-discharge) [130-135]. In this chapter we present data that show how the conductivity of one separator, Nafion[®], is affected by concentrations of vanadium species.

Discharge



Charge



Nafion[®], a perfluorinated membrane which has sulfonic acid moiety as an end group, has been used as a separator for the proton exchange membrane fuel cells (PEMFCs), and in the Na⁺ form as separator for Cl₂/NaOH electrolysis. It has been proposed for VRFB applications to fulfill of requirements such as proton conductivity at high hydration, low permeability, and good mechanical, thermal, and chemical resistivity. Based on Nafion[®]'s ability to exchange cations, discussed below, it may be hypothesized that its conductivity could change upon exposure to the various valence states of vanadium ions. The purpose of this paper is to present data for isotherms and conductivity of when exposed to vanadium solutions in an effort to quantify this hypothesis.

According to the contamination studies in PEMFCs, metal cations showed higher affinity to the sulfonic acid sites of Nafion[®] membrane than protons [136-139]. Metal cations can replace acid proton sites via an ion-exchange reaction resulting in

conductivity and performance loss. However, many electrolytes used in flow battery systems are include transition metal cations in strong acid solutions. Relatively few studies have been considered ion exchange behavior for Nafion[®] membrane with transition metals. For transition metals, Kelly et al., [138-139] reported the absorption Ni^{2+} , Cu^{2+} , and Fe^{3+} and the corresponding conductivity loss of a N117 membrane but isotherms were not presented. Li et al., [141] studied *in-situ* a single cell PEMFC with Co^{2+} contamination resulting from the bimetallic catalyst. Also, a few studies [143-149] for vanadium ion were conducted for the purpose of checking the durability of a Nafion[®] membrane with metrics of membrane resistance change, ion exchange capacity (IEC) change, and vanadium ion diffusivity change [143-149]. Here we expand the data for the four valences of vanadium by presenting and comparing these isotherms with those of Na^+ and Ca^{2+} . The data is most useful at RH=100% for flow batteries and at RH<100% for gas phase batteries or PEMFCs.

7.2 EXPERIMENTAL

7.2.1 MEMBRANE ISOTHERMS FOR VANADIUM

As received VCl_2 (s), V_2O_3 (s), VO_2SO_4 (aq), and V_2O_5 (s) were used for preparation of each vanadium ion solution by mixing with deaerated Ar gas purge in 2-5M sulfuric acid solutions at room temperature. The pH of the solutions was adjusted by changing the H_2SO_4 concentration to maintain the thermodynamic stable state: VO_2^+ ($\text{pH} \leq 1.45$), VO^{2+} ($\text{pH} \leq 4.97$), V^{3+} ($\text{pH} \leq 2.92$), V^{2+} ($\text{pH} \leq 2.92$). These pH values were obtained by consulting Ref. 147-149 for the predominance diagrams of dissolved species in the V- H_2O system. Several mixtures of sulfuric acid solutions and vanadium solutions were

prepared with the different molar ratios for the measurement of the absorption isotherm in a N115 at 23°C. The concentrations and pH of V_2O_5 , $VOSO_4$, V_2O_3 , VCl_2 and H_2SO_4 are shown in Appendix E.

The isotherm experiments included a pretreatment of the membrane, followed by immersion of the membrane in vanadium solution of interest, followed by extract of the vanadium from the membrane, and followed with digestion of the membrane to access the efficiency of extraction.

The isotherm experiments included a pretreatment of the membrane, followed by immersion of the membrane in vanadium solution of interest, followed by extract of the vanadium from the membrane, and followed with digestion of the membrane to access the efficiency of extraction. A pretreatment procedure used one piece of a dry N115 ($3.0 \times 3.0 \text{ cm}^2$) which was weighed prior to calculating the IEC and which was then boiled in 2M H_2SO_4 for 1hr followed by storage in DI water. The pretreated N115s were immersed in each of the mixtures in Table E1 and magnetic stirrer plates were used for mixing for 48 h to allow equilibrium conditions of the absorption/ion-exchange reaction between the vanadium cations and the proton form of the membrane. Solution concentrations before and after the immersion are measured as discussed below. To confirm the amount of vanadium exchanged, the membranes were placed in 2M H_2SO_4 to extract the previously exchanged vanadium. Finally after extraction, the membranes were digested with 10ml of a concentrated 1:1 mixture of HCl and HNO_3 under 900W in a microwave for 2 min.

The concentration of vanadium ions in the solutions used for immersion was measured with an atomic absorption spectrometry (AA) and a UV-vis. spectrophotometer.

For the UV-vis., 250nm wavelength was chosen for quantification of vanadium ions. The calibration curve for the UV-vis. measurement was linear with intensity at 250nm for the concentration of vanadium solutions at 0.05 to 5mM region with an accuracy of $\geq \pm 0.05\text{mM}$. The purpose of digestion was to confirm that there were no residual vanadium ions in the Nafion[®] membrane after acid extraction. The digested solutions were analyzed by ion chromatography inductively coupled plasma (ICP) and all reported data showed residual vanadium of less than 0.03 ppm in the digested solutions.

7.2.2 MEMBRANE CONDUCTIVITY MEASUREMENT

For the conductivity measurements, NE 211 was used to minimize the time to reach equilibrium. Membrane conductivities for pristine and vanadium absorbed^{*} NRE211s were determined at ten values of constant relative humidity (RH) (i.e., 10, 20, 30, 40, 50, 60, 70, 80, 90, 95%) by applying DC currents at the cell temperature of 80°C. The potentiostat (model PAR273) was used with a four-probe conductivity Teflon-based cell (model BT-112) made by Beckktech, LLC. The cell is equilibrated with a 300 sccm flow of N₂ at T_{cell}=80°C and RH =90% for 1 hour used a Scribner 890E PEMFC test station that was calibrated for both flow and humidity. The humidity was changed from low (20%) RH to high (95%) RH while the membrane conductivity was measured with a hold of 30 min for each RH to assure equilibrium conditions. A VAISALA dew point chamber was attached at the outlet of the conductivity cell to confirm dew point temperature of the exiting gases relative to those set by the test station.

^{*} We use 'absorbed' interchangeably with 'partial ion exchange' to describe the uptake of vanadium. Note that measurement of % exchanged did not change during the conductivity measurement.

We verified that the degree of absorption did not change during the conductivity measurements by digestion as described above.

7.3 RESULTS AND DISCUSSION

7.3.1 THE ABSORPTION ISOTHERMS OF VANADIUM ION INTO NAFION[®] MEMBRANE

Figure 7.1 shows absorption isotherms of N115 for different oxidation states of vanadium ions at room temperature. The results show that over all the range of vanadium ions, the exchange was 5 – 32% of the acid sites in N115. The number of acid sites was measured with batch titration methods to Na⁺ (e.g., 0.98 ± 0.05 $\mu\text{mol/g}$) [151]. The maximum exchange ratio for each vanadium ions is $\text{VO}_2^+ = 3\%$, $\text{VO}^{2+} = 12\%$, $\text{V}^{3+} = 29\%$, and $\text{V}^{2+} = 34\%$ respectively to IEC. That is for example, the IEC for N115 VO^{2+} was 0.15 ± 0.05 mmol/g as measured by extraction described above and that of measured with Na⁺ was 0.98 ± 0.05 mmol/g. Note that the affinity of vanadium ions for Nafion[®] is more for the lower valence than for the higher valence. That is, the isotherms showed greater affinity to N115 as the reverse order of valences of vanadium ions: $\text{VO}_2^+ (\text{V}^{5+}) < \text{VO}^{2+} (\text{V}^{4+}) < \text{V}^{3+} < \text{V}^{2+}$. This affinity is an initial measurement and may change with change over extended times (i.e. weeks) as described in Ref. 143 and 144 for the immersion of Nafion[®], Gore Select, and Selemion in 0.1M $\text{VO}_2^+ (\text{V}^{5+})$. All results here were obtained after 2 days soaking of N115 in the mixture of vanadium and sulfuric acid solution.

The contrast between sodium and vanadium ion exchange could be a result of the Donnan equilibrium potential [150], which explains an electric potential difference between the membrane and solution. This perspective would argue that concentration in VRFB (i.e., 2-5M electrolyte) precluded or minimized the ion exchange or absorption of

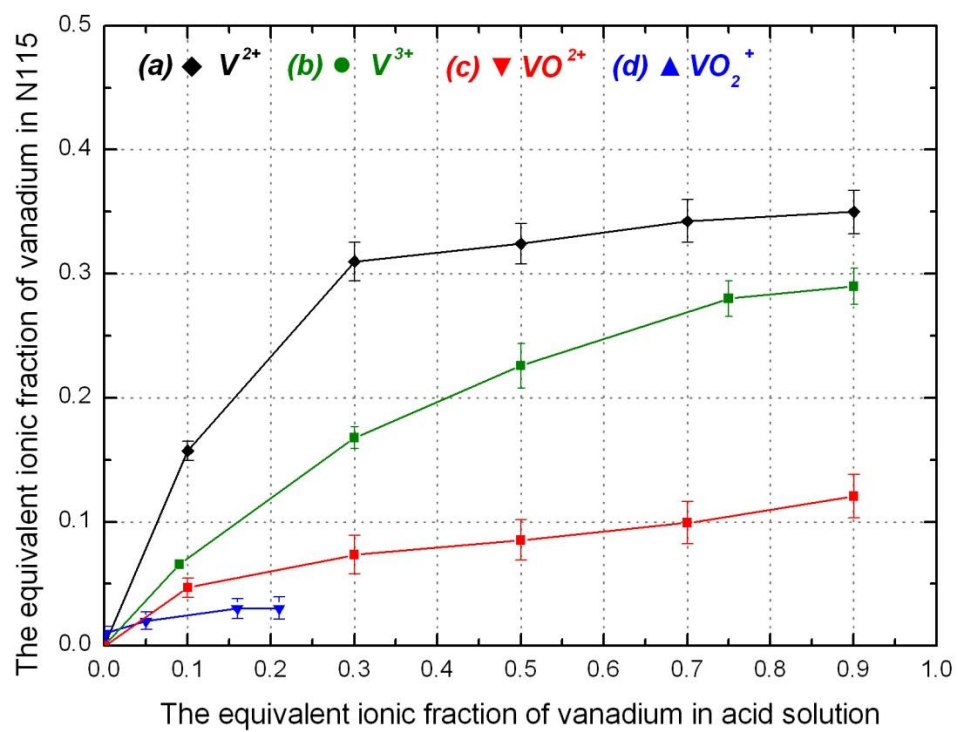


Figure 7.1 Absorption isotherm curves of vanadium ions for Nafion®

vanadium ions in the Nafion[®]. Thus, higher concentrations of vanadium would have less of a maximum % exchange. This concentration effect (i.e., increases the exclusion of electrolyte with an increase of external solution concentration) was not observed for V³⁺ as shown in Figure 7.3a. The Donnan potential effect on an ion is proportional to the ionic charge number so that the higher valence cation (i.e., V⁵⁺) is more strongly repulsed by the membrane. For example with alkali metals, the Ca²⁺ isotherm curves for Nafion[®] decreased as concentrations increased and this is in contrast to the Na⁺ isotherm curves as shown in Figure 7.3b [151]. Thus, higher concentrations of vanadium solution used in this experiment (up to 3.6M shown in Appendix E) compared Na⁺ solution (0.1M) in this experiment may increase the Donnan potential between membrane and vanadium solution. The Donnan potential effect on vanadium ions may also explain the order of affinities of vanadium ions to Nafion[®]. Figure 2a shows that the affinity for N115 was observed: V³⁺ (2M H₂SO₄) < V³⁺ (0.1M H₂SO₄) < V³⁺ (0.05M H₂SO₄) but this is not a significant change. Also, the maximum % exchanges for V³⁺ at different concentration were equal to about 0.3.

The lower % of exchange by vanadium may also be explained by a sieve or steric effect. Thus, the size of the complex would affect the % exchange by vanadium. We would expect a change in size since transition metals form covalent bonds with water in aqueous solutions [152-153]. The lone electron pairs of water molecules are shared with empty 3d, 4s, and 4p orbitals of the transition metal. The hydrolysis products of vanadium ions in acid solution are listed in Table 7.2 which shows the aqueous vanadium ions exist as hexagonal oriented in an octahedral shape in acid [153-154]. These ligands must associate with hydrophilic ionic clusters (ca. 5nm dia.) water channels in a Nafion[®]

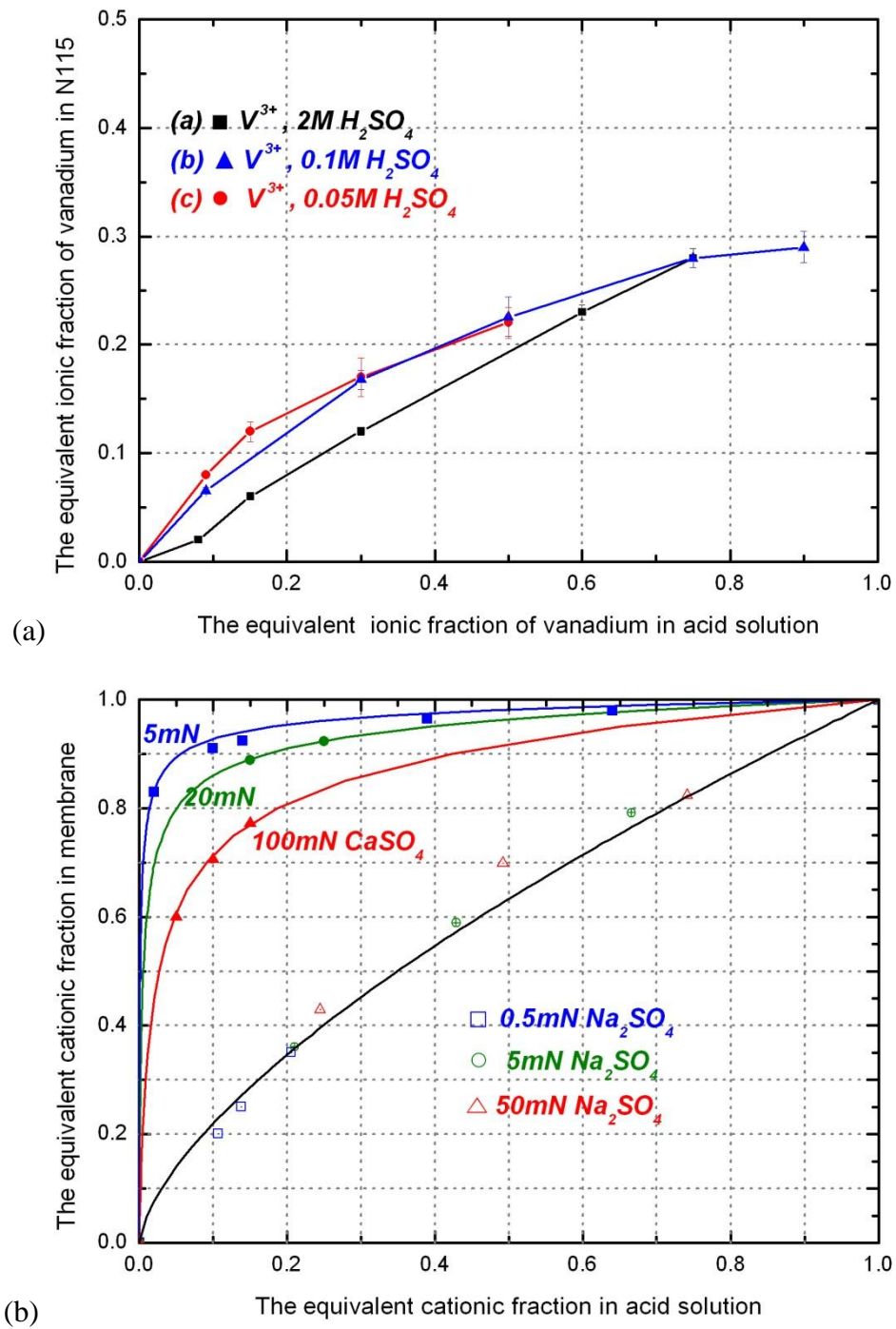


Figure 7.2 Comparison of absorption isotherm curves of Nafion[®] with (a) VO^{2+} in different concentration of H_2SO_4 solutions compared to (b) Na^+ and Ca^{2+}

Table 7.1 Vanadium ion form in acid solution (octahedral shape)

Vanadium	Hydrolysis product	Remark
V^{2+}	$[V(H_2O)_6]^{2+}$	Black, inert, slow kinetics
V^{3+}	$[V(H_2O)_6]^{3+}$	Black, blue aqua ion
VO^{2+}	$[VO(H_2O)_4]^{2+}$, $[VO(H_2O)_5]^{2+}$	Blue aqua ion
VO_2^+	$[VO_2(H_2O)_4]^+$	Pale yellow, colloidal materials

Table 7.2. Comparison of absorption isotherm curves of Nafion[®] with VO^{2+} in different concentration of H_2SO_4 solutions

V^{3+} in H_2SO_4					
0.05M H_2SO_4		0.1M H_2SO_4		2M H_2SO_4	
X in solution	X in N115	X in solution	X in N115	X in solution	X in N115
0.00	0.00	0.00	0.00	0.00	0.00
0.09	0.08	0.09	0.07	0.08	0.02
0.15	0.12	0.30	0.17	0.15	0.06
0.30	0.17	0.50	0.23	0.30	0.12
0.50	0.22	0.75	0.28	0.60	0.23
		0.90	0.29	0.75	0.28

X: The equivalent ionic fraction of vanadium (vanadium vs. proton)

membrane which were reported to be 1nm as measured through small angle X-ray spectrometer (SAXS) analysis [155]. Thus, the size exclusion or a sieve effect can occur for the vanadium hydrolysis complex and these support the smaller % of absorption for vanadium observed in Figure 7.1.

7.3.2 THE EX-SITU MEMBRANE CONDUCTIVITY MEASUREMENT

Figure 7.3 compare the conductivity for VO^{2+} and V^{3+} with Na^+ and Ca^{2+} absorbed (or exchanged) in NRE 211. It is interesting that although the % absorbed for V^{3+} (i.e., 21%) is less than that of Ca^{2+} (i.e., 60%), the conductivities are approximately the one order of magnitude for $40\% < \text{RH} < 93\%$.

Similarity for the conductivity for Na^+ and VO_2^+ are the same order of magnitude even though the Na^+ occupies many more sites than the VO_2^+ (i.e., compare 100% and 12% respectively). This high conductivity loss for less % exchanged is probably attributed to the formation of vanadium-water complex ion. In addition, the large size of complex ions may be accompanied by the water exclusion of Nafion[®] membrane. This has been shown for alkali metal cations with the comparison of sodium (smaller radius, larger hydrated radius) and potassium (larger radius, smaller hydrated radius) exchanged Nafion[®] membranes also showed the size effect on conductivity loss. The greater conductivity loss for potassium-exchange membrane was observed [153].

The *ex-situ* membrane data obtained here are for equilibrium between the membrane and water vapor. Thus, the data for $\text{RH} < 95\%$, it may useful for gas phase batteries or PEMFCs. Note that we extrapolated each conductivity data to $\text{RH} = 100\%$

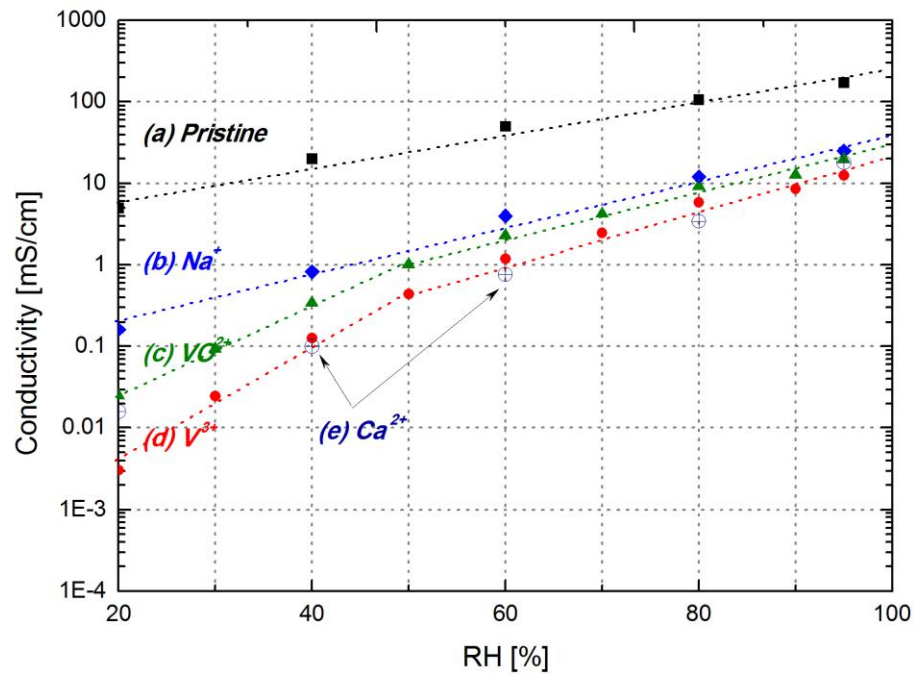


Figure 7.3 Comparison of membrane conductivity of Nafion[®] with VO²⁺, V³⁺, Na⁺ and Ca²⁺

Table 3 Comparison of membrane conductivity of N115 with VO^{2+} , V^{3+} , Na^+ , and Ca^{2+}

Pristine		Na^+ (99%)		Ca^{2+} (40%)		V^{3+} (21%)		VO^{2+} (12%)	
RH [%]	σ [mS/cm]	RH [%]	σ [mS/cm]	RH [%]	σ [mS/cm]	RH [%]	σ [mS/cm]	RH [%]	σ [mS/cm]
22	7.39	22	0.16	20	0.016	22	0.00302	22	0.0252
31	14.1	30	0.537			31	0.0244	30	0.0931
41	23.7	39	0.856	40	0.1	41	0.125	39	0.343
50	36	49	2.35			50	0.437	49	1.02
61	51.9	58	5	60	0.76	61	1.18	58	2.32
68	68.2	67	7.52			68	2.47	67	4.19
82	104	80	16	80	3.4	82	5.87	80	9.22
88	130	85	21.7			88	8.47	85	12.7
93	170	92	31.3	95	18	93	12.6	92	19.8
100	*242	100	*72	100	*26	100	*20	100	*30

* Extrapolation value from a linear relation between $\log \sigma$ and RH (i.e., $\log \sigma = a\text{RH} + b$ where a and b are constants)

from 93% and it is that conductivity which will be critical for a VRFB (liquid phase). For this 100% RH extrapolated value, Table 3 shows that the 242 mS/cm membrane conductivity for the pristine NRE211 decreased an order of magnitude (i.e., 30 and 20 mS/cm) with 12% of VO^{2+} and 21% of V^{3+} exchanged NRE211s respectively.

Li et al., [141] reported that *ex-situ* membrane conductivity for Co^{2+} absorbed NRE211 decreased from 272 to 32 mS/cm at RH=100% and T=80°C which is consistent with Table 3. They assumed that NRE211 membrane was fully exchanged by Co^{2+} but they did not measure the % absorbed for Co^{2+} . Kelly et al. [138-139] also reported the loss of membrane conductivity (N117) when fully exchange with Fe^{3+} to be from 77 to 2 mS/cm. In summary, it seems reasonable to conclude that the vanadium absorption into Nafion[®] membranes leads to the significant loss of conductivity even though there is lower absorption (or exchange). Note that Kelly et.al, [138] also reported less absorption of Fe^{3+} into N117. Also, the conductivity loss is greater at same % of exchange compared to the loss by the alkali metal absorption such as Na^+ and Ca^{2+} .

7.4 CONCLUSION

In this chapter, the ion-exchange/absorption behavior of vanadium in Nafion[®] membranes and the corresponding conductivity loss were studied. The maximum loss of IEC was measured to be less than 32% for all four oxidation states of vanadium. Also, the affinity of vanadium ions to Nafion[®] showed highest affinity (32%) for lowest valence, V^{2+} and lowest affinity (3%) for highest valence, VO_2^+ (V^{5+}). The low % exchange and the valence effect can be explained by either the Donnan potential or the steric (or sieve) effect. The absorption isotherm did not change for different concentrations of V^{3+} (i.e.,

similar to Na^+) and we do not expect concentration to significantly affect these. Finally, *ex-situ* membrane conductivity for vanadium exchanged NE211s (i.e., 12% of VO^{2+} and 21% of V^{3+}) were 2-3X lower than Na^+ exchanged (i.e., $\geq 99\%$) membranes at RH=100% but close to Ca^{2+} exchanged membrane (i.e., 60%). Thus one should expect an order of magnitude loss conductivity of the membrane in a VRFB compared to pristine Nafion[®].

CHAPTER 8

CONCLUSION AND PROPOSED FUTURE WORK

8.1 CONCLUSION

Simple, 2-D and time dependent contamination model in PEMFCs which accounts for fundamental mechanisms has been developed. The three dimensionless groups, Da (contamination reaction rate), ψ (capacity ratio), and Γ (coverage ratio) are found for each contamination sources (i.e., Pt, ionomer, and membrane) from the analysis. It is also found that the contamination phenomena are governed by these three dimensionless groups. For the case of in which leaching, operating conditions, components, dimension of system and contaminants are specified, two equilibrium isotherms and one property of compound in membrane are required: adsorption, ion-exchange isotherms, and diffusion coefficient in membrane.

Theses isotherms and diffusion coefficient for selected compounds are obtained by independent ex-situ studies such as RDE, membrane conductivity, water uptake, mass uptake, and capacity measurement. Selected model compounds chose from analysis of leachate solution arising from BOP materials which may be considered as possible structural materials, assembly aids etc. in PEMFCs. Also, ex-situ studies for selected compounds leads to understand that the functional groups of compounds determine the

contamination mechanisms. Thus, design equations have been prepared for each mechanism.

8.2 PROPOSED FUTURE WORK

The simple models developed here provide a base for advanced models of a contamination in PEFMCs. Future work could begin by extending the contamination model to liquid phase contaminants. To do that, energy balance equations for species are needed. The effects of water dilution could be important by adding materials and energy balance for water. Also, the effect of the interaction between ionomer and membrane contamination could be investigated by combining design equations of the ionomer and membrane contamination. The combining Da numbers for ionomer and membrane contamination could improve the model predictions. The contamination for multi compounds also could be investigated by combining design equations for different species. Once the design equations for multi-compounds are prepared, more precise predictions for leachate which includes many different species are allowed.

Future experimental work could compare the models. An experiment could be designed and performed for the purpose of obtaining the isotherms and diffusion coefficient of contaminants in Nafion[®] membrane at different temperature. These results will lead us to estimate the contamination impact in PEFMCs at different temperature conditions.

REFERENCES

1. M. L. Perry, T. F. Fuller, "A historical perspective of fuel cell technology in the 20th century," *J. Electrochem. Soc.*, 149, S59 (2002)
2. <http://www.europe.elecdesign.com>
3. R. Borup, J. Meyers, B. Pivovar, Y. Kim, R. Mukundan, N. Garland, D. Myers, M. Wilson, F. Garzon, D. Wood, P. Zelenay, K. More, K. Stroh, T. Zawodzinski, J. Boncella, J. E. McGrath, M. Inaba, K. Miyatake, M. Hori, K. Ota, Z. Ogumi, S. Miyata, A. Nishikata, Z. Siroma, Y. Uchimoto, K. Yasuda, K. Kimijima and N. Iwashita, "Scientific Aspects of Polymer Electrolyte Fuel Cell Durability and Degradation," *Chem. Rev.* 107, 3904-3951 (2007).
4. <http://www1.eere.energy.gov/hydrogenandfuelcells/mypp/2007>
5. J. Z. Tan, Y. J. Chao, J. W. Van Zee and W. K. Lee, "Degradation of elastomeric gasket materials in PEM fuel cells," *Mater. Sci. and Eng. A*, 445, 669–675 (2007).
6. T. Okada, Y. Ayato, H. Satou, M. Yuasa and I. Sekine, "The effect of impurity cations on the oxygen reduction kinetics at platinum electrodes covered with perfluorinated ionomer," *J. Phys. Chem. B*, 105, 6980-6986 (2001).
7. T. Okada, H. Satou and M. Yuasa, "Effects of additives on oxygen reduction kinetics at the interface between platinum and perfluorinated ionomer," *Langmuir*, 19, 2325-2332 (2003).
8. T. Okada, Y. Ayato, M. Yuasa, and I. Sekine, "The effect of impurity cations on the transport characteristics of perfluorosulfonated ionomer membranes," *J. Phys. Chem. B*, 103, 3315 (1999).
9. T. Okada, Y. Ayato, J. Dale, M. Yuasa, I. Sekine and O. A. Asbjornsen, "Oxygen reduction kinetics at platinum electrodes covered with perfluorinated ionomer in the presence of impurity cations Fe^{3+} , Ni^{2+} , and Cu^{2+} ," *Phys. Chem. Chem. Phys.*, 2, 3255-3261 (2000).
10. T. Okada, N. Arimura, H. Satou, M. Yuasa and T. Kikuchi, "Membrane transport characteristics of binary cation systems with Li^+ and alkali metal cations in perfluorosulfonated ionomer," *Electrochim. Acta*, 50, 3569-3575 (2005).
11. T. Okada, S. Moller-Holst, O. Gorseth and S. Kjelstrup, "Transport and equilibrium properties of Nafion membranes with H^+ and Na^+ ions," *J. Electroanal. Chem.*, 442, 137-145 (1998)

12. T. Okada, N. Nakamura, M. Yuasa, and I. Sekine, "Ion and water transport characteristics in membranes for Polymer Electrolyte Fuel Cells containing H^+ and Ca^{2+} cations," *J. Electrochem. Soc.*, 144, 2744-2750 (1997)
13. M. J. Kelly, G. Fafilek, J. O. Besenhard, H. Kronberger, G. E. Nauer, "Contaminant absorption and conductivity in polymer electrolyte membranes," *J. Power Sources*, 145 249 – 252 (2005).
14. M. J. Kelly, B. Egger, G. Fafilek, J. O. Besenhard, H. Kronberger, G. E. Nauer, "Conductivity of polymer electrolyte membranes by impedance spectroscopy with microelectrodes," *Solid State Ionics* 176 2111-2114 (2005).
15. H. Li, J. Gazzarri, K. Tsay, S. Wu, H. Wang, J. Zhang, S. Wessel, R. Abouatallah, N. Joos and J. Schrooten, "PEM fuel cell cathode contamination in the presence of cobalt ion (Co^{2+})," *Electrochim. Acta* 55, 5823-5830 (2010).
16. M. Sulek, J. Adams, S. Kaberline, M. Ricketts and J. R. Waldecker, "In-situ metal ion contamination and the effects on proton exchange membrane fuel cell performance," *J. Power Sources*, 196, 8967-8972 (2011).
17. H. Soto, W. K. Lee, J. W. Van Zee and M. Murthy, "Effect of transient ammonia concentrations on PEMFC performance," *Electrochem. Solid-State Letter*, 6, A133-135 (2003).
18. R. Mohtadi, W. K. Lee and J. W. Van Zee, "Assessing durability of cathodes exposed to common air impurities," *J. Power Sources*, 138, 216 (2004).
19. Y. Garsany, O. A. Baturina and K. E. Swider-Lyonsa, "Impact of sulfur dioxide on the oxygen reduction reaction at Pt/Vulcan carbon electrocatalyst," *J. Electrochem. Soc.*, 154, 7, B670-B675 (2007).
20. R. Mohtadi, W. K. Lee, S. Cowan, J. W. Van Zee and M. Murthy, "Effects of Hydrogen Sulfide on Performance of a PEMFC," *Electrochem. Solid-State Lett.*, 6(12) A272-A274 (2003).
21. T. Gu, W. K. Lee and J. W. Van Zee, "Quantifying the reverse water gas shift reaction inside a PEM fuel cell," *Appl. Catal. B-Environ.*, 56, 43-49, (2005).
22. Grot, W., To E.I. du Pont Nemours and Company, U.S. 3,718,627,1968
23. R. Halseid, P. J. S. Vie and R. Tunold, "Influence of ammonium on conductivity and water content of Nafion 117 membranes," *J. Electrochem. Soc.*, 151, A381-388 (2004).
24. F. A. Uribe and T. A. Zawodzinski Jr., "The effects of fuel impurities on PEM Fuel Cell performance," Paper #339, presented at the 200th ECS Meeting in San Francisco, CA, Sep. 2-7, 2001.

25. K. Hongsirikarn, J. Goodwin Jr., S. Greenway and S. Creager, "Influence of ammonia on the conductivity of Nafion membranes," *J. Power Sources*, 195, 30-38 (2010).
26. Masato Ohashi, Ph. D. dissertation, Department of Chemical Engineering, University of South Carolina (2008)
27. T. Zawodzinski, T. E. Springer, J. Davey, R. Jestel, C. Lopez, J. Valerio and S. Gottesfeld, "A comparative study of water uptake by and transport through ionomeric Fuel Cell membranes," *J. Electrochem. Soc.*, 140, 1981-1985 (1993).
28. M. C. Wintersgill and J. J. Fontanella, "Complex impedance measurements on Nafion[®]," *Electrochim. Acta*, 43, 1533-1538 (1998).
29. J. J. Fontanella, M. C. Wintersgill, R.S. Chen, Y. Wu and S.G. Greenbaum, "Charge transport and water molecular motion in variable molecular weight Nafion membranes: High pressure electrical conductivity and NMR," *Electrochim. Acta*, 40, 2321-2326 (1995).
30. S. J. Paddison, D.W. Reagor and T. A. Zawodzinski, "High frequency dielectric studies of hydrated Nafion," *J. Electroanal. Chem.*, 459, 91-97 (1998).
31. K. O'Leary, M. Budinski, B. Lakshmanan, "Methodologies for Evaluating Automotive PEM Fuel Cell System Contaminants," 2009 Canada-USA PEM Network Research Workshop, February 16, 2009
32. K. O'Leary and B. Lakshmanan, "*Methods for Screening Balance of Plant (BOP) Materials for Fuel Cell Contamination*," Paper #1036, presented at the 220th ECS Meeting & Electrochemical Energy Summit in Boston, MA, Oct. 13, 2011
33. C. S. Macomber, H. Wang, K. O'Neill, S. Coombs, G. Bender, B. Pivovar and H. N. Dinh, "Characterizing polymeric leachants for potential system contaminants of Fuel Cells contamination," *ECS Trans.*, **33**(1), 1637-1643 (2010).
34. C. S. Macomber, J. Christ, H. Wang, B. S. Pivovar and H. N. Dinh, "Characterizing leachant contaminants from Fuel Cell assembly aids, a prelude to effects on performance", *ECS Trans.*, 50(2), 603-618, (2013).
35. J. St.-Pierre, *Polymer Electrolyte Fuel Cell Durability* edited by F.N. Buchi, M. Inaba and T. J. Schmit, Springer, New York (2009).
36. http://www.hydrogen.energy.gov/pdfs/2011_budget_request_briefing.pdf
37. T. Okada, "Theory for water management in membranes for polymer electrolyte fuel cells Part 1. The effect of impurity ions at the anode side on the membrane performances," *J. Electroanal. Chem.*, 465, 1-17 (1999).
38. T. Okada, "Theory for water management in membranes for polymer electrolyte fuel cells Part 2. The effect of impurity ions at the cathode side on the membrane

- performances,” *J. Electroanal. Chem.*, 465, 18-29 (1999).
39. T. E. Springer and B. L. Kienitz, *Proton Exchange Membrane Fuel Cell: Contamination and Mitigation Strategies* edited by H. Li, S. Knights, Z. Shi, J. W. Van Zee, J. Zhang, p. 100, CRC press, New York (2010).
 40. B. L. Kienitz, H. Baskaran, T. A. Zawodzinski Jr., “Modeling the steady state effects of cationic contamination on polymer electrolyte membranes,” *Electrochimica Acta*, 54, 1671-1679 (2009).
 41. A. Z. Weber and C. Delacourt, “Mathematical modeling of cation contamination in a proton exchange membrane,” *Fuel Cells*, 8(6) 459-465 (2008).
 42. T. A. Greszler, T. E. Moylan and H. A. Gasteiger, “Handbook of Fuel Cells-Fundamentals, Technology and Application. Edited by W. Vielstich, H. A. Gasteiger, H. Yokokawa, Vol. 5: Advances in Electrocatalysis, Materials, Diagnostics and Durability, John Wiley & Sons, New York (2009).
 43. M. F. Serincan, U. Pasaogullari and T. Molter, “Modeling the cation transport in an operating polymer electrolyte fuel cell,” *Int. J. Hydrogen Energy*, 35, 5539-5551 (2010).
 44. J. St-Pierre, “PEMFC contamination model: Foreign cation exchange with ionomer protons,” *J. Power Sources*, 196, 6274-6283 (2011).
 45. J. St-Pierre, “PEMFC contamination tolerance limit – Foreign cation in ionomer,” *Int. J. Hydrogen Energy*, 36, 5527-5535 (2011).
 46. J. St-Pierre, N. Jia and R. Rahmani, “PEMFC contamination model: Competitive adsorption demonstrated with NO₂,” *J. Electrochem. Soc.*, 155, B315-B320 (2008).
 47. J. St-Pierre, “PEMFC contamination model: Competitive adsorption followed by an electrochemical reaction,” *J. Electrochem. Soc.*, 156, B291-300 (2009).
 48. J. Zhang, H. Wang, D. P. Wilkerson, D. Song, J. Shen and Z. Liu, “Model for the contamination of fuel cell anode catalyst presence of fuel stream impurities,” *J. Power Sources*, 147, 58-71 (2005).
 49. H. Cho, M. Jung, J. Navarro, M. Ohashi and J. W. Van Zee, “Aniline as a cationic and aromatic contaminant in PEMFCs contamination,” *ECS Trans.*, 33(1), 1627-1635 (2010).
 50. H. Cho, M. Ohashi and J. W. Van Zee, “The effect on PEMFC contamination of functional groups of some organic contaminants,” *ECS Trans.*, 41(1), 1487-1499 (2011).
 51. M. J. Martinez, S. Shimpalee and J. W. Van Zee, “Measurement of MacMullin numbers for PEMFC gas-diffusion media,” *J. Electrochem. Soc.*, 156, B80-B85 (2009).

52. M. J. Martinez, S. Shimpalee, J. W. Van Zee and A. J. Sakars, "Assessing methods and data for pore-size distribution of PEMFC gas-diffusion media," *J. Electrochem. Soc.*, 156, B558-B564 (2009).
53. M. J. Martinez, T. Cui, S. Shimpalee, S. Seraphin, B. Duong and J. W. Van Zee, "Effect of microporous layer on MacMullin number of carbon paper gas diffusion layer," *J. Power Sources*, 207, 91-100 (2012).
54. F. Helfferich, *Ion Exchange*, p157, Dover Publication Inc, New York (1995).
55. C. D. Holland and A. I. Liapis, *Computer Methods for Solving Dynamic Separation Problems*, p369, McGraw Hill Chemical Engineering Series, New York (1984)
56. H. L. Yeager and B. Kipling, "Ionic diffusion and ion clustering in a perfluorosulfonate ion-exchange membrane," *J. Phys. Chem.*, 83, 1836-1839 (1979).
57. H. L. Yeager and A. Steck, "Cation and water diffusion in Nafion ion exchange membranes: Influence of polymer structure," *J. Electrochem. Soc.*, 128, 1880-1884 (1981).
58. G. Xie and T. Okada, "Water transport behavior in Nafion 117 membranes," *J. Electrochem. Soc.*, 142, 3057-3062 (1995).
59. A. Gosawami, A. Acharya and K. Pandey, "Study of self-diffusion of monovalent and divalent cations in Nafion-117 ion-exchange membrane," *J. Phys. Chem. B*, 105, 9196-9201 (2001).
60. G. Suresh, Y. M. Scindia, A. K. Pandey and A. Gowasami, "Isotopic and ion-exchange kinetics in the Nafion-117 membrane," *J. Phys. Chem. B*, 108, 4104-4110 (2004).
61. C. R. C. Wang, J. W. Strojek, and T. Kuwana, "Spectrophotometric measurements of cation transport in Nafion," *J. Phys. Chem.*, 91, 3606-3612 (1987).
62. T. Nguyen and R. E. White, "A water and heat management model for proton exchange membrane fuel cells," *J. Electrochem. Soc.*, 140, 2178-2186 (1993).
63. S. Dutta, S. Shimpalee and J. W. Van Zee, "Three-dimensional numerical simulation of straight channel PEM fuel cells," *J. Appl. Electrochem.* 30, 135-146 (2000).
64. W-k. Lee, S. Shimpalee and J. W. Van Zee, "Verifying predictions of water and current distributions in a serpentine flow field Polymer Electrolyte Membrane Fuel Cell," *J. Electrochem. Soc.*, 150, A341-A348 (2003).
65. R. E. White, S. E. Lorimer and R. Darby, "Prediction of the current density at an electrode at which multiple electrode reactions occur under potentiostatic Control," *J. Electrochem. Soc.*, 130, 1123-1126 (1983).

66. D.B. Sepa, M.V. Vojnovic and A. Damjanovic, "Reaction intermediates as a controlling factor in the kinetics and mechanism of oxygen reduction at platinum electrodes," *Electrochim. Acta*, 26, 781-793 (1981).
67. K. Honsirikarn, X. Mo and J. G. Goodwin, "Esterification as a diagnostic tool to predict proton conductivity affected by impurities on Nafion components for proton exchange membrane fuel cells," *J. Power Sources*, 195, 3416-3424 (2010).
68. http://www1.eere.energy.gov/hydrogenandfuelcells/pdfs/htmwg_bekkedahl.pdf
69. J. M. LaManna and S. G. Kandlikar, "Determination of effective water vapor diffusion coefficient in pemfc gas diffusion layers," *Int. J. Hydrogen Energy*, 36, 5021-5029 (2011).
70. Q. Zhao, N. Carro, H. Y. Ryu and J. Benziger, "Sorption and transport of methanol and ethanol in H⁺-Nafion," *Polymer*, 53, 1267-1276 (2012).
71. C. M. Gates and J. Newman, "Equilibrium and Diffusion of Methanol and Water in a Nafion 117 Membrane," *AIChE Journal*, 46, 10, 2076-2085 (2000).
72. H. Cho, Md. Opu, M. Ohashi and J. W. Van Zee, "The contamination behavior of organic compounds on PEMFC," Paper#1295, presented at the 222nd ECS Meeting & Honolulu PRiME 2012, HI, Oct. 09, 2012.
73. Md. Opu, M. Ohashi, H. Cho, C. S. Macomber, H. N. Dinh, J. W. Van Zee "Understanding the effects of Contaminants from Balance of Plant Assembly Aids Materials on PEMFCs -In Situ Studies," *ECS Trans.*, 50(2), 619-634 (2013).
74. Allied Chemical National Aniline Division, *Aniline*, National Aniline Division, New York, 1964.
75. R. Halseid, P. J. S. Vie and R. Tunold, "Influence of ammonium on conductivity and water content of Nafion 117 membranes," *J. Electrochem. Soc.*, 151, A381-388 (2004).
76. O. Duman and E. Ayranci, "Structural and ionization effects on the adsorption behaviors of some anilinic compounds from aqueous solution onto high-area carbon-cloth," *J. Hazard. Mater.*, **120**, 173-181 (2005).
77. S. X. Huang, D. A. Fischer and J. L. Gland, "Correlation between the surface configurations and hydrogenolysis: Aniline on the Pt(111) surface," *J. Vac. Sci. Technol. A-Vac. Surf. Films*, **12**, 2164 (1994).
78. Z. Ogumi, K. Toyama, Z. I. Takehara, K. Katakura and S. Inuta, "Diffusion of aniline through perfluorosulfonate ion exchange membrane," *J. Membr. Sci.*, **65**, 205 (1992).
79. K. Katakura, M. Inaba, K. Toyama, Z. Ogumi and Z. Takehara, "Electrotransportation of aniline through a perfluorosulfonate ion-exchange membrane," *J. Electrochem. Soc.*, **141**, 1827 (1994).

80. H. N. Dinh and V. I. Birss, "Effect of substrate on polyaniline film properties a cyclic voltammetry and impedance study," *J. Electrochem. Soc.*, **147**, 3775 (2000).
81. H. N. Dinh and V. I. Birss, "The effect of film thickness and growth method on polyaniline film properties," *J. Electrochem. Soc.*, **147**, 3775 (2000).
82. H. N. Dinh, P. Vanysek and V. I. Birss, "The effect of film thickness and growth method on polyaniline film properties," *J. Electrochem. Soc.*, **146**, 3324 (1999).
83. D. E. Stilwell and S. M. Park, "Electrochemistry of conductive polymers: III. Some physical and electrochemical properties observed from electrochemically grown polyaniline," *J. Electrochem. Soc.*, **135**, 2491 (1988).
84. Z. Mandic, L. Duic and F. Kovacek, "The influence of counter-ions on nucleation and growth of electrochemically synthesized polyaniline film," *Electrochim. Acta*, **42**, 1389 (1997).
85. Handbook of Fuel Cells-Fundamentals, Technology and Application. Edited by W. Vielstich, H. A. Gasteiger, H. Yokokawa, Vol. 5: Advances in Electrocatalysis, Materials, Diagnostics and Durability, John Wiley & Sons, New York (2009).
86. T. R. Vidakovic, Ph.D. dissertation, Otto-von-Guericke-Universität Magdeburg (2004).
87. T. Okada, G. Xie and M. Meeg, "Simulation for water management in membranes for polymer electrolyte fuel cells," *Electrochim. Acta*, **43**, 2141 (1998).
88. T. Okada, J. Dale, Y. Ayato, O. A. Asbjornsen, M. Yuasa and I. Sekine, "Unprecedented effect of impurity cations on the oxygen reduction kinetics at platinum electrodes covered with perfluorinated ionomer," *Langmuir*, **15**, 8490 (1999).
89. K. Hongsirikarn, J. G. Goodwin, S. Greenway and S. Creager, "Effect of cations (Na^+ , Ca^{2+} , Fe^{3+}) on the conductivity of a Nafion membrane," *J. Power Sources*, **195**, 7213. (2010).
90. D. C. Harris, *Quantitative Chemical Analysis*, W. H. Freeman and Company, New York (2003).
91. D. L. Wood, J. Chlistunoff, J. Majewski and R. L. Borup, "Nafion structural phenomena at platinum and carbon interfaces," *J. Am. Chem. Soc.*, **131**, 18096 (2009).
92. A. P. Terzyk, "Molecular properties and intermolecular forces—factors balancing the effect of carbon surface chemistry in adsorption of organics from dilute aqueous solutions," *J. Colloid Interface Sci.*, **275**, 9 (2004).

93. B. G. Choi, H. Park, H. S. Im, Y. J. Kim and W. H. Hong, "Influence of oxidation state of polyaniline on physicochemical and transport properties of Nafion/polyaniline composite membrane for DMFC," *J. Membr. Sci.*, **324**, 102 (2008).
94. N. Gospodinova and L. Terlemezyan, "Conducting polymers prepared by oxidative polymerization: Polyaniline," *Prog. Polym. Sci.*, **23**, 1443 (1998).
95. D. E. Stilwell and S. M. Park, "Electrochemistry of conductive polymers: V. In situ spectroelectrochemical studies of polyaniline films," *J. Electrochem. Soc.*, **136**, 427 (1989).
96. G. Xie and T. Okada, "Water transport behavior in Nafion 117 membranes," *J. Electrochem. Soc.*, **142**, 3057 (1995).
97. Friedrich Helfferich, *Ion exchange*, p157, Dover publication inc, New York (1995)
98. R. E. White, S. E. Lorimer and R. Darby, "Prediction of the current density at an electrode at which multiple electrode reactions occur under potentiostatic Control," *J. Electrochem. Soc.*, **130**, 1123-1126 (1983).
99. T. Okada, Y. Ayato, J. Dale, M. Yuasa, I. Sekine and O. A. Asbjornsen, "Oxygen reduction kinetics at platinum electrodes covered with perfluorinated ionomer in the presence of impurity cations Fe^{3+} , Ni^{2+} , and Cu^{2+} ," *Phys. Chem. Chem. Phys.*, **2**, 3255-3261 (2000).
100. Q. Guo, R. Pollard, and J. Ruby, "Compatibility and durability of fuel cell materials," *ECS Trans.* **5**(1) 187-196 (2007).
101. J. St-Pierre, *Air impurities: Polymer electrolyte fuel cell durability* edited by F. Buchi, M. Inaba, T. J. Schmit, p. 289-321, Springer, New York (2009).
102. T. Okada, N. Nakamura, M. Yuasa and I. Sekine, "Ion and water transport characteristics in membranes for polymer electrolyte fuel cells containing H^+ and Ca^{2+} cations," *J. Electrochem. Soc.*, **144**, 2744 (1997).
103. T. Okada, "Theory for water management in membranes for polymer electrolyte fuel cells Part 2. The effect of impurity ions at the cathode side on the membrane performances," *J. Electroanal. Chem.*, **465**, 18-29 (1999).
104. K. Honsirikarn, X. Mo and J. G. Goodwin, "Esterification as a diagnostic tool to predict proton conductivity affected by impurities on Nafion components for proton exchange membrane fuel cells," *J. Power Sources*, **195**, 3416-3424 (2010).

105. W. P. Jencks and J. Regenstein, *Handbook of Biochemistry and Molecular Biology*, pp305-351, CRC Press, New York (2004).
106. K. Kortsdottir, R. W. Lindstrom, T. Akermarck, G. Lindbergh, "Influence of toluene contamination at the hydrogen Pt/C anode in a proton exchange membrane fuel cell," *Electrochim. Acta*, 55 (26) (2010).
107. D. M. Mohilner, R. N. Adams, and W. J. Argersinger, "Investigation of the Kinetics and Mechanism of the Anodic Oxidation of Aniline in Aqueous Sulfuric Acid Solution at a Platinum Electrode," *J. Am. Chem. Soc.*, 84, 3618 (1962).
108. J. Bacon and R. N. Adams, "Anodic oxidations of aromatic amines. III. Substituted anilines in aqueous media," *J. Am. Chem. Soc.*, 90, 6596 (1968).
109. Md. Opu, M. Ohashi, H. Cho, C. S. Macomber, H. N. Dinh, J. W. Van Zee "Understanding the effects of Contaminants from Balance of Plant Assembly Aids Materials on PEMFCs -In Situ Studies," *ECS Trans.*, 50(2), 619-634 (2013).
110. K. O'Leary, M. Budinski, B. Lakshmanan, "Methodologies for Evaluating Automotive PEM Fuel Cell System Contaminants," 2009 Canada-USA PEM Network Research Workshop, February 16, 2009.
111. C. S. Macomber, H. Wang, K. O'Neill, S. Coombs, G. Bender, B. Pivovar and H. N. Dinh, "Characterizing polymeric leachants for potential system contaminants of Fuel Cells contamination," *ECS Trans.*, 33(1), 1637-1643 (2010).
112. M. Jung, Ph. D. dissertation, Department of Chemical Engineering, University of South Carolina, 2010.
113. H. Cho, M. Jung, J. Navarro, M. Ohashi and J. W. Van Zee, "Aniline as a cationic and aromatic contaminant in PEMFCs contamination," *ECS Trans.*, 33(1), 1627-1635 (2010).
114. H. Cho, M. Ohashi and J. W. Van Zee, "The effect on PEMFC contamination of functional groups of some organic contaminants," *ECS Trans.*, 41(1), 1487-1499 (2011).
115. C. S. Macomber, H. Wang, K. O'Neil, J. Christ, M. Das, J. W. Van Zee, K. O'Leary and H. N. Dinh, "*Leachant Contaminants and Degradation Schemes of PEM Fuel Cell System Components*," paper #1040, presented at the 220th ECS Meeting & Electrochemical Energy Summit in Boston, MA, Oct. 12, 2011.

116. B.C. Challis and J. Challis, *The Chemistry of Amides* edited by J. Zabicky, p.731 Interscience, New York, 1970.
117. C. J. O'Connor, *Q. Rev.* 24, 553 (1970);
118. M. Liler, *Reaction Mechanisms in Sulfuric Acid*, p.189, Academic Press, New York. 1971.
119. G. B. Deacon, R. J. Phillips, "Diagnosis of the nature of carboxylate coordination from the direction of shifts of carbon-oxygen stretching frequencies," *Inorg. Chim. Acta.*, 104, 41-45 (1985).
120. T. Xue, R. B. Longwell and K. Osseo-Asare, "Mass transfer in Nafion membrane systems: Effects of ionic size and charge on selectivity," *J. Mem. Sci.*, 58 175-189 (1991).
121. R. Buzzoni, S. Bordiga, G. Ricchiardi, G. Spoto, and A. Zecchina, "Interaction of H₂O, CH₃OH, (CH₃)₂O, CH₃CN, and pyridine with the superacidic perfluorosulfonic membrane Nafion: An IR and Raman study," *J. Phys. Chem.*, 99, 11937-11951 (1995).
122. A. Gruger, A. Regis, T. Schmatko, P. Colomban, "Nanostructure of Nafion® membranes at different states of hydration: An IR and Raman study," *Vib. Spectrosc.*, 26, 215-225 (2001).
123. K. A. Mauritz and R. B. Moore, "State of Understanding of Nafion," *Chemical reviews*, 104, 4535-4585 (2004).
124. H. K. Reimschuessel, *Isomerization Polymerization of Lactams*, ACS symposium series, 59, 233-250 (1977).
125. Y. Want, Y. Kawano, S. R. Aubuchon, and R. A. Palmer, "TGA and time-dependent FTIR study of dehydrating Nafion-Na membrane," *Macromolecules*, 2003, 36, 1138-1146 (2003).
126. M. K. Petersen, A. J. Hatt and G. A. Voth, "Orientational Dynamics of Water in the Nafion Polymer Electrolyte Membrane and Its Relationship to Proton Transport," *J. Phys. Chem. B*, 112, 7754-7761 (2008).
127. W. Paik, S. Han, W. Shin, and Y. Kim, "Adsorption of carboxylic acids on Gold," *Langmuir*, 19, 4211-4216 (2003).
128. T. E. Springer, T. A. Zawodzinski, and S. Gottesfeld, "Polymer Electrolyte Fuel Cell Model," *J. Electrochem. Soc.*, 138, 2334-2342 (1991).

129. J. T. Hinatsu, M. Mizuhata and H. Takenaka, "Water uptake of perfluorosulfonic acid membranes from liquid water and water vapor," *J. Electrochem. Soc.*, 141, 1493-1498 (1994).
130. A. Weber, M. M. Mench, J. P. Meyer, P. N. Ross, J. T. Gostick and Q. Liu, "Redox flow batteries: a review," *J. Appl. Electrochem.* 41, 1137-1164 (2011).
131. M. Bartolozzi, "Development of redox flow batteries. A historical bibliography," *J. Power Sources*, 27 219-234 (1989).
132. A. Parasuraman, T. M. Lim, C. Menictas and M. Skyllas-Kazacos, "Review of material research and development for vanadium redox flow battery applications," *Electrochim. Acta*, <http://dx.doi.org/10.1016/j.bbr.2011.03.031>
133. Z. Xiea, Q. Liua, Z. Changa and X. Zhanga, "The developments and challenges of cerium half-cell in zinc–cerium redox flow battery for energy storage," *Electrochim. Acta*, 90, 695-714 (2013).
134. P. Leung, X. Li, C. P. Leon, L. Berlouis, C. T. J. Low and F. C. Walsh, "Progress in redox flow batteries, remaining challenges and their applications in energy storage," *RSC Advance*, 2, 10125-10156 (2012).
135. D. H. Doughty, P. C. Butler, A. A. Akhil, N. H. Clark, and J. D. Boyes "Batteries for large-scale stationary electrical energy storage," *The Electrochemical Society Interface* Fall 2010.
136. T. Okada, Y. Ayato, M. Yuasa, and I. Sekine, "The effect of impurity cations on the transport characteristics of perfluorosulfonated ionomer membranes," *J. Phys. Chem. B*, 103, 3315 (1999).
137. T. Okada, Y. Ayato, J. Dale, M. Yuasa, I. Sekine and O. A. Asbjornsen, "Oxygen reduction kinetics at platinum electrodes covered with perfluorinated ionomer in the presence of impurity cations Fe^{3+} , Ni^{2+} , and Cu^{2+} ," *Phys. Chem. Chem. Phys.*, 2, 3255-3261 (2000).
138. M. J. Kelly, G. Fafilek, J. O. Besenhard, H. Kronberger, G. E. Nauer, "Contaminant absorption and conductivity in polymer electrolyte membranes," *J. Power Sources*, 145 249 – 252 (2005).
139. M. J. Kelly, B. Egger, G. Fafilek, J. O. Besenhard, H. Kronberger, G. E. Nauer, "Conductivity of polymer electrolyte membranes by impedance spectroscopy with microelectrodes," *Solid State Ionics* 176 2111-2114 (2005).
140. M. Gattrell, J. Park, B. MacDougall, J. Apte, S. McCarthy and C. W. Wu, "Study of the mechanism of the vanadium 4+/5+ redox reaction in acidic

- solutions,” *J. Electrochem. Soc.*, 151, A123 (2004).
141. H. Li, J. Gazzarri, K. Tsay, S. Wu, H. Wang, J. Zhang, S. Wessel, R. Abouatallah, N. Joos and J. Schrooten, “PEM fuel cell cathode contamination in the presence of cobalt ion (Co^{2+}),” *Electrochim. Acta* 55, 5823-5830 (2010).
 142. T. Okada, Y. Ayato, M. Yuasa, and I. Sekine, “The effect of impurity cations on the transport characteristics of perfluorosulfonated ionomer membranes,” *J. Phys. Chem. B*, 103, 3315 (1999).
 143. T. Sukkar and M. Skyllas-kazacos, “Membrane stability studies for vanadium redox cell applications,” *J. Appl. Electrochem.* 34: 137-145 (2004).
 144. T. Mohammadi and M. Skyllas Kazcos, “Evaluation of the chemical stability of some membranes in vanadium solution,” *J. Appl. Electrochem.*, 27:153 (1997).
 145. D. Oei, “Permeation of vanadium cations through anionic and cationic membranes,” *J. appl. Electrochem.* 15, 231-235 (1985).
 146. . C. Sun, J. Chen, H. Zhnag, X. Han and Z. Luo, “Investigations on transfer of water and vanadium ions across Nafion membrane in an operating vanadium redox flow battery,” *J. Power Sources*, 195, 890-8997 (2010).
 147. G. Oriji, Y. Jatayama and T. Miura, “Investigations on V(IV)/V(V) and V(II)/V(III) redox reactions by various electrochemical methods,” *J. Power Sources*, 139, 321-324 (2005).
 148. G. Oriji, “Investigation on V(IV)/V(V) species in a vanadium redox flow battery,” *Electrochim. Acta*, 49, 3091 (2004).
 149. M. Vijayakumar, S. D. Burton, C. Huang, L. Li, Z. Yang, G. L. Graff, J. Liu, J. Hu, M. Skyllas-Kazacos, “Nuclear magnetic resonance studies on vanadium(IV) electrolyte solutions for vanadium redox flow battery,” *J. Power Sources*, 195, 7709 (2010).
 150. Friedrich Helfferich, *Ion Exchange*, p157, Dover publication inc, New York (1995).
 151. M. Ohashi, Ph. D. dissertation, Department of Chemical Engineering, University of South Carolina (2008).
 152. C. F. Baes and R. E. Mesmer, *The Hydrolysis of Cations*, John Wiely & Sons, New York (1976).

153. F. A. Cotton, *Advanced Inorganic Chemistry*, 5th edition, John Wiley & Sons, New York, (1988).
154. M. Pourbaix, *Atlas of Electrochemical Equilibria in Aqueous Solutions*, NACE International Cebelcor, 2nd edition, (1974).
155. K. A. Mauritz and R. B. Moore, "State of understanding of Nafion," *Chemical reviews*, 104, 4535-4585 (2004).

APPENDIX A – ESTIMATION OF RH CHANGES IN THE CHANNEL AND SCALING FACTOR

Water dilution

Table A1 shows the initial (i.e., feed) and the change of total moles of species on cathode. The maximum RHs of the inlet and outlet of channels are also listed in Table A1 at I=10A, P=150/150kPa, stoic=2.0/2.0. The calculation shows that the dilution effect on contaminant by the water can be negligible (i.e., $\frac{\Delta n_T}{n_{T0}}=0.1$) and the water saturation at the interface of the membranes on cathode may start over RH=50% (inlet).

Table A1. Total moles change of species and the range of RHs

RH _{in} [%]	n _{T0} [mol/s]	$\alpha^{41,42,43}$	Δn_T [mol/s]	RH _{out} [%]
25	2.68E-04	-5.00E-02	2.07E-05	74.8
32	2.74E-04	4.24E-02	3.03E-05	77.7
45	2.87E-04	2.14E-01	4.81E-05	82.9
50	2.93E-04	2.80E-01	5.49E-05	84.9

The water vapor concentration and RH can define:

$$C_w = \frac{n_w}{n_T} \frac{P}{RT} = \frac{n_w}{n_w + n_{O_2} + n_{N_2} + n_A} \frac{P}{RT} \quad [A.1]$$

$$\frac{RH}{100} = \frac{n_w}{n_T} \frac{P}{P^{sat}} \quad [A.2]$$

The molar flow rate for each species at inlet of channel can define as

$$n_{H_2} = s \frac{I}{2F}, \quad n_{O_2} = s \frac{I}{4F}, \quad n_{N_2} = s \frac{0.79}{0.21} \frac{I}{4F} \quad [A.3]$$

From the Eq. [36], the difference of water vapor concentrations between the interface and

the channel as $\Delta 10\%$ (i.e., $\frac{C_w^* - C_w}{C_w} \times 100$) with selected α (shown in Table A1). In other

words, we can speculate that the 10% of RH difference exists between the interface (electrode and membrane) and the channel. Thus, the water saturation may start at the interface of membrane with RH=90% of the channel condition. Thus, we can assume that the presented model can be applicable less than inlet 50% RHs at above conditions.

Scaling factor calculation

$$\zeta = y \left(\frac{a\nu}{3D_R} \right)^{1/3} \sqrt{\frac{\Omega}{\nu}} = 0.087 \text{ cm} \quad [B.1]$$

$a = 0.51$

ζ =dimensionless concentration for boundary layer=1.3

ν = kinematic viscosity of water at 20°C=1.004 [cm²/s]

D_R = diffusion coefficient of reactant [1×10^{-5} cm²/s]

Ω = angular velocity=2400 rpm=0.0636 [rad/s]

$$\frac{\Psi_{ex}}{\Psi_{in}} = \frac{C_{A0,ex}}{C_{A0,in}} \frac{h_{ex} (= y) A_{ex}}{h_{in} A_{in}} \frac{C_{S,in}(t=0)}{C_{S,ex}(t=0)} = 1 \quad [B.2]$$

The scaling factor is obtained as 40 by the Eq. [B.2].

$$A_{\text{ex}}=0.19\text{cm}^2, A_{\text{in}}=50\text{cm}^2$$

$$\text{Pt loading, ex-situ}=0.02\text{mg/cm}^2, \text{ in-situ}=0.4\text{mg/cm}^2$$

$$h_{\text{ex}}=0.087 \text{ cm}, h_{\text{in}}=0.084 \text{ cm}$$

APPENDIX B – MATLAB CODE FOR THE PREDICTION

Adsorption/absorption mechanism

```
function File name
    NV = 2; % number of dependent variables

    NP = 101; % number of node points
    NEQ = NV*NP - 1; % number of odes

    D = 9.21e-3;
    w = 1.74;
    G = 0.363;
    p = 7.18e-4;
    B = 0.60;
    u10 = 1.0;

    L = 1.0;
    hh = L/(NP-1);
    tf = 41935;
    NT = 8387;
    xx = linspace(0,L,NP);

    timearr = linspace(0,tf,NT);
    y0 = zeros(NEQ,1);
    MM = eye(NEQ,NEQ);
    opt = odeset('RelTol', 1.0e-6, 'AbsTol', 1.0e-6, 'Mass', MM);

    [T,Y] = ode15s(@odefun,timearr,y0,opt,D,w,p,G,B,u10,hh,NP,NEQ);

    u1 = Y(:,1:NP-1);
    u2 = Y(:,NP:NEQ);

    save('T_Pt_26DAT_a_t5.txt','T','-double','-ascii','-tabs');
    save('Y_Pt_26DAT_a_t5.txt','Y','-double','-ascii','-tabs');

end

function dy = odefun(t,y,D,p,w,B,G,u10,hh,NP,NEQ)
    dy = zeros(NEQ,1);

    %  o-----o-----o-----o-----o-----o-----o-----o-----o-----o-----
    %  -----o-----o-----o-----o-----o
    %  u10   u1(1)   u1(2)   u1(3)
    u1(NP-1)
```

```

% u2(1)   u2(2)   u2(3)   u2(4)
u2(NP)

u1 = y(1:NP-1);
u2 = y(NP:NEQ);

dy(1) = -(u1(2)-u10)/(2.0*hh) + w*D*(u2(2)-u1(1));
for i = 2 : NP - 2
    dy(i) = -(u1(i+1)-u1(i-1))/(2.0*hh) + w*D*(u2(i+1)-u1(i));
end
i = NP - 1;
dy(i) = -(3.0*u1(i)-4.0*u1(i-1)+u1(i-2))/(2.0*hh) + w*D*(u2(i+1)-
u1(i));

i = 1;
dy(NP-1+i) = -p*D*w*(u2(i)-u10)*(1+G*u2(i))*(1+G*u2(i))/(B*G);
for i = 2 : NP
    dy(NP-1+i) = -p*D*w*(u2(i)-u1(i-
1))*(1+G*u2(i))*(1+G*u2(i))/(B*G);
end

end

```

Ion-exchange mechanism

```

function file name
    NV = 2; % number of dependent variables

    NP = 101; % number of node points
    NEQ = NV*NP - 1; % number of odes

    D = 4.0e-3;
    p = 1.1e-3;
    w = 1.74;
    G = 72;
    u10 = 1.0;

    L = 1.0;
    hh = L/(NP-1);
    tf = 51426;
    NT = 8571;
    xx = linspace(0,L,NP);

    timearr = linspace(0,tf,NT);
    y0 = zeros(NEQ,1);
    MM = eye(NEQ,NEQ);
    opt = odeset('RelTol', 1.0e-6, 'AbsTol', 1.0e-6, 'Mass', MM);

    [T,Y] = ode15s(@odefun,timearr,y0,opt,D,p,w,G,u10,hh,NP,NEQ);

    u1 = Y(:,1:NP-1);
    u2 = Y(:,NP:NEQ);

```

```

save('T_S23_ANI_0401_t6_c.txt','T','-double','-ascii','-tabs');
save('Y_S23_ANI_0401_t6_c.txt','Y','-double','-ascii','-tabs');

figure(1)
plot(T,u2(:,2))
figure(2)
plot(xx',u2(end,1:NP)')

end

function dy = odefun(t,y,D,p,w,G,u10,hh,NP,NEQ)
    dy = zeros(NEQ,1);

%  o-----o-----o-----o-----o-----o-----o-----o-----o-----
%  -----o-----o-----o-----o-----o
%  u10    u1(1)    u1(2)    u1(3)
u1(NP-1)
% u2(1)   u2(2)   u2(3)   u2(4)
u2(NP)

    u1 = y(1:NP-1);
    u2 = y(NP:NEQ);

    dy(1) = -(u1(2)-u10)/(2.0*hh) + w*D*(u2(2)-u1(1));
    for i = 2 : NP - 2
        dy(i) = -(u1(i+1)-u1(i-1))/(2.0*hh) + w*D*(u2(i+1)-u1(i));
    end
    i = NP - 1;
    dy(i) = -(3.0*u1(i)-4.0*u1(i-1)+u1(i-2))/(2.0*hh) + w*D*(u2(i+1)-
u1(i));

    i = 1;
    dy(NP-1+i) = -D*w*p/G*(u2(i)-u10)*(u10+(G-1)*u2(i))*(u10+(G-
1)*u2(i));
    for i = 2 : NP
        dy(NP-1+i) = -D*w*p/G*(u2(i)-u1(i-1))*(u1(i-1)+(G-
1)*u2(i))*(u1(i-1)+(G-1)*u2(i));
    end

end

end

```

APPENDIX C – CALCULATION OF AMMONIA FEEDING INTO RDE

The total amount of ammonia feeding in RDE system can be calculated as assumed by ideal gas law. For example, total moles of feeding ammonium gas (997ppm) for 140sec with 60cc/min at standard condition, can calculate as following.

$$PV = nRT \quad [C.1]$$

$$V = \frac{nRT}{P} = \frac{1mol \times 0.082atm \cdot L / K \cdot mol \times (273.15 + 23)K}{1atm} = 24.3L \quad [C.2]$$

The volume of 1mole of ammonia gas was calculated with assumption of ideal gas law so that we can find total amount of feeding ammonia gas by multiple of the rate of ammonia gas and flow rates of ammonia gas.

$$1 \text{ mole ideal gas} = \frac{1}{24.3} \text{ moles} / L \quad [C.3]$$

$$997 \text{ ppm} = \frac{997}{10^6} \times \frac{1}{24.3} \times 10^6 = 41.0 \text{ moles} / L \quad [C.4]$$

$$41.0 \text{ moles} / L \times 60 \text{ cc} / \text{min} \times 140 \text{ sec} \cdot \text{min} / 60 \text{ sec} = 5.7 \text{ mol} \quad [C.5]$$

Based on this assumption, we can estimate the monolayer of feeding ammonia gas with ECSA of Pt/C electrode in Figure 6.9c.

APPENDIX D – DIFFUSION COEFFICIENTS FOR CATIONS

Table D 1. Literature review of diffusion coefficient for cations in PFSA membrane

Experimental Techniques	Author	Journal	Ion	Diffusivity $\times 10^6 [\text{cm}^2/\text{s}]$			Remark
				T=0°C	25°C	40°C	
Radiotracer permeation method	H. L. Yeager and A. Steck	J. Electrochem. Soc., Volume 128, Issue 9, pp. 1880-1884 (1981)	Na ⁺	0.278	1.12	1.49	after 2 years in as-received form
			Cs ⁺	0.052	0.170	0.301	
	Grrald Pourcelly et al.	Journal of Membrane Science 110 (1996) 69-78	Na ⁺ Ca ²⁺		1.7 0.34		
	Anne-Laure Rollet et al.	J. Phys. Chem. B 2004, 108, 1130-1136	N(CH ₃) ₄ ⁺		0.2 - 0.3/0.09		Dpr/Dtr, sulponated Polyimid membrane /EW = 792 g/equiv Dtr
			Na ⁺		0.09 - 0.1		
Streaming potential method	Gang Xie and Tatsuhiro Okada	J. Electrochem. Soc., Vol. 142, No. 9, September 1995, p3057	Li ⁺		10.3		N117
			Na ⁺		13.3		
			K ⁺		19.6		
			Rb ⁺		20.7		
			Cs ⁺		20.6		
			Mg ²⁺		7.1		
			Ca ²⁺		7.9		

			Sr ²⁺		7.9		
			Ba ²⁺		8.5		
Nonstationary radiotracer diffusion method	A. Goswami, Anjali Acharya, and A. K. Pandey	J. Phys. Chem. B 2001, 105, 9196-9201	Ag ⁺		1.61		N117 2009. published inter diffusion
			Na ⁺		1.03		
			K ⁺		0.73		
			Cs ⁺		0.194		
			Zn ²⁺		0.32		
			Ca ²⁺		0.25		
			Sr ²⁺		0.16		
			Ba ²⁺		0.146		
Pulsed-Field Gradient nuclear magnetic resonance spectroscopy	Anne-Laure Rollet et al.	J. Phys. Chem. B 2001, 105, 4503-4509	N(CH ₃) ₄ ⁺		0.20		molarity of N(CH ₃) ₄ Cl 0.1 - 0.5[mol/kg] molarity of N(CH ₃) ₄ Cl 1.0 - 2.0[mol/kg]
			N(CH ₃) ₄ ⁺		0.12		
	Morihiro Saito et al.	J. Phys. Chem. B, Vol. 108, No. 41, 2004 16064-16070	Li ⁺		1.4		Li-form N117
			Li ⁺		1.2 - 2.0		Li-Flemion
	Anne-Laure	J. Phys. Chem. B 2004, 108, 1130-	N(CH ₃) ₄ ⁺		0.2 - 0.3/0.09		Dpr/Dtr, sulponated

	Rollet et al.	1136					Polyimid membrane /EW = 792 g/equiv
	Thomas A. Zawodzinski	J. Phys. Chem. 1991, 95, 6040-6044	H ⁺		0.6 - 5.8		2-14 water molecules per sulfonate
Forward and Reverse (in Parentheses) Ion-Exchange Measurement	Zdenek Samec' and Antonin Trojhnek	The Journal of Physical Chemistry, Vol. 98, No. 25, 1994 6352-6358	Li ⁺ Na ⁺ K ⁺ Rb ⁺ Cs ⁺ Ru(bpy) ₃ ²⁺		0.17(0.37) 0.68(0.30) 0.68 0.93 1.06(0.059) 2.80		N117
the isotopic-exchange method in the absence of H ⁺ ions	G. Suresh et al.	J. Phys. Chem. B 2004, 108, 4104-4110	Cs ⁺ Cu ²⁺ Eu ³⁺		0.194 0.290 0.045		N117
Spectrophotometric Measurement	C. R. Chris, Theodore Kuwana	J. Phys. Chem. 1987, 91, 3606-3612	Co ²⁺ Cu ²⁺	pH = 0 1 2 pH = 0 1	3.55 2.03 0.604 2.93 3.17		N117

			Cr ³⁺	2 3 pH = 0 1 2 3	0.673 0.786 3.36 1.01 0.598 0.358		
Conductivity measurement	P. Millet et al.	JOURNAL OF APPLIED ELECTROCHEMISTRY 25 (1995) 227-232	Na ⁺ [Pt(NH ₃) ₄] ₂₊ OH ⁻		4.5 0.52 0.60		D _{NaBH₄} = 4.9x 10 ⁻⁷
	Kuo-Lin Huang et.al	Ind. Eng. Chem. Res. 2003, 42, 3620-3625	HSO ₄ ⁻ Cr(VI)		1.08 0.806		Anion transport @ low pH, a high ionic strength
Simulation	Aleksey Vishnyakov and Alexander V. Neimark	J. Phys. Chem. B 2001, 105, 9586-9594	K ⁺	5% 12.5% 17.0%	1.7 4.7 10.1		via water contents

Table D 2. Comparison of diffusion coefficients for various cations in Nafion® membrane

Experiment Technique	Dx10 ⁻⁶ [cm ² /s]	Temperature				Remark
		0°C	22°C	40°C	70°C	
Mass uptake	NH ₄ ⁺	-	2.57	-	11.0	University of South Carolina
	Ca ²⁺	-	2.20	-	7.0	
	Na ⁺	-	5.50	-	16.0	
Radiotracer permeation	Na ⁺	0.278	1.12	1.49	-	H.L.Yeager et al.
	Na ⁺	-	1.7	-	-	Pourcelly et al.
	Ca ²⁺	-	0.34	-	-	
	Na ⁺ _(Dtr)		0.1			Anne-Laure Rollet et al.
Nonstationary radiotracer diffusion	Na ⁺	-	1.03	-	-	A.Goswami et al.
	Ca ²⁺	-	0.25	-	-	
PFG-NMR	H ⁺	-	0.6 - 5.8	-	-	Zawodzinski et al.
	Li ⁺	-	1.2 - 2.0	-	-	Morihiro Saito et al.
Ion exchange	Na ⁺	-	0.68(0.30)	-	-	Zdenek Samec et al.
	Li ⁺	-	0.17	-	-	
	K ⁺	-	0.68	-	-	
	Cu ²⁺	-	0.29	-	-	G. Suresh et al.
Conductivity	Na ⁺		4.5			P. Millet et al.
Streaming potential method	Li ⁺	-	10.3	-	-	Gang Xie et al.
	Na ⁺	-	13.3	-	-	
	K ⁺	-	19.6	-	-	
	Ca ²⁺	-	7.9	-	-	

APPENDIX E – RAW DATA FOR VANADIUM ABSORPTION

Table E.1 Raw data for vanadium absorption measurement by AA, and UV-vis. (shown in Figure 7.1)

	pH	Concentration [N]		The ionic fraction of vanadium in acid solution	The measured amount of vanadium in N115 [μmol]	Equivalent vanadium in N115 [μmol]	The ionic fraction of vanadium in N115
		V	H ₂ SO ₄				
VCl (s) / V ²⁺	2.35 ~2.90	0.027	0.240	0.10	14	28	0.16
		0.086	0.200	0.30	30	60	0.33
		0.151	0.151	0.50	29	58	0.32
		0.233	0.100	0.70	31	62	0.34
		0.451	0.050	0.90	29	58	0.32
V ₂ O ₃ (s) / V ³⁺	1.04 ~2.00	0.01	0.09	0.09	4	12	0.06
		0.03	0.07	0.30	12	36	0.17
		0.05	0.05	0.50	15	45	0.22
		0.075	0.025	0.75	16	48	0.28
		0.09	0.01	0.90	16	48	0.29
VOSO ₄ (aq)/ VO ²⁺	1.1 ~2.7	0.4	3.6	0.10	4	9	0.05
		1.2	2.8	0.30	7	14	0.07
		2.0	2.0	0.50	9	18	0.09
		2.8	1.2	0.70	10	20	0.10
		3.6	0.4	0.90	12	24	0.12
V ₂ O ₅ (s) / VO ₂ ⁺	-0.28 ~0.07	0.005	4.395	0.001	1	1	0.01
		0.22	4.18	0.05	4	4	0.02
		0.7	3.7	0.16	4	4	0.03
		0.9	3.5	0.21	5	5	0.03

Capacity of N115 sample = 180 μmol

Table E.2 Raw data for vanadium absorption measurement by AA, and UV-vis. (shown in Figure 7.2)

	pH	Concentration [N]		The ionic fraction of vanadium in acid solution	The measured amount of vanadium in N115 [μmol]	Equivalent vanadium in N115 [μmol]	The ionic fraction of vanadium in N115
		V	H ₂ SO ₄				
V ₂ O ₃ (s)	1.34 ~2.30	0.009	0.091	0.09	5	15	0.08
		0.015	0.085	0.15	7	21	0.12
		0.03	0.07	0.3	10	30	0.17
		0.050	0.05	0.5	13	39	0.22
	1.04~ 2.00	0.01	0.09	0.09	4	12	0.06
		0.03	0.07	0.30	12	36	0.17
		0.05	0.05	0.50	15	45	0.22
		0.075	0.025	0.75	16	48	0.28
		0.09	0.01	0.90	17	51	0.29
	-0.27 ~0.30	0.3	3.7	0.08	1	3	0.02
		0.6	3.4	0.15	4	12	0.06
		1.2	2.8	0.3	7	21	0.12
		2.4	1.6	0.6	14	42	0.23
		3.0	1.0	0.75	17	51	0.28

Capacity of N115 sample = 180 μmol

VITA

Hyun-Seok Cho was born in Suwon, Gyeonggi in Korea to Ki-Young Cho and Myungha Park on December 3, 1980. He graduated from Kwonsun High School in February 1999 and from the Sogang University in February 2005 with a B.S. (*Magna Cum Laude*) in Chemical Engineering.

The author worked for Samsung SDI Co., Ltd. in Yongin, Korea during the summer of 2004 for internship for Portable Fuel Cell Project in Corporate R&D Center. In August 2005, the author joined the Samsung SDI Co., Ltd and began work as an associate research engineer for Portable Fuel Cell Project in the Energy Lab of the Corporate R&D Center. During his stay with Samsung SDI Co., Ltd., the author optimized and developed the automated roll-to-roll MEA fabrication units and also analyzed rheological properties of Pt catalyst paste slurry for Direct Methanol Fuel Cell (DMFC).

The author left Samsung SDI Co., Ltd. in April 2007 and began to work at Korea Electronics Technology Institute (KETI) in Seongnam, Korea before beginning graduate studies in Chemical Engineering at University of South Carolina in Columbia SC. While at KETI, he involved in the project of the carbon nano tube (CNT)-back light unit development using writing method. He began the graduate studies (Ph.D.) in August 2008 and the research topic included the modeling and experimental works about the contamination studies in PEMFCs. The author has accepted an appointment as post doctor of Engineering in the Department of Chemical and Biological Engineering at the University of Alabama in Tuscaloosa, AL.

The author's permanent address is: 68-10, 301 Bansong, Hwaseong, Gyeonggi, S. Korea